TUDelft

Delft University of Technology

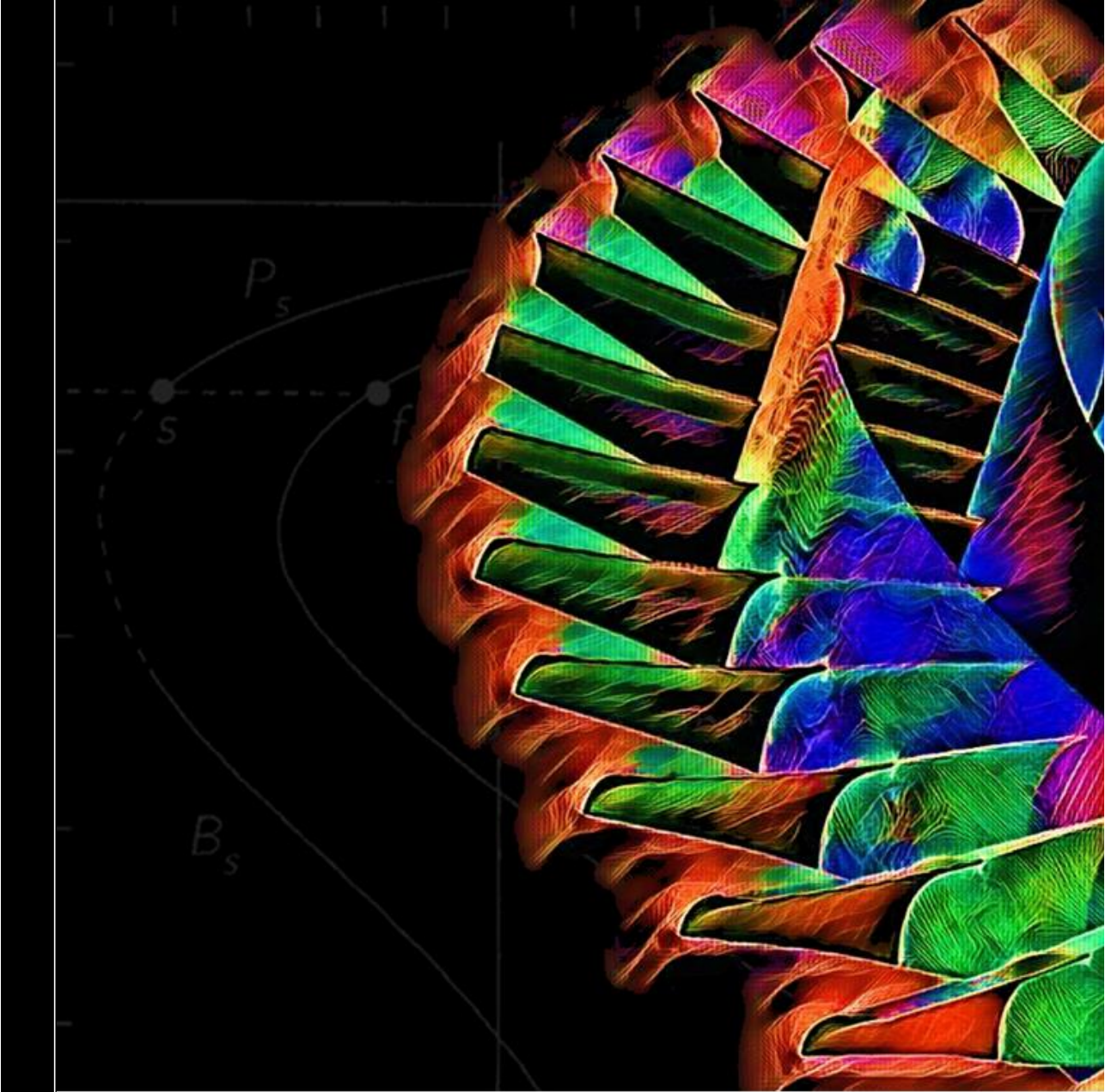# Numerical investigation of dense condensing flows for next-generation power units

Azzini, Lucia

Important note
To cite this publication, please use the final published version (if applicable).
Please check the document version above.

Numerical investigation of dense condensing flows for next-generation power units

Lucia Azzini

Numerical investigation of dense condensing flows for next-generation power units

NUMERICAL INVESTIGATION OF DENSE CONDENSING FLOWS FOR NEXT-GENERATION POWER UNITS

Dissertation

for the purpose of obtaining the degree of doctor
at Delft University of Technology
by the authority of the Rector Magnificus prof.dr.ir. T.H.J.J. van der Hagen
chair of the Board for Doctorates
to be defended publicly on
Wednesday 6th March 2019 at 12:30 o'clock

by

Lucia AZZINI

Dottore magistrale in ingegneria meccanica, Universita degli studi di Brescia, Italy
born in Asola, Italy.

This dissertation has been approved by the promotors.

Composition of the doctoral committee:

Rector Magnificus   chairperson
Prof. dr. P. Colonna   Technische Universiteit Delft, promotor
Dr. M. Pini   Politecnico di Milano, copromotor

Independent members:

Prof. dr. S. Hickel	Technische Universiteit Delft
Prof. dr. F. di Mare	Ruhr-Universität Bochum
Prof. dr. ir. Thomas Thiemann	Siemens energy
Dr. ir. R. Pecnik	Technische Universiteit Delft
Dr. ir. V.I. Kalikmanov	Technische Universiteit Delft
Prof. dr. ir. L.L.M. Veldhuis	Technische Universiteit Delft (reserve)

Engineers have the power to destroy entropy,
as long as they set a suitable engineering accuracy.

CONTENTS

LIST OF FIGURES

LIST OF TABLES

NOMENCLATURE

Acronyms		c	Interpolation coefficient for the empirical corrections $r_{\sigma,J,G}$
BPR	By-Pass Ratio		
CCE	Combined-Cycle Engine		
DA	Discrete Adjoint	$c1$	A matrix component
EoS	Equation of State	$c2$	$|A|$ matrix component
FD	Finite Differences	D	Diameter
FFD	Free-Form Deformation	e	Internal energy
FPR	Fan Pressure Ratio	$F, \mathbf{F}$	Numerical flux
GDE	General Dynamic Equation	f	Distribution function
HEX	Heat EXchanger	G	Growth rate
HP	High pressure	G_{s}	Non-corrected growth rate
IRE	Intercooled Recuperative Engine	$\mathfrak{G}$	Generic function to calculate the system solution
LP	Low pressure	h	Enthalpy
NTU	Number of Transfer Units	I	Turbulence intensity
OPR	Overall Pressure Ratio	J	Nucleation rate
ORC	Organic Rankine cycle	J_{s}	Non-corrected nucleation rate
SA	Spalart-Allmaras turbulence model	$\mathfrak{J}$	Objective function
SFC	Specific fuel consumption	k	thermal conductivity
SLSQP	Sequential Least SQuares Programming	$k_{1,2}$	Coefficients for the Wilson point semi-analytical model
TIT	Turbine Inlet Temperature	k_{b}	Boltzmann constant
WHR	Waste Heat Recovery	k_G	Growth rate correction factor
Latin letters		k_{σ}	Surface tension correction factor
A	Numerical flux jacobian		
A_{hex}	Heat transfer area	L	Lagrangian function
Ar	Aspect ratio	$\dot{L}$	Latent heat
a	Interpolation coefficient for the empirical corrections $r_{\sigma,J,G}$	L_{eig}	Left eigenvectors matrix
		M	Mach number
		$\mathbf{M}$	Function for the mesh deformation algorithm
$a1$	A matrix component		
$a2$	$|A|$ matrix component	MM	Molecular mass
A_{c}	Cross sectional area	m	Mass
B_j	Surface tension coefficient	$\dot{m}$	Mass flow rate
b	Interpolation coefficient for the empirical corrections $r_{\sigma,J,G}$	N	Droplet number per unit total mass
		$\mathcal{N}$	Generic function for fixed point iteration algorithm
$b1$	A matrix component		
$b2$	$|A|$ matrix component	P	Pressure
Cr	Cooling rate	$\mathbf{P}$	Generic inverse matrix

$\dot{P}$	Expansion rate		ΔP	Total pressure loss
P_{max}	Maximum operative pressure		$\Delta \dot{s}$	Entropy generation per unit of mass
P_{min}	Minimum operative pressure		ΔT_{sub}	Degree of subcooling
Pr	Prandtl number		γ	Heat capacity ratio
Q	Source terms vector		θ	Nucleation rate parameter
q_c	Condensation coefficient		κ	Thermal conductivity
R	Droplet radius		ζ	Loss coefficient
$\mathfrak{R}$	Gas constant		Λ	Eigenvalues matrix
R_{eig}	Right eigenvectors matrix		$\boldsymbol{\lambda}$	Lagrangian multiplier
R^2	Correlation coefficient		$\boldsymbol{\mu}$	lagrangian multiplier
$\mathfrak{R}$	Gas constant		μ_j	Moment of order -j
$\mathbf{R}$	Residual vector		μ_v	Steam viscosity
r_σ	Empirical correction for the surface tension		ρ	Density
			σ	Surface tension
r_J	Empirical correction for the nucleation rate		σ_{yield}	Surface tension
			σ_{s}	Non-corrected surface tension
r_G	Empirical correction for the growth rate			
			τ	Viscous tensor
S	Source term (mass balance)			
s	Entropy		**Subscripts**	
s_{thick}	Tube thickness		$*$	Critical, correspondent to the Gibbs free energy maximum
T	Temperature			
t	Time			
t_{act}	Activation time		0	Total property
U	Solution vector		2phase	Term of the two-phase equations
U_{hex}	Global heat transfer coefficient			
			average	Average properties on the domain (integral approximation)
V	Generic vector (Residual jacobian)			
			b	Baseline case
v	Velocity		c	Continuum phase
Wi	Wilson number		coolant	Relative to the cooling fluid
$\mathbf{X}$	Vector of grid points in the domain		core	Relative to the turbofan core
x	Space coordinate			
Y	Liquid mass fraction		cr	Relative to the critical point
			d	Dispersed phase
Greek letters			duct	Relative to the turbofan by-pass duct
α	Steam volume fraction			
$\boldsymbol{\alpha}$	Vector of the design variables		flow	Term of the flow equations
			inlet	Domain inlet
α_{out}	Averaged outlet flow angle		in	Quantity at domain inlet
β	Empirical parameter (in J)		irr	Irreversibility
$\Delta \mathcal{G}$	Gibbs free energy variation		l	Property of the liquid phase

m	Property of the two-phase mixture	vol	Volumetric quantity
mass	Mass quantity	w	Property at the Wilson point
metal	Metal property	x	Component along the x-axis
outlet	Domain outlet	y	Component along the y-axis
out	Quantity at domain outlet		
SA	Related to the turbolence model SA		
s	Static property		
sat	Saturation property		
turb	Term of the turbulent equations		
v	Property of the vapor phase		

Superscripts

-	Average property
c	convective flux
n	solution at time n
v	viscous flux

1

INTRODUCTION

"Definiteness of purpose is the starting point of all achievement."

W. C. Stone

1

Metastable condensation is the phase transition from vapor to liquid that occurs in a fluid subjected to rapid temperature variations. Under these conditions, the nucleation process is triggered when the fluid is in a supersaturated thermodynamic state. The dispersed phase forming during the process of condensation is not in stable thermodynamic equilibrium with the surrounding vapor. As a consequence, models suitable for condensing flows under large temperature gradients, which are relevant to many scientific studies and industrial applications, are rather complex as they must correctly treat metastable thermodynamic states.

Applications of metastable condensation flow models include improved climate models [1], biomedical treatments [2], heat transfer enhancement for industrial purposes [3], natural gas separation [4], power conversion [5] and many others.

The scope of the research documented in this dissertation is the numerical investigation of metastable condensing flows in turbomachinery for propulsion and power applications. The flow inside turbomachinery components is highly compressible, with absolute temperature gradients that can reach values of the order of 1e6 K/s[6], in the case of supersonic expansions. In such extreme conditions, metastable phenomena impact severely on the component performance in terms of both thermodynamic and fluid dynamic losses and lifetime.

The number of technologies for propulsion and power characterised by the presence of condensing mixtures in turbomachinery is increasing. Considerable research and development efforts are currently concerned with components of next-generation thermal power and refrigeration systems, in which the flow undergoes metastable condensation. The characterization of metastable condensing flows and the development of advanced fluid dynamic design tools capable of treating these complex flow phenomena are fundamental steps towards the commercial application fo such promising technologies.

1.1. CONDENSING FLOW IN TURBOMACHINERY AND COMPONENTS FOR PROPULSION & POWER

Research on metastable condensation started at the beginning of the 20th century. After the deployment of the first steam turbines for energy conversion, the relevance of the study of condensing flows grew rapidly, covering a wide range of applications and working fluids. An overview of the most significant applications provides the context for the method, models and simulations carried out.

1.1.1. STEAM TURBINES

Steam turbines are one of the oldest energy conversion technologies in which metastable condensation plays a key role. Figure 1.1 shows the processes of a traditional steam Rankine cycle in the *T-s* chart characterized by two expansion units, HP (high-pressure) and LP (low-pressure), with intermediate fluid reheating. Additionally, Figure 1.2 displays a second cycle configuration, commonly employed for light-water-cooled nuclear reactors.

As stated for example in Ref. [5], LP turbines are subjected to severe erosion due to the presence of the liquid phase in the flow. The mechanical damage caused by the droplets impingement on the blades drastically reduces the service life of these compo-
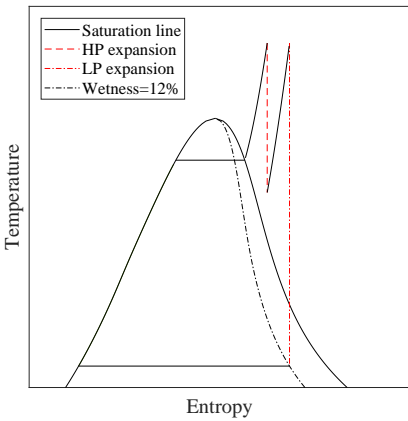
Figure 1.1: Representation of an exemplary steam Rankine cycle with fluid reheating on the water *T-s* chart.
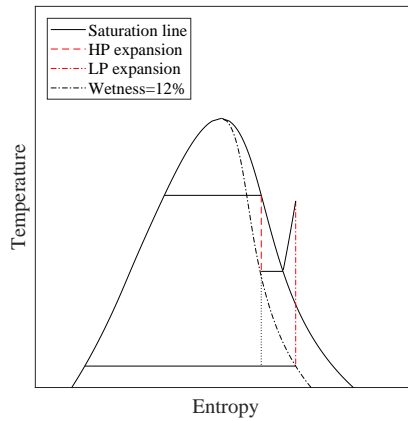
Figure 1.2: Representation of an exemplary steam power cycle for light-water-cooled nuclear plants on the water *T-s* chart.
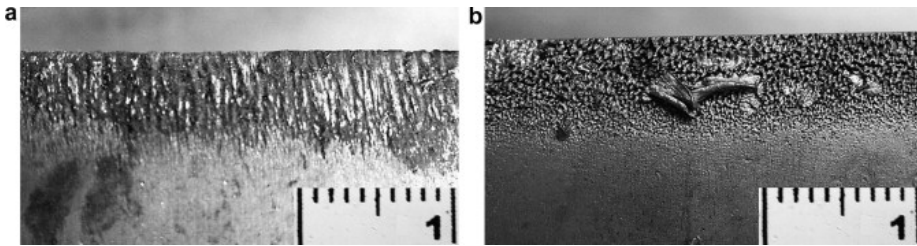
Figure 1.3: Severe superficial damage on low-pressure steam blades from Ref. [9]

nents [7, 8], see Figure 1.3. Moreover, according to Baumann's rule [10], the aerodynamic efficiency for wet stages drops by approximately 1% per wetness percentage in the flow.

The detailed analysis and design of steam turbines requires the use of complex two-phase CFD tools. However, the computational cost of such models make simulations of this kind impractical for engineering purposes [11]. No clear design rules are available, and only an indicative, empirical limit of 10-12% on the liquid fraction allowed at the LP turbine outlet is currently used [5]. Steam turbines provide approximately 80% of the global electricity demand [12], and their market is projected to have a CAGR (Compound Annual Growth Rate) of 5.8% for the next decade [13]. The adoption of innovative design methods, targeted to flow problems involving condensing flows, can have a considerable impact on the efficiency of these systems and, thus, on the global electricity production.

1.1.2. SUPERSONIC NOZZLES FOR NATURAL GAS SEPARATION

Aside from the more traditional applications in power systems, two-phase expansions are used for a much wider range of purposes. For instance, recent studies investigated
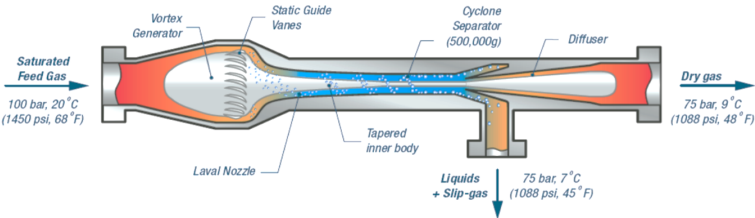
Figure 1.4: Schematic of the separation process for natural gas in a supersonic separator [4].

the possibility of exploiting high-speed metastable expansions to develop cost-effective natural gas separators [4, 14, 15]. The proposed concept consists in the expansion of a natural gas mixture in a supersonic nozzle, to enhance the condensation of water vapor and other heavy hydrocarbons in the flow. Condensate can then be removed from the main flow, in order to obtain pipeline quality natural gas at the nozzle outlet. Figure 1.4 shows the schematic of the supersonic nozzle reported in Ref. [4].

These components have relatively low maintenance requirements and they do not need chemical regeneration. However, the characterization of the condensation phenomena along these nozzles is a crucial step for their optimal design. To highlight the importance of employing design methods targeted to non-equilibrium condensing flows, a qualitative example is reported. Consider a supersonic nozzle with given total inlet conditions and outlet static pressure. Figure 1.5 shows the comparison between the computed pressure field for a single- and a two-phase steam expansion [16]. In case
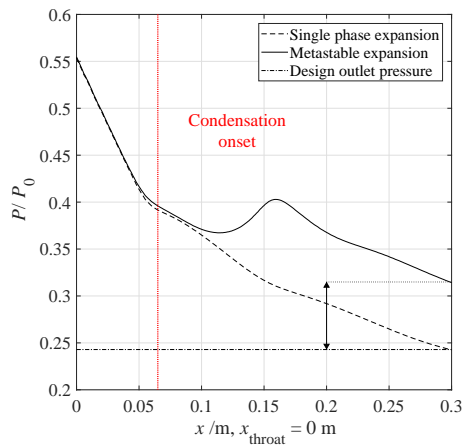
Figure 1.5: Comparison between a single-phase and a two-phase expansion accounting for metastable condensation. The nozzle profile and total conditions for the simulations are taken from Ref. [16]

the profile is designed by adopting conventional design tools for single-phase flows, i.e., without accounting for the presence of liquid, the pressure field in operation deviates

considerably from the expected design case. An accurate prediction of the flow field is then strictly necessary to maximize the fraction of water extracted from the gas mixture and obtain a high-quality gas flow.

1.1.3. SUPERCRITICAL CO_2 COMPRESSORS

The reduction of the CO_2 footprint of propulsion and power applications is nowadays a topic of the utmost relevance in engineering. The latest studies are investigating several solutions, among which the use of advanced supercritical carbon dioxide (scCO_2) compressors for large-scale carbon capture and sequestration [17, 18], see Figure 1.6.

(a) Centrifugal compressor stage

(b) Supersaturated vapor near the impeller leading edge
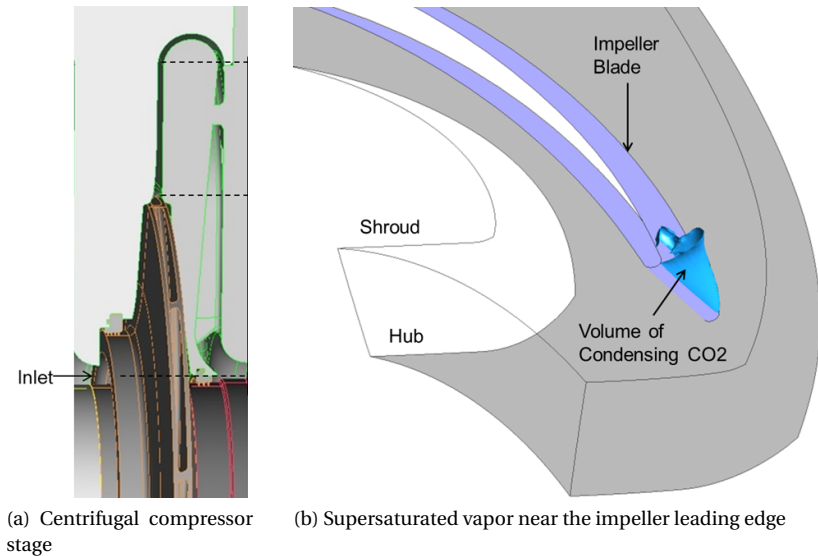
Figure 1.6: Exemplary stage of a scCO_2 centrifugal compressor from Ref. [17] featuring condensation at the impeller leading edge

As reported in [17], due to the high amount of work required to compress scCO_2, the efficiency of these components is a key factor to enable their large-scale applicability. To reduce the required power, these compressors are designed to work with scCO_2 vapor at relatively low temperatures, in the proximity of the saturation line. The lower the temperature at the compressor inlet, the lower is the compression power. Although the expansions are nominally in the dry vapor region, thus, they do not occur in the two-phase region, local reductions of pressure along the suction side of the blades can anyway bring the fluid thermodynamic state below the saturation point, eventually leading to condensation. In these cases, metastable effects are expected to have a considerable impact on the system performance. At present, in order to avoid metastable condensation, indicative, empirical safety boundaries are adopted [17]. As an example, Figure 1.7 displays a representative compression process in the CO_2 T-s chart. Suitable inlet conditions have to be selected in order to guarantee, throughout the entire compression, a
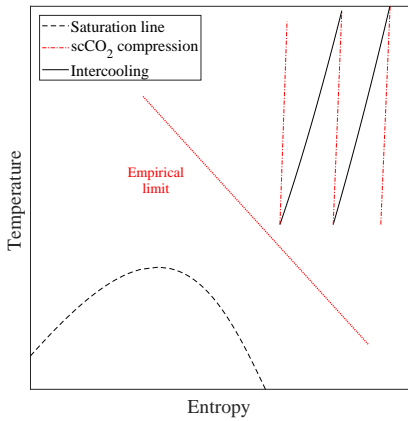
Figure 1.7: Example of multistage intercooled compression process for CO_2 capture and sequestration applications in the *T-s* chart of carbon dioxide. The empirical operational boundary for the operation of the compressor train is taken from Ref. [17].
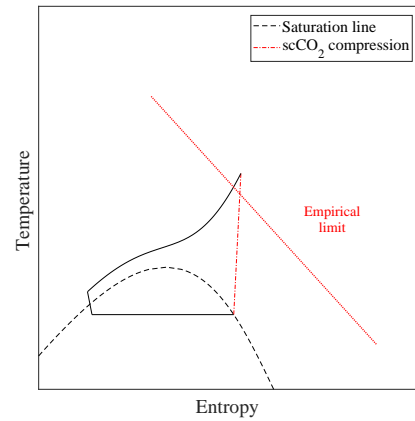
Figure 1.8: Example of a transcritical refrigeration cycle operating with CO_2 in the *T-s* chart of the working fluid. The empirical operational boundary for the operation of the compressor train is taken from Ref. [17].

sufficient temperature superheating.

Little is still known about the characterization of metastable scCO₂. Moreover, the correct modeling of the flow in this type of compressor is even more challenging that that of steam turbines, as in this case phase transition occurs with the fluid in highly non-ideal thermodynamic states.

Similar operating conditions are also expected in next-generation transcritical inverse cycle machines recently proposed for refrigeration [19], [20]. Figure 1.8 reports an exemplary cycle configuration for these systems in the CO_2 *T-s* chart. As can be seen, in order to increase the cycle efficiency, scCO₂ compressors are required to work at few degrees of vapor superheating from the saturation line, increasing the risk of metastable, two-phase phenomena in the components. For the sake of clarity, the empirical boundary reported in Fig.1.7 from Ref.[17] is displayed.

The use of advanced two-phase design tools arguably allows to control the liquid fraction in the flow and to operate closer to the empirical limit suggested in [17], thus, and reduce the compression power required by these components without reducing considerably their service life. Under these conditions, configurations as the one in Figure 1.8 appear particularly promising for the replacement of outdated inverse Rankine cycles featuring regulated substances such as fluorocarbons.

1.1.4. NEXT-GENERATION POWER SYSTEMS

The development of alternative technologies for power generation and heat recovery has been a constant drive for the research on condensing turbomachinery. Since the 1960's, investigations on working fluids such as alkali metals where carried out for the realization of space power units [21]. Studies as those in Refs. [22, 23] attempted to gain insights on the processes of condensation, evaporation and expansion for these non-

conventional fluids, in order to obtain a preliminary design for the cycle components.

In the early 1980's, innovative triangular ORC (Organic Rankine Cycle) configurations have been proposed for low-temperature applications [24], [25]. Figure 1.9 displays the exemplary comparison between the thermodynamic processes of a traditional configuration and those of a triangular ORC in the *T-s* diagram of the working fluid. The condensing expansion occurring in the triangular ORC system is beneficial as it allows to maximize the thermal power recoverable from the heat source. At the same time, the degree of superheating of the flow is reduced.

(a) Example of a traditional ORC configuration featuring a single-phase expansion in the *T-s* chart of the working fluid

(b) Example of a triangular ORC configuration featuring a two-phase expansion in the *T-s* diagram of the working fluid
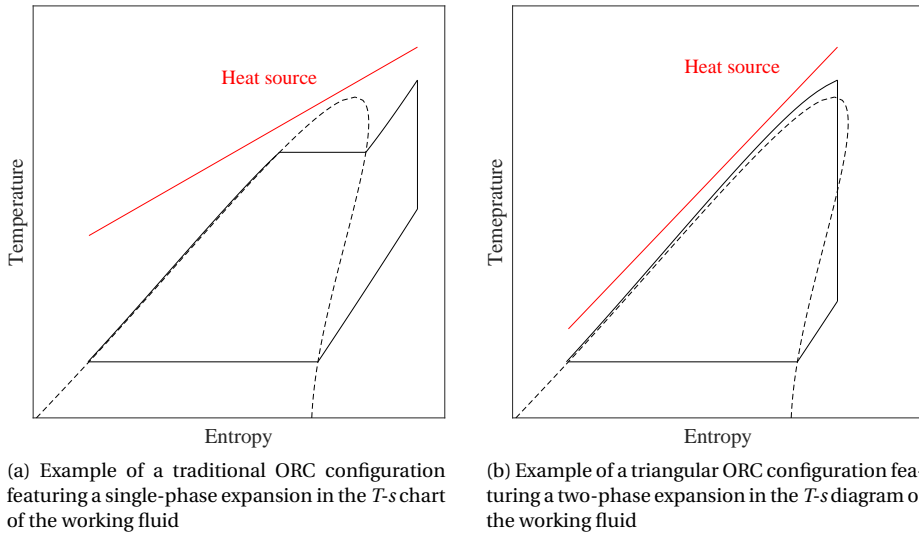
Figure 1.9: Comparison between two exemplary ORC configurations featuring pentane as working fluid in the *T-s* chart. The use of a triangular cycle configuration (right) allows for a higher thermal power recovered, and for a lower superheating of the working fluid after the expansion.

Finally, alternative cycles with $scCO_2$ as working fluid has been recently proposed and developed for concentrated solar power applications and high-temperature heat recovery [26]. Figure 1.10 shows an exemplary $scCO_2$ cycle configuration in the *T-s* chart. The compactness and the high-power density of these systems make them potentially suitable for a wide range of applications, including, possibly, waste heat recovery systems for the aviation industry [27]. However, a large number of questions related to the feasibility of this technology are still unanswered [26, 27]. In order to gain preliminary insights on the operating conditions and on the thermodynamic potential of these systems, the last chapter of this thesis reports the exploratory study that was carried out on a $scCO_2$ recovery unit for long-haul passenger aircraft.

The detailed characterization of metastable flows and the use of advanced design tools are ultimately of utmost importance to achieve high performance of components operating with such flows and push towards more-efficient power systems.

1
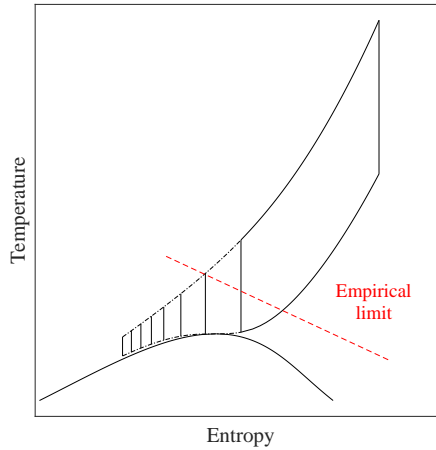
Figure 1.10: Exemplary configuration of a supercritical CO_2 cycle for different minimum temperatures. The empirical limit reported in Ref.[17] is displayed

1.2. FUNDAMENTALS OF CONDENSING FLOWS

1.2.1. PHYSICAL PROBLEM

Figure 1.11 displays a comparison between two expansions, one in which the fluid expands in stable equilibrium, and another in which the fluid undergoes metastable condensation. Total conditions are set to $P_0 = 0.25$bar, $T_0 = 358$K for both cases. If stable equilibrium is assumed, condensation is triggered in correspondence with the dew temperature $T_{sat}(s_0)$, where s_0 is the entropy

$$s_0 = s(P_0, T_0), \tag{1.1}$$

see Figure 1.11a. According to the phase rule for multiphase systems [28], for each temperature $T < T_{sat}(s_0)$ along the expansion, the vapor and the liquid phase are characterized by equal pressure and temperature.

In practice, the fluid characteristics in high-speed expansions are far from these ideal conditions. Due to the rapid temperature variation and the high kinetic energy of the flow, the molecules in the vapor phase have little time to rearrange their structure and create the first nuclei. Therefore, the process of condensation is delayed, and occurs in correspondence with the so called Wilson temperature $T_w < T_{sat}(s_0)$, see Figure 1.11b. The supersaturated states of the vapor phase, i.e., the states characterized by a temperature $T_w < T < T_{sat(s_0)}$, are called metastable, as a small perturbation, such as the creation of a nucleus, would alter the system state irreversibly, leading to condensation.

Once T_w is reached, latent heat is released during the nucleation process, causing a local increase in the pressure and temperature of the vapor. The liquid pressure and temperature are higher than those of the vapor, due to the droplets curvature. Therefore, heat transfer occurs between phases, causing irreversibility [5, 29].

Beside the thermodynamic losses associated with the expansion, the presence of liquid phase has important consequences on the fluid-dynamics of the flow. Droplets that

(a) Equilibrium condensation

(b) Metastable condensation
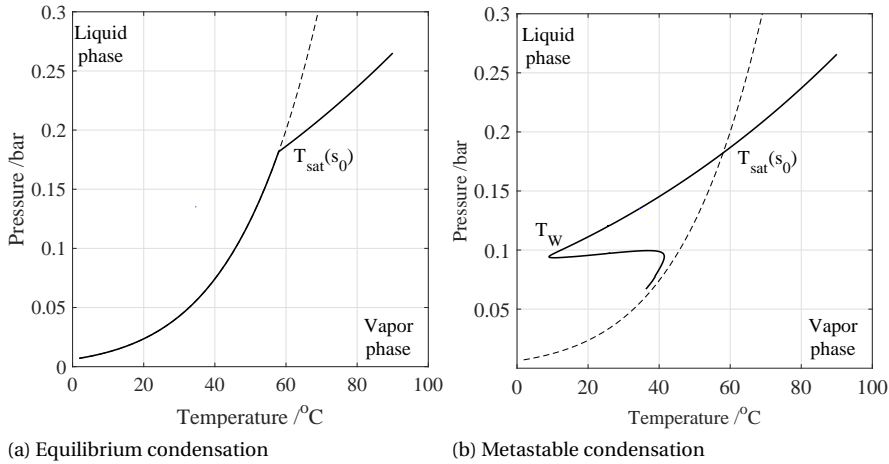
Figure 1.11: Representation of two steam expansions in equilibrium (left) and metastable (right) conditions in the water *P-T* chart

are too heavy with respect to the surrounding continuum phase do not follow the flow-path of the vapor phase, inducing additional drag and possibly causing separation phenomena [30, 31].

One of the most relevant concern in industrial turbomachinery and in high-speed nozzles is the drastic impact of droplet condensation on the component service life. Droplets can detach from the main flow and deposit in the proximity of the walls causing i) thermal stress in the material due to the high difference between the liquid and the vapor heat capacity, ii) erosion due to droplets impingement against the walls and, iii) corrosion [32, 33].

1.2.2. NUMERICAL MODELING

The phenomenon of condensation occurs when molecules, initially in the vapor state, bound to form a liquid cluster. The evolution of a cluster c_l containing l molecules can be described as

$$\frac{\partial c_l}{\partial t} = A_{l-1} - A_l, \tag{1.2}$$

where A_l is the rate at which clusters of size l acquire one single monomer and grow to become $l+1$-size. In theory, in order to characterize a condensing mixture, (1.2) has to be written for each possible size l that the clusters can assume in the flow. This approach is the most general, and can be arguably applied to any physical phenomenon that involves the exchange of monomers among clusters, including the case of condensation. Models such as the one presented by Becker and Döering [34] were developed using this theory as starting point, with an intent of obtaining a detailed characterization of the condensation phenomena at molecular level. However, the number of equations required to describe a condensing mixture makes these models extremely demanding
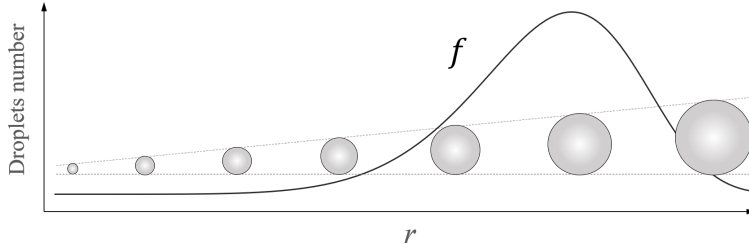
Figure 1.12: Schematic of the droplet distribution f as a function of the radius r

from the computational point of view, even for simple quasi-1D cases. As a matter of fact, these models are rather utilized to compute solutions against which solutions obtained by reduced order models commonly used in RANS and URANS CFD tools can be benchmarked.

A simplification of the physical problem can be obtained by assuming homogeneous condensation. This is the only case of interest in this thesis, as it is proven that this assumption holds for the cases of interest here, i.e., high-speed expansions with negligible liquid volume of condensate inside turbomachinery [29]. Consider a vapor flow with a high number of uniformly dispersed droplets. It is then possible to define a droplet distribution function $f(r)$, where r is the radius of the nuclei, see Figure 1.12. The total number of droplets in the flow is then given by

$$N = \int_0^\infty f(\text{r})\,dr,\qquad(1.3)$$

in which $f(\text{r})$ is the number of droplets characterized by a radius r. The evolution in time of f, in absence of coagulation or segregation, can be written in the form [35]

$$\frac{\partial f}{\partial t} + \nabla \cdot (f\mathbf{v}) + \frac{\partial}{\partial r}(fG) = \delta(r - r_*)\,J,\qquad(1.4)$$

where δ is a Dirac delta function, $\mathbf{v}$ the flow velocity, r_* is the critical radius, i.e. the radius required for the nuclei to be stable and grow, and J and G represent the nucleation rate of the droplets and the growth rate respectively. Figure 1.13 displays a schematic of a two-phase system with dispersed droplets.

Multiple approaches can be adopted to evaluate the function $f(r)$. A high accuracy in the prediction of the droplets distribution can be achieved by adopting an eulerian-lagrangian approach, such as the one described in Ref. [36]. A set of n equations is written, each one to describe the evolution of the function $f(r_k)$ for a specific droplet group characterized by radius r_k, where $1 <= k <= n$. The higher the value n, the higher the points of the distribution f that are determined, increasing the accuracy of the prediction. Alternatively, one could write the liquid mass conservation for each of the droplets groups k, adopting the fully eulerian approach described in Ref. [36]. The latter models can provide information on the full droplet spectra inside the flow. However, also

time t_1 time t_2
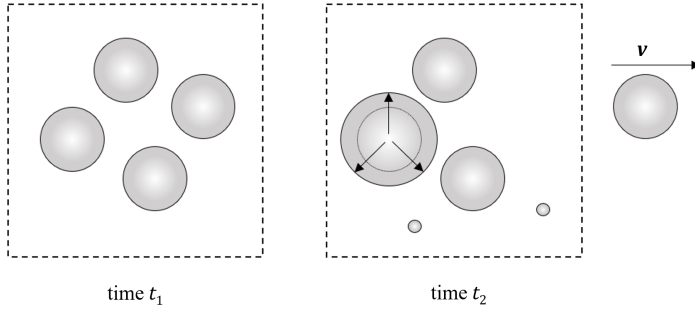
Figure 1.13: Schematic of control volume - exemplary droplet distribution evolution in time

for these cases the resolution of such a high number of equations requires the allocation of considerable computational resources. In practice, when in presence of multi-D domains and complex geometries different numerical models have to be adopted.

Especially for industrial applications, flow characterizations based on average properties can provide a sufficient number of information to predict the flow field. The determination of the distribution function f is not required, and simplified models can be adopted.

As an example, one could use a so called single-fluid model, constituted by i) three conservation laws for the mixture and ii) two additional equations for the droplets number and the liquid fraction. A more accurate solution is to use a two-fluid model. In this case, the conservation laws are written for both the vapor and the liquid phase. Additionally, an evolution equation for the droplets number is solved. Ref.[37] presents a detailed comparison between these two models for the simulation of condensing flows.

An alternative option with respect to these eulerian methods is to resort ot the method of moments [35, 36, 38]. From the mathematical point of view, (1.4) is replaced by the conservation low for the generic moment of order $-j$, defined as

$$\mu_j = \int_0^\infty \mathrm{r}^j f(\mathrm{r}) dr, \tag{1.5}$$

in the form

$$\frac{\partial}{\partial t}(\rho_\mathrm{m} \mu_j) + \nabla \cdot (\rho_\mathrm{m} \mu_j \mathbf{v}) = \rho_\mathrm{m} J R_*^j + \int_0^\infty j \rho_\mathrm{m} \mathrm{r}^{j-1} G f(\mathrm{r}) dr, \tag{1.6}$$

where ρ_m is the mixture density. For the details of the derivation of (1.6) from the GDE (General dynamic equation) see Ref. [39]. If limited results on the liquid phase are required, one can solve only the equations related to the first moments, reducing the computational cost of the simulation.

For all the mentioned models, additional closure relations for the quantities J and G are required in order to model the nucleation process along an expansion. However, as clearly stated in Ref. [40], a general formulation, valid for a wide range fo operating conditions and Mach number, for these parameters is still missing. The choice of best closure relations for J and G depends on the test-case considered.

1

	Model	Time	Complexity	Accuracy steam	all	3D/Opt
Full droplets spectrum	Becker-Döring [34]	- -	- -	++	++	NA
	Lagrangian [36]	-	-	+	+	- -
	Eulerian [36]	-	-	+	+	- -
Average properties	Two-fluid [37]	+	+	-	-	+
	Moments [41]	+	+	-	-	+
	Analytical [43]	++	++	- -	NA	++(steam)

Table 1.1: Qualitative comparison between some of the approaches for the simulations of metastable condensing flows

Several other CFD models are available in literature, such as those described in Refs. [38, 41, 42]. However, as these models are computationally expensive for industrial applications, semi-analytical models for the prediction of the Wilson point and the degree of subcooling have been developed, in particular for low pressure steam. Examples of this approach are reported in Refs. [43], [44], [45]. The number of equations in these models is reduced through additional assumptions on the nucleation and on the flow characteristics. The computational cost of these models is considerably lower than that of CFD. However, their application is limited. For example, Ref. [43] reports the assumptions of i) nucleation rate J shaped as a Dirac function and ii) large exponent in the nucleation rate expression, to simplify the evaluation of the condensed mass flow rate. As shown in Chapter 4, such assumptions are acceptable for low pressure steam, but they do not hold when the working fluids are refrigerants.

Advantages and drawbacks for each of the methods briefly described here have to be evaluated depending on the case at hand. Table 1.1 shows a synopsis the comparison among these methods in terms of i) computational time, ii) complexity of the implementation, iii) accuracy for the prediction of both steam and organic flows and, iv) possible usage for multi-D domains and design optimization.

1.3. EXPERIMENTAL OBSERVATIONS AND GAPS OF KNOWLEDGE

A detailed overview of the available data sets regarding experiments on compressible steam expansions is reported in Ref. [29]. Some of the most adopted data sets for the validation of two-phase models at low pressure are those reported in Refs. [16] and [46]. Ref. [47] reports systematic measurements for supersonic nozzle expansions with a total pressure P_0 in the range 25-35 bar with three different nozzle profiles. Additionally, the work in Refs. [48, 49] included measurements up to a total pressure of 150 bar.

Several attempts were made to determine the parameters affecting the location of the Wilson point in high-speed expansions. A mathematical demonstration outlined in Ref. [29] shows that the temperature T_w is mainly a function of i) the saturation temperature $T_{sat}(s_0)$ and of ii) the expansion rate. However, there is still no general consensus on how these dependencies should be quantified. As an example, although it is reported
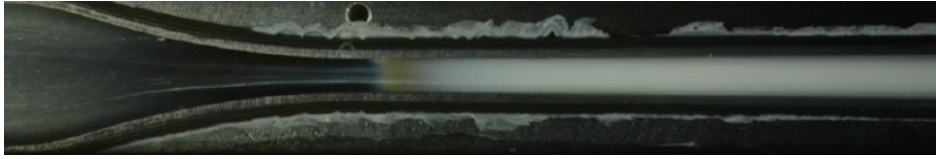
Figure 1.14: Inception of condensation in a supersonic nozzle with $scCO_2$, high-speed footage of the nozzle test section from Ref.[18], test N2 for the location of the Wilson point along the nozzle.

by multiple authors [48, 50] that the flow subcooling ΔT_{sub}, defined as

$$\Delta T_{sub} \stackrel{\text{def}}{=} T_{sat}(s_0) - T_w, \qquad (1.7)$$

increases for high cooling rates, the observed trends are qualitatively different and contradictory, as stated in Ref. [29].

Little information is available on the droplets number and the radius, as the uncertainty in the determination of these parameters is considerably high, see Ref. [49]. Additionally, it is pointed out that the experimental observations refer to a specific range of temperatures, pressures and cooling rates. It is not verified whether the same conclusions can be extrapolated to wider ranges of operating conditions.

Measurements related to condensing flows of fluids other than steam are rather limited. Ref. [51] is one of the first papers presenting a detailed study on ammonia in supersonic nozzle expansions. The tests carried out are characterized by total temperatures in the range $270 - 290$ K and by total pressures in the $2 - 4$ bar range. In 1966, Duff [52] reported a systematic investigation on CO_2 for three different supersonic nozzle profiles, with temperatures T_w belonging to the range $160 - 200$K.

A comprehensive study on multiple fluids was carried out in 1969 by Jaeger et Al. [53] and Dawson et Al.[54]. The investigation was conducted on ammonia, benzene, chloroform, freon 11 and ethanol adopting two different supersonic nozzle shapes. The measurements were taken in the same thermodynamic region as for those presented in Ref. [52].

In the late 1980's, metastable nozzle expansions with CO_2, R22, R12 as working fluids were documented in Ref. [55]. The measurements are taken on five different nozzle profiles, and cover a wide range of testing conditions, up to reduced temperatures $T_{sat,r}(s_0)$ of more than 0.9. For these reasons, the results of these experiments are the main reference for the work in this thesis.

Several recent works treat condensing flows of $scCO_2$ in supersonic nozzles. Ref.[18] reports an analysis carried out with a single nozzle profile in the transcritical region. Figure 1.14 shows the experimental observation for test *N2* as reported in the paper.

As stated in Ryzhov et Al. [29], no systematic data for organic fluids are available to isolate the dependence of the Wilson temperature T_w from the expansion rate and the temperature $T_{sat,r}(s_0)$. All the investigations are conducted in different thermodynamic regions and with multiple experimental set-ups. As a consequence, the measures cannot be directly compared, and it is a challenging task to find similarities among the experiments carried out with different fluids.

1

1.4. MOTIVATION

The estimation of the Wilson point carried out during the design phase of a component arguably allows i) to establish whether metastable condensation occurs in operation and ii) to predict the degree of subcooling, thus, the thermodynamic losses due to condensation. However, the experimental data available in literature do not allow to calculate such thermodynamic point given generic expansion rates and operating conditions. No explicit guidelines are available to estimate T_w for generic metastable expansions, and, at present, only empirical limits have been established to aid the design of two-phase turbomachinery components [5, 17]. Therefore, the objective of this work is twofold, i) gain insights into how the main flow parameters impact on the condensation onset at all possible thermodynamic conditions and for fluids other than steam. The second objective is to apply efficient numerical methods for the automated fluid-dynamic optimization of components operating with condensing flows, allowing the use of advanced component design in replacement of the old empirical boundaries.

The research questions at the foundation of this study are:

1. *What are the main parameters that influence the Wilson temperature T_w in high-speed expansions? Is it possible to quantify such dependence?*

2. *Based on scaling analysis, how much does the prediction of the onset of metastable condensation for generic fluids differs with respect ot steam?*

3. *What is the computational cost and memory requirement to perform adjoint-based optimization of devices operating with two-phase condensing flow? What is the performance improvement achievable with this methods?*

1.5. ORIGINAL CONTRIBUTIONS OF THE WORK

The points of novelty and originality of this work are mainly three:

1. an alternative CFD model is derived from the method of moments in order to reduce the computational cost required for quasi-1D condensing flow simulation;

2. a new semi-analytical model is proposed for the determination of T_w. An original, time-dependent approach is adopted, with the purpose of exploiting similarities among fluids rather then develop a detailed condensation model for each test-case selected. The model does not make use of any two-phase simulations, minimizing the computational resources that have to be allocated;

3. a discrete adjoint method has been developed and tested. The software framework allows to carry out the fluid dynamic design of turbomachinery shapes optimized for two-phase flows. The method arguably provides the best trade off between computational demand and simulated performance improvement.

REFERENCES

[1] M. Kulmala, H. Vehkamäki, T. Petäjä, M. D. Maso, A. Lauri, V.-M. Kerminen, W. Birmili, and P. McMurry, *Formation and growth rates of ultrafine atmospheric particles: a review of observations,* Journal of Aerosol Science **35**, 143 (2004).

[2] P. S. Sheeran, N. Matsuura, M. A. Borden, R. Williams, T. O. Matsunaga, P. N. Burns, and P. A. Dayton, *Methods of generating sub-micron phase-shift perfluorocarbon droplets for applications in medical ultrasonography,* IEEE Transactions on Ultrasonics, Ferroelectrics, and Frequency Control (2016).

[3] A. Leipertz and A. P. Fröba, *Improvement of condensation heat transfer by surface modifications,* Heat Transfer Engineering **29**, 343 (2008).

[4] A. Esmaeili, *Supersonic separation of natural gas liquids by twister technology,* Chemical Engineering Transactions **52** (2016).

[5] M. Moore and C. Sieverding, *Two-phase steam flow in turbines and separators: theory, instrumentation, engineering,* Series in thermal and fluids engineering (Hemisphere Pub. Corp., 1976).

[6] L. Azzini, M. Pini, and P. Colonna, *Semi-analytical model for the prediction of the wilson point for homogeneously condensing steam flow,* Internation Journal of Heat and Fluid Flows **70**, 1 (2018).

[7] J. Starzmann, M. M. Casey, J. F. Mayer, and F. Sieverding, *Wetness loss prediction for a low pressure steam turbine using computational fluid dynamics,* Proceedings of the Institution of Mechanical Engineers, Part A: Journal of Power and Energy **228**, 216 (2013).

[8] V. A. Ryzhenkov, A. I. Lebedeva, and A. F. Mednikov, *Erosion wear of the blades of wet-steam turbine stages: Present state of the problem and methods for solving it,* Thermal Engineering **58**, 713 (2011).

[9] C. Azevedo and A. Sinatora, *Erosion-fatigue of steam turbine blades,* Engineering Failure Analysis **16**, 2290 (2009).

[10] A. Lei̇zerovich, *Wet-steam Turbines for Nuclear Power Plants* (PennWell Corporation, 2005).

[11] T. Guo, W. J. Sumner, and D. C. Hofer, *Development of highly efficient nuclear HP steam turbines using physics based moisture loss models,* in *Turbo Expo*, Vol. 6 (ASME International, 2007).

[12] A. Lei̇zerovich, *Steam Turbines for Modern Fossil-fuel Power Plants* (Fairmont Press, 2008).

[13] *Global Steam Turbines Market Analysis & Trends - Industry Forecast to 2025,* Report (Accuray Research LLP, 2017) iD: 4115243.

1

[14] C. Wen, X. Cao, Y. Yang, and J. Zhang, *Swirling effects on the performance of super-sonic separators for natural gas separation,* Chemical Engineering & Technology **34**, 1575 (2011).

[15] R. H. A. IJzermans, R. Hagmeijer, and P. J. van Langen, *Accumulation of heavy parti-cles around a helical vortex filament,* Physics of Fluids **19** (2007), 10.1063/1.2771658.

[16] M. Moore, P. Walters, R. Crane, and B. Davidson, *Predicting the fog-drop size in wet-steam turbines,* in *Proceedings of the IMechE Conference on Heat and Fluid Flow in Steam and Gas Turbine Plant,* paper C37/73 (1973) pp. 101–109.

[17] N. D. Baltadjiev, *An Investigation of Real Gas Effects in Supercritical CO2 Compres-sors,* Master's thesis, Massachusetts Institute of Technology (2012).

[18] C. Lettieri, D. Paxson, Z. Spakovszky, and P. Bryanston-Cross, *Characterization of non-equilibrium condensation of supercritical carbon dioxide in a de laval nozzle,* in *Oil and Gas Applications; Supercritical CO2 Power Cycles; Wind Energy,* Vol. 9 (ASME, 2017).

[19] S. Fangtian and M. Yitai, *Thermodynamic analysis of transcritical co2 refrigeration cycle with an ejector,* Applied Thermal Engineering **31**, 1184 (2011).

[20] J. Gu, S. Wang, and Z. Gan, *Two-Phase Flow in Refrigeration Systems* (Springer New York, 2014).

[21] M. A. Zipkin, *Alkali-metal, rankine-cycle power systems for electric propulsion.* Jour-nal of Spacecraft and Rockets **4**, 852 (1967).

[22] L. Nichols, S. M. Nosek, C. H. Winzig, and L. J. Goldman, *Experimental Determina-tion of Sodium Vapor Expansion Characteristics with Inert-Gas Injection Pressure-Measuring Technique,* Tech. Rep. (NASA, 1964).

[23] R. J. Rossbach, *Critical flow of potassium vapor through instrumented converging-diverging nozzle,* in *ASME Gas Turbine Conference and Products Show* (ASME, 1965).

[24] D. Elliot, *Theory and Tests of Two-Phase Turbines,* Tech. Rep. 81-105 (Office of Sci-entific and Technical Information (OSTI), 1982).

[25] H. Chen, D. Y. Goswami, and E. K. Stefanakos, *A review of thermodynamic cycles and working fluids for the conversion of low-grade heat,* Renewable and Sustainable Energy Reviews **14**, 3059 (2010).

[26] V. Dostal, P. Hejzlar, and M. Driscoll, *High-performance supercritical carbon dioxide cycle for next-generation nuclear reactors,* Nucl. Technol. **154**, 265 (2006).

[27] C. D. Servi, L. Azzini, M. Pini, A. G. Rao, and P. Colonna, *Exploratory assessment of a combined-cycle engine concept for aircraft propulsion,* (2017), global Propulsion and Power Forum, Zurich, Switzerland.

[28] J.M.Smith, H. Ness, and M.M.Abbott, *Introduction to Chemical Engineering Ther-modynamics* (McGraw-Hill education, 2005).

1

[29] Y. A. Ryzhov, U. G. Pirumov, and V. N. Gorbunov, *Nonequilibrium Condensation in High-Speed Gas Flows* (New York : Gordon and Breach Science Publishers, 1989).

[30] E. Michaelides, C. Crowe, and J. Schwarzkopf, *Multiphase Flow Handbook*, 2nd ed., Mechanical and Aerospace Engineering Series (CRC Press, 2016).

[31] D. G. Elliot and E. Weimberg, *Proceedings of Offshore Europe*, Tech. Rep. (NASA, Jet Propulsion Laboratory, California Institute of Technology, Pasadina, California, 1968) iD:19680017730.

[32] J. Starzmann, M. V. Casey, and J. F. Mayer, *Water droplet flow paths and droplet deposition in low pressure steam turbines,* in *High Performance Computing in Science and Engineering '12* (Springer Berlin Heidelberg, 2012) pp. 351–365.

[33] R. I. Crane, *Droplet deposition in steam turbines,* Proceedings of the Institution of Mechanical Engineers, Part C: Journal of Mechanical Engineering Science **218**, 859 (2004).

[34] R. Becker and W. Döring, *Kinetische behandlung der keimbildung in übersättigten dämpfen,* Annalen der Physik **416**, 719 (1935).

[35] F. Put, *Numerical simulation of condensation in transonic flows*, Ph.D. thesis (2003), phD Thesis, University of Twente, Enschede, The Netherlands.

[36] A. J. White, *A comparison of modelling methods for polydispersed wet-steam flow,* International Journal for Numerical Methods in Engineering **57**, 819 (2003), wiley-Blackwell.

[37] S. Dykas and W. Wróblewski, *Single- and two-fluid models for steam condensing flow modeling,* International Journal of Multiphase Flow **37**, 1245 (2011).

[38] F. R. Hughes, J. Starzmann, A. J. White, and J. B. Young, *A comparison of modelling techniques for polydispersed droplet spectra in steam turbines,* in *Microturbines, Turbochargers and Small Turbomachines, Steam Turbines*, Vol. 8 (ASME, 2015).

[39] R. Sidin, *Droplet size distribution in condensing flow*, Ph.D. thesis, University of Twente (2009).

[40] F. Bakhtar, J. B. Young, A. J. White, and D. A. Simpson, *Classical nucleation theory and its application to condensing steam flow calculations,* Proceedings of the Institution of Mechanical Engineers, Part C: Journal of Mechanical Engineering Science **219**, 1315 (2005).

[41] A. Gerber and M. Kermani, *A pressure based eulerian–eulerian multi-phase model for non-equilibrium condensation in transonic steam flow,* International Journal of Heat and Mass Transfer **47**, 2217 (2004), elsevier BV.

[42] A. Gerber and A. Mousavi, *Application of quadrature method of moments to the polydispersed droplet spectrum in transonic steam flows with primary and secondary nucleation,* Applied Mathematical Modelling **31**, 1518 (2007).

1

[43] R. A. Dobbins, *A theory of the wilson line for steam at low pressures,* Journal of Fluids Engineering **105**, 414 (1983).

[44] J. Young, *Semi-analytical techniques for investigating thermal non-equilibrium effects in wet steam turbines,* International Journal of Heat and Fluid Flow **5**, 81 (1984).

[45] L. Huang and J. B. Young, *An analytical solution for the wilson point in homogeneously nucleating flows,* Proceedings of the Royal Society A: Mathematical, Physical and Engineering Sciences **452**, 1459 (1996).

[46] D. Barschdorff, *Verlauf der zustandsgrößen und gasdynamische zusammenhänge bei der spontanen kondensation reinen wasserdampfes in lavaldüsen,* Forschung im Ingenieurwesen **37**, 146 (1971).

[47] F. Bakhtar and K. Zidi, *Nucleation phenomena in flowing high-pressure steam: experimental results,* ARCHIVE: Proceedings of the Institution of Mechanical Engineers, Part A: Journal of Power Engineering **203**, 195 (1989).

[48] G. Gyarmathy, *Zur wachstumsgeschwindigkeit kleiner flüssigkeitstropfen in einer übersättigten atmosphäre,* Journal of Applied Mathematics and Physics (ZAMP) **14**, 280 (1963).

[49] G. Gyarmathy, *Nucleation of steam in high-pressure nozzle experiments,* Proceedings of the Institution of Mechanical Engineers, Part A: Journal of Power and Energy **219**, 511 (2005).

[50] G. Saltanov, *Sverkhzvukovye Dvukhfaznye techeniya (Supersonic Two-Phase Flows)* (Vysheishaya shkola, 1972).

[51] M. Kremmer and O. Okurounmu, *Condensation of Ammonia Vapor during Rapid Expansion*, Tech. Rep. (1965).

[52] K. M. Duff, *Non-Equilibrium Condensation of Carbon Dioxide in Supersonic Nozzles*, Ph.D. thesis, Massachusetts Institute of Technology (1966).

[53] H. L. Jaeger, E. J. Willson, P. G. Hill, and K. C. Russell, *Nucleation of supersaturated vapors in nozzles. i. h2o and NH3,* The Journal of Chemical Physics **51**, 5380 (1969).

[54] D. B. Dawson, E. J. Willson, P. G. Hill, and K. C. Russell, *Nucleation of supersaturated vapors in nozzles. II. c6h6, CHCl3, CCl3f, and c2h5oh,* The Journal of Chemical Physics **51**, 5389 (1969).

[55] G. Theis, *Spontankondensation in übersättigten Dampfströmungen von Kohlendioxid und von Difluordichlormethan*, Ph.D. thesis, Uni Karlsruhe (1985).

2

NUMERICAL MODELING OF STEAM FLOWS AT HIGH PRESSURE

"All models are wrong. The practical question is how wrong do they have to be to not be useful."

G. P. E. Box

High-pressure non-equilibrium condensing flows are here investigated through a Euler model coupled to the method of moments for the physical characterization of the dispersed phase. Two different numerical approaches, namely the so-called (a) the mixture and (b) continuum phase model, are compared in terms of computational efficiency and accuracy. The results are verified against experimental data of high-speed condensing steam.

The analysis demonstrates that Model (b) markedly outperforms the mixture model in terms of computational cost, while retaining comparable accuracy. However, both models, in their original formulation, lead to considerable deviations in the nucleation onset prediction as well as an overestimation of the average droplet radius for high pressure cases.

A further investigation is then conducted to figure out the main physical parameters affecting the condensation process, i.e. the surface tension, the growth rate and the nucleation rate. It is eventually inferred that applying proper correction to these three quantities allows to obtain best fit with the experimental data. A final calculation is carried out to show the dependence of these three correcting factors from the thermodynamic conditions of the mixture.

2.1. GOVERNING EQUATIONS

In this chapter, quasi 1-D condensing flows are considered. In principle, eight governing equations are needed to obtain the averaged properties of the liquid and vapor phase, namely their thermodynamic states, the velocities, the liquid mass fraction and the droplet radius.

For condensing flows with limited liquid mass fractions, the following assumptions proved to be adequate: i) the liquid and vapor are in mechanical equilibrium, ii) no slip between the two phases, and iii) the temperature of the dispersed phase is determined through a capillarity model. As a result, three conservation laws supplemented by two additional equations for the dispersed phase properties are sufficient to characterize the mixture in terms of average properties.

2.1.1. CONSERVATION LAWS

The comparison between two main approaches, i.e. the employment of the mixture conservation laws and the continuum phase balance equations is here reported. The chapter refers to these models as (a) and (b) respectively hereafter.

The Eulerian set of equations for model (b) is

$$
\begin{cases}
\frac{\partial \rho_v}{\partial t} + \frac{\partial (\rho_v v)}{\partial x} = S_v - \rho_v v_v \frac{\partial A_c}{\partial x} \frac{1}{A_c}, \\
\frac{\partial \rho_v v}{\partial t} + \frac{\partial (\rho_v v^2 + P)}{\partial x} = S_v v - \rho_v v^2 \frac{\partial A_c}{\partial x} \frac{1}{A_c}, \\
\frac{\partial (\rho_v e_{0,v})}{\partial t} + \frac{\partial (\rho_v h_{0,v})}{\partial x} = S_v h_{0,l} - \rho_v h_{0,v} \frac{\partial A_c}{\partial x} \frac{1}{A_c},
\end{cases}
\tag{2.1}
$$

where ρ_v, v, P_v, $e_{0,v}$, $h_{0,v}$ are the density, velocity, pressure, total energy and total enthalpy of the vapor phase, A_c is the cross sectional area of the nozzle and S_v is the source

term accounting for mass exchange across the interface vapor-liquid, equal to

$$S_{\mathrm{v}} = -\rho_{\mathrm{m}} \frac{3Y}{R} \frac{\partial R}{\partial t}, \tag{2.2}$$

in which R is the averaged droplet radius and Y the liquid mass fraction. The interested reader can refer to Appendix A.1 for the derivation of such equations. On the other hand, the relations for model (a) are obtained from the previous system using mixture properties (here indicated with the pedex -m) and setting the source term S_v equal to 0.

Important differences arise between the two models: model (b) may suffer from more severe stiffness due to condensation source terms. On the contrary, in model (a) the thermodynamic non-equilibrium of the vapor phase renders the computation of the mixture properties iterative [4]. This procedure entails an extra computational burden and may affect the solver robustness. Note that the validity of model (b) is restricted to vapors containing negligible liquid volume fractions [3]. This assumption can be adequate for low-pressure supersonic nozzle expansions, due to the very high difference in specific volume between the liquid and the vapor phase. On the other hand, the densities of the two phases get closer when moving towards the critical point, and the approximation on the droplet volume can lead to inaccuracies in the final solution.

2.1.2. LIQUID PHASE EQUATIONS

The method of moments is selected to write the additional two equations for the dispersed phase. The generic moment of order $-j$ is defined as

$$\mu_j = \int_0^\infty R^j f \, dr, \tag{2.3}$$

where f is the distribution function, i.e. the radial derivative of the droplet number density, such that the total number of droplets N is equal to

$$N = \int_0^\infty f \, dr. \tag{2.4}$$

As described in [5], the conservation law for each moment stems from the GDE (General Dynamic Equation) and (2.3), obtaining

$$\frac{\partial}{\partial t}(\rho_{\mathrm{m}} \mu_j) + \frac{\partial}{\partial x}(\rho_{\mathrm{m}} \mu_j v) = j \cdot \int_0^\infty \rho_{\mathrm{m}} R^{j-1} G f \, dr + \rho_{\mathrm{m}} J(R_*) R_*^j, \tag{2.5}$$

where G is the growth rate, R_* the critical radius, and J the nucleation rate.

These equations are usually solved through the formulation in [6]. However, this method involves the resolution of four equations instead of the two theoretically required.

In order to minimize the computational time required by the simulations, a 2-equations method is adopted. In particular, only the transport equations for the moments of order -0 and -3 in the form

$$\frac{\partial}{\partial t}(\rho_m \mu_0) + \frac{\partial}{\partial x}(\rho_m \mu_0 v) + \rho_m \mu_0 v \frac{\partial A_c}{\partial x}\frac{1}{A_c} = \rho_m J(R_*), \tag{2.6}$$

$$\frac{\partial}{\partial t}(\rho_m \mu_3) + \frac{\partial}{\partial x}(\rho_m \mu_3 v) + \rho_m \mu_3 v \frac{\partial A_c}{\partial x}\frac{1}{A_c} = \rho_m J(R_*)R_*^3 + 3\rho_m R^2 G N, \tag{2.7}$$

where μ_0 and μ_3 are

$$\mu_0 = \int_0^\infty f\, dr = N, \tag{2.8}$$

$$\mu_3 = \int_0^\infty R^3 f\, dr = R^3 \int_0^\infty f\, dr = N R^3. \tag{2.9}$$

are solved.

2.1.3. CLOSURE MODELS
The nucleation rate J and the growth rate G are modelled as in [8]. The empirical parameter β inside the growth rate model is here set to 1. The critical radius R_* is evaluated as

$$R_* = \frac{2\sigma}{\rho_l \Delta \mathscr{G}}, \tag{2.10}$$

where σ is the surface tension, ρ_l is the liquid density and $\Delta \mathscr{G}$ is free Gibbs energy variation due to the condensation process, see A.2.

2.1.4. THERMOPHYSICAL MODEL
The thermodynamic model used for the continuum phase is the polytropic Van der Waals EoS (Equation of State), that allows to account for metastabilities inside the two-phase region. The liquid enthalpy is taken from the IF-97 library [9], as well as the saturation temperature and pressure. The liquid density is taken as in [3]. At last, the capillarity model adopted for the liquid temperature is the one reported in [3]. See A.2.

The thermodynamic properties for the mixture can be retrieved following the procedure in [4] by using the quasi-Newton algorithm. Furthermore, the speed of sound of the mixture is estimated through the expression

$$c_m = \left[\left(1 - \frac{\rho_m}{\rho_l}Y\right)\frac{1}{c_v^2} + \left(\frac{\rho_v}{\rho_l}Y\right)\frac{1}{c_l^2}\right]^{-\frac{1}{2}}. \tag{2.11}$$

Appendix A.3 shows the procedure to obtain such relation.

The surface tension is given by the model in A.2 [10], whereas viscosity and thermal conductivity are determined through the Chung's model [11].

2.2. NUMERICAL METHODOLOGY
The balance equations for both a) the mixture and b) the continuum phase are discretized using a cell-centered finite volume scheme of first order of accuracy [12]. The

source terms are directly incorporated in the numerical flux without special treatment. On the contrary, the transport equations are discretized by using an upwind scheme specifically conceived in this study, which is further detailed in the following. The full set of governing equations is advanced in time by an implicit, segregated strategy. More precisely, at each iteration the mass, momentum, and energy equations are solved assuming frozen droplet properties.

2.2.1. UPWIND SCHEME FOR TRANSPORT EQUATIONS

As can be observed, the last term of (2.7) is a function of the radius R of the dispersed phase. Since R is in turn a combination of μ_0 and μ_3 through (2.9) it can be readily incorporated in the left hand-side of (2.7) by a simple algebraic manipulation as

$$\frac{\partial}{\partial t}(\rho_{\mathrm{m}}\mu_3) + \frac{\partial}{\partial x}(\rho_{\mathrm{m}}\mu_3 v) + \frac{\rho_{\mathrm{m}}\mu_3 v_{\mathrm{m}}}{A_{\mathrm{c}}}\frac{\partial A_{\mathrm{c}}}{\partial x} = \rho_{\mathrm{m}}J(R_*)R_*^3 + \frac{\partial}{\partial x}\left(\int 3\rho_{\mathrm{m}}R^2 GN dx\right). \quad (2.12)$$

The last integral is approximated as

$$\int 3\cdot\rho_{\mathrm{m}}R^2 GN dx = 3\left(\rho_{\mathrm{m}}R^2 GN\right)_{\mathrm{average}}\cdot(x - x_{\mathrm{inlet}}) =$$
$$\sum_{i=0}^{x_{\mathrm{outlet}}} 3\left(\rho_{\mathrm{m}}R^2 GN \frac{\Delta x}{x_{\mathrm{outlet}} - x_{\mathrm{inlet}}}\right)_i \cdot(x - x_{\mathrm{inlet}}), \quad (2.13)$$

where x_{inlet} and x_{outlet} are the inlet and outlet abscissas of the domain. Concisely, the 2 transport equations can be written as

$$\frac{\partial}{\partial t}U + \frac{\partial}{\partial x}F = Q, \quad (2.14)$$

where

$$U = \left[\begin{array}{c} \rho_{\mathrm{m}}\mu_0 \\ \rho_{\mathrm{m}}\mu_3 \end{array}\right] = \left[\begin{array}{c} \rho_{\mathrm{m}}N \\ \rho_{\mathrm{m}}NR^3 \end{array}\right], \quad (2.15)$$

$$Q = \left[\begin{array}{c} \rho_{\mathrm{m}}J(R_*) \\ \rho_{\mathrm{m}}J(R_*)R_*^3 \end{array}\right] - U\cdot v\frac{\partial A_{\mathrm{c}}}{\partial x}\frac{1}{A_{\mathrm{c}}}, \quad (2.16)$$

$$F = \left[\begin{array}{c} \rho_{\mathrm{m}}\mu_0 v \\ \rho_{\mathrm{m}}\mu_3 v - \sum_{i=0}^{x_{\mathrm{outlet}}} 3\left((\rho_{\mathrm{m}}\mu_0)^{\frac{1}{3}}(\rho_{\mathrm{m}}\mu_3)^{\frac{2}{3}}G\cdot\frac{\Delta x}{x_{\mathrm{outlet}} - x_{\mathrm{inlet}}}\right)_i \cdot(x - x_{\mathrm{inlet}}) \end{array}\right]. \quad (2.17)$$

The final up-wind flux is given by

$$F_{\frac{i+j}{2}} = \frac{F_i + F_j}{2} - |A|_{\frac{i+j}{2}}\frac{U_j - U_i}{2}, \quad (2.18)$$

in which the physical flux F is approximated for every cell -i as

$$\sum_{j=1}^{i} 3\left(\rho_{\mathrm{m}}R^2 GN\cdot\frac{\Delta x}{x_{\mathrm{outlet}} - x_{\mathrm{inlet}}}\right)_j \quad (2.19)$$

Appendix A.4 reports the spectral decomposition of A while Appendix A.5 illustrates the derivation of the Jacobian.

2.3. VALIDATION

2.3.1. LOW-PRESSURE INVESTIGATION

In this section, the results of model (a) and (b) are compared with the experimental data reported in [7] and with existing numerical solutions obtained with more sophisticated methods. The selected test case is the well-established Moore nozzle [13], which is representative of supersonic wet-steam flows occurring in turbine flow passages. The shape of the profile is reported in Appendix A.6. All the calculations are performed on a 1000-cells grid.

Figure 2.1 shows the dimensionless pressure distribution along the nozzle for the present models, the Hill's method [5] and experimental observations. No significant differences are found, especially prior and after the onset of condensation.

(a) Comparison bewtween model (a), model (b) and Hill's method

(b) Comparison between model (b) and the three approaches reported in [7]
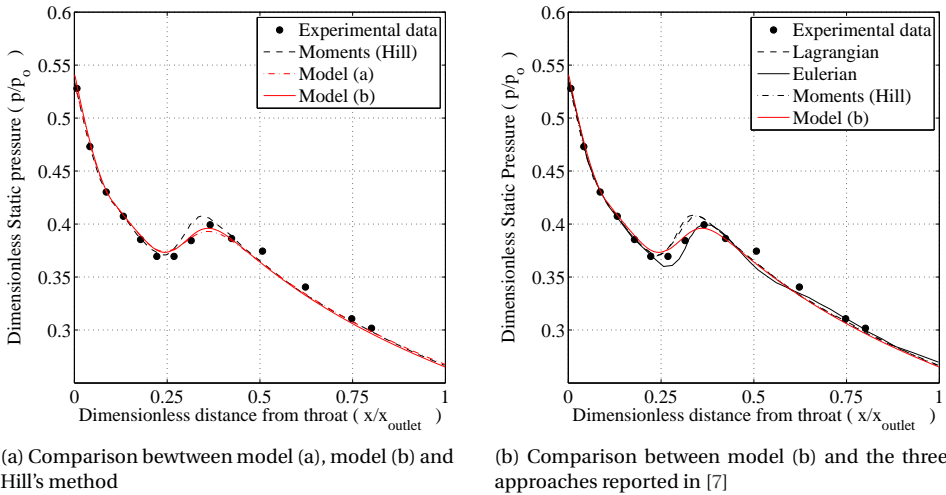
Figure 2.1: Pressure distribution along the nozzle, $x_{\text{throat}} = 0$

The pressure trends of both liquid and vapor are depicted in the *T-s* chart of Figure 2.2. The same diagram shows the experimentally derived Wilson points, extrapolated from [14] for the considered pressure range. For the sake of clarity, the curves are also displayed in the *P-v* plane in Figure 2.3. When the steam subcooling is close to 50K (from Figure 2.2) and the continuum phase reaches the Wilson point, condensation starts rapidly. The sudden release of latent heat leads to a considerable static temperature rise of the continuum phase which is quickly brought back to thermodynamic equilibrium. The amount of heat released increases for high values of the nucleation rate, Figure 2.4 shows a steep peak from 0 to $2 \cdot 10^{21} \, kg^{-1} s^{-1}$ in a narrow portion of the nozzle close to the throat.

A more in-depth physical explanation of the condensation phenomenon can be figured out by inspecting (2.20), valid for ideal compressible channel flow with heat addition [15]

$$\frac{dP}{P} = \frac{\gamma M^2}{1 - M^2} \left(\frac{dA_\mathrm{c}}{A_\mathrm{c}} - \left(1 + \frac{\gamma - 1}{2} M^2\right) \frac{dT_0}{T_0} \right), \tag{2.20}$$

in which M is the mach number, T_0 is the total temperature, and γ the specific heat ratio. In the early stage of condensation, the dominant term of (2.20) is the total temperature increase which causes a sudden static pressure rise, usually referred to as condensation shock wave. The flow then departs from metastable conditions to reach thermodynamic equilibrium. As the condensation proceeds, the nucleation rate J falls down, therefore the release of latent heat and the total temperature variation reduce correspondingly. The flow motion is thus mainly governed by the area variation dA_c, which is positive for the given nozzle shape. Provided that the flow remains supersonic downstream of the shock, the expansion continues along the saturation line, as shown in both Figures 2.2 and 2.3.

(a) Liquid and vapor thermodynamic conditions   (b) Detail of the vapor expansion
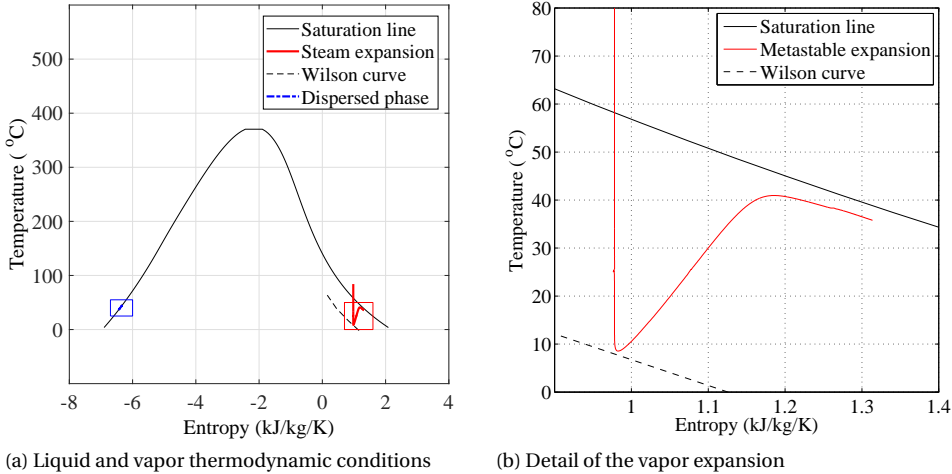
Figure 2.2: Liquid and vapor expansion reported in the *T-s* diagram for model (a)

As stated in [3], the liquid properties are barely dependent on the pressure in the specific thermodynamic range considered ($P < 0.25$ bar), see Figure 2.6. Furthermore, the temperature of the droplets T_d is few degrees higher than the vapor, according to the capillarity model. Therefore, it can be inferred that the dispersed phase expansion is located close to the saturation line, with a slight temperature difference with respect to the steam, as proved by Figures 2.2 and 2.3.

Figure 2.7 shows that the major deviations between the various models are located in the condensation region. In particular, the Lagrangian and the Hill's method overestimate the pressure local maximum, whereas the Eulerian simulation predicts a higher degree of subcooling. However, the pressure slope between the two pressure extrema predicted by the three models is very similar, suggesting a fairly close value of nucleation rate. On the other hand, model (a) and (b) tend to underestimate the pressure

(a) Liquid and vapor thermodynamic conditions   (b) Detail of the vapor expansion
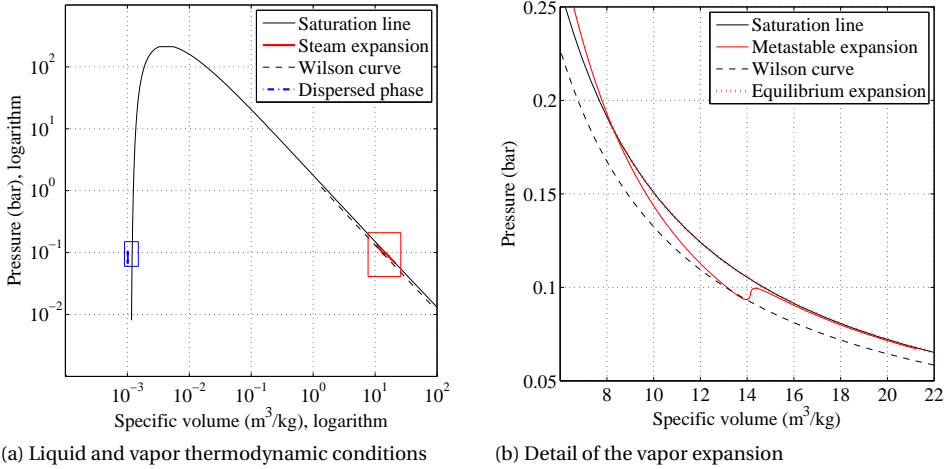
Figure 2.3: Liquid and vapor expansion reported in the *P-v* diagram for model (a)

bump. The reason can be partly attributed to the inaccuracy of the thermodynamic model adopted for the calculations. As anticipated, the polytropic Van der Waals EoS is adopted, arguably less accurate than the model devised in [7].

The droplet averaged radius is recognized as remarkably challenging to detect for all two-phase computational models. Figure 2.8 depicts the droplet radius along the nozzle. Unexpectedly, the results of model (a) and (b) are in good agreement with the experimental data, with an deviation of 5% (0.095μm diameter instead of 0.1μm nominal) for model (b) and much lower for model (a). Conversely, the discrepancy for the Hill's method has been found higher than 20% (with a diameter of 0.077μm) and even worse for the Eulerian approach, which features deviations larger than 30%.

A numerical study was conducted to assess the convergence rate of model (a) and (b). The benchmark is the so-called single phase simulation, where it is supposed the vapor expanding in the nozzle without inception of condensation. Despite this simulation has no physical meaning, it is commonly utilized as reference for examining the convergence properties of the various methods. The simulations were carried out by discretizing the nozzle with 400 cells and employing the Euler explicit integration scheme with CFL number equal to 1. Convergence was achieved after reducing the residuals of all equations by five orders of magnitude. Table 2.1 reports the final results. Notwithstanding comparable accuracy, model (a) is three times more demanding than model (b). The rationale of this difference has been found in the iterative algorithm, i.e. quasi-Newton method, adopted for computing the mixture properties.

A final analysis was carried out to investigate the numerical stability of both models. Several simulations were run on a mesh of 400-cells with the implicit method for progressively increasing CFL numbers. Table 2.2 lists the obtained results in terms of maximum allowable CFL number.
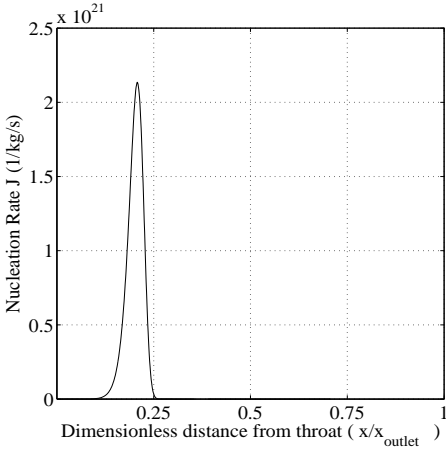
Figure 2.4: Nucleation rate along the nozzle, $x_{\text{throat}} = 0$
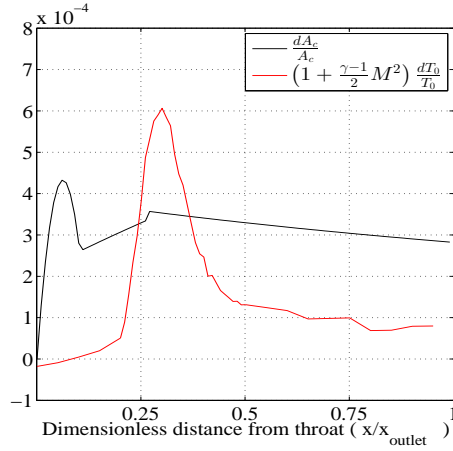
Figure 2.5: Main terms of (2.20) along the nozzle, $x_{\text{throat}} = 0$

	Benchmark	Model (a)	Model (b)
Iterations	5024	4700	4823
Physical time (s)	14	79	25

Table 2.1: Simulation time required for the benchmark (single-phase), model (a) and model (b), explicit time integration, CFL=1

As expected, the maximum time step for the two-phase flow systems is significantly lower than for the benchmark. This is mainly due to the stiffness introduced by the onset of condensation which occurs at much faster time scale than wave propagation in the flow. On the other hand, the comparison shows that model (a) allows for a maximum CFL that is nearly half of the one of model (b).

2.3.2. HIGH PRESSURE INVESTIGATION

The test-case considered is No.18, with total inlet conditions $P_0 = 100.7$bar and $T_0 = 615.2$K ($P_r = 0.46$, $T_r = 0.95$). The simulations were made on a 1000-cell mesh with implicit time integration. The expansion of highly superheated steam at same total pressure [16] is taken as reference.

Figure 2.9 shows the expansion in the *P-T* chart obtained with model (a).

For the assumptions made, the liquid state is again close to the saturation line from the condensation onset till the nozzle outlet. Therefore, the droplets can be considered as saturated liquid (Figure 2.9b).

Figure 2.10 depicts the pressure field along the nozzle. Both model (a) and (b) provide similar results in terms of static pressure distribution (Figure 2.10b). The solution at the nozzle inlet and outlet is close to the measurements. However, a considerable deviation is observed in the condensation onset with respect to experimental observation. The

2
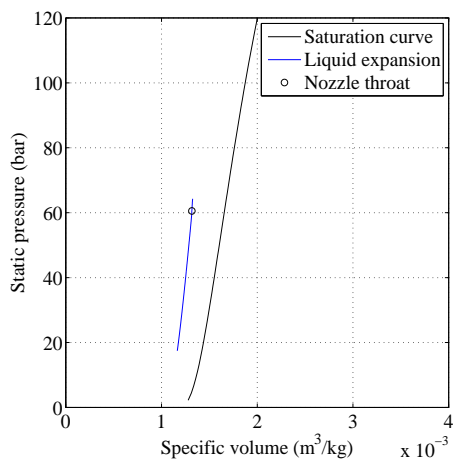
Figure 2.6: Detail of the liquid expansion from Figure 2.3a, $x_{\text{throat}} = 0$
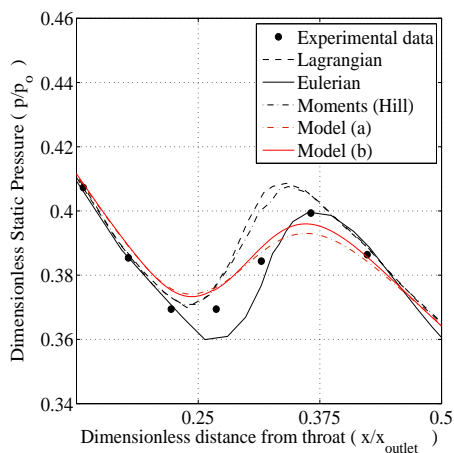
Figure 2.7: Detail of the pressure profile, comparison with [7], $x_{\text{throat}} = 0$
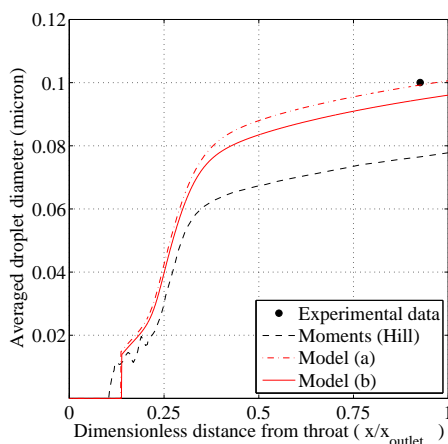
(a) Comparison between model (a), model (b) and Hill's method
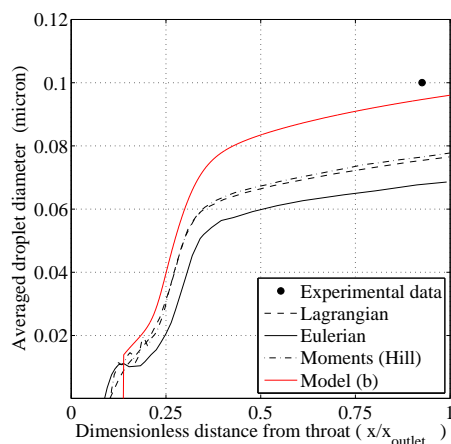
(b) Comparison between model (b) and the three approaches reported in [7]

Figure 2.8: Averaged droplet diameter along the nozzle, $x_{\text{throat}} = 0$

characteristic pressure bump caused by the latent heat is observed in correspondence of a dimensionless static pressure of around 0.62 (62 bar) instead of 0.42 (42 bar) as for the experimental data.

Figure 2.11 depicts the average droplets radius along the nozzle. The trend for model (a) is similar to the experimental curve, however the results obtained are almost twice the nominal values measured. The prediction for model (b) is very close to the one of the first
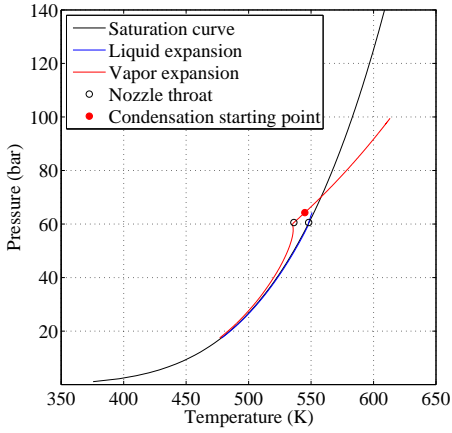
(a) Liquid and vapor expansion
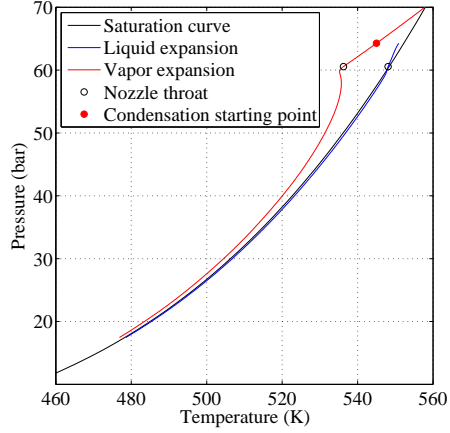
(b) Detail of the expansion

Figure 2.9: Nozzle expansion on the *P-T* chart
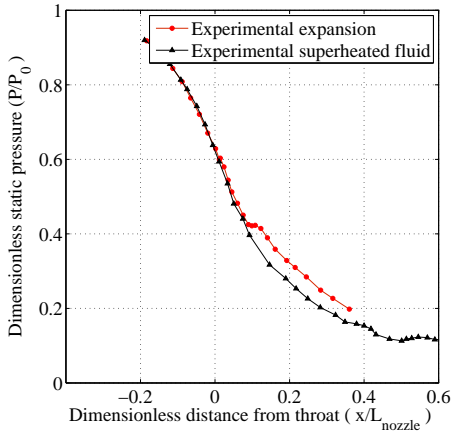
(a) Static pressure field along the nozzle, experimental
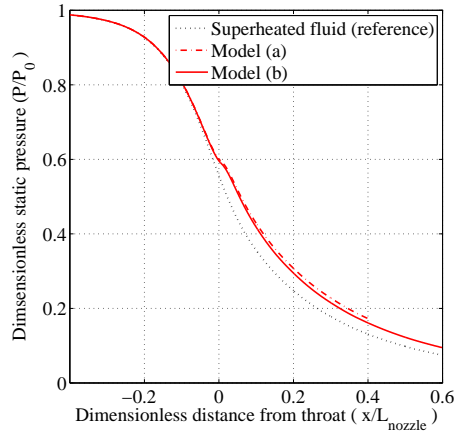
(b) Static pressure field along the nozzle, numerical

Figure 2.10: Comparison between model (a), model (b) and the results in [16], $x_{\text{throat}} = 0$

	Benchmark	Model (a)	Model (b)
Maximum CFL	102	28	46

Table 2.2: Maximum allowable CFL for the benchmark (single-phase), model (a) and model (b). The computations are performance with implicit time integration and constant CFL

	Initial field	Single Phase	Model (a)	Model (b)
Physical time	Constant sol.	5 min, 47 s	83 min, 31 s	11 min, 29 s
	Superheated sol.	-	20 min, 20 s	8 min, 1 s

Table 2.3: Computational time for single-phase (reference), model (a) and model (b), explicit time integration, CFL = 1

model (the difference is around 1%), even though the radius increases faster along the nozzle. For the sake of completeness, Figure 2.12 displays also the critical radius along the nozzle obtained from the simulations.
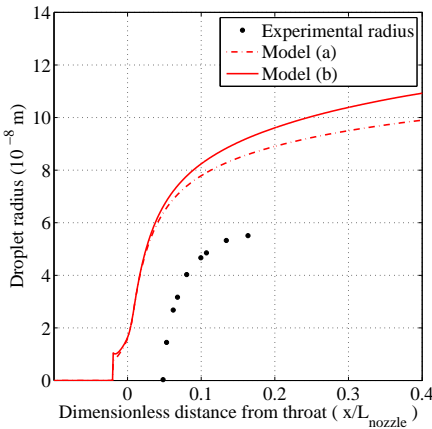
Figure 2.11: Averaged droplet radius, comparison between model (a) and model (b), $x_{\text{throat}} = 0$
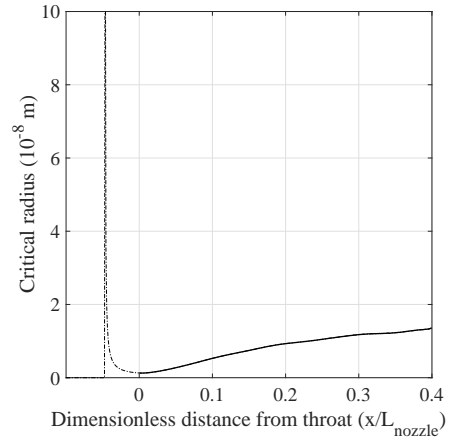
Figure 2.12: Critical radius along the nozzle for test *18C*

COMPARISON BETWEEN MODEL (A) AND (B)

A first analysis is made with explicit time integration and CFL = 1. The simulations are stopped after a decrease of 4 orders of magnitude of the residual vector components. A single-phase simulation with highly superheated vapor at same total pressure is taken as benchmark.

Two different tests are made changing the initial motion field, i.e. (i) constant solution along the nozzle or (ii) superheated solution. Table 2.3 shows the physical time required by the benchmark, model (a) and model (b) respectively. For the first case, the

comparison shows that the simulation time for model (b) is two times higher than the single-phase one. On the other hand, it is worth pointing out that model (a) requires a computational time that is more than 15 times greater with respect to the benchmark.

As already observed by [2], the quasi-Newton algorithm adopted represents a large penalty for model (a). Even for the second test, in which the initial motion field is close to the final solution, the presence of such iterative procedure leads to a time that is more than 2 times higher than model (b).

To test the numerical stability of the two models, a second analysis on the maximum CFL allowable is made. The tests are made on the same 1000-cell mesh with implicit time integration and constant CFL. The initial motion field is again the constant solution along the nozzle. Table 2.4 shows the final result.

	Single Phase	Model (a)	Model (b)
Max CFL allowable	11	4	9

Table 2.4: Maximum CFL (constant) allowable for single-phase (reference), model (a) and model (b), implicit time integration

Also for the high pressure test case, the presence of the quasi-Newton algorithm does cause a considerable penalty for model (a). Note that the maximum CFL allowable for all the models is relatively low, as it is kept as constant during the simulation. The introduction of a time-dependent CFL allows for a maximum value of more than 30 for both model (a) and (b).

2.4. DISCUSSION

One of the key properties affecting the characteristics of metastable condensation is the surface tension σ. The underestimation of this parameter leads to substantial anticipation of condensation onset resulting in fairly large difference in pressure and temperature trends. The work in [17] introduced a new surface tension σ^* defined as

$$\sigma^* = r_\sigma \sigma, \tag{2.21}$$

in which r_σ is an empirical correction incorporating the effect of droplets curvature. It is reported that in the case $r_\sigma > 1$ the condensation onset is delayed when compared to $r_\sigma = 1$. However, the change in the nucleation starting point comes along with a considerable increase in the droplet radius. To gain insights of this behaviour, a simulation was performed with $r_\sigma = 1.5$. Figure 2.13 shows the pressure field and the radius obtained. Additionally, Figure 2.14 presents the values of the nucleation and the growth rate for both $r_\sigma = 1$ and $r_\sigma = 1.5$.

It can be observed that J decreases of one order of magnitude (Figure 2.14a): (2.10) shows that an increase in σ^* reflects on the critical radius value. Furthermore, the nucleation rate model has an exponential dependence from R_*^2 and σ. As a consequence, J goes from $1.3 \cdot 10^{24} \mathrm{kg}^{-1}\mathrm{s}^{-1}$ to $1.8 \cdot 10^{23} \mathrm{kg}^{-1}\mathrm{s}^{-1}$, and the number of drops N significantly decreases (from $3.2 \cdot 10^{16}\mathrm{kg}^{-1}$ to $8.4 \cdot 10^{15}\mathrm{kg}^{-1}$). At the same time, the higher critical radius required for the nucleation causes a delay in the condensation onset, thus, an increase

2

(a) Static pressure field along the nozzle

(b) Droplet radius along the nozzle
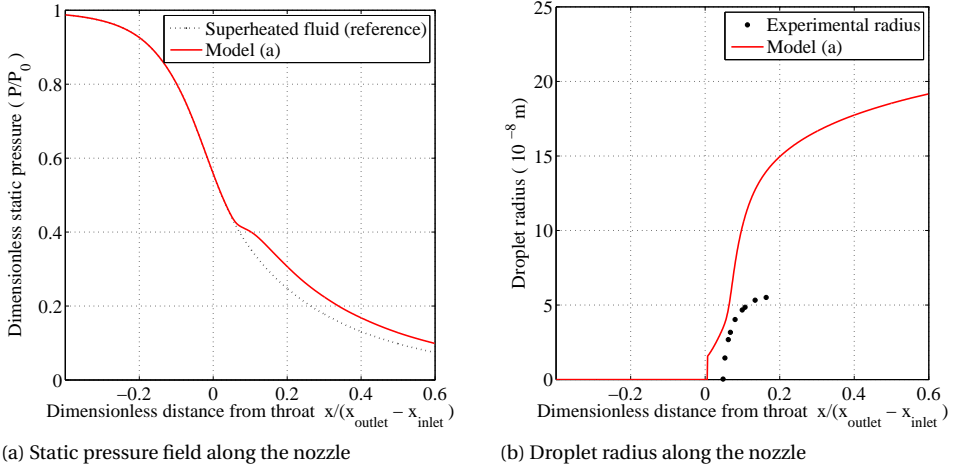
Figure 2.13: Static pressure and radius for model (a) with $r_\sigma = 1.5$, $x_{\text{throat}} = 0$

in the steam degree of subcooling ΔT_{sub}. Due to the linear dependence of the growth rate from ΔT_{sub}, G reaches a value that is 1.5 times higher than the one obtained with $r_\sigma = 1$.

Finally, the combined effect of the droplets number reduction and the increase in G takes the average radius to exceedingly high values (close to $0.2 \cdot 10^{-6}$m, Figure 2.13b).

2.4.1. NUMERICAL INVESTIGATION ON J AND G

After these considerations, a further investigation is made on the nucleation and the growth rate. Two additional factors r_J, r_G are introduced, in analogy with what done for the surface tension, to evaluate the new values J^* and G^*. Multiple tests are done on the expansion No. *18C* to empirically determine the values of all the three coefficients for the best data fit (Table 2.5). The analysis showed that the variation of the nucleation rate slightly affects the location of the condensation onset (test (3) and (4) in Table 2.5). In particular, the reduction of J causes a nucleation delay, in agreement with the behaviour observed in the previous section. However, the influence of this parameter is relatively limited: the change in r_J from 1 to 0.3 moves the pressure bump from 0.44 to 0.42. More-over, the correspondent radius variation is also minimal, from $5.7 \cdot 10^{-8}$m to $5.5 \cdot 10^{-8}$m (the value is taken in correspondence with the last experimental point in [16]).

As observed in test (2) and (3) in Table 2.5, the growth rate has a minor influence on the pressure field with respect to the surface tension. However, it considerably affects the final average radius, that passes from $13 \cdot 10^{-8}$m to $5.7 \cdot 10^{-8}$m. The best fit with the experimental data is obtained for $r_\sigma = 1.4$, $r_J = 0.3$ and $r_G = 0.25$. Figure 2.15 shows the new pressure field and average radius obtained.

It is worth pointing out that the three corrections are approximatively equal to 1 for the low-pressure test case. In particular, the final solution presents no deviation in the
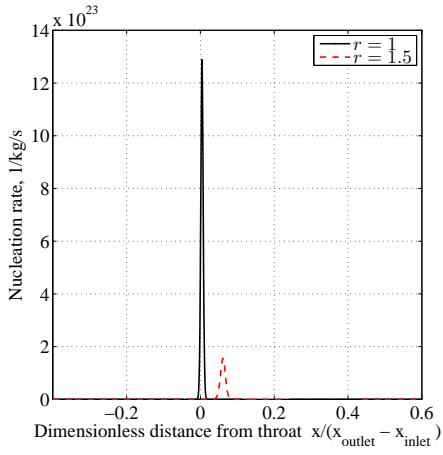
(a) Nucleation rate along the nozzle
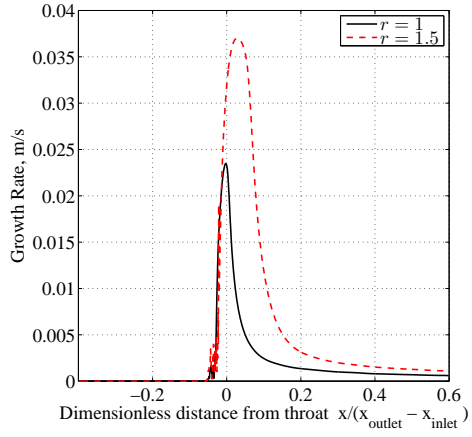
(b) Growth rate along the nozzle

Figure 2.14: Comparison between nucleation and growth rate for $r_\sigma = 1$ and $r_\sigma = 1.5$, $x_{\text{throat}} = 0$
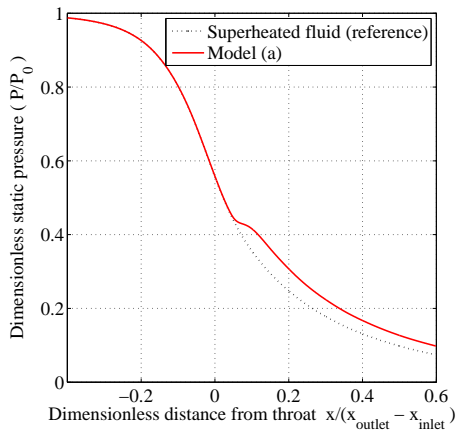
(a) Static pressure field along the nozzle
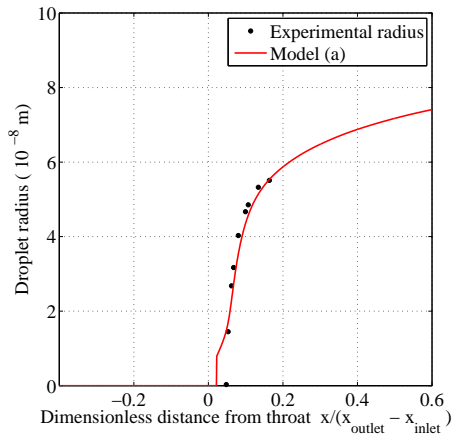
(b) Droplet radius along the nozzle

Figure 2.15: Static pressure and radius for model (b) with $r_\sigma = 1.4$, $r_J = 0.3$ and $r_G = 0.25$, $x_{\text{throat}} = 0$

2

	(1) $r_\sigma = 1$ $r_J = 1$ $r_G = 1$	(2) $r_\sigma = 1.4$ $r_J = 1$ $r_G = 1$	(3) $r_\sigma = 1.4$ $r_J = 1$ $r_G = 0.25$	(4) $r_\sigma = 1.4$ $r_J = 0.3$ $r_G = 0.25$	Exp.
Pressure bump location (Dimensionless static pressure)	0.62	0.46	0.44	0.42	0.42
Average radius $\left(\frac{x}{L_{\text{nozzle}}} = 0.16\right)$, 10^{-8}m	8.6	13	5.7	5.5	5.5

Table 2.5: Four tests made for the determination of r_σ, r_J, r_G: static pressure at condensation onset and average radius, Test No. *18C*

condensation starting point, and a very high accuracy on the radius (Figure 2.1) with respect to the nominal values of the measurements. Additionally, the droplet dimension is comparable for both the low and high pressure test case ($5.0 \cdot 10^{-8}$m and $5.5 \cdot 10^{-8}$m as average radius respectively at the nozzle outlet). Therefore, it can be inferred that the parameters r_σ, r_J, r_G are not only a function of the droplet curvature as in [17], but they present a dependence from the fluid thermodynamic conditions. To support this hypothesis, a second simulation is made on the test No. *18B* in [16], characterized by the same total pressure (100.7 bar) and a total temperature of 638.53 K. Figure 2.16 shows the two steam expansions in the *P-T* chart. Table 2.6 reports the tests made. As condensation starts in the same thermodynamic region at a slightly lower pressure and temperature, it is expected to find r_σ, r_J, r_G with values comparable or closer to 1 with respect to the previous case *18C*. In agreement with these considerations, the final values found are $r_\sigma = 1.35$, $r_J = 0.35$, $r_G = 0.26$. A further investigation is required to gain insights on i) the influence of pressure and temperature on these parameters, ii) the role of metastabilities and iii) whether a correction of σ, J, G could be sufficient to extend the solver in the critical region without penalties in the final accuracy.

	(1) $r_\sigma = 1$ $r_J = 1$ $r_G = 1$	(2) $r_\sigma = 1.4$ $r_J = 0.3$ $r_G = 0.25$	(3) $r_\sigma = 1.35$ $r_J = 0.35$ $r_G = 0.25$	(4) $r_\sigma = 1.35$ $r_J = 0.35$ $r_G = 0.26$	Exp.
Pressure bump location (Dimensionless static pressure)	0.43	0.29	0.30	0.30	0.30
Average radius $\left(\frac{x}{L_{\text{nozzle}}} = 0.45\right)$, 10^{-8}m	7.6	6.5	6	6.2	6.2

Table 2.6: Four tests made for the determination of r_σ, r_J, r_G: static pressure at condensation onset and average radius, Test No. *18B*
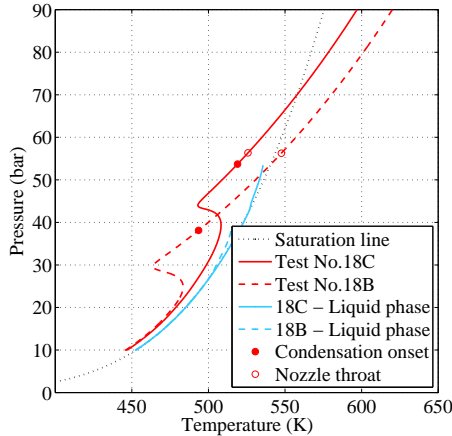
Figure 2.16: Steam metastable expansion in the *P-T* chart, comparison between test No. *18B* ($r_\sigma = 1.35$, $r_J = 0.35$, $r_G = 0.26$) and *18C* ($r_\sigma = 1.4$, $r_J = 0.3$, $r_G = 0.25$)

2.5. CONCLUSIONS

In this chapter, high-pressure condensing steam flows were investigated using the method of moments. A comparison in terms of accuracy, computational cost and numerical stability was carried out between two alternative approaches proposed in [2], employing the mixture or the continuum phase conservation laws, i.e. model (a) and (b) respectively. The test-case considered was the so-called No. *18C* by [16], characterized by $P_0 = 100.7$bar and $T_0 = 615.2$K.

The study highlighted the robustness of model (b) as well as its higher computational efficiency, almost 8 times less than model (a). As pointed out by [2], the bottleneck for model (a) is the iterative procedure employed for determining the mixture thermodynamic properties. For both models, the results showed a good agreement with the experimental data for low-pressure cases. However, a considerable deviation is observed in the predicted pressure field at high-pressure. Furthermore, the average radius was found almost two times larger than the measurements.

To gain insight of these deviations, a sensitivity analysis was performed on the closure models adopted. In particular, three correction factors in the surface tension, the nucleation rate and the growth rate model r_σ, r_J, r_G where introduced.

It was observed that the rise of the surface tension significantly affects the final solution, causing a delay in the condensation onset as well as an increase of the average radius predicted. Additionally, the droplet dimension are significantly affected by the growth rate *G*. It is worth pointing out that *J* is the parameter with the smallest influence on the final motion field, as shown in Table 2.5. The values of r_σ, r_J, r_G were determined empirically to obtain the best fit with the experimental data, reaching almost the same accuracy as in the low-pressure test case studied in [2]. A second analysis was carried out on the so-called No. *18B* (Table 2.6) to confirm the dependence of r_σ, r_J and r_G on the thermodynamic conditions of the fluid.

Chapter 3 will try to establish a physically-based correlation for these three parameters exploiting the data in [16] in order to make the model reliable for metastable condensation close to the critical point, while maintaining the relatively high computational efficiency achieved with the proposed solver.

2

REFERENCES

[1] L. Azzini and M. Pini, *Numerical investigation of high pressure condensing flows in supersonic nozzles,* Journal of Physics: Conference Series **vol. 821** (2017), 10.1088/1742-6596/821/1/012008.

[2] L. Azzini, T. P. Van Der Stelt, and M. Pini, *Numerical investigation of metastable condensing flows with an implicit upwind method,* in *ECCOMAS Congress - Proceedings of the 7th European Congress on Computational Methods in Applied Sciences and Engineering*, Vol. 4 (2016) pp. 7165–7181.

[3] A. Gerber and M. Kermani, *A pressure based eulerian–eulerian multi-phase model for non-equilibrium condensation in transonic steam flow,* International Journal of Heat and Mass Transfer **47**, 2217 (2004), elsevier BV.

[4] S. Dykas and W. Wróblewski, *Numerical modelling of steam condensing flow in low and high-pressure nozzles,* International Journal of Heat and Mass Transfer **55**, 6191 (2012), elsevier BV.

[5] F. Put, *Numerical simulation of condensation in transonic flows,* Ph.D. thesis (2003), phD Thesis, University of Twente, Enschede, The Netherlands.

[6] P. Hill, *Condensation of water vapour during supersonic expansion in nozzles,* Journal of Fluid Mechanics **25**, 593 (1966).

[7] A. J. White, *A comparison of modelling methods for polydispersed wet-steam flow,* International Journal for Numerical Methods in Engineering **57**, 819 (2003), wiley-Blackwell.

[8] M. Giordano, S. Hercus, and P. Cinnella, *Effects of modelling uncertainties in condensing wet-steam flows through supersonic nozzles,* V European Conference on Computational Fluid Dynamics ECCOMAS, Lisbon, Portugal (2010).

[9] W. Wagner *et al.*, *IAPWS industrial formulation 1997 for the thermodynamic properties of water and steam,* (2008) pp. 7–150, springer Science + Business Media.

[10] N. B. Vargaftik, B. N. Volkov, and L. D. Voljak, *International tables of the surface tension of water,* Journal of Physical and Chemical Reference Data **12** (1983), AIP Publishing.

[11] E. Poling, J. Prausnitz, and J. O'Connell, *The Properties of Gases and Liquids*, 5th ed., edited by McGraw-Hill (2001).

[12] R. LeVeque, *Numerical Methods for Conservation Laws* (1992) birkhliuser Verlag, Basel, Switzerland.

[13] M. Moore, P. Walters, R. Crane, and B. Davidson, *Predicting the fog-drop size in wet-steam turbines,* in *Proceedings of the IMechE Conference on Heat and Fluid Flow in Steam and Gas Turbine Plant*, paper C37/73 (1973) pp. 101–109.

[14] Y. A. Ryzhov, U. G. Pirumov, and V. N. Gorbunov, *Nonequilibrium Condensation in High-Speed Gas Flows* (New York : Gordon and Breach Science Publishers, 1989).

[15] E. M. Greitzer, C. S. Tan, and M. B. Graf, *Internal flow: Condept and Applications* (Cambridge University Press, 2004).

[16] G. Gyarmathy, *Nucleation of steam in high-pressure nozzle experiments,* Proceedings of the Institution of Mechanical Engineers, Part A: Journal of Power and Energy **219**, 511 (2005).

[17] D. S. Lai and J. R. Kadambi, *Monodisperse droplet generation by spontaneous condensation of steam flow in nozzles,* Particulate Science and Technology **8**, 55 (1990), informa UK Limited.

2

3

SEMI-ANALYTICAL MODEL FOR THE WILSON POINT PREDICTION

"Everything should be made as simple as possible, but not simpler."

A. Einstein

Parts of this chapter have been published in
L. Azzini et Al., Semi-analytical model for the prediction of the Wilson point for homogeneously condensing steam flow, Internation Journal of Heat and Fluid Flows 70, 1 (2018)

This chapter aims at addressing these issues by theoretically and numerically investigating the onset of condensation for different types of nozzle geometries and operating conditions. At first, the determining parameters driving the process of condensation are recognized by using an analytical approach based on the classical nucleation theory. Then, a systematic analysis on supersonic flow expansions is conducted by means of a quasi-1D numerical model to calculate the degree of subcooling for each case. By introducing a new dimensionless quantity, referred to as *Wilson number W i*, a simplified and computationally affordable method to estimate the Wilson temperature T_w is derived. This enables to gain physical insights on the conditions affecting the Wilson point, and to predict its trend in the vicinity of the critical point. Eventually, the potential of the method for design purposes is illustrated. Given the large number of experiments on condensing steam flows, the proposed semi-analytical model has been developed based on these data, but it can be easily extended to any other condensing fluid.

3.1. NUMERICAL METHODOLOGY

The numerical calculations are conducted with an eulerian-eulerian quasi-1D model constituted by i) the three conservation laws for the continuum phase and ii) two additional transport equations for the droplet properties (number and liquid title). These relations are formulated by exploiting the method of moments described in Ref. [2]. As demonstrated in Ref. [3], this approach proved to be computationally more efficient and numerically more robust than other methods. The interested reader can find a detailed description of the model in Chapter 2.The solution of the equations giving the moments requires two closure relations for the nucleation rate J_s and the growth rate G_s. In this study, the non-isothermal nucleation rate reported in Ref. [4] and the growth rate in Ref. [5] have been adopted. The dispersed phase is assumed to be in mechanical and kinematic equilibrium with the vapor, i.e., no-slip between the two phases. Additionally, the liquid phase temperature is evaluated by using a simplified capillarity model [6]. The thermo-physical properties of the vapor phase are estimated with a thermodynamic model based on the iPRSV equation of state [7]. The use of a complex thermodynamic model allows to account for the non-ideal thermodynamic behaviour of the flow at high reduced pressure. The droplet properties are calculated with the IF-97 model, see A.2 [8]. Finally, the surface tension σ_s is estimated using the model described in Ref. [9].

3.1.1. MODEL CALIBRATION

As observed in Refs. [5, 10, 11], the adoption of J_s, G_s, σ_s in the classical form Chapter 2 leads to an exceedingly high Wilson pressure P_w, deviating from the experimental value by a large amount. Part of this difference is caused by the intrinsic limitations of the classical nucleation theory. It was established that the location of the nucleation onset is particularly sensitive to the steam heat capacity ratio γ [4]. Especially when approaching high-pressures, small variations of this parameter can increase the discrepancy between the theoretical solution and the measurements. Moreover, the surface tension is usually affected by considerable uncertainties, and existing correlations do not take into account any droplet curvature effects [10]. As a consequence, due to the exponential dependence of J_s on σ_s, the theoretical Wilson pressure P_w and the droplet properties are far from the
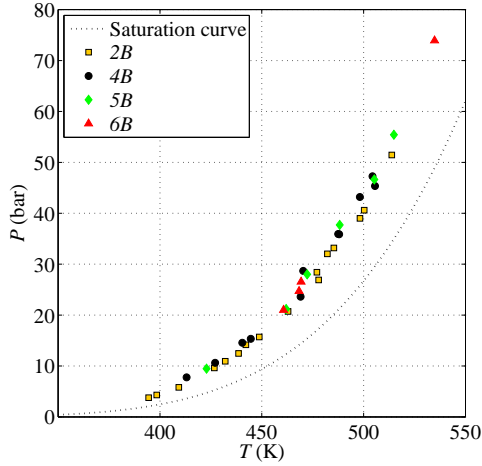
Figure 3.1: Wilson point on the P-T chart obtained from the simulations, see Table B.3 and B.4

experimental data.

Therefore, empirical coefficients are customarily introduced [4, 10] to correct the parameters σ_s, J_s, G_s in order to reach a better accuracy. Following chapter 2, σ_s, J_s, G_s are then multiplied by an empirical factor, yielding to

$$\sigma = r_\sigma \sigma_s, \qquad J = r_J J_s, \qquad G = r_G G_s, \tag{3.1}$$

in which the values r_σ, r_J, r_G are calibrated to achieve the best fit with the measurements. The database for the calibration includes experimental measurements on four different nozzle profiles reported in Ref. [14]. The nozzle geometries are also here referred to as *2B*, *4B*, *5B*, *6B*, and the experiments cover a wide range of pressures (total pressure P_0 from 20.82 bar to 149.74 bar).

For each test, the three corrections r_σ, r_J, r_G have been determined empirically, in order to match the experimental observations in terms of Wilson pressure P_w, droplet average radius $\bar{R}_w$ and number N_w. For some of the tests, no uncertainty interval on the measurements is reported. In all cases in which uncertainty is unknown, the nominal values were used for the calibration. These cases are marked with the superscript − ∗ − hereinafter. Appendix B.1 reports the procedure to obtain the correction factors for expansion test *21As*∗ as an exemplary case. Appendix B.2 reports the calibration factors obtained from all available experiments. Figure 3.1 depicts the Wilson point in the P-T chart obtained from the calculations.

Correlation of r_σ, r_J, r_G for nozzle 2B   Initially, in order to limit the number of parameters affecting the calibration, only the data of a single nozzle profile, i.e., *2B*, were considered. Figure 3.2 shows the values of r_σ, r_J, r_G as a function of the Wilson pressure P_w.

	a(bar)	b(bar)	c
r_σ	-13.3057	-13.3057	0.6086
r_J	-23.4400	-6.9865	0.4241
r_G	-7.7696	-7.7696	4.9642

Table 3.1: Correlation between r_σ, r_J, r_G and P_w: hyperbola coefficients according to (3.2) for nozzle *2B*.

3
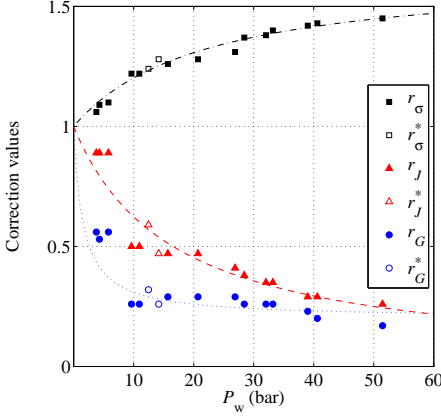
Figure 3.2: Values of r_σ, r_G, r_J for nozzle *2B* and interpolation function according to (3.2) (coefficients reported in Table 3.1).
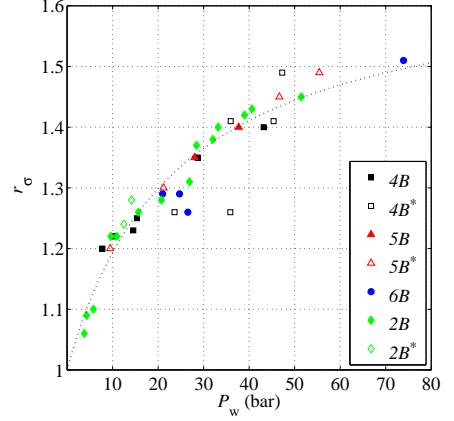
Figure 3.3: Values of r_σ for nozzles *2B, 4B, 5B, 6B* and interpolation function according to (3.2) (coefficients reported in Table 3.2).

Several fitting functions, i.e. logarithmic, exponential, polynomial, power law, have been tested in order to find the best fit for the values of the calibration parameters according to the L2 norm. The best fitting function is given by

$$r_{\sigma,J,G} = \frac{P_w - a}{cP_w - b} + 1 - \frac{a}{b}, \tag{3.2}$$

in which the pressure P_w is in bar. In cases in which the fitting leads to a and b having very similar values, a and b are set equal in order to avoid numerical problems.

The coefficients a, b, c are reported in Table 3.1. Note that, as the low-pressure simulations documented in Ref. [5, 12, 15] well correlate with the measurements, the curve in (3.2) is constrained to pass through the point $(0, 1)$. In other words, it is assumed that low P_w expansions can be modelled with values of r_σ, r_J, r_G equal to one.

Dependence of r_σ, r_J, r_G on the expansion rate   The analysis was repeated for the data of all the four nozzle geometries in order to account for different expansion rates. Figures 4.8, 3.4, and 3.5 display the values for r_σ, r_J, r_G as a function of P_w.

Remarkably, r_σ and r_J appear to be independent from $\dot{P}$. The fitting functions based on (3.2) are displayed in Figures 4.8 and 3.4. The coefficients a, b, c are reported in Table 3.2.
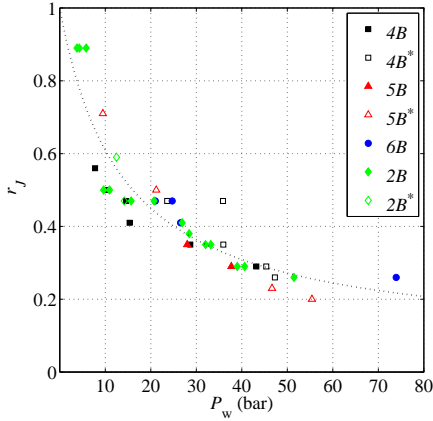
Figure 3.4: Values of r_J for nozzles *2B*, *4B*, *5B*, *6B* and interpolation function according to (3.2) (coefficients reported in Table 3.2).
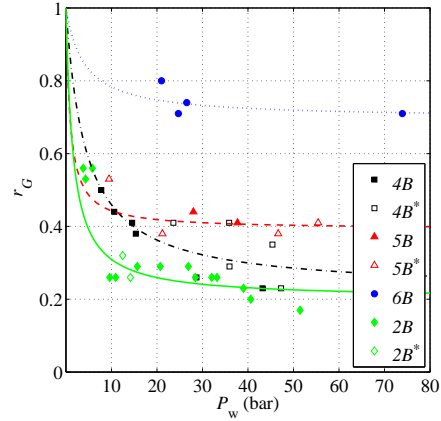
Figure 3.5: Values of r_G for nozzles *2B*, *4B*, *5B*, *6B* and interpolation function according to (3.2) (coefficients reported in Table 3.2).

Parameter	Valid for nozzles	a(bar)	b(bar)	c
r_σ	all nozzles	-14.5208	-14.5208	0.6031
r_J	all nozzles	-34.7273	-22.5671	1.6392
	nozzle *2B*	-7.7696	-7.7696	4.9642
	nozzle *4B*	-11.4766	-9.1298	2.0838
r_G	nozzle *5B*	-2.3322	-2.3322	2.5498
	nozzle *6B*	-5.7402	-5.7402	1.4348

Table 3.2: Correlation between r_σ, r_J, r_G and P_w: hyperbola coefficients according to (3.2) for nozzles *2B*, *4B*, *5B*, *6B*.

As can be noted, Figure 3.5 shows that r_G values related to high cooling rate are much closer to one compared to the others. Therefore, if the expansion rate of the nozzle is high, the correction of the growth rate G must be correspondingly large. As a consequence, the r_G fitting function must be dependent on $\dot{P}$. However, it can be observed from B.1 that r_G mainly affects the radius and the droplet number, whereas the influence on the Wilson point is rather low.

3.1.2. COMPARISON WITH LITERATURE

A summary of the simulations can be found in Table B.3, B.4, while the corresponding Wilson points are depicted in Figure 3.6.

In order to verify the compatibility of the simulations with a wider range of measurements, the results were first compared to the data collected in the test cases of Ref. [16]. Figure 3.6 reports the values of T_w as a function of the temperature $T_{sat}(s_0)$, i.e., the sat-
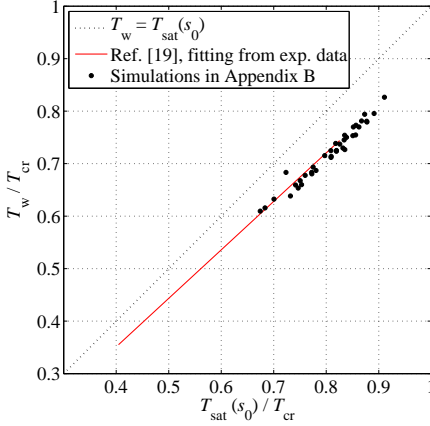
Figure 3.6: Wilson temperature T_w as a function of the saturation temperature $T_{sat}(s_0)$: comparison between the present work and the results in Ref. [16].
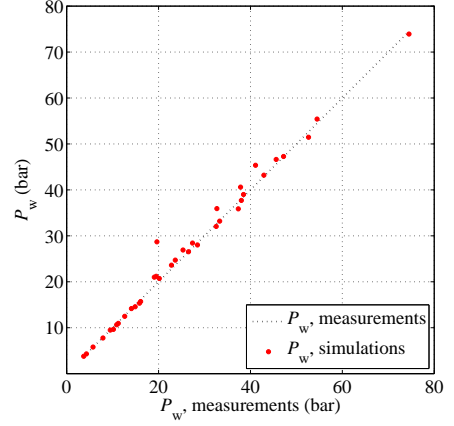
Figure 3.7: Comparison between the condensation pressure evaluated through the numerical model and the experimental measurements in Ref. [16].

uration temperature in correspondence with the entropy

$$s_0 = s(P_0, T_0), \tag{3.3}$$

where P_0, T_0 are the total inlet conditions of the flow. The correlation coefficient R^2 associated with the simulation results and the experimental data is 0.997 (Figure 3.7), which is deemed satisfactory.

Note that Figure 3.6 shows the linear trend as reported in Ref. [16]. However, such trend is misleading, and the dependence of T_w from the rate of the expansion is commonly accepted.

3.2. PARAMETERS AFFECTING THE CONDENSATION ONSET

Physical evidence and more recent studies suggest that the difference $T_{sat}(s_0) - T_w$ is intimately related to the expansion rate [14]. Ideally, for $\dot{P}$ values approaching 0 the fluid must condense at saturation conditions. Formally, the determining parameters influencing the condensation onset can be retrieved by working out the classical nucleation theory. Let be α the liquid volume, defined as

$$\alpha = \frac{4}{3}\pi N \bar{R}^3, \tag{3.4}$$

i.e., the volume occupied by a number N of spherical droplets with an average radius $\bar{R}$. The time derivative of α can thus be expressed as

$$\dot{\alpha} = \frac{4}{3}\pi \bar{R}^2 \left(R\dot{N} + 3N\dot{\bar{R}} \right) = \dot{\alpha}(\dot{N}, \dot{\bar{R}}, \bar{R}, N) \simeq \dot{\alpha}(J, G, \bar{R}, N), \tag{3.5}$$

in which the nucleation and the growth rate J and G are used to model the two derivatives $\dot{N}$, $\dot{\bar{R}}$.

The four terms J, G, $\bar{R}$, N are now analysed separately. The nucleation rate adopted in the present study has the form

$$J = \frac{1}{1+\theta} \frac{\rho_v}{\rho_l} \sqrt{\frac{2\sigma}{\pi MM^3}} \exp\left(-\frac{4\pi \bar{R}_*^2 \sigma}{3KT_v}\right), \tag{3.6}$$

where

$$\theta = 2\frac{\gamma-1}{\gamma+1} \frac{h_v - h_l}{\mathscr{R}T_v} \left(\frac{h_v - h_l}{\mathscr{R}T_v} - 0.5\right), \tag{3.7}$$

$$\bar{R}_* = \frac{2\sigma}{\rho_l \Delta\mathscr{G}}. \tag{3.8}$$

In (3.8), σ is the surface tension, MM is the molecular mass, K is the Boltzmann constant, $\rho_{v,l}$ and $h_{v,l}$ are the densities and the specific enthalpies of the vapor and the liquid phase, $\Delta\mathscr{G}$ is the free Gibbs energy variation of the steam and $\mathscr{R}$ is the gas constant.

Moreover, it is assumed that the liquid and the vapor are in mechanical equilibrium, and that the temperature of the droplets depends on the vapor temperature through a capillarity model (chapter 2). It can be concluded that the liquid properties are a function of T_v, P_v and $\bar{R}$. From (3.6), (3.7), (3.8) and the last consideration it can be inferred that

$$J = J(P_v, T_v, \bar{R}, MM, \gamma). \tag{3.9}$$

The growth rate G is now examined. The relation adopted is in the form

$$G = \frac{\kappa_v (T_{sat}(P_v) - T_v)\left(1 - \frac{\bar{R}_*}{\bar{R}}\right)}{\rho_l (h_v - h_l)\left(1.89 + \bar{R} - 1.89\nu \frac{\lambda_v}{Pr_v}\right)}, \tag{3.10}$$

in which λ_v is given by

$$\lambda_v = \frac{1.5\mu_v \sqrt{\mathscr{R}T_v}}{P_v}, \tag{3.11}$$

κ_v and μ_v are the thermal conductivity and viscosity of the vapor phase and ν is defined as

$$\nu = \frac{\mathscr{R}T_{sat}(P_v)}{h_v - h_l} \left[0.5 - \frac{1}{4}\frac{\gamma+1}{\gamma-1}\frac{\mathscr{R}T_{sat}(P_v)}{h_v - h_l}\right]. \tag{3.12}$$

It follows that

$$G = G(T_v, P_v, \bar{R}, MM, \gamma), \tag{3.13}$$

and, by replacing G with the temporal derivative of the radius $\dot{\bar{R}}$, we have that

$$\bar{R} = \bar{R}(T_v, P_v, MM, \gamma). \tag{3.14}$$

Substituting (3.9) and (3.14) in (3.5) yields

$$\dot{\alpha} = \dot{\alpha}(T_v, P_v, N, MM, \gamma), \tag{3.15}$$

or, equivalently, by inverting the relation,

$$T_v = T_v(\dot{\alpha}, P_v, N, MM, \gamma). \tag{3.16}$$

The term N is now considered. By applying the conservation law for the moment of order 0 (chapter 2), it can be noted that N is a function of the density mixture ρ_m, the velocity v of the flow, the cross sectional area variation along the nozzle $\frac{dA}{dx}$, the critical radius $\bar{R}_*$ and J. In mathematical terms, this results in

$$N = N(\rho_m, v, \frac{dA}{dx}, \bar{R}_*, J) = N(\rho_v, \rho_l, \alpha, v, \frac{dA}{dx}, \bar{R}_*, J) = N(T_v, P_v, \alpha, v, \frac{dA}{dx}, MM, \gamma). \tag{3.17}$$

Finally, the conservation law for the moment of order 3 states that

$$\alpha = \alpha(\rho_m, \rho_l, v, \frac{dA}{dx}, N, J, G, \bar{R}, \bar{R}_*) = \alpha(T_v, P_v, v, \frac{dA}{dx}, N, MM, \gamma). \tag{3.18}$$

As a consequence, the combination of (3.16), (3.17) and (3.18) leads to

$$T_v = T_v(P_v, v, \frac{dA}{dx}, MM, \gamma). \tag{3.19}$$

The temperature $T_{sat}(s_0)$ is now introduced. The bulk of a nozzle flow before inception of condensation can be assumed to be isentropic. The mass and energy balances between a generic state characterized by T_v and the saturation state $T_{sat}(s_0)$ along the expansion can be written as

$$\begin{cases} \rho_v(T_v, s_0) A_v v_v = \rho_{sat}(T_{sat}, s_0) A_{sat} v_{sat} \\ h_v(T_v, s_0) + \frac{1}{2} v_v^2 = h_{sat}(T_{sat}, s_0) + \frac{1}{2} v_{sat}^2 \end{cases}. \tag{3.20}$$

Given the nozzle geometry and the value $T_{sat}(s_0)$, system (3.20) determines the velocities v_v, v_{sat}, thus the steam mass flow $\dot{m}_{flow}$ and the total enthalpy h_0. From (3.19) and (3.20) it can be deduced that

$$T_v = T_v\left(\frac{dA}{dx}, T_{sat}(s_0), MM, \gamma\right), \tag{3.21}$$

as the velocity v as well as the vapor pressure P_v can be easily retrieved through T_v, $\dot{m}_{flow}$, h_0 and the nozzle area distribution.

Finally, $\frac{dA}{dx}$ can be expressed as a function of $\frac{dT_v}{dx}$, i.e., the temperature gradient along the nozzle. The mass balance for an isentropic expansion is

$$\frac{d\rho_v}{\rho_v} - \frac{dh_v}{v_v^2} + \frac{dA}{A} = 0. \tag{3.22}$$

At each value dT_v corresponds a unique variation in density $d\rho_v$ and in specific enthalpy dh_v along the same isentrope. Thus, it is possible to write

$$\frac{d\rho_v(dT_v, s_0)}{\rho_v} - \frac{dh_v(dT_v, s_0)}{v_v^2} + \frac{dA}{A} = 0. \tag{3.23}$$

The term dA is then related to dT_v and s_0. As a result, if the temperature is the temperature of the Wilson point, (3.19) becomes

$$T_w = T_w(dT_v, T_{sat}(s_0), MM, \gamma), \tag{3.24}$$

where dT_v can be expressed through the time derivative $\frac{\partial T}{\partial t}$. From (3.24) it follows that the Wilson point T_w is primarily a function of i) the temperature $T_{sat}(s_0)$ ii) the temperature variation along the nozzle and iii) the fluid under scrutiny. The proposed analytical derivation is not a general proof, as it is valid only for the stated specific set of equations, closure relations and assumptions. A more formal mathematical demonstration, which led to the same conclusions, is treated in Ref. [16]. The analytical closure of (3.24) is discussed in Sec. 3.2.1.

3.2.1. NUMERICAL DETERMINATION OF THE WILSON POINT

The key-idea for the calculation of the Wilson temperature is the fact that there exists a correlation between the average cooling rate $\overline{Cr}$ to which the subcooled vapor is subjected and the time elapsing from the instant in which saturated conditions are achieved until the onset of stable condensation. This time interval, defined as *activation time t_{act}*, allows to cast the temperature difference $T_{sat}(s_0) - T_w$ in dimensionless form as

$$\frac{T_{sat}(s_0) - T_w}{T_{cr}} = \overline{Cr} \cdot t_{act}, \tag{3.25}$$

where $\overline{Cr}$ is the average cooling rate in s^{-1} of the subcooled steam [1]. Hereinafter the left term of (3.25) is referred to as *Wilson number Wi*. Thus, from the physical point of view Wi can be seen as the dimensionless vapor subcooling along an isentrope. From the same relation it follows that

$$T_w \overset{def}{=} T_{sat}(s_0) - T_{cr} Wi \left(T_{sat}(s_0), t_{act} \right), \tag{3.26}$$

B.3 reports the activation time and the cooling rate for all the simulations, whereas Figure 3.8 depicts t_{act} as a function of $\overline{Cr}$. Notably, the activation time in Figure 3.8 can be well approximated by a rectangular hyperbola characterized by Wi equal to 0.1012. Only for the considered range of temperatures and $\overline{Cr}$, the Wilson point is nearly independent from the cooling rate and thermodynamic conditions of the fluid, as already highlighted in Figure 3.6.

The dependence of t_{act} on $\overline{Cr}$, namely $t_{act} = f\left(\overline{Cr}\right) = Wi/\overline{Cr}$, can be interpreted starting from what is commonly known about the physical mechanism of condensation. All the states for which $t > f(\overline{Cr})$ are characterized by the presence of condensate, whereas for time values $t < f(\overline{Cr})$ stable nucleation does not occur.

Therefore, by conventionally defining $t = 0$ s the time instant at which the fluid is at saturation conditions, t_{act} can be viewed as the temporal limit for which stable droplet formation is inhibited. In physical terms, for each value $\overline{Cr}$, the steam remains subcooled for a finite time, after which stable condensation is triggered.

The activation time t_{act} is a characteristic of the condensation process , and as such it depends on the same parameters determining T_w. Sec. 3.2.1 illustrates the quantitative dependence of cooling rate and dew point temperature on t_{act}.

---

[1] The local cooling rate Cr is defined as $\frac{1}{T_{cr}} \frac{\partial T}{\partial t}$

Simulation	Profile	Stretch^2	P_0(bar)	T_0(K)
M	Moore [17]	1	0.250	358.0
$Mx10$	Moore [17]	10	0.250	358.0
$Mx25$	Moore [17]	25	0.250	358.0
$Mx1e5$	Moore [17]	1e5	0.281	380.2^3
$Mx1e10$	Moore [17]	1e10	0.281	380.2^3

Table 3.3: Synthetic simulations characterized by low $\overline{Cr}$ values: nozzle profile and total inlet conditions.

DEPENDENCE OF THE WILSON NUMBER ON THE COOLING RATE $\overline{Cr}$

To explicitly assess the impact of the cooling rate on Wi, three further calculations were carried out for different values of $\overline{Cr}$. Additionally, two expansion simulations with $\overline{Cr}$ approaching 0, namely $Mx1e5$ and $Mx1e10$, were also performed, to prove that at very low $\overline{Cr}$ the subcooling reduces considerably, and the temperature T_w is almost equal to $T_{sat}(s_0)$. Table 3.3 reports the nozzle profiles and the total inlet conditions for these test cases, whereas table B.7 and B.12 report the Wilson point and the activation time.

Figure 3.9 displays the activation time as a function of the cooling rate for all the test considered cases. The fitting led to

$$t_{act} = k_1 \overline{Cr}^{-k_2}, \qquad k_1 = 0.0539, \qquad k_2 = 0.9257. \tag{3.27}$$

It is pointed out that a simple quasi-1D model is not sufficiently reliable for an accurate prediction of the flow motion field for tests $Mx1e5$ and $Mx1e10$, due to the high stretch factor adopted. However, the results obtained are not visibly influencing the trend in Figure 3.9^4.

From the definition of Wi and (3.27) it follows that

$$Wi = t_{act} \overline{Cr} = k_1 \overline{Cr}^{1-k_2}. \tag{3.28}$$

For specified $T_{sat}(s_0)$, the Wilson point is weakly dependent on the cooling rate ($k_2 \approx 1$), suggesting that very large cooling rates $\overline{Cr}$ variations are necessary to obtain appreciable changes of the Wilson temperature, see Figure 3.10. In practice, the range of $\overline{Cr}$ values considered in Figure 3.10 comprises all the Wilson states that can be typically encountered in steam expansion processes. Figure 3.11 reports a T-s diagram indicating the locus of the Wilson points evaluated according to (3.28) for $\overline{Cr}$ values of 1, 100 and 10 000 s^{-1}. The dimensional values of the cooling rates are therefore 6.47e2, 6.47e4, 6.47e6 K/s.

Finally, it can be observed that for $\overline{Cr}$ values ideally approaching 0 Wi vanishes according to (3.28). As a consequence, the Wilson temperature coincides with the saturation temperature, in agreement with the definition of thermodynamic equilibrium.

---

^{2}Due to the lack of data for low $\overline{Cr}$ values, synthetic data were generated by stretching the nozzle to further reduce the cooling rate.

^{3}Total conditions are imposed such that the flow enters at sonic conditions in the two-phase region, at the same temperature as for the test M.

^{4}The values for k_1, k_2 neglecting the last two tests are 0.05794 and 0.9339 respectively.
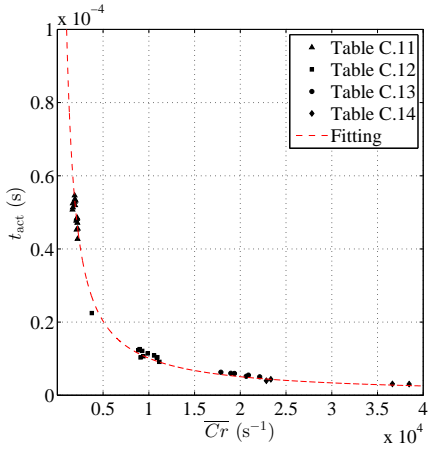
Figure 3.8: Activation time as a function of the cooling rate for the simulations in Tables B.8, B.9, B.10, B.11. Fitting with $Wi = 0.1012$, constant.
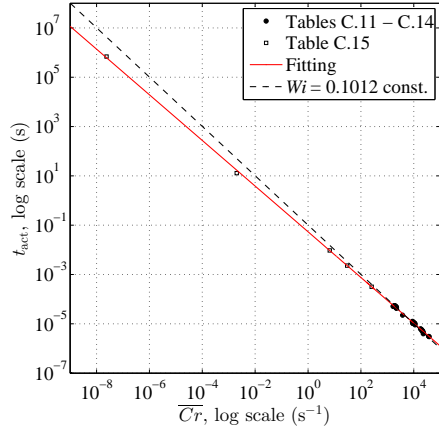
Figure 3.9: Activation time as a function of the cooling rate for the simulations in Tables B.8, B.9, B.10, B.11, B.12.
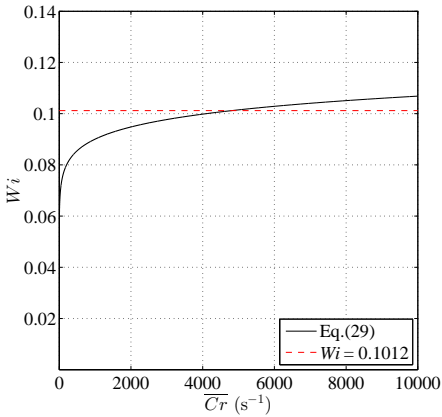
Figure 3.10: Wilson number Wi as a function of $\overline{Cr}$ according to (3.28).
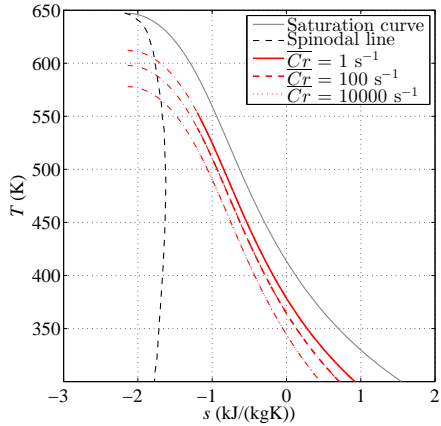
Figure 3.11: T-s chart reporting i) saturation curve, ii) spinodal curve and iii) Wilson point as in (3.28) for $\overline{Cr}$ values of 1, 100 and $10\,000$ s^{-1}.
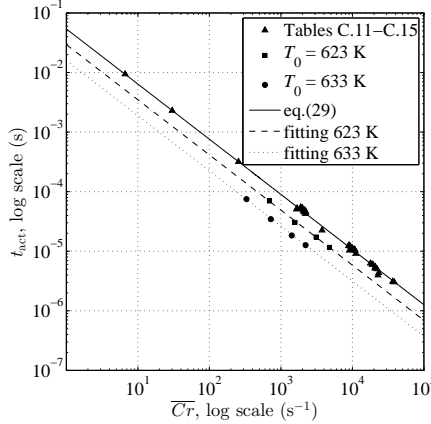
Figure 3.12: Activation time as a function of the cooling rate for the simulations in B.3, $k_2 = 0.9257$.

From a mathematical point of view, for $\overline{Cr}$ approaching 0, t_{act} must tend to $+\infty$, see (3.27): the physical time required to reach almost zero subcooling, i.e. $Wi \to 0$, with a cooling rate approaching 0 is an indeterminate form 0/0.

DEPENDENCE OF THE WILSON NUMBER ON $T_{sat}(s_0)$

The curves obtained with (3.27) predicts non-physical states in the vicinity of critical point, since these predicted states are unstable, see Figure 3.11. Thus, (3.28) must be modified in order to i) maintain the same dependence on $\overline{Cr}$ observed for low temperatures and ii) fulfil the condition

$$T_{\mathrm{w}} = T_{\mathrm{cr}} \tag{3.29}$$

for $T_{sat=T_{cr}}$, as in the proximity of the critical point the spinodal curve is increasingly closer to the saturation line, and the Wilson temperature is constrained to also approach T_{sat} [1, 18].

Therefore, synthetic data in the vicinity of the critical point and instrumental to this purpose were generated. Two simulations with total reduced inlet conditions equal to (a) $P_{0,r} = 0.70$, $T_{0,r} = 0.96$ and (b) $P_{0,r} = 0.81$, $T_{0,r} = 0.98$ were carried out for each of the nozzle profiles reported in Ref. [14]. It was not possible to perform simulations with inlet total conditions with $P_{0,r} > 0.81$ because the calculation of metastable states fails due to numerical singularities. For the sake of conciseness, the test cases (a) will be referred to as *A623K, B623K, C623K, D623K*, whereas the tests (b) will be called *A633K, B633K, C633K, D633K* hereafter.

The correction factors r_σ, r_J, r_G for the numerical simulations are retrieved from Table 3.2. Tables B.5, B.6 and B.13 report Wilson temperature and the activation time obtained with these simulations, whereas Figure 3.12 depicts t_{act} as a function of $\overline{Cr}$.

It is observed that the values t_{act} and $\overline{Cr}$ are correlated by lines (hyperbolas in a linear scale) having very similar slopes. Thus k_2 can be assumed constant and equal to the value in (3.28), as the fitting of (3.28) gives values of k_2 which are only marginally different.
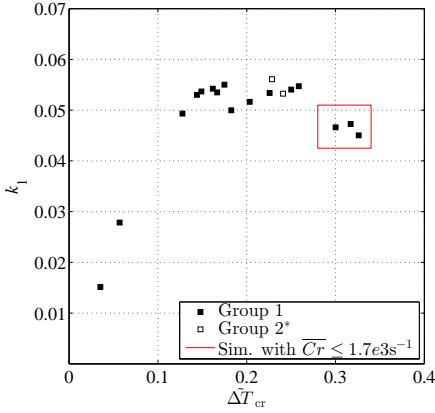
Figure 3.13: Values of k_1 for nozzle *2B* as a function of $\tilde{\Delta T}_{\mathrm{cr}}$ (obtained from (3.28) and Table B.8).
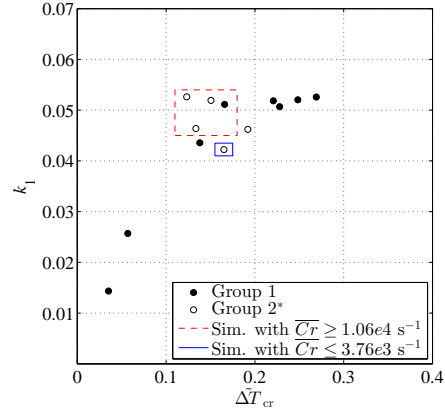
Figure 3.14: Values of k_1 for nozzle *4B* as a function of $\tilde{\Delta T}_{\mathrm{cr}}$ (obtained from (3.28) and Table B.9).

In order to determine an expression for k_1, the relation in (3.28) is inverted. The quantity $Wi\overline{Cr}^{k_2-1}$ for the profiles *2B*, *4B*, *5B*, *6B* is displayed in Figures 3.13 - 3.16 as a function of the dimensionless temperature difference

$$\tilde{\Delta T}_{\mathrm{cr}} = 1 - \frac{T_{\mathrm{sat}}(s_0)}{T_{\mathrm{cr}}}. \tag{3.30}$$

$\tilde{\Delta T}_{\mathrm{cr}}$ is only a function of s_0: for each test case this variable is defined only by the total inlet conditions P_0, T_0.

The values of k_1 can be fitted with an exponential function. Thus, (3.27) can be rewritten as

$$t_{\mathrm{act}} = k_1\left(\tilde{\Delta T}_{\mathrm{cr}}\right)\overline{Cr}^{-k_2} = \hat{k}_1\left(1 - \exp\left(-\frac{\tilde{\Delta T}_{\mathrm{cr}}^{k_3}}{\tau_T}\right)\right)\overline{Cr}^{-k_2}. \tag{3.31}$$

with $k_1 \rightarrow \hat{k}_1(\Delta T \approx 1)$. As (3.31) must reduce to (3.27) for low $T_{\mathrm{sat}}(s_0)$ values, the coefficient $\hat{k}_1$ is taken equal to 0.0539. This results in $k_3 = 1.359$ and $\tau_T = 0.0299$. Consequently, the Wilson number reads

$$Wi = \hat{k}_1\left(1 - \exp\left(-\frac{\tilde{\Delta T}_{\mathrm{cr}}^{k_3}}{\tau_T}\right)\right)\overline{Cr}^{1-k_2}. \tag{3.32}$$

Figure 3.17 reports the function $k_1 = k_1(\tilde{\Delta T}_{\mathrm{cr}})$. Additionally, Figure 3.18 reports the Wilson curve according to (3.31) for $\overline{Cr}$ values of 1, 100 and $10\,000$ s^{-1}.

The deviation between the best fit and the values of k_1 for the majority of the cases is less than 10%. However, for a limited number of test cases such value is considerably higher. For instance, three points in Figure 3.13 deviate considerably from the exponential trend. These points correspond to nozzle expansions characterized by the lowest $\overline{Cr}$. The same is also observed for nozzle *4B* (Figure 3.14): the measurements that are farther
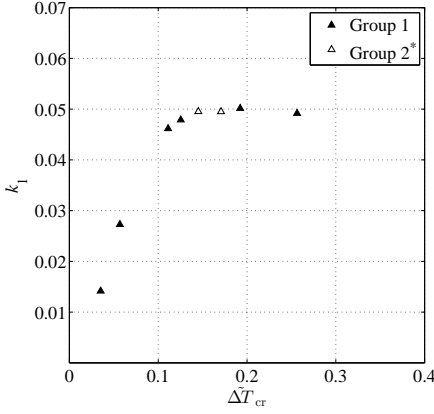
Figure 3.15: Values of k_1 for nozzle *5B* as a function of $\Delta \tilde{T}_{cr}$ (obtained from (3.28) and Table B.10).
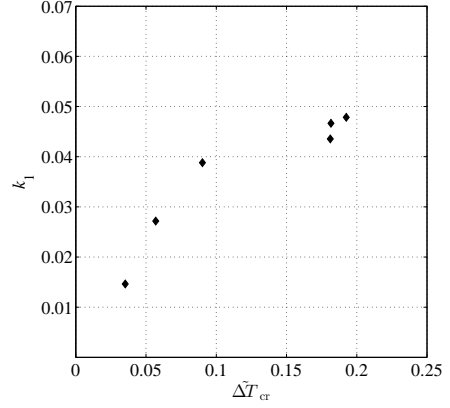
Figure 3.16: Values of k_1 for nozzle *6B* as a function of $\Delta \tilde{T}_{cr}$ (obtained from (3.28) and Table B.11).

from the fitting curve (Tests *21As**, *21Bs**, *21Cs**, *18B* and Test *19Cs**) feature the highest and the lowest cooling rates respectively. A possible explanation for the deviation of these points from the fitting is that k_1 might depend on $\overline{Cr}$.

Figure 3.17 shows that the term $\Delta \tilde{T}_{cr}$ visibly affects the value of k_1 only at high reduced temperatures, namely for $T_{sat}(s_0) > 0.8 T_{cr}$. In these conditions, the surface tension starts slowly vanishing, thus reducing the degree of subcooling needed for stable droplets to form. For $T_{sat}(s_0) > 0.9 T_{cr}$ the degree of subcooling falls down rapidly, and the thermodynamic state of the condensing vapor is quickly reverted back to equilibrium, even in very fast expansion processes.

By inverting (3.31), the cooling rate $\overline{Cr}$ can be rewritten as

$$\overline{Cr} = \left(\frac{k_1 \left(\Delta \tilde{T}_{cr} \right)}{t_{act}} \right)^{\frac{1}{k_2}} , \tag{3.33}$$

thus, in terms of activation time, the Wilson number becomes

$$Wi = \overline{Cr} \cdot t_{act} = k_1 \left(\Delta \tilde{T}_{cr} \right)^{\frac{1}{k_2}} \cdot (t_{act})^{1 - \frac{1}{k_2}} . \tag{3.34}$$

Therefore, given a set of total inlet conditions, thus a set of $\Delta \tilde{T}_{cr}$ value, the isentropic subcooling Wi becomes only a function of a single variable, i.e., the activation time. (3.34) is particularly useful for analysis and design purposes as exemplified in sec. 3.3.

3.3. Application

3.3.1. Condensation onset prediction in a supersonic nozzle

Equation (3.34) for the estimation of the Wilson number Wi allows to interpret T_w as a time-dependent function, i.e., $T_w(t)$. Figure 3.19 displays $T_w(t)$ for $T_{sat}(s_0) = 550$ K, 580 K, 610 K, 630 K, corresponding to $\Delta \tilde{T}_{cr} = 0.15, 0.10, 0.06, 0.03$ respectively. In order to
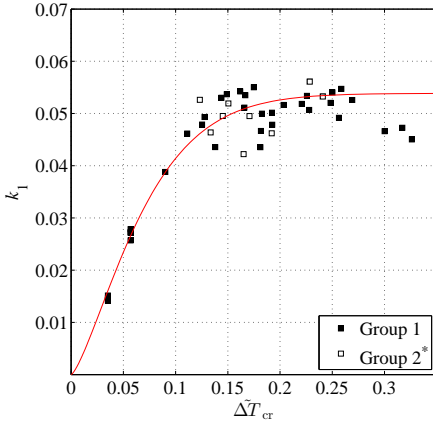
Figure 3.17: Values of k_1 as a function of $\tilde{\Delta T}_{cr}$ obtained from (3.28) and Tables B.8, B.9, B.10, B.11, fitting function (see (3.31)).
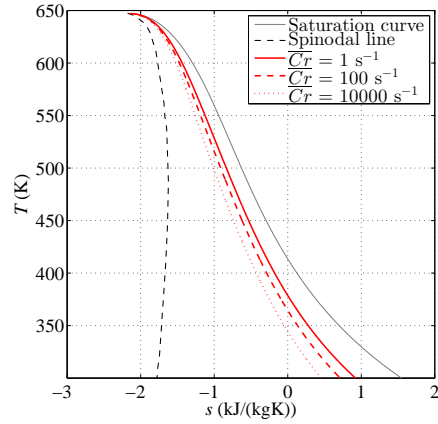
Figure 3.18: T-s chart reporting saturation curve, spinodal curve and Wilson point as in (3.31) for $\overline{Cr} = 1, 100, 10000$ s^{-1}.

3

determine the onset of condensation for an arbitrary expansion process, the following procedure, involving the use of plotted information, is proposed:

1. the curve $T_w(t)$ is drawn for a specified $T_{sat}(s_0)$ in a T-t chart;

2. a single-phase simulation allowing for metastable conditions is carried out;

3. the temperature profile along the expansion is displayed in the same T-t chart. From the definition of t_{act}, at the time $t = 0$ s the fluid is in saturated conditions, i.e., $T(0) = T_{sat}(s_0)$;

4. stable condensation occurs if the flow reaches the Wilson state. Thus, the nucleation onset corresponds to the intersection point between $T(t)$ and $T_w(t)$.

Once the degree of subcooling is known, the thermodynamic wetness loss can be calculated with the approach proposed in Ref. [19].

Figure 3.20 reports the curve $T(t)$ for the Barshdorff test-case [11] along with the correspondent $T_w(t)$. $T_{sat}(s_0)$ is approximately equal to 361 K. Additional notes on this time-dependent representation are reported in B.4.

3
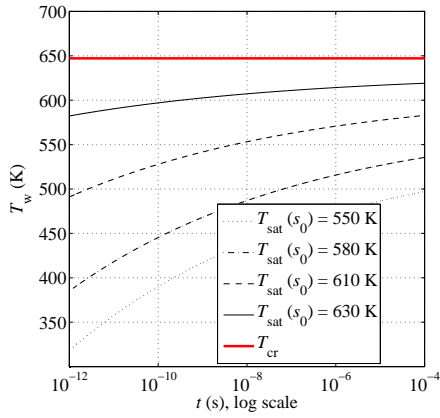
Figure 3.19: Wilson cure $T_w(t)$ as a function of the time t_{act}, $T_{sat}(s_0) = 550$ K, 580 K, 610 K, 630 K.
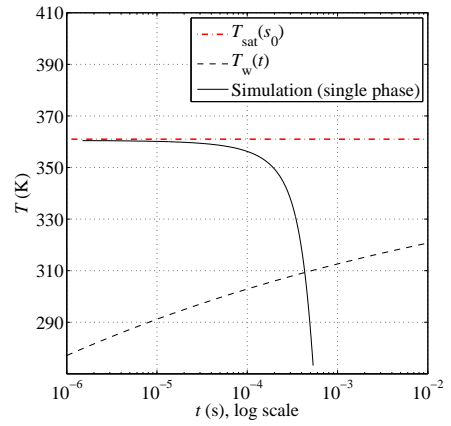
Figure 3.20: Temperature profile for the Barshdorff test case[11] and Wilson point as a function of the time, $T_{sat}(s_0) \simeq 361$ K.

	Barshdorff [11]							
	P_0	T_0	$T_{\text{sat}}(s_0)$	$P_{\text{w,exp}}$	t_{act}	$\overline{Cr}$	P_{w}	Dev.%
B	0.784 bar	373.2 K	361.0 K	0.370 bar	4.33e-4 s	173 s^{-1}	0.366 bar	-1.1
	Bakhtar [20]							
	P_0	T_0	$T_{\text{sat}}(s_0)$	$P_{\text{w,exp}}$ ($\pm$0.14 bar)	t_{act}	$\overline{Cr}$	P_{w}	Dev.%
S1	32.0 bar	535.0 K	491.9 K	13.50 bar	5.03e-5 s	1865 s^{-1}	13.71 bar	+1.6
M2	32.0 bar	531.0 K	494.7 K	13.76 bar	4.82e-5 s	1952 s^{-1}	14.49 bar	+5.3
L2	32.0 bar	544.7 K	485.6 K	10.08 bar	3.02e-5 s	3236 s^{-1}	11.70 bar	+16.0
	31.86 bar	546.7 K	484.0 K	10.08 bar	2.93e-5 s	3369 s^{-1}	11.24 bar	+11.5

Table 3.4: Validation of (3.31) with four steam supersonic expansions from Refs. [20] and [11]. Comparison between the experimental Wilson pressure $P_{\text{w},exp}$ and the value predicted by using the proposed semi-analytical method.

Table 3.4 shows the Wilson point predictions obtained for four different test-cases reported in Refs. [20] and [11]. With reference to the tests *B* and *S1*, the deviation between the predicted and the experimental P_w values is less than 2%, whereas for the test *L2* the difference is more pronounced, i.e., approximately 16%. On average, the computational cost of each test case, if the domain is discretized with 1000 cells, is of the order of five minutes on a single processor Intel(R) Core(TM) i7-4600U CPU @ 2.10GHz.

In order to assess the effect of experimental uncertainty, which is ±2 K on T_0 and ±0.14 bar on P_0, another simulation was performed with a value of P_0 decreased of the uncertainty interval and a value of T_0 increased by the the uncertainty interval. This is done in order to obtain a simulation result that is closer to the measurement, with input conditions that are still within the experimental uncertainty (Table 3.4). The deviation in this case is 11.5%. Deviations are arguably due to the dependence of k_1 from $\overline{Cr}$, see (3.31). The *L2* test features a value of $\overline{Cr}$, see Figure 3.13.

Overall, the accuracy of the proposed method is of the same order of that of more complex models [21] and better if compared to other numerical models based on the method of moments documented in the literature. As an example, the model used in the simulations of the *L2* test case discussed in Ref. [5] leads to a value of P_w that is 40 % different from the measured value.

From the results in Table 3.4 , it can be seen that the higher is the cooling rate, the higher is the difference between measured and estimated P_w values. This can be ascribed to the assumptions affecting k_1, k_2. Additional measurements are required to fully work out the dependence of k_1 and k_2 on the cooling rate, especially for values in excess of 2e3 s^{-1} (i.e. 1.3e6 K/s).

3.3.2. DESIGN OF CONVERGING-DIVERGING NOZZLES

The proposed semi-analytical model can be exploited for design purposes. For example, consider the design of an adapted nozzle free of condensation, thus unaffected by the associated thermodynamic wetness losses. The specified operating conditions are P_0, T_0 and static back-pressure.

Figure 3.21 shows three expansions in the T-t chart characterized by $\overline{Cr}$ values of (a) 0.06 s^{-1}, (b) 24 s^{-1}, and (c) 6000 s^{-1}. $T_{\text{sat}}(s_0)$ is 361 K, the same as that in the Barsh-dorff test case, whereas a nozzle static back-pressure of 0.42 bar is arbitrarily imposed at the outlet boundary, corresponding to a static back temperature of 320 K assuming isentropic expansion.

As anticipated, the onset of stable condensation is located at the intersection of the curves $T_w(t)$ and $T(t)$. For instance, the Wilson temperature for expansion (a) is approximately 326 K, whereas in expansion (b) condensation will occur only in correspondence of the nozzle outlet section. In expansion (c) the Wilson temperature is well below the outlet temperature of the nozzle, thus it can be argued that condensation does not occur.

In essence, homogeneous condensation is not triggered if the residence time of sub-cooled steam within the nozzle is lower than the activation time corresponding to a characteristic $\overline{Cr}$, cf. expansion (b) and (c). Therefore, given the total inlet conditions and the outlet back-pressure leading to an expansion process below the saturation conditions, the curve $T_w(t)$ provides the minimum cooling rate $\overline{Cr}$ required to avoid the formation of condensing fog inside the channel. $\overline{Cr}$ can be used as input or constraint for a design
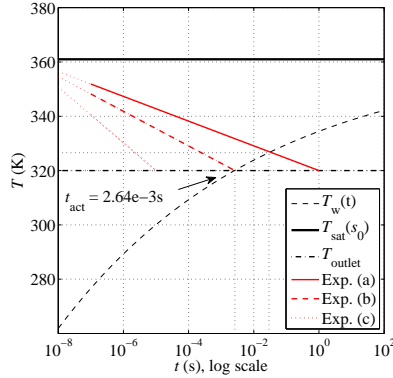
Figure 3.21: Examples of (a) condensation inside the nozzle, (b) condensation at the nozzle outlet and (c) no condensation, $T_{\text{sat}}(s_0) \simeq 361$ K (from Barshdorff [11]). Due to the log scale adopted, for the sake of clarity the expansions are displayed starting from $t = 10^{-9}$ s instead of 0 s.

of condensation-free supersonic nozzles expanding steam.

Note that the cooling rate is directly related to the nozzle length L, as the activation time t_{act} can be defined for a 1D test case as

$$t_{\text{act}} = \int_{x(T_{\text{sat}}(s_0))}^{x(T_w)} \frac{dx}{v},$$ (3.35)

where x is the coordinate along the nozzle axis and v is the velocity of the flow. By stretching the nozzle geometry along the coordinate x, one can modify the final cooling rate. As an example, $\overline{Cr}$ can be doubled by reducing the total length L of the nozzle by a factor 2.

Suppose that the method of characteristics is used to design the divergent section of a nozzle profile [22]. In this case, the parameter L is calculated as a function of i) the flow conditions and ii) the throat curvature radius r_t. Equation (3.34) can provide the minimum cooling rate required to avoid condensation, thus, a reference value L that can be used to determine a suitable r_t value for a revised nozzle design.

3.4. CONCLUSIONS

A new semi-analytical model for the estimation of the Wilson point in steam supersonic expansions has been developed and validated by comparison with experimental information. The goal of the modelling effort was two-fold: first, identifying the most significant flow parameters affecting the condensation onset and quantifying the impact of such parameters on the Wilson point; secondly, the establishment of a simplified procedure for the prediction of condensation in nozzle flows suitable for analysis and design.

In order to account for the influence of $\overline{Cr}$ and $T_{\text{sat}}(s_0)$, the Wilson point definition was reformulated in such a way that T_w could be obtained in terms of the Wilson number $Wi(t)$, a new dimensionless and time-dependent quantity. It was therefore found that:

1. for the range of cooling rates observed in steam nozzle expansions documented in Ref. [14] (order of $10^6 - 10^7$ K/s), the Wilson number Wi weakly depends on $\overline{Cr}$;

2. the effect of T_{sat} on the location of the Wilson point becomes significant for $T_{\text{sat}}(s_0) > 0.8T_{\text{cr}}$. For $T_{\text{sat}}(s_0) > 0.9T_{\text{cr}}$, the surface tension rapidly vanishes and stable condensation is promoted, regardless of the cooling rate of the expansion.

Furthermore, the Wilson temperature $T_{\text{w}}(t)$ can be used to predict the onset of condensation without the need of performing demanding two-phase simulations. The application of (3.34) in four different test cases revealed that the accuracy of the obtained predictions is of the same order of those estimated with more complex models available in the literature. Once the degree of subcooling is known, associated thermodynamic wetness losses can be estimated a priori with available models [19].

Finally, the model can also be applied in the design of condensation-free nozzles, as it allows to retrieve the minimum cooling rate needed to prevent inception of stable condensation.

REFERENCES

[1] L. Azzini, M. Pini, and P. Colonna, *Semi-analytical model for the prediction of the wilson point for homogeneously condensing steam flow,* Internation Journal of Heat and Fluid Flows **70**, 1 (2018).

[2] F. Put, *Numerical simulation of condensation in transonic flows*, Ph.D. thesis (2003), phD Thesis, University of Twente, Enschede, The Netherlands.

[3] A. J. White, *A comparison of modelling methods for polydispersed wet-steam flow,* International Journal for Numerical Methods in Engineering **57**, 819 (2003), wiley-Blackwell.

[4] F. Bakhtar, J. B. Young, A. J. White, and D. A. Simpson, *Classical nucleation theory and its application to condensing steam flow calculations,* Proceedings of the Institution of Mechanical Engineers, Part C: Journal of Mechanical Engineering Science **219**, 1315 (2005).

[5] M. Giordano, S. Hercus, and P. Cinnella, *Effects of modelling uncertainties in condensing wet-steam flows through supersonic nozzles,* V European Conference on Computational Fluid Dynamics ECCOMAS, Lisbon, Portugal (2010).

[6] S. Dykas and W. Wróblewski, *Numerical modelling of steam condensing flow in low and high-pressure nozzles,* International Journal of Heat and Mass Transfer **55**, 6191 (2012), elsevier BV.

[7] T. P. van der Stelt, N. R. Nannan, and P. Colonna, *The iPRSV equation of state,* Fluid Phase Equilib. **330**, 24 (2012).

[8] W. Wagner *et al.*, *IAPWS industrial formulation 1997 for the thermodynamic properties of water and steam,* (2008) pp. 7–150, springer Science + Business Media.

[9] N. B. Vargaftik, B. N. Volkov, and L. D. Voljak, *International tables of the surface tension of water,* Journal of Physical and Chemical Reference Data **12** (1983), AIP Publishing.

[10] D. S. Lai and J. R. Kadambi, *Monodisperse droplet generation by spontaneous condensation of steam flow in nozzles,* Particulate Science and Technology **8**, 55 (1990), informa UK Limited.

[11] J. Halama and J. Fort, *Numerical simulation of steam condensation in a nozzle,* EPJ Web of Conferences **25** (2012), 10.1051/epjconf/20122501020, EDP Sciences.

[12] L. Azzini, T. P. Van Der Stelt, and M. Pini, *Numerical investigation of metastable condensing flows with an implicit upwind method,* in *ECCOMAS Congress - Proceedings of the 7th European Congress on Computational Methods in Applied Sciences and Engineering*, Vol. 4 (2016) pp. 7165–7181.

[13] L. Azzini and M. Pini, *Numerical investigation of high pressure condensing flows in supersonic nozzles,* Journal of Physics: Conference Series **vol. 821** (2017), 10.1088/1742-6596/821/1/012008.

[14] G. Gyarmathy, *Nucleation of steam in high-pressure nozzle experiments,* Proceedings of the Institution of Mechanical Engineers, Part A: Journal of Power and Energy **219**, 511 (2005).

[15] A. Gerber and M. Kermani, *A pressure based eulerian–eulerian multi-phase model for non-equilibrium condensation in transonic steam flow,* International Journal of Heat and Mass Transfer **47**, 2217 (2004), elsevier BV.

[16] Y. A. Ryzhov, U. G. Pirumov, and V. N. Gorbunov, *Nonequilibrium Condensation in High-Speed Gas Flows* (New York : Gordon and Breach Science Publishers, 1989).

[17] M. Moore, P. Walters, R. Crane, and B. Davidson, *Predicting the fog-drop size in wet-steam turbines,* in *Proceedings of the IMechE Conference on Heat and Fluid Flow in Steam and Gas Turbine Plant*, paper C37/73 (1973) pp. 101–109.

[18] K. Bier, F. Ehrler, and G. Theis, *Spontaneous condensation in stationary nozzle flow of carbon dioxide in a wide range of density,* in *Adiabatic Waves in Liquid-Vapor Systems* (Springer Science + Business Media, 1990) pp. 129–141.

[19] J. Young, *Semi-analytical techniques for investigating thermal non-equilibrium effects in wet steam turbines,* International Journal of Heat and Fluid Flow **5**, 81 (1984).

[20] F. Bakhtar and K. Zidi, *Nucleation phenomena in flowing high-pressure steam: experimental results,* ARCHIVE: Proceedings of the Institution of Mechanical Engineers, Part A: Journal of Power Engineering **203**, 195 (1989).

[21] F. Bakhtar and K. Zidi, *Nucleation phenomena in flowing high-pressure steam part 2: theoretical analysis,* ARCHIVE: Proceedings of the Institution of Mechanical Engineers, Part A: Journal of Power and Energy 1990-1996 **204**, 233 (1990).

[22] A. Guardone, A. Spinelli, and V. Dossena, *Influence of molecular complexity on nozzle design for an organic vapor wind tunnel,* Journal of Engineering for Gas Turbines and Power **135**, 042307 (2013).

4

METASTABLE CONDENSATION IN ORGANIC FLOWS

"Two men walk into a bar. One man orders H_2O.
The other says   -I'll have H_2O, too-.
The second man dies."

The impact of fluid characteristics on the process of non-equilibrium condensation of high-speed vapors in supersonic nozzles is investigated. Physical insights are derived by estimating the degree of vapor sub-cooling and thermodynamic wetness loss as function of fluid characteristics using a fully turbulent two-phase numerical model. In particular, the analysis is conducted for H_2O, CO_2 and refrigerant R22. Based on the results, it can be inferred that i) the dependence of the Wilson point from the cooling rate of the expansion is not affected by the type of fluid, and ii) the entity of the flow subcooling is proportional to the molecular mass fo the fluid. Additionally, the thermodynamic losses are arguably higher for fluids for fluids that feature heavier molecules, and of the same order of magnitude of the flow viscous losses.

4.1. NUMERICAL MODEL

The adopted condensing model is based on the moments theory. In particular, the Hill formulation [1] is at the basis of the condensation model utilized for the nozzle simulations. This choice is mainly dictated by the high computational efficiency of this method with respect to other eulerian-lagrangian and fully-eulerian approaches [2], especially for multi-dimensional calculations. The SU2 open source CFD tool for compressible flows was adopted as the base for the implementation [3]. The conservation laws for the continuum phase are

$$
\begin{cases}
\frac{\partial \rho_v}{\partial t} + \nabla \cdot \left(\rho_v \mathbf{v} \right) = S_v \\
\frac{\partial \rho_v v_x}{\partial t} + \nabla \cdot \left(\rho_v v_x \cdot \mathbf{v} \right) + \frac{\partial P}{\partial x} = \nabla \cdot \tau_\mathbf{x} + S_v v_x + S_{\mathrm{SA},v_x} \\
\frac{\partial \rho_v v_y}{\partial t} + \nabla \cdot \left(\rho_v v_y \cdot \mathbf{v} \right) + \frac{\partial P}{\partial y} = \nabla \cdot \tau_\mathbf{y} + S_v v_y + S_{\mathrm{SA},v_y} \\
\frac{\partial (\rho_v e_{0,v})}{\partial t} + \nabla \cdot \left(\rho_v h_{0,v} \mathbf{v} \right) = \nabla \cdot (\tau \mathbf{v}) + S_v h_{0,l} + S_{\mathrm{SA},e},
\end{cases}
\tag{4.1}
$$

in which ρ_v is the vapor phase density, v_x, v_y the components of the velocity vector $\mathbf{v}$, P the pressure, $e_{0,v}$ and $h_{0,v}$ the total energy and enthalpy of the vapor and $h_{0,l}$ the liquid total enthalpy and τ is the viscous tensor and S_{SA,v_x}, S_{SA,v_y}, $S_{\mathrm{SA},e}$ are the turbulent source terms. Additionally, the source term S_v models the exchange of mass at the interface between the two phases, given by

$$
S_v = -\rho_m \frac{3Y}{R} \frac{\partial R}{\partial t},
\tag{4.2}
$$

where ρ_m, Y, R are the mixture density, the liquid mass fraction and the droplet average radius respectively. For details on the derivation of S_v, see A.1.

The system of transport equations that describe the evolution of the liquid phase is

$$
\begin{cases}
\frac{\partial}{\partial t} (\rho_m \mu_0) + \nabla \cdot (\rho_m \mu_0 \mathbf{v}) = \rho_m J(R_*) \\
\frac{\partial}{\partial t} (\rho_m \mu_1) + \nabla \cdot (\rho_m \mu_1 \mathbf{v}) = \rho_m J(R_*) R_* + \mu_0 G \\
\frac{\partial}{\partial t} (\rho_m \mu_2) + \nabla \cdot (\rho_m \mu_2 \mathbf{v}) = \rho_m J(R_*) R_*^2 + 2\mu_1 G \\
\frac{\partial}{\partial t} (\rho_m \mu_3) + \nabla \cdot (\rho_m \mu_3 \mathbf{v}) = \rho_m J(R_*) R_*^3 + 3\mu_2 G
\end{cases},
\tag{4.3}
$$

in which μ_j is the generic moment of order -j and $\mathbf{v}$ is the velocity of the flow. The models for the nucleation rate J, the growth rate G and the critical radius R_* are reported in C.2.

Liquid and vapor are assumed to be in mechanical and kinematic equilibrium, i.e., they are characterized by the same pressure and velocity. Additionally, the liquid temperature T_l is evaluated through the capillarity model also reported in C.2.

The chosen turbulence model is the one of Spalart-Allmaras [3]. The systems (4.1) and (4.3) are solved using a segregated approach. The equations are discretized in space through a second-order upwind numerical scheme and are integrated in time with an implicit Euler method.

4.1.1. THERMODYNAMIC MODELING OF THE TWO-PHASE MIXTURE

The thermodynamic properties of the vapor phase are calculated with the iPRSV equation of state (EoS) [4], implemented in an external library [5] linked to SU2. Viscosity and thermal conductivity are calculated using the model [5] and fixed to the values obtained with the total conditions P_0, T_0 at the nozzle inlet.

The model for the liquid density of water is reported in A.2.1, while that of the other fluids is documented in Ref. [6]. The liquid enthalpy is calculated as in C.1. Saturation properties for water are given as in A.2.3, A.2.4, whereas they are calculated as in [6] for the other fluids. These last choices are due to the long computational time required by the thermodynamic model selected if the computed state is in the vapor-liquid and liquid region. Finally, the surface tension is evaluated using the relations given in A.2.5 for steam and in Ref. [6] for the other fluids. All these models are implemented in SU2 to reduce the computational cost of the simulations.

4.2. VALIDATION

The two-phase flow solver was validated by comparison to measurements of nozzle flow experiments carried out with H_2O, CO_2, R22. The numerical results reported in the following were obtained using a mesh composed by approximately 80k cells. The mesh resolution was determined by means of a grid-independence study related to the droplet average radius. Multiple tests were carried to assess the impact of the turbulence model on the Wilson temperature T_w. It was observed that for the considered test cases the difference between laminar and turbulent simulations is below 0.5 K.

4.2.1. STEAM

Only the results of the comparison with two experimental tests are reported here, i.e., a) *Moore B* presented in Ref. [7] and b) *18C* described in Ref. [8].

Figure 4.1 shows the comparison between the experimental measurements of the *Moore B* case (pressure and radius) and the results obtained from the simulation. The difference between measured and calculated pressure values is small and satisfactory for the stated purposes, and the pressure increase after the inception of stable condensation is predicted with sufficient accuracy.

Figure 4.2 compares the pressure distribution from the computation with the experimental data for case *18C*. The Wilson pressure obtained from the simulations is 44.9 bar, against the average value of 42.9 bar reported in Ref. [9] (pressure measurement between 42.4 and 43.5 bar). The radius $\overline{R}$ is correctly predicted in the proximity of the Wilson point. However, the value of $\overline{R}$ calculated by the simulation rapidly increase in the last
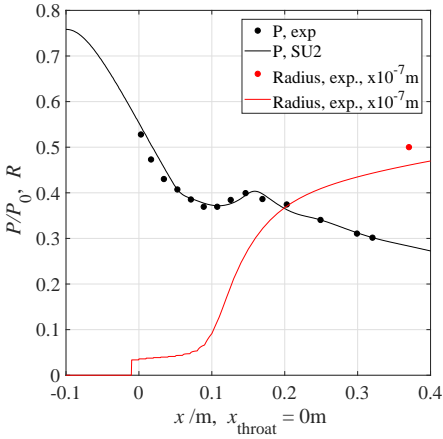
Figure 4.1: Meanline pressure field for the nozzle expansion *Moore B* in Ref. [7]
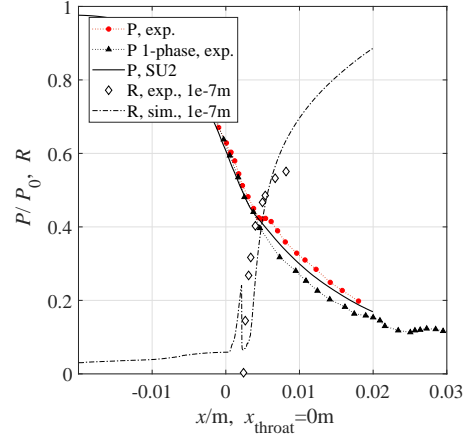
Figure 4.2: Pressure field and average radius for nozzle expansion *18C* in Ref. [8]. Points are taken from the streamline that passes in the middle of the nozzle throat

part of the expansion. This is arguably due to the adopted growth rate , which was initially formulated for low pressure test-cases [10]. Additionally, the number of droplets is slightly lower than what has been measured ($N = 3\mathrm{e}16$ kg^{-1} at the Wilson point against $6\mathrm{e}16$ - $9\mathrm{e}16$ kg^{-1} from Ref. [8]). Thus, less latent heat is released in the vapor phase in the proximity of the Wilson point, and the pressure increase after the Wilson temperature T_{w} is lower than the measured value.

Several inaccuracies in the calculation of the droplets properties were observed. However, this investigation is limited to the location of the Wilson point along the expansion, while the properties of the liquid phase are not included in the analysis. The accuracy of the calculated T_{w} is therefore deemed satisfactory for the purpose of this study.

4.2.2. CARBON DIOXIDE

The experimental data for metastable condensation in CO_2 were taken from Refs. [6, 11]. The results are reported in tables C.14 and C.15 . Figure 4.3 shows the comparison between the test *N2* from Ref. [11] and the numerical simulation. The location of the Wilson point along the expansion is predicted with sufficient accuracy: the deviation between the experimental and the calculated value of T_{w} is approximately 0.2 K (see table C.14 and C.3 for details about the evaluation of the Wilson point).

Larger deviations between numerical and experimental results can be observed in the pressure distribution after the condensation onset. No measurements on the CO_2 droplets properties (droplet size, number) are available to validate the calculated liquid properties. It is therefore impossible to assess the role of the nucleation and growth rate models *J*, *G* in relation to this discrepancy.

However, one consideration can be made by looking at the average radius. Figure 4.4 reports the average radius $\overline{R}$ for the *N2* test and the values at the nozzle outlet for the two
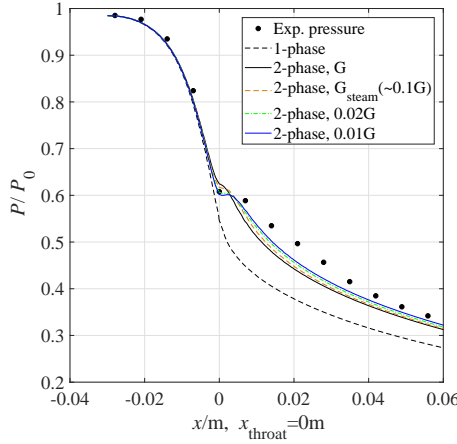
Figure 4.3: Static pressure for nozzle expansion *N2* in Ref. [11] along the meanline. Experimental data, super-heated expansion and simulations with i) *G* from Ref. [6], ii) *G* from Ref. [12], iii) *G* from Ref. [6] reduced by a factor 50 and, iv) *G* from Ref. [6] reduced by a factor 100.

steam test cases previously reported, i.e., *18C* and *Moore B*. It can be inferred that the values of *G* are too high. The surface tension of steam is higher than that of CO_2 for the same reduced thermodynamic conditions. As reported in chapter 3, the surface tension tends to vanish in the proximity of the critical point, arguably leading to a decrease in the properties R_* and $\overline{R}$. The reduced saturation temperature $T_{\text{sat,r}}(s_0)$ in correspondence with the entropy

$$s_0 = s(P_0, T_0) \tag{4.4}$$

is much higher for CO_2 (0.93 as in table C.14) than for steam (0.51 and 0.86 for tests *Moore B* and *18C* respectively). However, it can be seen that $\overline{R}$ is more than 2 orders of magnitude higher than that obtained of test *18C* and *Moore B*. Additionally, this discrepancy is unlikely caused by the inaccuracy of the surface tension model, as the Wilson point is fairly well predicted. Therefore, it can be conjectured that the adopted growth rate model leads to the overestimation of the average droplet radius for CO_2.

In order to assess the impact of the growth rate on the quantities of interest for the study, namely the Wilson point and the liquid mass fraction, further simulations were performed using i) the growth rate from Ref. [12] (around 10 times smaller than the one in Ref. [6]), ii) the model in Ref. [6] reduced by a factor 50 and, iii) the same model reduced by a factor 100.

Figure 4.3 and 4.4 display the results. As expected, the reduction of *G* causes a substantial decrease in the average radius $\overline{R}$. At the same time, the calculated pressure profile correlates better with the experimental data, and the deviation from the superheated case in correspondence with T_{w} is more pronounced.

Remarkably, large variations of *G* have a minute impact on the Wilson point location and on the value of the liquid mass fraction Y, in agreement with literature [13]. Figure 4.5 shows Y for all the simulations. It can be seen that the liquid mass fraction Y at
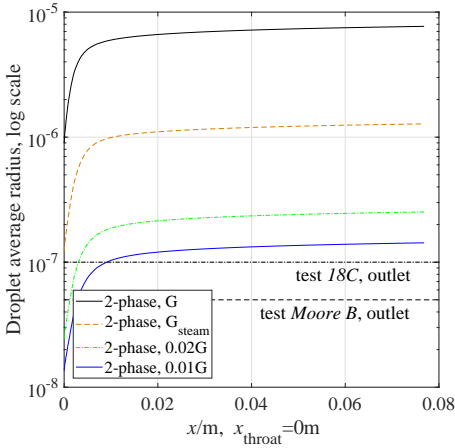
Figure 4.4: Droplets average radius for nozzle expansion *N2* in Ref. [11] along the meanline. Simulations with i) *G* from Ref. [6], ii) *G* from Ref. [12], iii) *G* from Ref. [6] reduced by a factor 50 and, iv) *G* from Ref. [6] reduced by a factor 100
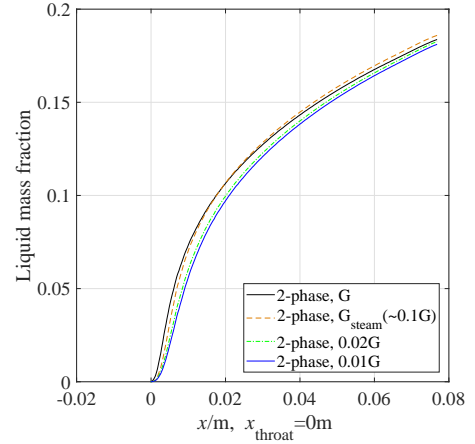
Figure 4.5: Liquid mass fraction for nozzle expansion *N2* in Ref. [11] along the meanline. Simulations with i) *G* from Ref. [6], ii) *G* from Ref. [12], iii) *G* from Ref. [6] reduced by a factor 50 and, iv) *G* from Ref. [6] reduced by a factor 100

the nozzle outlet differs by less than 2% if the results of the simulation with the largest growth rate are compared with those of the one with the lowest growth rate.

As for the growth rate, the nucleation model J is also expected not to be suitable for supercritical expansions. However, no considerations on the droplets number can be made, and more data are needed for a more detailed assessment on J.

4.2.3. REFRIGERANTS

The numerical model was validated also by comparison with the data reported in Ref. [6] concerning non-equilibrium condensation of refrigerant R22 in supersonic nozzles.

The numerical results reveal an unexpected trend in the nucleation rate. As apparent from Figure 4.7, the trend of the nucleation rate largely departs from the classical Dirac-type function, typical of two-phase flow expansions of H_2O and CO_2, see Figure 4.6. This different trend has substantial physical implications on the process of condensation. When J resembles an impulse, the number of new liquid nuclei rapidly goes from zero to the maximum value in correspondence with the peak of the function, at the Wilson point, and then drops with the same rate. Instead, for R22, the number of critical nuclei continues to rise monotonically.

Note that, as can be seen in Figure 4.7, the nucleation rate J reaches its maximum value in the proximity of the nozzle outlet. In other words, J increases monotonically for the whole expansion process. A much higher expansion ratio is required to see the decay of J along the nozzle. The same was observed for all the tests reported in Table C.16.

Figure 4.8 displays the surface tension of H_2O, CO_2 and R22 for the range of reduced temperature $0.89 < T_{sat,r}(s_0) < 0.94$. It can be seen that the surface tension for R22 is the lowest among the three fluids. As a consequence, the ratio σ/T_v in the exponent of J
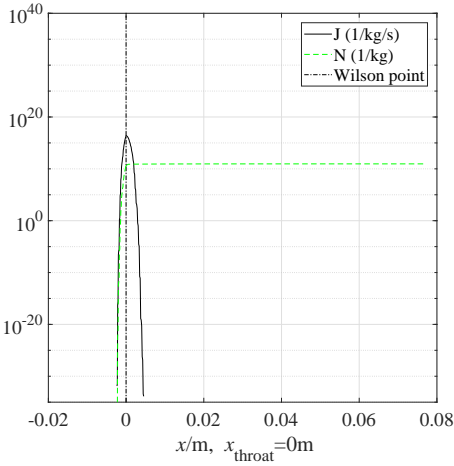
Figure 4.6: Nucleation rate and droplets number for nozzle expansion *N2* with CO_2 [11] along the meanline
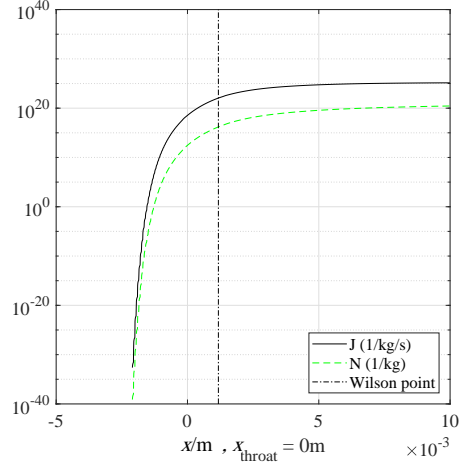
Figure 4.7: Nucleation rate and droplets number for nozzle expansion *N67* with R22 [6] along the meanline

reduces, see Figure 4.9, increasing the width of the function J.

Additionally, it was found that, in all test cases, the model predicted a liquid droplet temperature T_l lower than the vapor temperature T_v, leading to unrealistic values of the growth rate along the expansion. Further modeling work is required to replace the typical capillarity model used for steam with a more suitable one. Therefore the applicability of the proposed two-phase model to refrigerants still needs proper verification.

The results of the comparison with the data reported in Ref. [6] are listed in table C.16, see C.3 for additional details on the estimation of the Wilson point for R22. Although at a first view it appears that the relative discrepancy between numerical predictions and experimental observations is small, in absence of additional experimental results to validate the model, the analysis on R22 can only be conducted qualitatively by using the experimental data in Ref. [14].

4.3. CHARACTERIZATION OF METASTABLE CONDENSATION FOR H_2O, CO_2, AND R22

The process of metastable condensation for steam, CO_2 and R22 is comparatively investigated using the Wilson number Wi, or dimensionless subcooling, defined as

$$Wi \stackrel{\text{def}}{=} \frac{\Delta T_{\text{sub}}}{T_{\text{cr}}} = \frac{T_{\text{sat}}(s_0) - T_{\text{w}}}{T_{\text{cr}}}. \tag{4.5}$$

In chapter 3 it is shown that Wi is mainly dependent on i) the cooling rate of the expansion, defined as

$$\overline{Cr} = \frac{1}{T_{\text{cr}}} \frac{\overline{\partial T}}{\partial t} = \frac{1}{T_{\text{cr}}} \frac{T_{\text{sat}}(s_0) - T_{\text{w}}}{t_{\text{act}}}, \tag{4.6}$$
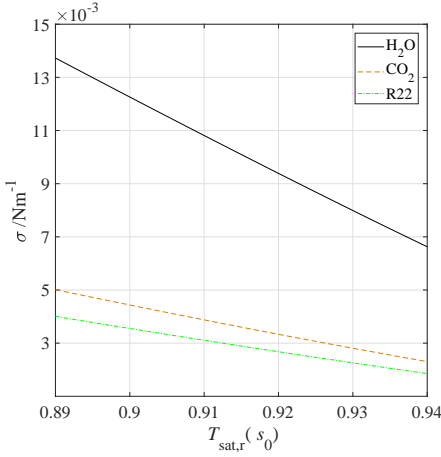
Figure 4.8: Surface tension for H_2O, CO_2 and R22 in the range $0.89 < T_{\text{sat,r}}(s_0) < 0.94$
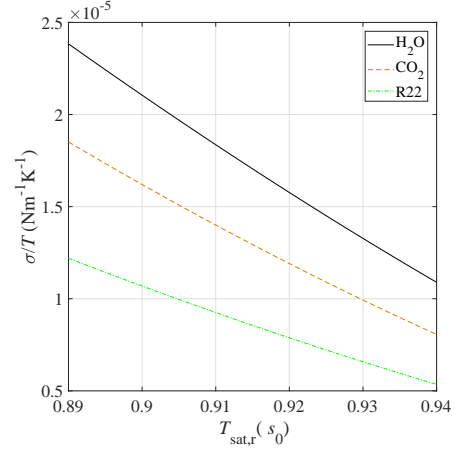
Figure 4.9: Ratio σ / T_v for H2O, CO_2 and R22 in the range $0.89 < T_{\text{sat,r}}(s_0) < 0.94$

ii) the reduced saturation temperature $T_{\text{sat,r}}(s_0)$ and, iii) the fluid. The interested reader can find the general mathematical demonstration in Ref. [13].

The impact of these three parameters on Wi is separately investigated using the following procedure. At first, a suitable range of reduced saturation temperature $T_{\text{sat,r}}(s_0)$ is chosen. For each value $T_{\text{sat,r}}(s_0)$ a set of six simulations is carried out, each with different nozzle profiles, namely *2B*, *4B*, *5B*, *6B*, *Moore*, *Moorex25*. The geometry for the first four nozzles is taken from Ref. [8], whereas the profile for nozzles *Moore*, *Moorex25* is reported in C.4. In order to maintain similar fluid dynamic conditions, a Mach number of ≈ 0.8 is imposed in correspondence with $T_{\text{sat,r}}(s_0)$. The total conditions upstream of the nozzle are calculated accordingly. The Wilson temperature is then retrieved, along with $\overline{Cr}$. The same steps are repeated for multiple values of $T_{\text{sat,r}}(s_0)$ within the selected range.

4.3.1. Dependence of the Wilson point on the cooling rate

First, for simplicity, the comparison between H_2O and CO_2 is carried out only at $T_{\text{sat,r}}(s_0) = 0.86$. In analogy to what is described in chapter 3, in order to derive an expression for Wi as a function of $\overline{Cr}$, an additional parameter is introduced, namely the activation time t_{act}, defined as the time interval required for the vapor phase to reach T_w from $T_{\text{sat}}(s_0)$ along the expansion.

Figures 4.10 and 4.11 display the trend of t_{act} and Wi as a function of $\overline{Cr}$. Following chapter 3, the fitting functions for such curves are chosen in the form

$$t_{\text{act}} = k_1 \overline{Cr}^{-k_2}. \tag{4.7}$$

The coefficients k_1, k_2 are reported in table C.18. Thus, from (4.5), (4.6) and (4.7) it follows that

$$T_w \overset{\text{def}}{=} T_{\text{sat}}(s_0) - T_{\text{cr}} Wi, \qquad Wi = k_1 \overline{Cr}^{k_{\text{cr}}}, \qquad k_{\text{cr}} = 1 - k_2. \tag{4.8}$$
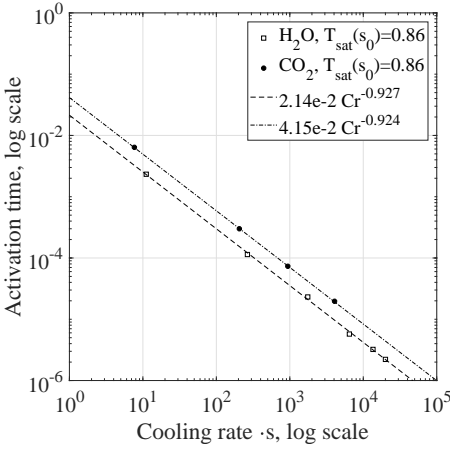
Figure 4.10: Activation time as a function of $\overline{Cr}$ for H_2O and CO_2 at $T_{\text{sat,r}}(s_0) = 0.86$
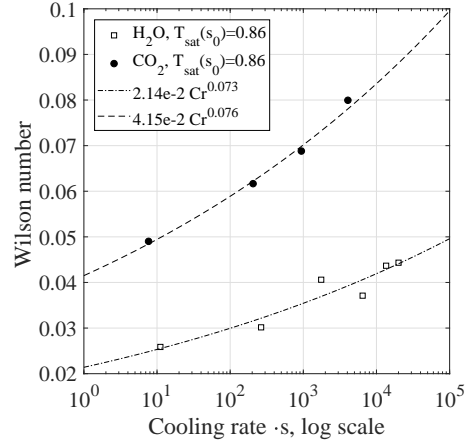
Figure 4.11: Wilson number as a function of $\overline{Cr}$ for H_2O and CO_2 at $T_{\text{sat,r}}(s_0) = 0.86$

Note that for $\overline{Cr} \to 0$, i.e., in case the vapor phase reaches T_{w} in a time $t_{\text{act}} \to \infty$, it is always true that

$$\lim_{\overline{Cr} \to 0} T_{\text{sat}}(s_0) - T_{\text{cr}} k_1 \overline{Cr}^{k_{\text{cr}}} = T_{\text{sat}}(s_0), \tag{4.9}$$

thus, the locus of the Wilson points asymptotically tends to the saturation curve, in agreement with the classical theory.

The results of CO_2 simulations with nozzles *5B* and *6B* reported in table C.27 feature a cooling rate of approximately 1e4 s^{-1}, i.e., 3e6 K/s. $\overline{Cr}$ values are therefore much higher than those of typical industrial applications (cf. Ref. [11]). The fitting is thus carried out only with the values of simulations related to nozzles *Moorex25*, *Moore*, *2B*, *4B*. The slope of the curves in Figure 4.10 is comparable for the two fluids, thus, k_2 is approximately constant.

This result has one main physical consequence. According to (4.7), and (4.8), an increase in the cooling rate by a factor f leads to a Wilson number variation of f^{1-k_2}. As k_2 can be considered constant in correspondence with a given $T_{\text{sat,r}}(s_0)$, equal variations of $\overline{Cr}$ leads to the same relative change in Wi. In other words, from the physical point of view, a change in the average cooling rate value affects the condensation onset of different fluids in the same way.

4.3.2. DEPENDENCE OF THE WILSON POINT ON THE REDUCED SATURATION TEMPERATURE

The analysis is repeated for several values $T_{\text{sat,r}}(s_0)$, see C.7. Figure 4.14 shows the value Wi for the simulations with H_2O, CO_2 and R22 using nozzle *2B* as a function of $T_{\text{sat,r}}(s_0)$, whereas Figure 4.15 displays the same parameter for the tests with H_2O.

As previously mentioned, the results obtained for R22 need further validation, to assess whether they can be used for a qualitative analysis. Therefore, first the Wilson point
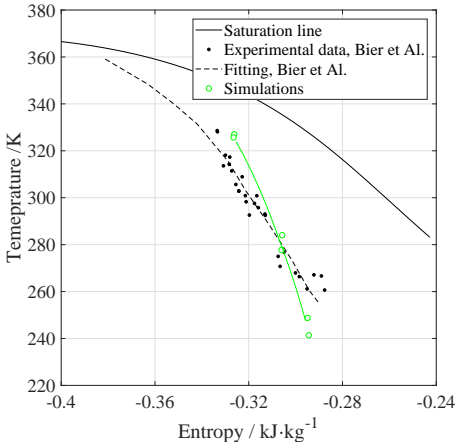
Figure 4.12: Simulation results and experimental measurements from Ref. [14] in the *T-s* chart.
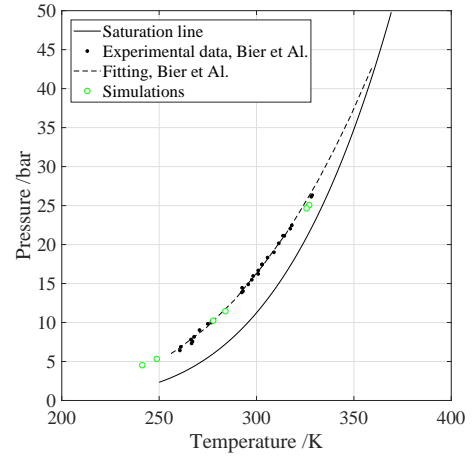
Figure 4.13: Simulation results and experimental measurements from Ref. [14] in the *P-T* chart.

calculated in C.31, C.32, C.33 are first compared with the experimental dataset reported in Ref. [14]. For the comparison, only the simulations with nozzles *2B*, *4B* are considered, as their cooling rate is close to that of the experimental test-cases. Figures 4.12 and 4.13 report both the data sets in the *T-s* and *P-T* chart. A discrepancy can be seen the trend of Figure 4.12. The slope of the two fitting curves in Figure 4.12 differs significantly. Therefore, the results can only be used for a qualitative analysis. However, the magnitude of the difference between simulation results and experimental data is much lower than the deviation between the Wi for CO_2 and that for R22, and cannot, alone, justify the differences between the physical behavior of the two fluids.

In addition, Figure 4.14 put into evidence that the higher is the saturation temperature $T_{\text{sat,r}}(s_0)$ the lower is the subcooling, in agreement with Refs. [6, 15].

Figures 4.16 and 4.17 report the values of k_1 and $k_{\text{cr}} = 1 - k_2$ as a function of $T_{\text{sat,r}}(s_0)$. The exponent of the cooling rate for both CO_2 and R22 tends to zero in the proximity of the critical point. Therefore, the impact of $\overline{Cr}$ on Wi appears to vanish when $T_{\text{sat,r}}(s_0)$ tends to 1 (see Figure 4.17). In other words, expansions at high reduced temperatures are expected to have comparable Wi values, independently from the cooling rate value. Additional data on steam at reduced temperatures higher than 0.9 are required to verify this theory.

4.3.3. ANALOGIES AND DIFFERENCES AMONG THE FLUIDS

Figure 4.18 and 4.19 display i) the saturation curve, ii) the spinodal curve and, iii) the Wilson point evaluated as in (4.8) for H_2O, CO_2, R22 in the *P-T* and *T-s* diagrams of the fluids. An arbitrary cooling rate of 1000 s^{-1} is chosen to evaluate T_w for H_2O and CO_2, whereas the curve for R22 is taken from Ref. [14].

In non-equilibrium CO_2 flows, the Wilson number, thus the degree of subcooling, is higher than that of H_2O, in agreement with Ref. [15]. According to what is documented
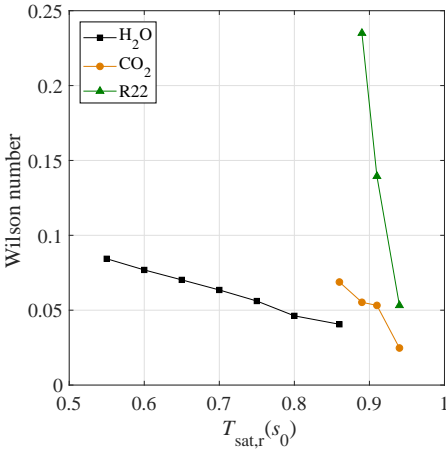
Figure 4.14: Wilson number as a function of $T_{sat,r}(s_0)$ for H_2O, CO_2 and R22, nozzle 2B ($\overline{Cr} \approx 1e3$ s^{-1})
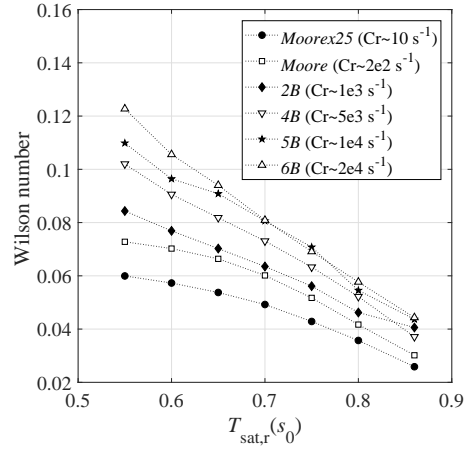
Figure 4.15: Wilson number as a function of $T_{sat,r}(s_0)$ for H_2O
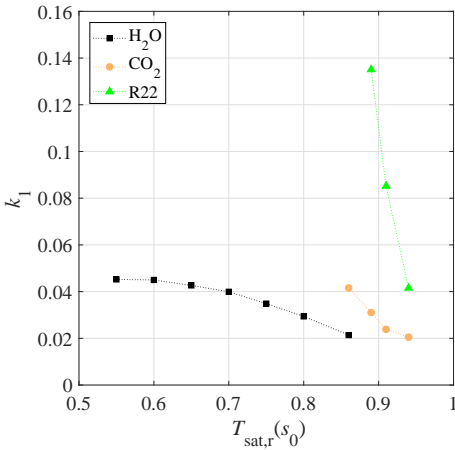
Figure 4.16: Coefficient k_1 as a function of $T_{sat,r}(s_0)$ for H_2O, CO_2 and R22
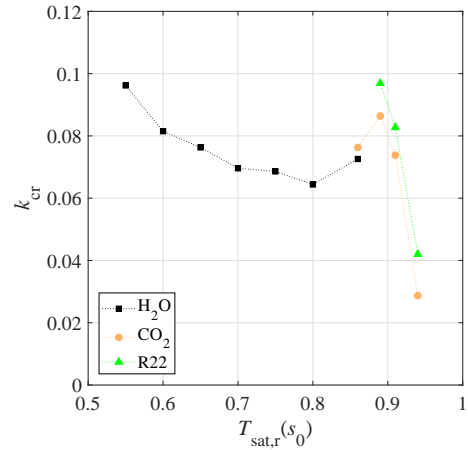
Figure 4.17: Coefficient $k_{cr} = 1 - k_2$ as a function of $T_{sat,r}(s_0)$ for H_2O, CO_2 and R22
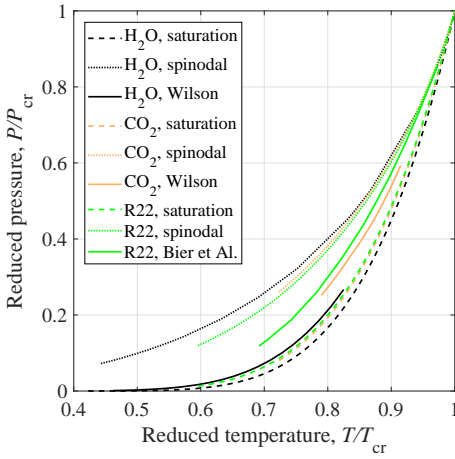
Figure 4.18: *P-T* diagram reporting i) saturation line, ii) spinodal line and, iii) Wilson point calculated as in (4.8) with $\overline{Cr} = 1000 \text{ s}^{-1}$ for H_2O, CO_2, R22
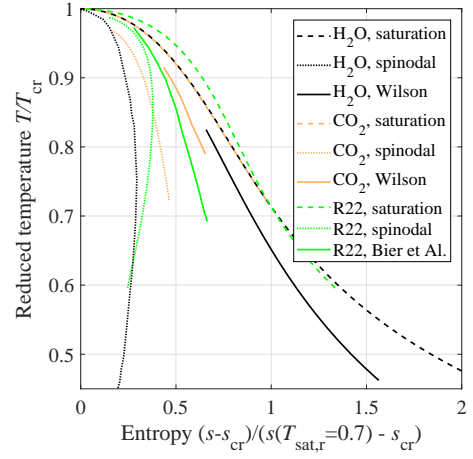
Figure 4.19: *T-s* diagram reporting i) saturation line, ii) spinodal line and, iii) Wilson point calculated as in (4.8) with $\overline{Cr} = 1000 \text{ s}^{-1}$ for H_2O, CO_2, R22

in Ref. [15], this discrepancy was associated to the stronger molecular forces of H_2O with respect to those of CO_2. However, it can be observed that condensing flows of R22 are characterized by a degree of subcooling significantly higher than that of the flows of the other two fluids (see Figure 4.16), though the molecule features high polarity. C.6 reports the main physical and molecular properties of H_2O, CO_2 and R22.

In order to gain knowledge of the influence of the working fluid on the Wilson point location, the set of numerical data is complemented by the experimental data obtained for R12 in Ref. [6]. Note that the tests in Ref. [6] for refrigerant R12 are close to the critical point. This would lead to a deviation between experiments and numerical results of the same order than that of the reported degree of subcooling, which is less than 3 K. Thus, it was decided to make use of the experimental values, instead of numerical values taken from nozzle simulations.

Figure 4.20 displays i) the saturation line, ii) the spinodal line and, iii) the Wilson point for R12 and R22. The temperature T_w for R22 is determined with (4.8) by linearly interpolating the coefficients in table C.18 within the range of $T_{sat,r}(s_0)$ reported in C.16. In order to choose a suitable value of $\overline{Cr}$ for the comparison, a series of single phase expansion simulations were carried out for R12, see table C.34. The cooling rate estimated for the selected test-cases is in the range $1200 - 1600 \text{ s}^{-1}$.

In agreement with Refs. [15] and [6], the curves for R22, R12 and CO_2 seem to overlap in the *P-T* chart. However, the actual degree of subcooling for R12 is much higher than that of the other two fluids. As an example, the experimental value of Wi for R22 in test *N67* with $T_{sat,r}(s_0) = 0.94$ (see Table C.16 is approximately 8.11e-2, whereas the dimensionless subcooling for R12 in test *N44*, characterized by $T_{sat,r}(s_0) = 0.98$ is around 9.42e-2.

With reference to equation (4.8), the provided example would suggest that the coef-
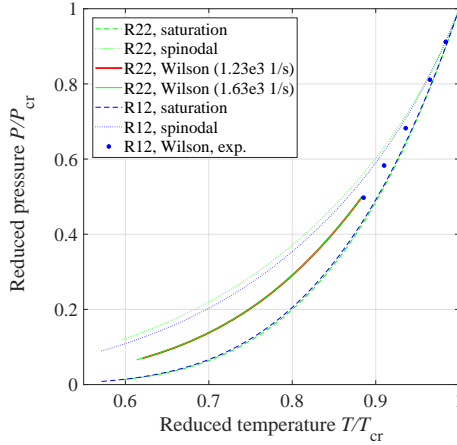
Figure 4.20: *P-T* diagram reporting i) saturation line, ii) spinodal line and, iii) Wilson point for R22 (from (4.8)) and R12 (experimental data)
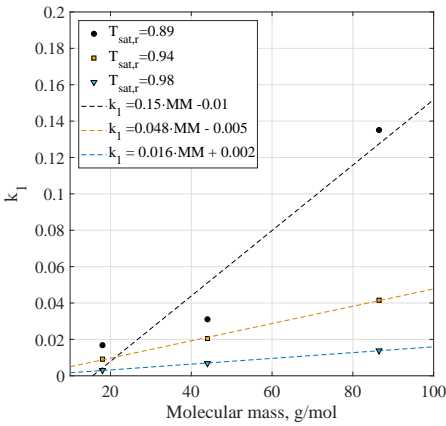
Figure 4.21: Coefficient k_1 as a function of the molecular mass for $T_{sat,r}(s_0) = 0.89$, 0.94 and 0.98 with linear interpolation.
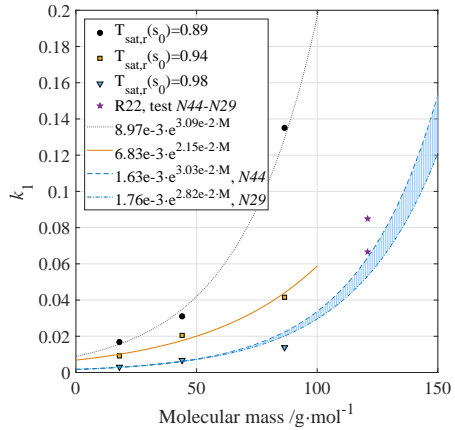
Figure 4.22: Coefficient k_1 as a function of the molecular mass for $T_{sat,r}(s_0) = 0.89$, 0.94 and 0.98 with exponential interpolation. The last two fittings are made with tests *N44* and *N29* for R12.

ficient k_1 is unlikely a function of the polarity of the molecule, as stated in Ref. [15], but instead of the molecular mass of the fluid. Figure 4.21 shows the value of k_1 at $T_{\text{sat,r}}(s_0) =$ 0.89, 0.94 and 0.98 for H_2O, CO_2, R22 as a function of the molecular mass MM. The values are calculated with a linear interpolation from table C.18 assuming $k_1 = 0$ for $T_{\text{sat,r}}(s_0) = 1$. A linear interpolation was carried out, and the resulting coefficients are reported in the legend.

Additionally, Fig.4.22 reports the same data together with two experimental tests with R12, i.e. tests *N44* and *N29*, characterized by $T_{\text{sat,r}}(s_0) =$ 0.979 and 0.982 respectively. The value k_1 for such cases was calculated with the estimated $\overline{Cr}$ and (4.8) assuming a coefficient k_2 equal to that of R22.

The dependence of k_1 from the molecular mass is justified from the physical point of view as following. From the ideal gas theory, the thermal agitation of a molecule is given by

$$MM v_{\text{t}}^2 \propto k_{\text{b}} T, \tag{4.10}$$

where v_{t} is the thermal velocity and k_{b} is the Boltzmann constant. Normalizing (4.10) with respect to $k_{\text{b}} T_{\text{cr}}$, i.e., the thermal agitation of a molecule at T_{cr} yields

$$\tilde{v}_{\text{t}}^2 \propto \frac{T_{\text{r}}}{MM}, \qquad \tilde{v}_{\text{t}}^2 = \frac{v_{\text{t}}^2}{k_{\text{b}} T_{\text{cr}}}. \tag{4.11}$$

Expressed in different words, when considering the same reduced temperature T_{r}, fluids with a high molecular mass are characterized by a lower relative thermal velocity $\tilde{v}_{\text{t}}$ [16].

A reduction in $\tilde{v}_{\text{t}}$ arguably causes a delay in the condensation process, as the molecules do not collide with the same frequency as they would do in a fluid featuring low molecular mass. In order to increase the collision frequency, the average distance between the molecules has to reduce. A lower temperature T_{w} is then required, or equivalently, a higher degree of subcooling. Therefore, k_1 has to grow accordingly.

From the same considerations it is inferred that k_2 is poorly dependent on MM. The cooling rate is a macroscopic property associated with the flow kinetics. $\overline{Cr}$ does not affect directly $\tilde{v}_{\text{t}}$, but only the average stream velocity v. Thus, k_2 is approximately the same for all fluids (see Figure 4.17).

The trend of the curve in Fig.4.22 for $T_{\text{sat}}(s_0) = 0.89$ and the points extrapolated for R12, might suggest an exponential dependence of k_1 from the molecular mass MM. The correspondent interpolation is displayed in the same graph. However, the data collected in this thesis are not sufficient to conclude anything about the mathematical dependence of k_1 and MM, and additional experimental points are required for further considerations.

Furthermore, these observations can be applied only for molecules with a simple tetrahedral geometry as the ones considered in this study. In case of molecules with higher MM values, the level of complexity of the molecular structure arguably increases. As a consequence, the molecules can vibrate with more complex patterns and feature multiple bonding configurations. Experimental data on fluids with different molecular structures are required to draw more general conclusions.
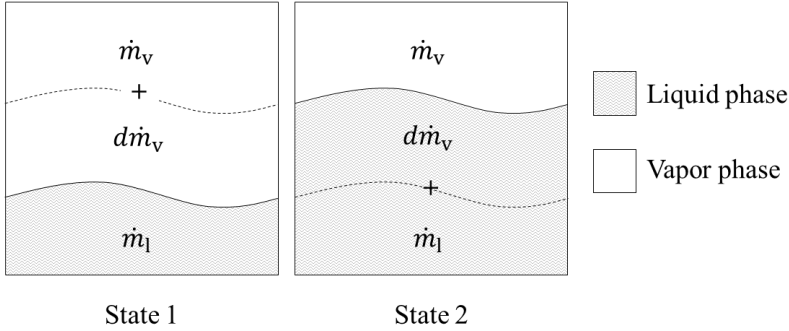
Figure 4.23: Schematic of a two-phase system with condensation, States t_1 and t_2 are, respectively, the system states at the time t_1, t_2, i.e., before and after condensation occurs.

4.4. FLUID-DYNAMIC LOSSES ASSOCIATED TO ONSET OF CONDENSATION

The significant variations in the Wilson number among the fluids would suggest that the fluid-dynamic losses associated to the process of non-equilibrium condensation are strongly fluid-dependent. Among the identified loss mechanisms involved in metastable condensation [17, 18], the so-called thermodynamic wetness losses cause the largest share of entropy generation in turbomachinery applications. This section documents a study aimed at comparing the magnitude of these losses in nozzle flows operating with fluids other than steam.

Consider i) a mass flow $\dot{m}_v$ of vapor, ii) a mass flow $\dot{m}_l$ of liquid and, iii) a mass flow $d\dot{m}_v$ that is undergoing a phase transition from vapor to liquid (see Figure 4.23) flowing through an adiabatic control volume. For each of the three mass flows one can write the entropy balance as

$$\begin{cases} S_{\mathrm{irr},\dot{m}_v} = \dot{m}_v s_{v,2} - \dot{m}_v s_{v,1} - \frac{\dot{L}}{T_v} \\ S_{\mathrm{irr},\dot{m}_l} = \dot{m}_l s_{l,2} - \dot{m}_l s_{l,1} \\ S_{\mathrm{irr},d\dot{m}_v} = d\dot{m}_v s_{l,2} - d\dot{m}_v s_{v,1} + \frac{\dot{L}}{T_{\mathrm{sat}}(P)} \end{cases}, \qquad (4.12)$$

where 1 and 2 represent the states at time t_1, t_2, i.e., before and after $d\dot{m}_v$ condenses, $\dot{L}$ is the latent heat released during condensation and S_{irr} is the entropy production. The equations are derived using the following assumptions. First, the vapor and the liquid phase are in mechanical equilibrium at the pressure P. Second, the temperatures T_v, T_l are constant. Additionally, the transition to liquid for $d\dot{m}_v$ occurs at the saturation temperature $T_{\mathrm{sat}}(P)$. The entropy balance for the whole system can be written as

$$S_{\mathrm{irr,tot}} = S_{\mathrm{tot},2} - S_{\mathrm{tot},1} + \dot{L}\left(\frac{1}{T_{\mathrm{sat}}(P)} - \frac{1}{T_v}\right), \qquad (4.13)$$

in which $S_{\mathrm{tot},1}$ and $S_{\mathrm{tot},2}$ are the total entropy before and after condensation occurs, or

equivalently,

$$S_{\text{irr}} + S_{\text{irr},\dot{L}} = S_{\text{tot},2} - S_{\text{tot},1}, \tag{4.14}$$

where

$$S_{\text{irr},\dot{L}} = \dot{L}\left(\frac{1}{T_{\text{v}}} - \frac{1}{T_{\text{sat}}(P)}\right) \approx \dot{dm}_{\text{v}}(h_{\text{v}} - h_{\text{l}})\left(\frac{1}{T_{\text{v}}} - \frac{1}{T_{\text{sat}}(P)}\right). \tag{4.15}$$

Therefore, the total entropy variation $S_{\text{tot},2} - S_{\text{tot},1}$ consists of two contributions, representing i) the viscous losses in the flow and ii) the thermal non-equilibrium between the two phases. The term $S_{\text{irr},\dot{L}}$ is always positive, as the saturation temperature $T_{\text{sat}}(P)$ is, by definition, higher than T_{v} in the metastable region. The kinetic energy loss coefficient associated to thermodynamic wetness loss can be written as

$$\zeta = S_{\text{irr},\dot{L}} \frac{T_{\text{out}}}{\frac{1}{2}\dot{m}v_{\text{out}}^2}, \tag{4.16}$$

where T_{out} and v_{out} are the temperature and velocity at the outlet, and $\dot{m}$ is the mass flow of the two-phase mixture. In the following, ζ is determined only for H_2O and CO_2, as the results of the simulations for R22 cannot be validated see section 4.2.3.

4.4.1. COMPARISON BETWEEN H_2O AND CO_2

The loss coefficient values for all the tests are reported in C.7. Figure 4.24 shows the values of ζ for H_2O at different $T_{\text{sat,r}}(s_0)$, i.e., 0.55, 0.65, 0.75 and 0.86.

In agreement with literature, the growth of ζ is directly proportional to Wi. The coefficient ζ is higher at low reduced saturation temperature and for increasing value of cooling rates.

Given that Wi tends to increase for fluids featuring higher molecular mass (see Figure 4.22), it can be hypothesized that, for expansions characterized by the same cooling rate and reduced temperature, the condensation process of CO_2 and refrigerants implies larger losses than that of H_2O. Figure 4.25 displays ζ for H_2O and CO_2 as a function of $\overline{Cr}$ for $T_{\text{sat,r}}(s_0) = 0.86$. It can be seen that the loss coefficient for CO_2 is two times higher than that of H_2O, thus validating the hypothesis. The deviation in Y observed in the validation process (see section 4.2.2) does not justify alone the magnitude of this discrepancy.

4.5. APPLICATIONS

4.5.1. PREDICTION OF CONDENSATION ONSET FOR ARBITRARY FLUIDS

The dependence of the Wilson number on the molecular mass of the fluid can be exploited to roughly estimate the i) condensation onset and ii) the thermodynamic losses associated to an expansion process of a given fluid for which the process of spontaneous condensation has never been investigated.

Consider for example refrigerant R32 (chemical formula CH_2F_2), a synthetic fluid that is replacing hydroclorofluorocarbons refrigeration and heat pump systems [19]. R32 is characterized by low GWP (Global Warming Potential) and by an ODP (Ozone Depleting Potential) equal to 0. Additionally, R32 is not explosive, difficult to ignite and only mildly toxic [20].
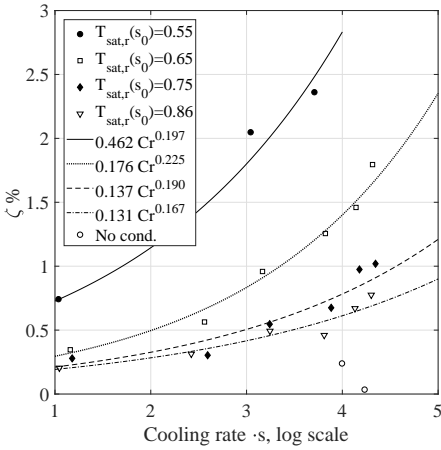
Figure 4.24: Loss coefficient ζ as a function of $\overline{Cr}$ for H_2O at $T_{\text{sat,r}}(s_0)$= 0.55, 0.65, 0.75 and 0.86
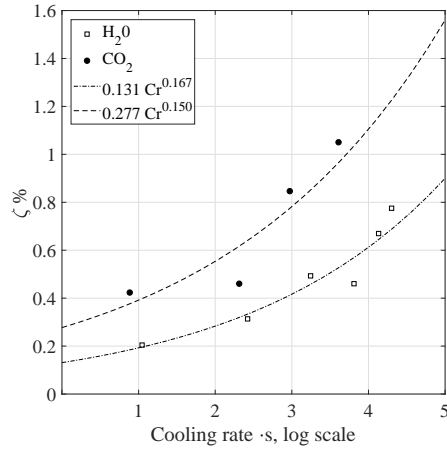
Figure 4.25: Loss coefficient ζ as a function of $\overline{Cr}$ for H_2O and CO_2 at $T_{\text{sat,r}}(s_0)$ =0.86

One of the strategies currently being pursued to enhance the performance of inverse cycle systems is to reduce the degree of superheating at the inlet of the compressor. The reduced superheating can increase the risk of metastable condensation at the leading-edge of the blades. Understanding of the physical aspects of metastable condensation for such fluid can then be relevant for the design of compressors, in particular for what concerns aspects of safe operation.

The linear interpolation of the data reported in table C.18 as function of MM yields

$$k_{1,\text{R32}} = k_{1,\text{CO}_2} + \frac{k_{1,\text{R22}} - k_{1,\text{CO}_2}}{MM_{\text{R22}} - MM_{\text{CO}_2}} \left(MM_{\text{R22}} - MM_{\text{CO}_2} \right). \tag{4.17}$$

Figure 4.26 shows the comparison between H_2O and R32 in the T-s chart, for values of activating time t_{act} equal to 1e-3s, 1e-1s, 1e1s.

R32 is expected to have a higher degree of subcooling Wi with respect to water for expansions characterized by the same $T_{\text{sat}(s_0)}$ and cooling rate. As a consequence, the thermodynamic losses associated with the presence of liquid are arguably more significant, and have to be taken into account for the preliminary design of a compressor. However, if the pressure ratio is low, the model predicts that metastable condensation does not occur along the expansion.

Although additional data are required to obtain a more accurate calibration of the coefficients k_1, k_2 for a wider range of operating conditions, this simple method allows to quickly predict the Wilson line of generic fluids for which metastable condensation is of practical interest.

4.5.2. OPTIMAL NOZZLE DESIGN AND LOSS PREDICTION
The findings of this study can be also exploited for the optimal design of supersonic nozzles operating with two-phase condensing flows. Consider a supersonic expansion
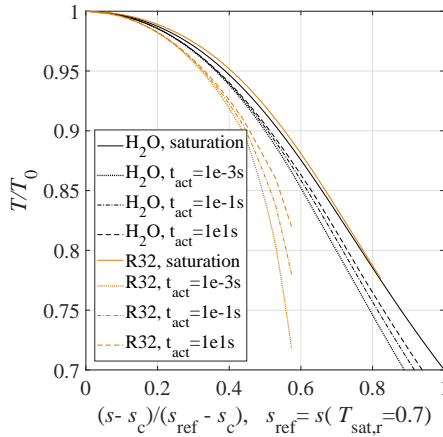
Figure 4.26: Comparison between H_2O and R32 on a T-s chart, $t_{act} = 1e-3, 1e-1, 1e1s$

process characterized by total conditions P_0, T_0 and prescribed expansion ratio. A typical design problem consists in determining the nozzle shape characterized by the minimum thermodynamic wetness loss. For a given nozzle profile, a method in three-steps is devised, i.e, i) the cooling rate $\overline{Cr}$ is estimated by means of a single phase computation, ii) the Wilson temperature T_w is retrieved by using (4.8) and, iii) the thermodynamic wetness losses are predicted by interpolating the analytical relations resulting in the curves reported in Figure 4.24. The method can be repeated for a set of nozzle profiles to find the optimal shape.

The accuracy of the semi-empirical method is assessed by using the nozzle profile documented in Ref. [21]. Four test cases, characterized by different reduced saturation temperatures, are investigated, namely $T_{sat,r}(s_0)$ equal to 0.58, 0.63, 0.68. 0.73. An expansion ratio of 4 is imposed. A quasi-1D eulerian simulation is used to estimate the average cooling rate of the nozzle, equal to about 800 1/s. For the sake of brevity, refer to chapter 3 for the determination of T_w according to (4.8). The fitting curves in Figure 4.24 can be used to calculate the correspondent loss coefficient ζ. Figure 4.27 reports the values found as a function of the saturation temperature $T_{sat,r}(s_0)$.

A two-phase simulation is carried out for each of the selected temperatures, and the coefficient ζ is evaluated according to (4.16). Figure 4.28 displays the comparison between the simulations and the predicted values.

Additional data are required to increase the accuracy of the proposed relations for general test-cases. However, it can be observed that the losses trend is correctly predicted, and the estimated loss coefficient ζ is sufficiently close to the values predicted by the simulations.

4.6. CONCLUSIONS

This chapter documents a comparative study on metastable condensation occurring in supersonic flows of steam and organic fluids. The investigation was carried out with a
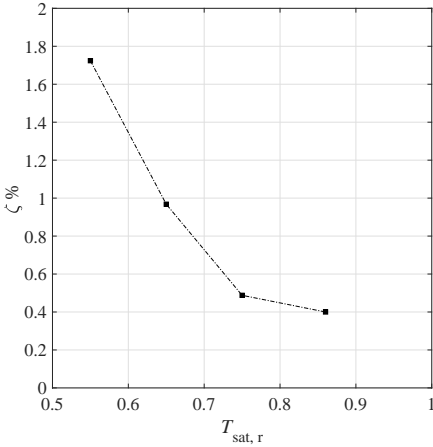
Figure 4.27: Loss coefficient ζ for $\overline{Cr} = 800$ s^{-1}, values extrapolated using the fitting curves in Figure 4.24
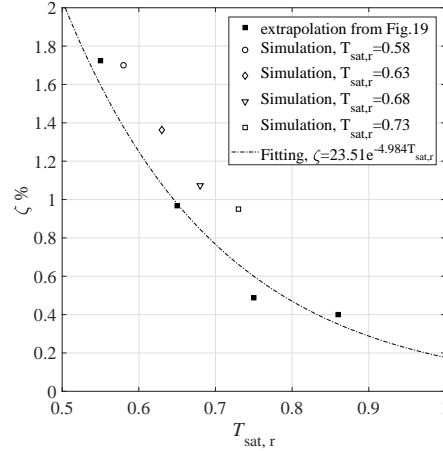
Figure 4.28: Loss coefficient ζ, comparison between simulations and fitting curves in Figure 4.24

validated CFD tool implementing a model for the dispersed phase based on the method of moments.

The dependence of the Wilson number Wi, defined in (4.5), on i) the cooling rate $\overline{Cr}$, ii) the saturation temperature $T_{\text{sat,r}}(s_0)$ and, iii) the working fluid was investigated. Based on the obtained results, the following considerations can be drawn:

1. the impact of the cooling rate on the Wilson point is, as a first approximation, independent from the fluid under scrutiny. Additionally, such dependence arguably vanishes at high reduce temperatures;

2. Wi is arguably a function of the molecular mass MM, i.e., fluids with a higher molecular weight are characterised by a higher Wi (Figure 4.22).

In addition, the thermodynamic losses associated with metastable condensation were analysed. For this purpose, a loss coefficient ζ was defined as in (4.16). It was observed that:

1. the higher the Wilson number Wi, the higher is ζ;

2. an increase in $T_{\text{sat,r}}(s_0)$ leads to a reduction of the thermodynamic losses;

3. the loss coefficient for flows of organic fluids with a high molecular mass is higher than that of flows of simple molecules at same $T_{\text{sat,r}}(s_0)$, $\overline{Cr}$.

For each $T_{\text{sat,r}}$, a simplified expression for ζ as a function of $\overline{Cr}$ is reported.Such relations were applied to estimate the wetness losses for four additional expansions, showing a good agreement with the CFD simulations results.This model is suitable for preliminary component design, as it allows to i) predict the Wilson point location and ii) estimate the losses associated with condensation with a significantly low computational cost.

4.7. Limitations of the work and envisaged next steps
Aspects of this present work would require further investigation to consolidate the research findings. These aspects, subdivided in thematic areas, are discussed starting from the suggestions provided by the reviewers of this dissertation and they have to be intended as guidelines to allow one to increase the confidence level on the impact of modeling practices on the results, as also pointed out in 4.2.3.

4.7.1. Numerical method
1. numerical schemes more advanced than the Roe-type method adopted in this work can be considered to improve numerical accuracy. In particular, the numerical scheme described in Ref.[22] proved capable of handling all important physical phenomena in compressible flows, such as expansion waves, shock waves, contact surfaces and vortices in combination with non-equilibrium condensation;

4.7.2. Thermodynamic modeling of non-equilibrium condensation
1. the droplet temperature can be estimated by means of the model proposed in Ref.[23], which is based on an energy balance at the droplet surface. The results can then be compared to those obtained with the adopted capillarity model;

2. the nucleation model adopted in this study does not account for re-evaporation phenomena. To consider possible reheat of the fluid due to re-compression phenomena, e.g. across shock waves, the Internally Consistent Classical Nucleation Theory [24] can be utilized;

3. the growth rate model was developed for low pressure steam. Models based on the Knudsen number are arguably superior in correctly modeling the mass and energy exchange between the two phases during the condensation process. A example can be found in Ref.[25].

4.7.3. Comparative analysis among the fluids
1. the onset of condensation is controlled by the energy barrier to nucleation. The non dimensional surface energy and the excess chemical potential should be estimated for each fluid, as they are directly linked to the degree of subcooling. This information can provide further physical insights on the impact of fluid molecular mass on the subcooling ΔT_{sub};

4.7.4. Estimation of wetness losses
1. the results obtained by using the entropy loss coefficient as defined in (4.16) should be compared to those obtained with more rigorous and general expressions for the entropy production rate in condensation phenomena involving non-equilibrium thermodynamics, as the one provided by [26];

References
[1] P. Hill, *Condensation of water vapour during supersonic expansion in nozzles,* Journal of Fluid Mechanics **25**, 593 (1966).

[2] A. J. White, *A comparison of modelling methods for polydispersed wet-steam flow,* International Journal for Numerical Methods in Engineering **57**, 819 (2003), wiley-Blackwell.

[3] T. D. Economon, F. Palacios, S. R. Copeland, T. W. Lukaczyk, and J. J. Alonso, *SU2: An open-source suite for multiphysics simulation and design,* AIAA Journal **54**, 828 (2016).

[4] T. P. van der Stelt, N. R. Nannan, and P. Colonna, *The iPRSV equation of state,* Fluid Phase Equilib. **330**, 24 (2012).

[5] P. Colonna, T. V. der Stelt, and A. Guardone, *Fluidprop (version 3.0.6): A program for the estimation of thermo physical properties of fluids. a computer program since 2004,* (2018).

[6] G. Theis, *Spontankondensation in übersättigten Dampfströmungen von Kohlen-dioxid und von Difluordichlormethan,* Ph.D. thesis, Uni Karlsruhe (1985).

[7] M. Moore, P. Walters, R. Crane, and B. Davidson, *Predicting the fog-drop size in wet-steam turbines,* in *Proceedings of the IMechE Conference on Heat and Fluid Flow in Steam and Gas Turbine Plant,* paper C37/73 (1973) pp. 101–109.

[8] G. Gyarmathy, *Nucleation of steam in high-pressure nozzle experiments,* Proceedings of the Institution of Mechanical Engineers, Part A: Journal of Power and Energy **219**, 511 (2005).

[9] G. Gyarmathy, *Grundlagen einer Theorie der Naßdampfturbine,* Phd thesis, Eidgenössischen technischen hochschuole, Zurich (1962).

[10] J. Young, *Spontaneous condensationof steam in supersonic nozzles,* PCH. Physico-chemical hydrodynamics **3**, 57 (1982).

[11] C. Lettieri, D. Paxson, Z. Spakovszky, and P. Bryanston-Cross, *Characterization of non-equilibrium condensation of supercritical carbon dioxide in a de laval nozzle,* in *Oil and Gas Applications; Supercritical CO2 Power Cycles; Wind Energy,* Vol. 9 (ASME, 2017).

[12] M. Giordano, S. Hercus, and P. Cinnella, *Effects of modelling uncertainties in condensing wet-steam flows through supersonic nozzles,* V European Conference on Computational Fluid Dynamics ECCOMAS, Lisbon, Portugal (2010).

[13] Y. A. Ryzhov, U. G. Pirumov, and V. N. Gorbunov, *Nonequilibrium Condensation in High-Speed Gas Flows* (New York : Gordon and Breach Science Publishers, 1989).

[14] K. Bier, F. Ehrler, G. Kissau, V. Lippig, and R. Schorsch, *Homogene spontankonden-sation in expandierenden dampfstrahlen des kältemittels r 22 bei hohen normierten drücken,* Forschung im Ingenieurwesen **43**, 165 (1977).

[15] K. Bier, F. Ehrler, and G. Theis, *Spontaneous condensation in stationary nozzle flow of carbon dioxide in a wide range of density,* in *Adiabatic Waves in Liquid-Vapor Systems* (Springer Science + Business Media, 1990) pp. 129–141.

4

[16] J. Jeans and J. Jeans, *An Introduction to the Kinetic Theory of Gases*, Cambridge Science Classics (Cambridge University Press, 1940).

[17] T. Guo, W. J. Sumner, and D. C. Hofer, *Development of highly efficient nuclear HP steam turbines using physics based moisture loss models,* in *Turbo Expo*, Vol. 6 (ASME International, 2007).

[18] J. Young, *Semi-analytical techniques for investigating thermal non-equilibrium effects in wet steam turbines,* International Journal of Heat and Fluid Flow **5**, 81 (1984).

[19] *Refrigerant options now and in the future,* Produced by Danfoss A/S (RA Marketing)© (2010).

[20] I. S. . Refrigerants and refrigeration lubricants, *Iso 817:2014 refrigerants - designation and safety classification,* (2014).

[21] D. Barschdorff, *Verlauf der zustandsgrößen und gasdynamische zusammenhänge bei der spontanen kondensation reinen wasserdampfes in lavaldüsen,* Forschung im Ingenieurwesen **37**, 146 (1971).

[22] X. Luo, B. Prast, M. E. H. van Dongen, H. W. M. Hoeijmakers, and J. Yang, *On phase transition in compressible flows: modelling and validation,* Journal of Fluid Mechanics **548**, 403 (2006).

[23] H. J. Smolders, *Non-linear wave phenomena in a gas-vapour mixture with phase transition,* Ph.D. thesis (1992).

[24] S. L. Girshick, C.-P. Chiu, and P. H. McMurry, *Time-dependent aerosol models and homogeneous nucleation rates,* Aerosol Science and Technology **13**, 465 (1990).

[25] G. Lamanna, H. Kamoun, B. Weigand, C. Manfletti, A. Rees, J. Sender, M. Oschwald, and J. Steelant, *Flashing behavious of rocket engine propellants,* Atomization and Sprays **25**, 837 (2015).

[26] P. Ván, *"non-equilibrium thermodynamics of heterogeneous systems" by signe kjelstrup and dick bedeaux,* Journal of Non-Equilibrium Thermodynamics **34** (2009), 10.1515/jnetdy.2009.006.

4

5

DISCRETE ADJOINT METHOD FOR TWO-PHASE CONDENSING FLOW

"For every complex problem there is an answer that is clear, simple, and wrong."

H. L. Mencken

5.1. INTRODUCTION

The adjoint method for aerodynamic shape optimization was first developed by Jameson [2] and since then it has been extensively applied to external flow design problems using either the continuous or the discrete adjoint formulation [3–5]. Its application to turbomachinery flows is relatively recent and its advantages in relation to such problems are less known, due to the additional complexity of deriving the adjoint equations for wall-bounded flows, in particular regarding the linearization of the boundary conditions and the turbulence closures. Adjoint-based optimization applied to turbomachinery design is documented for instance in Refs. [6], [7] and [8].

The advent of automatic differentiation techniques based on operator overloading [9] has opened up the possibility of efficiently performing the differentiation of complex CFD scripts in a black-box fashion, provided that the solver is implemented in such a way that it allows the linearization of all the routines in a sequential manner. If any piece of the code can be automatically differentiated, one can focus on implementing new physical models and numerical algorithms in the flow solver, while being able to obtain its adjoint counterpart almost automatically.

The open-source SU2 solver [10] is becoming increasingly popular within the CFD community because it implements a flexible, accurate, and efficient discrete adjoint (DA) solver [9]. The DA solver is automatically derived by means of advanced algorithmic differentiation (AD) techniques [11]. Various applications of this new design framework have been presented. In Ref. [9], the authors described an application of the SU2 DA solver to external aerodynamic problems. Ref. [12] documents the application of the method to the design of aircraft wings, taking into account aeroacoustic constraints, while the solution of aero elastic design problems is treated in Ref. [13]. Ref. [14] illustrates the extension fo the adjoint framework to design problems involving more complex fluid flows, namely the aerodynamic performance optimization of Organic Rankine Cycle turbine cascades. Aerodynamic shape optimization accounting for the fully turbulent and unsteady natureof flows is reported in Ref. [15]. the approximation fo te harmonic balance method allows in this case to keep the computational time within feasible limits.

This chapter documents the extension of the SU2 design framework to turbomachinery flow problems characterized by phase change. Specifically, the focus here is on vapor flows condensing at non-equilibrium thermodynamic conditions [16]. This typo of flows occur, among others, in the last stages of steam turbines [17] or in centrifugal compressors operating with supercritical carbon dioxide [18] and lead to aero-mechanical performance degradation. For example, droplet formation is a highly irreversible process leading to a work reduction of up to 1-2% for each stage of large steam turbines in which condensation occurs [19]. The performance fo turbomachinery affected by fluid condensation can be improved by re-shaping blades using automated design algorithms in combination with high-fidelity, two-phase CFD models.

According to open literature, a limited body of research deals with shape optimization of turbomachinery components operating with condensing flows [20, 21], arguably due to the challenges and the computational cost associated to the two-phase flow simulations. The objective of this work is to develop and demonstrate the capability of a computationally efficient design approach based on the adjoint method. To this end, the

adjoint-based shape optimization method for single phase turbulent flows implemented in the SU2 solver has been extended to account for the occurrence of non-equilibrium condensation using the method of moments [22]. The method is based on a duality-preserving approach, which guarantees that the two-phase adjoint solver inherits the same convergence rate of the primal flow solver. The capability and computational performance of the novel two-phase design method are illustrated by describing the shape optimization of two exemplary steam turbine cascades

5.2. NUMERICAL MODEL

The vapor flow is modelled with the equations of mass, momentum and energy conservation (4.1), while the liquid phase is described by eq.(4.3). for more details on the flow model the reader can refer to Chapter 4.

5.2.1. ADJOINT SOLVER

The set of governing equations (4.1) and (4.3) written in compact form reads

$$\frac{\partial \boldsymbol{U}}{\partial t} + \nabla \cdot (\boldsymbol{F^c} + \boldsymbol{F^v}) = \boldsymbol{Q}, \tag{5.1}$$

$$\boldsymbol{U} = \begin{bmatrix} U_{\text{flow}} \\ U_{\text{2phase}} \\ U_{\text{turb}} \end{bmatrix}, \quad \boldsymbol{F^c} = \begin{bmatrix} F^c_{\text{flow}} \\ F^c_{\text{2phase}} \\ F^c_{\text{turb}} \end{bmatrix}, \quad \boldsymbol{F^v} = \begin{bmatrix} F^v_{\text{flow}} \\ 0 \\ F^v_{\text{turb}} \end{bmatrix}, \quad \boldsymbol{Q} \begin{bmatrix} Q_{\text{flow}} \\ Q_{\text{2phase}} \\ Q_{\text{turb}} \end{bmatrix}, \tag{5.2}$$

where $\boldsymbol{U}$ indicates the vector containing the conservative variables of (4.1), (4.3) and the turbulent equations, $\boldsymbol{F^c}$ and $\boldsymbol{F^v}$ represent the convective and viscous fluxes respectively and $\boldsymbol{Q}$ the source terms. The solution of 5.1 at time $n+1$ $\boldsymbol{U}^{n+1}$, in case an implicit integration scheme is adopted, can be expressed as

$$\boldsymbol{U}^{n+1} = \boldsymbol{U}^n + \Delta \boldsymbol{U}^n = \boldsymbol{U}^n - \boldsymbol{P}^{-1} \boldsymbol{R}(\boldsymbol{U}^n, \boldsymbol{X}), \tag{5.3}$$

in which $\boldsymbol{R}$ is the residual vector of the equations and $\boldsymbol{X}$ denotes the vector of grid points of the domain. Equation (5.3) can be reformulated in terms of fixed point iteration as

$$\boldsymbol{U}^{n+1} = \mathfrak{G}(\boldsymbol{U}^n, \boldsymbol{X}). \tag{5.4}$$

According to the Banach fixed-point theorem [23], equation (5.3) admits a unique converged solution $\boldsymbol{U}^*$ if $\mathfrak{G}$ is contractive, i.e. $\|\mathfrak{G}\| < 1$.

The aerodynamic design problem can be formulated by including in the notation the explicit dependence of the objective function J from the vector of the design variables, resulting in

$$\begin{aligned} \min \quad & \mathfrak{J}(\boldsymbol{\alpha}, \boldsymbol{U}(\boldsymbol{\alpha}), \boldsymbol{X}(\boldsymbol{\alpha})) \\ \text{constraints} \quad & \boldsymbol{U}(\boldsymbol{\alpha}) = \mathfrak{G}(\boldsymbol{U}(\boldsymbol{\alpha}), \boldsymbol{X}(\boldsymbol{\alpha})) \quad, \\ & \boldsymbol{X}(\boldsymbol{\alpha}) = \boldsymbol{M}(\boldsymbol{\alpha}) \end{aligned} \tag{5.5}$$

where $\boldsymbol{M}(\boldsymbol{\alpha})$ is a differentiable function denoting the mesh deformation algorithm. The Lagrangian of the constrained optimization problem L can be then written as

$$
\begin{aligned}
L(\boldsymbol{\alpha}, \boldsymbol{U}(\boldsymbol{\alpha}), \boldsymbol{X}(\boldsymbol{\alpha}), \boldsymbol{\lambda}, \boldsymbol{\mu}) = \quad & \mathfrak{J}(\boldsymbol{U}(\boldsymbol{\alpha}), \boldsymbol{X}(\boldsymbol{\alpha}), \boldsymbol{\alpha}) \\
& (\mathfrak{G}(\boldsymbol{U}(\boldsymbol{\alpha}), \boldsymbol{X}(\boldsymbol{\alpha})) - \boldsymbol{U}(\boldsymbol{\alpha}))^T \boldsymbol{\lambda} \quad , \\
& + (\boldsymbol{M}(\boldsymbol{\alpha}) - \boldsymbol{X}(\boldsymbol{\alpha}))^T \boldsymbol{\mu}
\end{aligned}
\tag{5.6}
$$

where $\boldsymbol{\lambda}$ and $\boldsymbol{\mu}$ are the Lagrangian multipliers or adjoint variables. The differential of the lagrangian function with respect to the vector of the design variables $\boldsymbol{\alpha}$ yields

$$
dL = \frac{\partial L}{\partial \boldsymbol{\alpha}} d\boldsymbol{\alpha} + \frac{\partial L}{\partial \boldsymbol{U}(\boldsymbol{\alpha})} \frac{\partial \boldsymbol{U}(\boldsymbol{\alpha})}{\partial \boldsymbol{\alpha}} d\boldsymbol{\alpha} + \frac{\partial L}{\partial \mathrm{X}(\boldsymbol{\alpha})} \frac{\partial \boldsymbol{X}(\boldsymbol{\alpha})}{\partial \boldsymbol{\alpha}} d\boldsymbol{\alpha},
\tag{5.7}
$$

thus, omitting the explicit dependence from the independent variables, it reads

$$
\frac{dL}{d\boldsymbol{\alpha}} = \frac{\partial \mathfrak{J}}{\partial \boldsymbol{\alpha}} + \left[\frac{\partial \mathfrak{J}}{\partial \boldsymbol{U}} + \left(\frac{\partial \mathfrak{G}}{\partial \boldsymbol{U}} \right)^T \boldsymbol{\lambda} - \boldsymbol{\lambda} \right] \frac{\partial \boldsymbol{U}}{\partial \boldsymbol{\alpha}} +
$$

$$
+ \left[\frac{\partial \mathfrak{J}}{\partial \boldsymbol{X}} + \left(\frac{\partial \mathfrak{G}}{\partial \boldsymbol{X}} \right)^T \boldsymbol{\lambda} - \boldsymbol{\mu} \right] \frac{\partial \boldsymbol{X}}{\partial \boldsymbol{\alpha}} + \left(\frac{\partial \boldsymbol{M}}{\partial \boldsymbol{\alpha}} \right)^T \boldsymbol{\mu}
\tag{5.8}
$$

from which the adjoint equations are derived as

$$
\frac{\partial \mathfrak{J}}{\partial \boldsymbol{U}} + \left(\frac{\partial \mathfrak{G}}{\partial \boldsymbol{U}} \right)^T \boldsymbol{\lambda} - \boldsymbol{\lambda} = 0,
\tag{5.9}
$$

and

$$
\frac{\partial \mathfrak{J}}{\partial \boldsymbol{X}} + \left(\frac{\partial \mathfrak{G}}{\partial \boldsymbol{X}} \right)^T \boldsymbol{\lambda} - \boldsymbol{\mu} = 0.
\tag{5.10}
$$

Similarly to the flow solver (5.4), (5.9) can be viewed as a fixed-point iteration in λ, namely

$$
\boldsymbol{\lambda}^{n+1} = \frac{\partial \mathfrak{J}}{\partial \boldsymbol{U}} + \left(\frac{\partial \mathfrak{G}}{\partial \boldsymbol{U}} \right)^T \boldsymbol{\lambda}^n = N(\boldsymbol{\lambda}^n, \boldsymbol{U}^*, \boldsymbol{X}),
\tag{5.11}
$$

where $\boldsymbol{U}^*$ is the numerical solution of the two-phase flow equations. Since N is contractive, (5.11) will converge at the same rate as the primal flow solver when using the same time-marching scheme. The right hand-side of (5.11) is obtained by resorting to Algorithmic Differentiation applied to the source code of the program that computes $\mathfrak{J}$ and $\mathfrak{G}$ in black-box fashion. This is made possible at the expense of a small runtime overhead by the use of the *Jacobi taping method* implemented in the AD tool CodiPack [24] in combination with the *Expression Templates* feature of C++. Equation (5.10) is instead evaluated only once the adjoint solution vector has been computed. Finally, by replacing (5.9), (5.10) in (5.8) one obtains the gradient of the objective function $\mathfrak{J}$ with respect of the design variables $\boldsymbol{M}(\boldsymbol{\alpha})$ as

$$
\frac{dL}{d\boldsymbol{\alpha}} = \frac{d\mathfrak{J}}{d\boldsymbol{\alpha}} = \frac{\partial \mathfrak{J}}{\partial \boldsymbol{\alpha}} + \frac{\partial \boldsymbol{M}^T}{\partial \boldsymbol{\alpha}} \boldsymbol{\mu}.
\tag{5.12}
$$

The same approach is used to calculate the gradients of any of the constraints of the optimization problem featuring explicit dependence on the design variables. A full description of the aerodynamic design chain can be found in Refs. [9] and [14]. Both the two-phase flow and adjoint solvers can be run in serial or parallel mode using a mesh partitioning approach and an implementation of the message-passing interface standard.

5.3. THERMODYNAMIC MODELING OF THE TWO-PHASE FLUID

The equilibrium and metastable thermodynamic properties of the vapor phase states are computed by means of a thermodynamic model based on an improved Peng-Robinson equation of state (EoS) [25], implemented in the external fluid property library [26] linked to SU2. Viscosity and thermal conductivity are computed by the same library in correspondence with the total conditions P_0, T_0 at the nozzle inlet and kept constant along the expansion.

The liquid density is the one reported in A.2.1, while the liquid enthalpy is calculated as in C.1. Saturation properties are calculated as in A.2.3, A.2.4 Finally, the surface tension is evaluated using the relations given in Ref. [28]. All these models are implemented in SU2 to reduce the time required by the selected external thermodynamic library for calculations in the liquid and two-phase region.

5.4. OBJECTIVE FUNCTION FOR TURBOMACHINERY DESIGN PROBLEMS WITH CONDENSING FLOWS

A comprehensive review of loss mechanisms associated to metastable condensation in turbomachinery is provided in Ref.[29]. The largest share of entropy generation due to non-equilibrium condensation is due to heat transfer between the liquid and the vapor phase and this loss is usually termed *thermodynamic wetness loss*. Furthermore, the formation of tiny liquid droplets generally leads to pitting and erosion of the blades leading-edge, which eventually may affect their structural integrity, thus, the final performance [29, 30]. Stemming from these considerations, the objective function $\mathfrak{J}$ for the two-phase adjoint-based optimization framework can be defined in terms of i) minimization of liquid volume fraction Y_{vol} in order to reduce the amount of liquid condensate ii) and minimization of entropy loss coefficient ζ in order to mitigate all irreversible flow phenomena, thus including those due to non-equilibrium condensation. The way in which the two objective functions are calculated from CFD results described in the following.

5.4.1. LIQUID VOLUME FRACTION

The liquid volume fraction Y_{vol} can be directly computed from the transport equation of the third moment μ_3 as

$$Y_{\text{vol}} = \frac{4\pi}{3} U_{\text{2phase},4} = \frac{4}{3}\pi\rho_{\text{m}}\mu_3.$$ (5.13)

Due to the order of magnitude of $U_{\text{2phase},4}$, i.e., approximately 1e-6, the resolution tolerance was set to 1e-10.

The quantity Y_{vol} was selected over the liquid mass fraction Y_{mass}, defined as

$$Y_{\mathrm{mass}} = \frac{4}{3}\pi U_{\mathrm{2phase,4}}\frac{\rho_{\mathrm{l}}}{\rho_{\mathrm{m}}} = \frac{U_{\mathrm{2phase,4}}\rho_{\mathrm{l}}}{U_{\mathrm{2phase,4}}(\rho_{\mathrm{l}} - \rho_{\mathrm{v}}) + \frac{3}{4\pi}\rho_{\mathrm{v}}} \tag{5.14}$$

to avoid numerical issues related to the different order of magnitude of the terms at the denominator of (5.14).

5.4.2. ENTROPY LOSS COEFFICIENT
Using first principles, for a fixed control volume in which the condensing vapor flows through, the entropy generation $\Delta\dot{s}$ due to loss mechanisms can be computed as

$$\Delta\dot{s} = s_{\mathrm{out}} - s_{\mathrm{in}}, \tag{5.15}$$

in which

$$s_{\mathrm{out}} = Y_{\mathrm{mass_{out}}}s_{\mathrm{l,out}} + (1 - Y_{\mathrm{mass_{out}}})s_{\mathrm{v,out}}, \tag{5.16}$$

$s_{\mathrm{l,out}}$ are the liquid and the vapor entropy fluxes at the outlet boundary of the control volume, s_{in} is the entropy flux of the inlet flow stream, determined starting from the inlet total conditions P_0, T_0 assuming single phase in thermodynamic equilibrium conditions. Y_{out} is the liquid mass fraction per unit mass. The entropy loss coefficient ζ is finally expressed as

$$\zeta = \Delta\dot{s}\frac{T_{\mathrm{out,s}}}{\frac{1}{2}v_{\mathrm{out}}^2}, \tag{5.17}$$

where $T_{\mathrm{out,s}}$ and v_{out} are the outlet static temperature and flow absolute velocity.

In all calculations, the entropy values at inlet and outlet boundaries are obtained by applying mass-flow averaging to the non-uniform flow. The use of a coefficient lumping all dissipative contributions coming from viscous effects, shock waves, and thermodynamic wetness losses is a convenient choice in turbomachinery applications as loss mechanisms are seldom independent and performance parameters eventually depends on global entropy increase.

For either objective functions, the optimization runs were conducted using the Sequential Least SQuares Programming (SLSQP) optimizer described in [31].

5.5. APPLICATIONS
The capability of the adjoint-based design framework are demonstrated by performing shape optimization of two exemplary steam cascades made of blades that are representative of typical blade profiles for steam turbines. The first blades row corresponds to the stator of the last stage of a 200 MW$_{\mathrm{e}}$ steam turbine [32], while the second one is taken from the fifth stage of an industrial steam turbine of large power capacity and is described in Ref. [33]. The illustration of the test cases follows the same structure. First, it is reported the validation of the numerical model. Then, the results of the optimization using the two objective functions are discussed. For the sake of clarity, the two turbine cascades are referred to as the *Dykas cascade* and the *White cascade* in the following,

P_0 (Pa)	T_0 (K)	P_{out} (Pa)	μ (Pa*s)	k (W/mK)	$\frac{\mu_{turb}}{\mu}$	I
0.89e5	373.15	0.39e5	12.252e-6	24.626e-3	100	0.05

Table 5.1: *Dykas cascade*, boundary conditions and simulation parameters
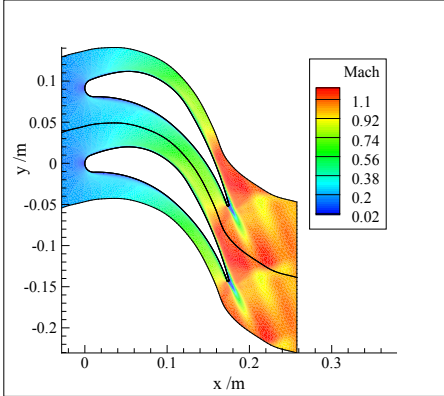
Figure 5.1: *Dykas cascade*, Mach number distribution within the flow field
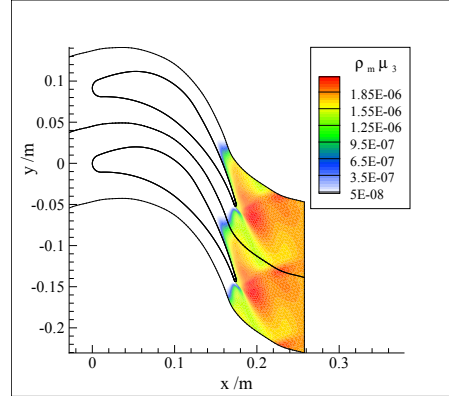
Figure 5.2: *Dykas cascade*, $U_{2phase,4}$ distribution within the flow field

from the name of the first author of the paper where the experimental studies were published. It is assumed that both the considered low-pressure steam turbine stages were designed using best design practices for condensing flows in steam turbines.

5.5.1. DYKAS CASCADE

VALIDATION OF THE NUMERICAL MODEL

The boundary conditions and the simulation parameters are listed in Table 5.1. Simulations were run using second-order numerical schemes on a mesh comprising 30k elements. The CFL number was set to 20 and kept constant during the simulation.

The contour of the dimensionless pressure field and liquid volume fraction is shown in Figures 5.1 and 5.2. The condensation onset occurs right after the impingement of the expansion fan on the suction side. The release of latent heat in the supersonic flow stream induces the formation of a condensation shock at about $x = 0.16$ m, followed by a further flow expansion up to the trailing-edge. The pressure distribution along the blade surface obtained by the numerical model is compared to that obtained experimentally in Figure 5.3. It can be observed that the largest deviations are located in correspondence of the so-called condensation shock. However, the location of condensation inception, i.e., the Wilson point, is correctly predicted by the model. Overall, the accuracy of the model is deemed adequate for design purposes.

The adjoint solver is validated by comparing the gradient of the objective function against the one computed by centered finite differences with a step size of 1e-3. The blade is parametrized using an FFD (Free-Form Deformation) box constituted by 25 con-
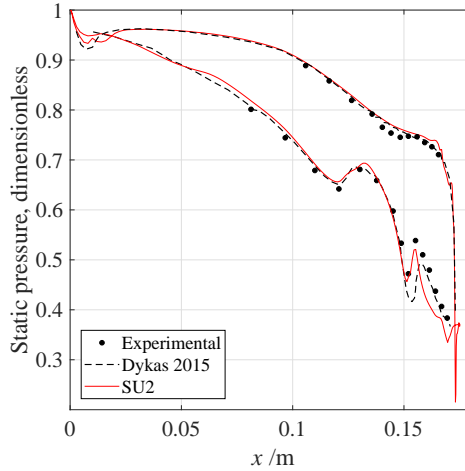
Figure 5.3: *Dykas cascade*, pressure distribution on the blade surface, comparison between simulation results and the experimental data in Ref. [32]

	1ph, visc	1ph, turb	adj 1ph turb	2ph, turb	Adj 2ph, turb
Rel. time	1	1.12	1.58	1.26	3.06
Max memory	1	1.05	3.96	1.92	5.26

Table 5.2: *Dykas cascade*, physical time and peak memory allocated required for i) single-phase laminar (1ph, visc), ii) single-phase turbulent (1ph, turb), iii) adjoint single-phase turbulent (Adj 1ph, turb), iv) two-phase turbulent (2ph, turb) and v) adjoint two-phase turbulent (Adj 2ph, turb) simulations

trol points, see Figure 5.4. These are the design variables of the vector $\boldsymbol{\alpha}$ used to define the optimization problem.

Figure 5.5 shows that the gradients of the entropy loss coefficient computed by the adjoint method are well in agreement with the correspondent FD values. Additionally, Figures 5.6, 5.7 depict the convergence history of both solvers. The use of the duality-preserving approach allows the adjoint solver to inherit the same convergence rate of the primal solver.

The computational cost and peak memory requirement of the two-phase numerical model are normalized with the values of a single phase viscous computation and summarized in Table 5.2. If compared with the performance of a single-phase turbulent model, the extra cost demanded by the two-phase model is of the order of 20% for the flow and two times higher for the adjoint solver, while in terms of memory requirement the increase is of the same order of magnitude.

SHAPE OPTIMIZATION

The simulated performance for the *Dykas cascade* was optimized under the constraint of preserving the baseline mass flow rate. The resulting optimization problem is then set as follows
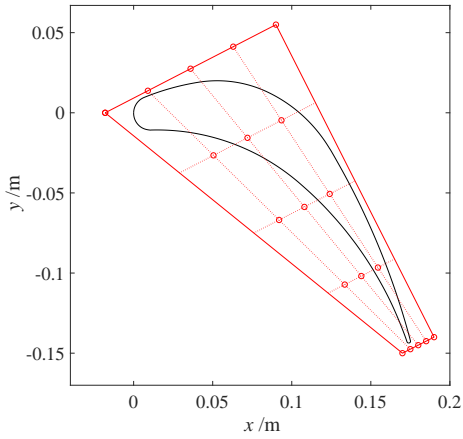
Figure 5.4: *Dykas cascade,* blade profile and FFD box control points
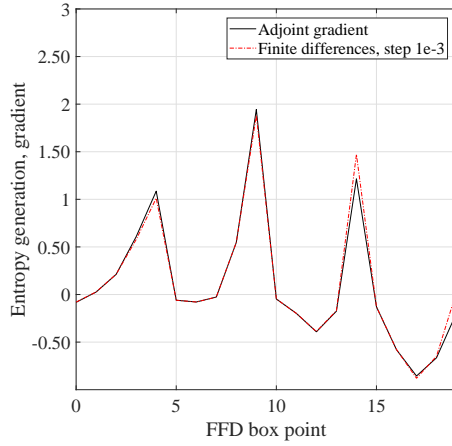
Figure 5.5: *Dykas cascade,* comparison between the entropy generation gradient calculated with the adjoint solver and the same quantity calculated with finite differences

5
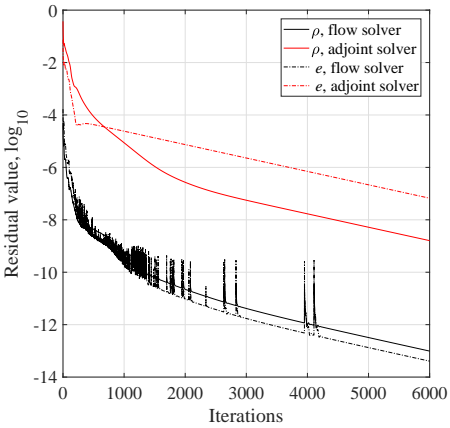
Figure 5.6: *Dykas cascade,* convergence history of the solutions $U_{\text{flow},1}$ and $U_{\text{flow},4}$
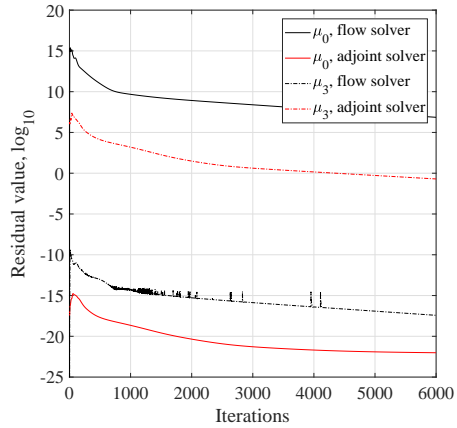
Figure 5.7: *Dykas cascade,* convergence history of the solutions $U_{\text{2phase},1}$ and $U_{\text{2phase},4}$
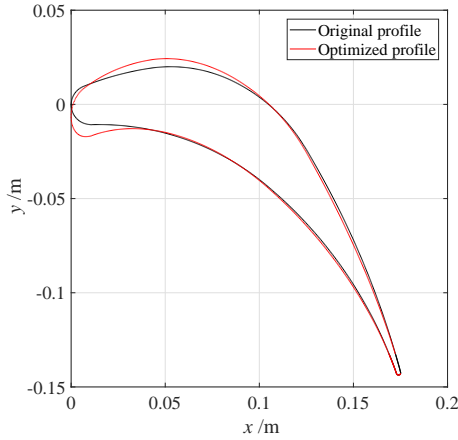
Figure 5.8: *Dykas cascade*, comparison between the original profile and the optimized profile in case the objective is the minimization of the liquid volume fraction
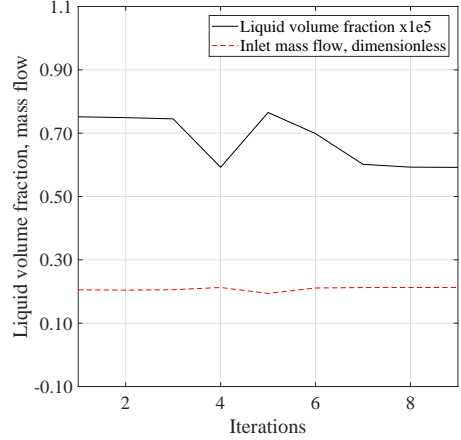
Figure 5.9: *Dykas cascade*, optimization history in case the objective si the minimization of the liquid volume fraction

$$\begin{aligned} \underset{\boldsymbol{\alpha}}{\text{minimize}} \quad & Y_{\text{vol}}(\boldsymbol{\alpha}), \zeta(\boldsymbol{\alpha}) \\ \text{subject to:} \quad & \dot{m} = \dot{m}_{\text{b}}, \end{aligned} \tag{5.18}$$

The outcomes of the optimization achieved by minimizing the liquid volume fraction are discussed first. Figures 5.8 and 5.9 illustrate the original and optimized blade profile and the convergence history of the optimization, respectively. As it can be observed, the automated shape optimization allowed to reduce the liquid volume fraction by about 20% in 6 design iterations. This is also evident from the the contour of the third moment μ_3 displayed in Figure 5.11.

Figure 5.12 shows the distribution of the mass-flow averaged Mach number in the streamwise direction, in order to support insights on the physical cause of lower liquid volume level calculated for the optimized cascade. The reshape of the leading edge provided by the optimization entails larger flow over-speed in the aft-part of the blade, which causes the vapor to undergo larger excursion into the metastable region. The net result is a delay of condensation onset which leads to a larger number of tiny droplets to form in the region downstream of the blade. However, the reduction of liquid volume fraction obtained by shaping the leading-edge comes at the expense of a higher degree of vapor subcooling, which directly affects the fluid-dynamic performance of the cascade, i.e., the higher the subcooling the higher the fluid-dynamic losses. For the optimized cascade, the thermodynamic wetness loss increases by approximately 12% with respect to the baseline cascade when the flow reverts back to thermodynamic equilibrium at the outflow boundary. A further simulation performed with an extended flow domain confirmed that thermodynamic equilibrium conditions are practically met at an axial distance lower than a typical stator-rotor clearance in axial turbines. Figure 5.13 reports the degree of subcooling, defined as
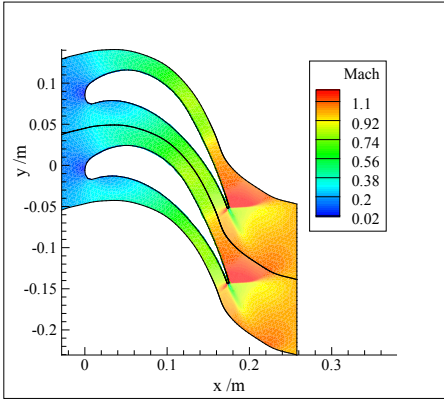
Figure 5.10: *Dykas cascade*, Mach number distribution for the optimized profile in case the objective is the minimization of the liquid volume fraction
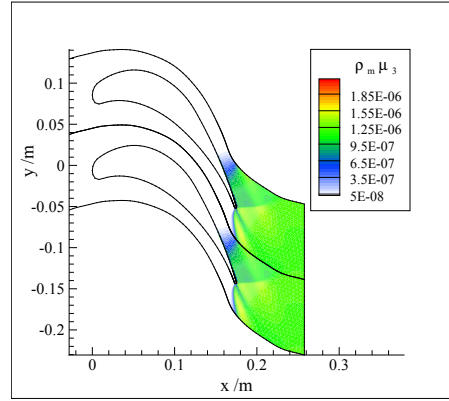
Figure 5.11: *Dykas cascade*, $U_{2\text{phase},4}$ distribution for the optimized profile in case the objective is the minimization of the liquid volume fraction

5

$$\Delta T_{\text{sub}} = T_{\text{sat}}(P_{\text{v}}) - T_{\text{v}}, \tag{5.19}$$

obtained for the original and optimized profile with the extended domain, whereas Figure 5.14 displays solution $U_{2\text{phase},1}$, given by

$$U_{2\text{phase},1} = \rho_{\text{m}} N, \tag{5.20}$$

where N is the average number of droplets, for the original profile and the optimized case.

From the previous findings it can be inferred that a reduction of liquid volume fraction does not directly yield an improvement of cascade fluid-dynamic efficiency, which instead is attainable by minimizing the entropy coefficient. The results of this second optimization are reported in Figures 5.15 and 5.16. The loss coefficient is reduced by about 11%, but the liquid volume fraction turned out to increase by about 3%. Figures 5.17,5.18 report the simulation results in terms of Mach number and liquid volume fraction contour. This result suggests that, for the problem at hand, a simultaneous reduction of liquid volume fraction and entropy generation can be obtained only by concurrently minimizing both objectives.

The fluid-dynamic performance gain is found to be due to improved aerodynamic characteristics of the blade as well as a reduction of vapor subcooling throughout the channel, as visible from the contour of vapor subcooling and blade pressure distribution in Figures 5.19 and 5.20.

5.5.2. White cascade

Validation of the numerical model

The boundary conditions and the simulation parameters for the second test case are reported in Table 5.3. The number of mesh elements and the CFL number were set equal to the previous case.
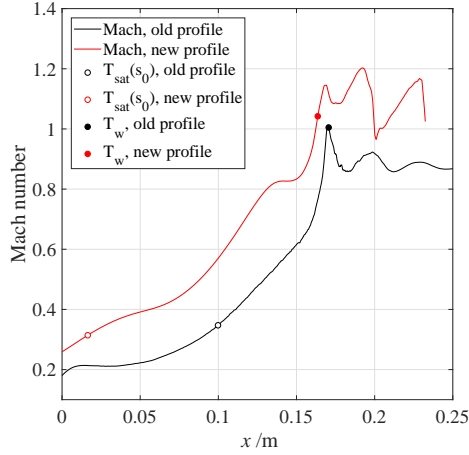
Figure 5.12: *Dykas cascade*, comparison between the averaged streamwise Mach number distribution for the original profile and the optimized profile in case the objective is the minimization of the liquid volume fraction

5
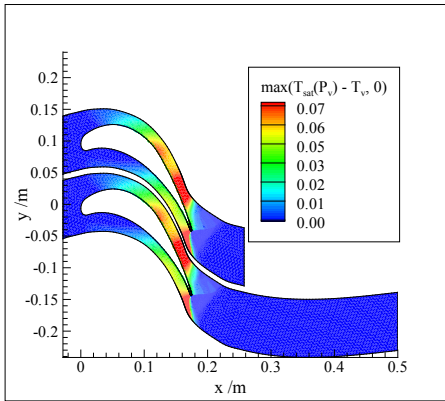
Figure 5.13: *Dykas cascade*, degree of subcooling ΔT_{sub} for the simulations with the optimized profile in case the objective is the minimization of the liquid volume fraction, comparison between short and extended domain.
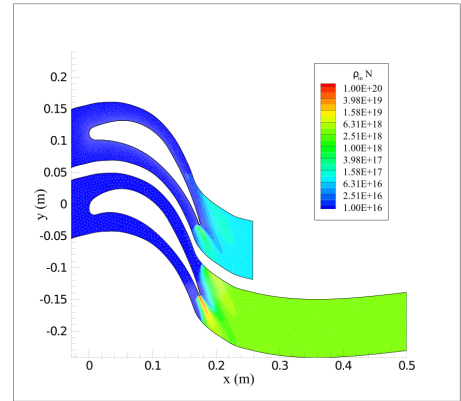
Figure 5.14: *Dykas cascade*, solution $U_{2\text{phase},1}$ for the original profile (up) and the optimized profile in case the objective is the minimization of the liquid volume fraction (down)

P_0 (Pa)	T_0 (K)	P_{out} (Pa)	μ (Pa·s)	k (W/m/K)	$\frac{\mu_{\text{turb}}}{\mu}$	I
0.409e5	354.0	0.196e5	11.579e-6	22.971e-3	100	0.05

Table 5.3: *White cascade*, boundary conditions and simulation parameters
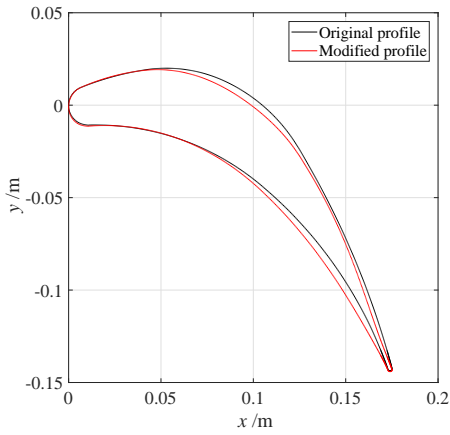
Figure 5.15: *Dykas cascade,* comparison between the original profile and the optimized profile in case the objective is the minimization of the thermodynamic losses
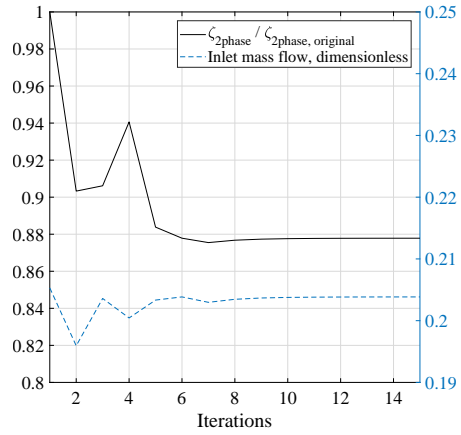
Figure 5.16: *Dykas cascade,* optimization history in case the objective is the minimization of the thermodynamic losses
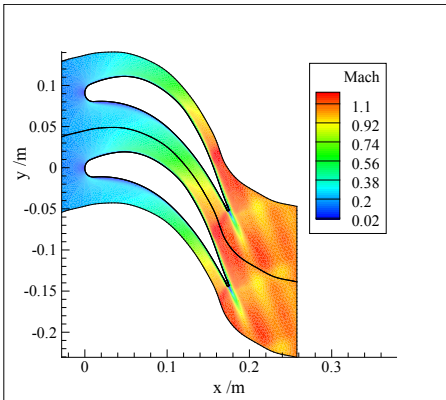
Figure 5.17: *Dykas cascade,* Mach number distribution for the optimized profile in case the objective is the minimization of the thermodynamic losses
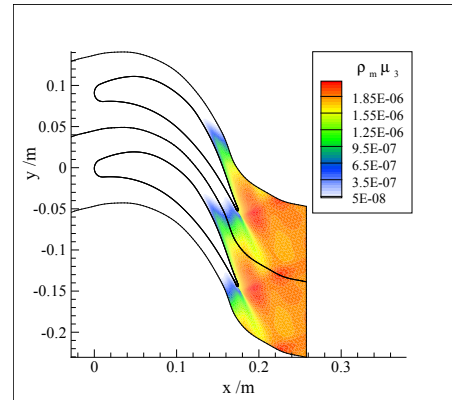
Figure 5.18: *Dykas cascade,* $U_{2\text{phase},4}$ distribution for the optimized profile in case the objective is the minimization of the thermodynamic losses
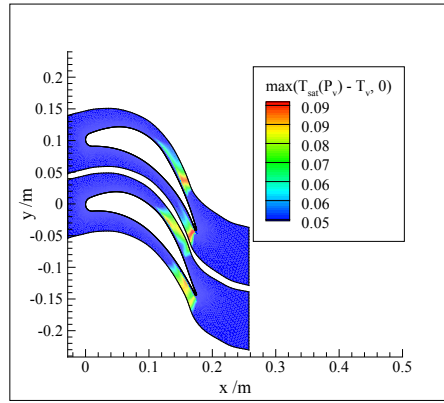
Figure 5.19: *Dykas cascade*, comparison between the vapor subcooling of the original blade and that of optimized profile in case the objective is the minimization of the thermodynamic losses

5

Figure 5.21 shows the comparison between the blade load obtained from the simulations and the experimental data in Ref. [33]. Figures 5.22 and 5.23 display the results of the two-phase simulation. Similarly to the results obtained with the *Dykas cascade*, the condensation onset is predicted with sufficient accuracy, while the pressure distribution on the rear suction side shows the largest deviations as compared to experimental data. This is attributed to an over estimation of the amount of latent heat released after condensation onset, which causes a more pronounced pressure peak followed by a smoother flow expansion before the final recompression.

Figures 5.24 and 5.25 show the FFD box used for the optimization and the adjoint gradient validation. As for the previous case, the gradients obtained by adjoint and second-order finite differences are well in accordance.

SHAPE OPTIMIZATION

The minimization of the liquid volume fraction and entropy loss coefficient was carried out by imposing an inequality constraint on the averaged outlet flow angle α_{out}. The optimization problem is then formulated as

$$
\begin{aligned}
&\underset{\boldsymbol{\alpha}}{\text{minimize}} && Y_{\text{vol}}(\boldsymbol{\alpha}), \zeta(\boldsymbol{\alpha}) \\
&\text{subject to:} && \alpha_{\text{out}} > \alpha_{\text{out,b}},
\end{aligned}
\tag{5.21}
$$

Figures 5.26 and 5.27 depict the optimal profile and the convergence history when minimizing the liquid volume fraction. The optimal profile is characterized by a liquid volume fraction reduced by 25% with respect to the original case. The contour of Mach number and volume fraction are reported in Figures 5.28, 5.29.

As opposed to the results obtained with the *Dykas cascade*, the flow reaches thermodynamic equilibrium at approximately one chord downstream of the cascade. Figure 5.30 shows the subcooling ΔT_{sub} for the optimized profile resulting from the use of i) a
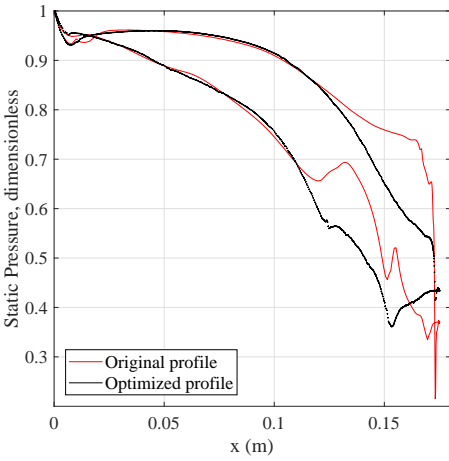
Figure 5.20: *Dykas cascade*, blade loading of the baseline and optimized configuration in case the objective is the minimization of the thermodynamic losses
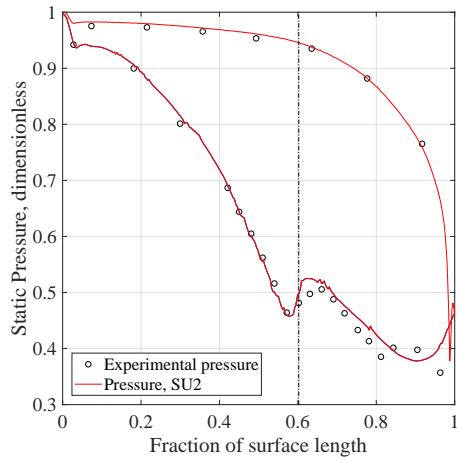
Figure 5.21: *White cascade*, pressure distribution on the blade surface, comparison between the simulation results and the experimental data in Ref. [33]
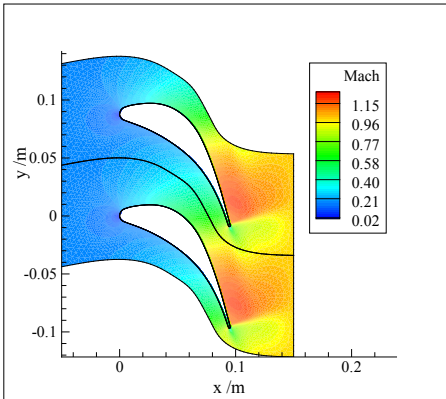
Figure 5.22: *White cascade*, Mach number distribution within the flow field
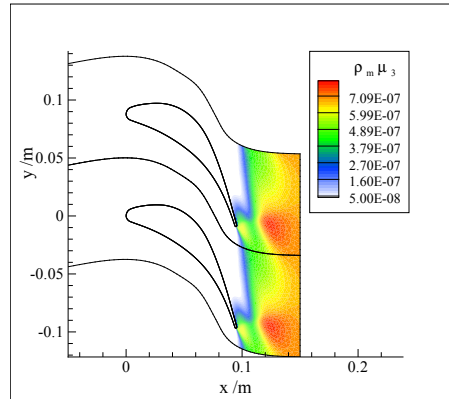
Figure 5.23: *White cascade*, $U_{2\text{phase},4}$ distribution within the flow field
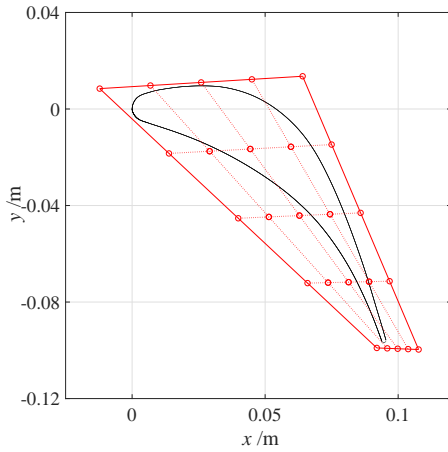
Figure 5.24: *White cascade*, blade profile and FFD box control points
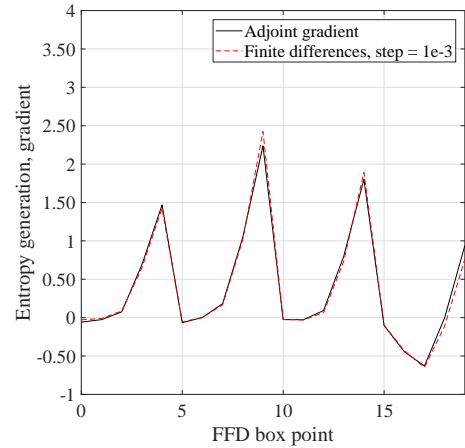
Figure 5.25: *White cascade*, comparison between the entropy generation gradient calculated with the adjoint solver and the same quantity calculated with finite differences

short and ii) an extended simulation domain. The thermodynamic wetness losses for the optimized profile calculated using an extended flow domain are comparable to those of the original cascade. Therefore, the decrease in liquid volume fraction does not translate in a reduction of the loss coefficient $\zeta_{2\text{phase}}$.

Lastly, Figures 5.31 and 5.32 show the optimal profile obtained when minimizing the entropy loss coefficient and the associated optimization history. Full convergence is achieved after four iterations and the value fo the objective function is reduced by about 12%, while the outlet flow angle remains practically unaltered.

The contours of the Mach number and the liquid volume fraction are instead displayed in Figures 5.33 and 5.34. By comparison with the same contours of the baseline geometry of Figures 5.22 and 5.23 it can be deduced that the optimization provides a geometry configuration that leads to lower Mach number flows and a shift of the condensation onset further downstream close to the blade trailing-edge. As a consequence thereof, the flow reaches a lower degree of subcooling with positive impact in terms of wetness loss reduction. Differently from the Dykas cascade, the averaged liquid volume fraction also decreases by about 20%.

Figure 5.35 reports the blade loading of the original and the optimized configuration. The pressure distribution of the optimized cascade is obtained by using the two-phase and the single-phase model, namely assuming that no condensation is triggered when expanding the flow between the same conditions. The trends show that the pressure distribution around the optimal blade is comparatively equivalent in the two cases, suggesting that viscous dissipation on the blade walls is in turn mitigated by virtue of the removal of the condensation shock and of the velocity peak on the rear suction side.

Ultimately, these results further corroborate the potential and the effectiveness of shape optimization for turbomachinery flow problems characterized by phase change.
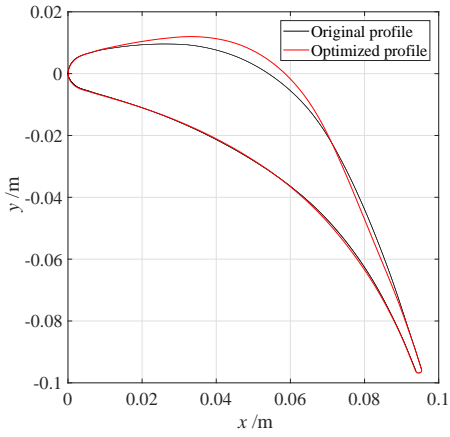
Figure 5.26: *White cascade,* comparison between the original profile and the optimized profile in case the objective is the minimization of the liquid volume fraction
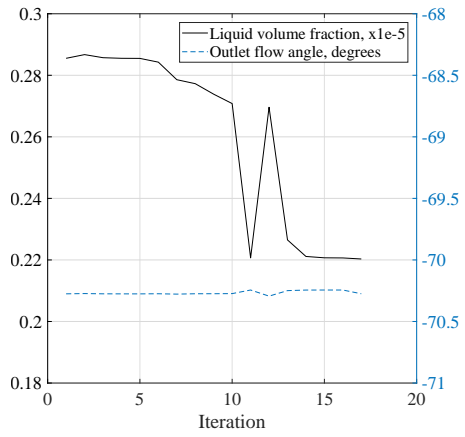
Figure 5.27: *White cascade,* optimization history in case the objective is the minimization of the liquid volume fraction history
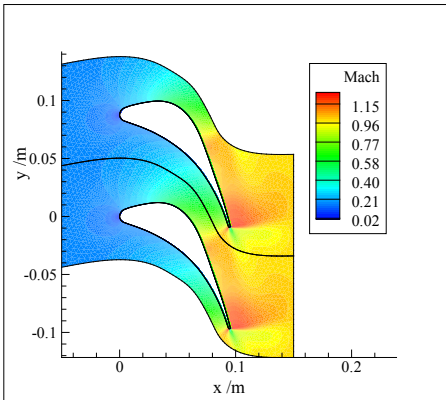
Figure 5.28: *White cascade,* Mach number for the optimized profile in case the objective is the minimization of the liquid volume fraction
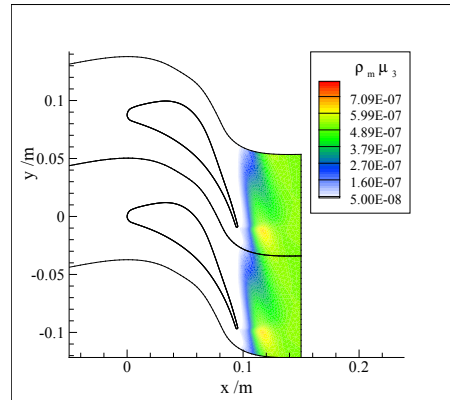
Figure 5.29: *White cascade,* solution $U_{2\text{phase},4}$ for the optimized profile in case the objective is the minimization of the liquid volume fraction
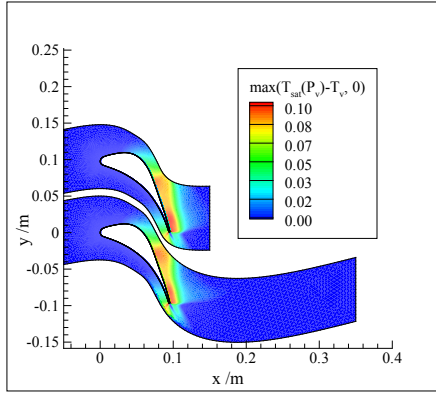
Figure 5.30: *White cascade,* degree of subcooling ΔT_{sub}, comparison between the simulations with the original domain and the extended domain using the optimized profile in case the objective is the minimization of the liquid volume fraction
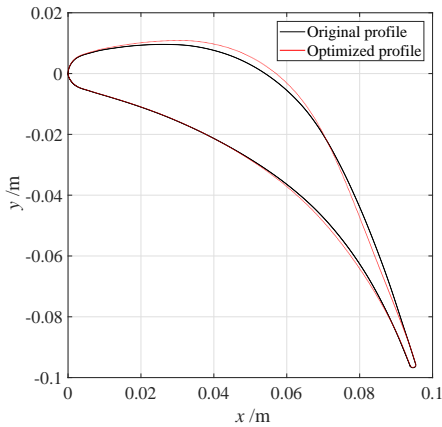
Figure 5.31: *White cascade,* comparison between the original profile and the optimized profile in case the objective is the minimization of the thermodynamic losses
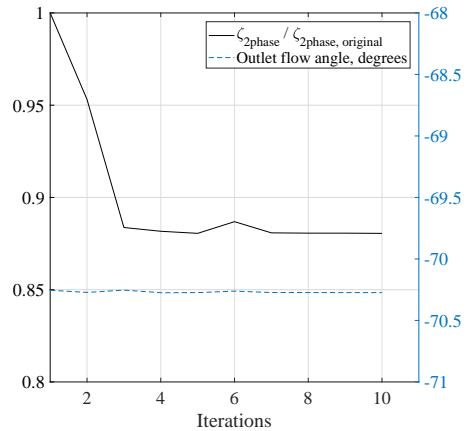
Figure 5.32: *White cascade,* optiization history in case the objective is the minimization of the thermodynamic losses
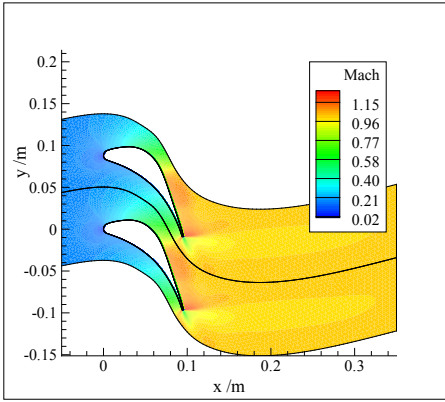
Figure 5.33: *White cascade,* Mach number distribution for the optimized profile in case the objective is the minimization of the thermodynamic losses
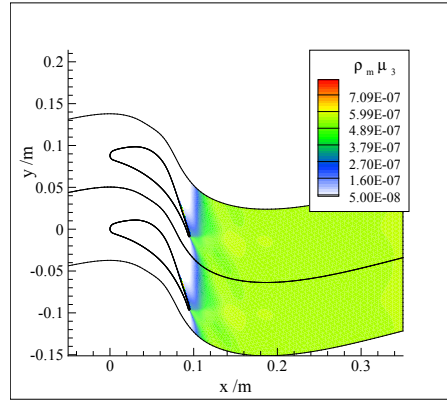
Figure 5.34: *White cascade,* $U_{2\text{phase},4}$ distribution for the optimized profile in case the objective is the minimization of the thermodynamic losses

5
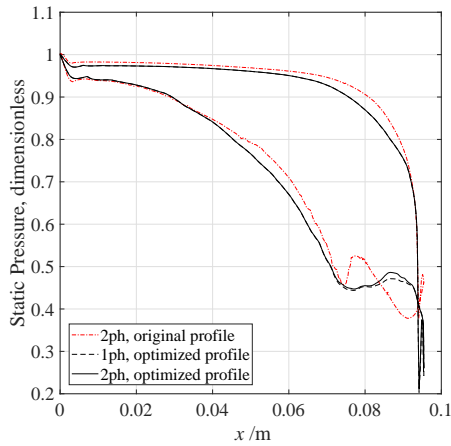
Figure 5.35: *White cascade,* comparison between the blade loading of the baseline and that of the optimized configuration in case the objective is the minimization of the thermodynamic losses obtained by using both single- and two-phase simulations
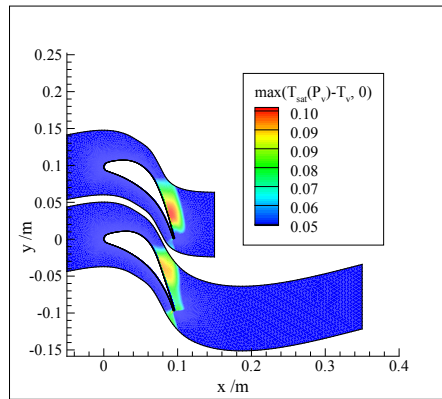
Figure 5.36: *White cascade*, comparison between the degree of subcooling of the baseline (up) and that of the optimized configuration in case the objective is the minimization of the thermodynamic losses (down)

5.6. CONCLUSIONS

A fully turbulent adjoint-based optimization method for two-phase condensing flow problems in turbomachinery was developed and documented. The method was implemented in the open-source SU2 CFD software, which was extended to simulate metastable condensing flows by means of the method of moments. The adjoint solver is based on a duality-preserving algorithm, which enables the adjoint solver to inherit the same convergence properties of the primal flow solver. The optimization framework was then applied to the re-design of two turbine cascades representative of blade profiles adopted in steam turbines of large power capacity. The main outcomes of the study can be summarized as follows:

1. The adjoint solver is approximately two times computationally more expensive than the primal two-phase flow solver, while in terms of memory requirement the extra demand for the adjoint solver is of the order of three times. The computational performance is expected to scale similarly for three-dimensional cases.

2. For both cascade configurations, the adjoint-based constrained minimization of the liquid volume fraction led to abating the amount of condensate by nearly 24%, but at the expense of an increase of the entropy loss coefficient for the *Dykas cascade*.

3. The adjoint-based constrained minimization of the entropy coefficient allowed to considerably improve the simulated performance of both turbine cascades. In particular, the entropy loss coefficient reduced by 11% for the *Dykas cascade* and by 12% for the *White cascade*. The averaged liquid volume fraction at the outlet boundary obtained with the *Dykas cascade* turned out to be similar, while for the *White cascade* it decreased by 20%. These observations suggest that the minimization of both objectives can be assured only by taking into account both objectives concurrently.

The development of an efficient fully-turbulent adjoint optimization framework for two-phase flows and the demonstration of its capabilities for the re-design of steam turbine cascades paves the way for shape optimization of a number of turbomachinery applications characterized by phase change, such as supercritical CO_2 compressors, centrifugal compressors for refrigeration systems, and rocket engine turbo-pumps.

REFERENCES

[1] M. Pini, L. Azzini, S. Vitale, and P. Colonna, *A two-phase discrete adjoint method applied to the shape optimization of steam turbine cascades,* submitted to the ASME Journal of Turbomachinery .

[2] A. Jameson, *Aerodynamic design via control theory,* Journal of Scientific Computing **3**, 233 (1988).

[3] A. Jameson, L. Martinelli, and N. A. Pierce, *Optimum aerodynamic design using the navier–stokes equations,* Theoretical and Computational Fluid Dynamics **10**, 213 (1998).

[4] J. J. Reuther, A. Jameson, J. J. Alonso, M. J. Rimlinger, and D. Saunders, *Constrained multipoint aerodynamic shape optimization using an adjoint formulation and parallel computers, part 1, Journal of Aircraft,* Journal of Aircraft **36**, 51 (1999).

[5] C. A. Mader, J. R. R. A. Martins, J. J. Alonso, and E. V. Der Weide, *Adjoint: An approach for the rapid development of discrete adjoint solvers, AIAA Journal,* AIAA Journal **46**, 863 (2008).

[6] M. S. Campobasso, M. C. Duta, and M. B. Giles, *Adjoint calculation of sensitivities of turbomachinery objective functions, Journal of Propulsion and Power,* Journal of Propulsion and Power **19**, 693 (2003).

[7] J. Luo, C. Zhou, and F. Liu, *Multipoint design optimization of a transonic compressor blade by using an adjoint method,* Journal of Turbomachinery **136** (2014).

[8] B. Walther and S. Nadarajah, *Adjoint-based constrained aerodynamic shape optimization for multistage turbomachines,* Journal of Propulsion and Power **31** (2015).

[9] T. A. Albring, M. Sagebaum, and N. R. Gauger, *Efficient aerodynamic design using the discrete adjoint method in su2,* 17th AIAA/ISSMO Multidisciplinary Analysis and Optimization Conference (2016).

[10] D. T. Economon, F. Palacios, S. R. Copeland, T. W. Lukaczyk, and J. J. Alonso, *Su2: An open-source suite for multiphysics simulation and design,* AIAA Journal **54**, 828 (2015).

[11] M. Sagebaum, T. Albring, and N. R. Gauger, *Codipack – code differentiation package | scientific computing,* (2017).

[12] B. Y. Zhou, T. Albring, T. Gauger, T. Ilario, T. D. Economon, and J. J. Alonso, *Reduction of airframe noise components using a discrete adjoint approach,* AIAA 2017-3658 (2017).

5

[13] R. Sanchez, R. Palacios, T. D. Economon, J. J. Alonso, J. J. Albring, and J. J. Gauger, *Optimal actuation of dielectric membrane wings using high-fidelity fluid-structure modelling,* AIAA 2017-0857 (2017).

[14] S. Vitale, T. A. Albring, M. Pini, N. R. Gauger, and P. Colonna, *Fully turbulent discrete adjoint solver for non-ideal compressible flow applications, Journal of the Global Power and Propulsion Society,* **1**, 252.

[15] A. Rubino, M. Pini, P. Colonna, T. Albring, S. Nimmagadda, T. Economon, and J. Alonso, *Adjoint-based fluid dynamic design optimization in quasi-periodic unsteady flow problems using a harmonic balance method, Journal of Computational Physics,* **372**, 220 (2018).

[16] J. Young, *Semi-analytical techniques for investigating thermal non-equilibrium effects in wet steam turbines,* International Journal of Heat and Fluid Flow **5**, 81 (1984).

[17] G. Gyarmathy, *Nucleation of steam in high-pressure nozzle experiments,* Proceedings of the Institution of Mechanical Engineers, Part A: Journal of Power and Energy **219**, 511 (2005).

[18] N. D. Baltadjiev, *An Investigation of Real Gas Effects in Supercritical CO2 Compressors,* Master's thesis, Massachusetts Institute of Technology (2012).

[19] J. Starzmann, M. M. Casey, J. F. Mayer, and F. Sieverding, *Wetness loss prediction for a low pressure steam turbine using computational fluid dynamics,* Proceedings of the Institution of Mechanical Engineers, Part A: Journal of Power and Energy **228**, 216 (2013).

[20] S. M. A. Noori Rahim Abadi, A. Ahmadpour, S. M. N. R. Abadi, and J. P. Meyer, *Cfd-based shape optimization of steam turbine blade cascade in transonic two phase flows,* Applied Thermal Engineering **112**, 1575 (2017).

[21] S. Jamali Keisari and M. Shams, *Shape optimization of nucleating wet-steam flow nozzle,* Applied Thermal Engineering **103**, 812 (2016).

[22] P. Hill, *Condensation of water vapour during supersonic expansion in nozzles,* Journal of Fluid Mechanics **25**, 593 (1966).

[23] S. Banach, *Sur les opérations dans les ensembles abstraits et leur application aux équations intégrales,* Fundamenta Mathematicae **3**, 133 (1922).

[24] M. Sagebaum, T. Albring, and N. R. Gauger, *High-Performance Derivative Computations using CoDiPack,* arXiv preprint arXiv:1709.07229 (2017).

[25] T. P. van der Stelt, N. R. Nannan, and P. Colonna, *The iPRSV equation of state,* Fluid Phase Equilib. **330**, 24 (2012).

[26] P. Colonna, T. V. der Stelt, and A. Guardone, *Fluidprop (version 3.0.6): A program for the estimation of thermo physical properties of fluids. a computer program since 2004,* (2018).

[27] M. Giordano, S. Hercus, and P. Cinnella, *Effects of modelling uncertainties in condensing wet-steam flows through supersonic nozzles,* V European Conference on Computational Fluid Dynamics ECCOMAS, Lisbon, Portugal (2010).

[28] N. B. Vargaftik, B. N. Volkov, and L. D. Voljak, *International tables of the surface tension of water,* Journal of Physical and Chemical Reference Data **12** (1983), AIP Publishing.

[29] M. Moore and C. Sieverding, *Two-phase steam flow in turbines and separators: theory, instrumentation, engineering,* Series in thermal and fluids engineering (Hemisphere Pub. Corp., 1976).

[30] J. Starzmann, M. V. Casey, and J. F. Mayer, *Water droplet flow paths and droplet deposition in low pressure steam turbines,* in *High Performance Computing in Science and Engineering '12* (Springer Berlin Heidelberg, 2012) pp. 351–365.

[31] D. Kraft, *A software package for sequential quadratic programming.,* Tech. Rep. (DLR German Aerospace Center — Institute for Flight Mechanics, Koln, Germany, 1998).

[32] S. Dykas, M. Majkut, M. Strozik, and K. Smołka, *Experimental study of condensing steam flow in nozzles and linear blade cascade,* International Journal of Heat and Mass Transfer **80**, 50 (2015).

[33] A. J. White, J. B. Young, and P. T. Walters, *Experimental validation of condensing flow theory for a stationary cascade of steam turbine blades,* Philosophical Transactions of the Royal Society A: Mathematical, Physical and Engineering Sciences **354**, 59 (1996).

5

6

CC-ENGINE CONCEPT FOR AIRCRAFT PROPULSION

In this chapter, one of the proposed solutions for next-generation heat recovery systems in paragraph 1.1.4 is presented in details. This preliminary study considers a combined cycle configuration for aeroengines, whereby thermal energy from the exhaust of the gas turbine is partly recovered in order to obtain additional mechanical power. The waste heat recovery system is based on a closed thermodynamic bottoming cycle with supercritical carbon dioxide (scCO$_2$) as working fluid, allowing to achieve a very high power density. As first step of the investigation a thermodynamic cycle analysis of the combined-cycle engine (CCE) is carried out. Results are compared to those of the intercooled-recuperative engine (IRE) configuration for the same operating conditions and calculated under the same modeling assumptions. The estimated nominal SFC of the proposed CCE configuration is approximately 20% lower compared to that of a conventional turbofan, and 6% lower than that of the IRE, if pressure drops in the heat exchangers are neglected.

Such large gain justified further analysis, by including the preliminary sizing of main components. Once the sizing of heat exchangers is factored in, the thermodynamic benefit of the CCE is offset by the penalty due to the weight of the additional equipment. This is mainly caused by i) the space constraints of the turbofan nacelle, which strongly limit the recoverable thermal power, and ii) the lack of proper heat exchanger technology for such a highly unconventional application.

These issues, and the many other that need consideration, will be addressed in an upcoming research project encompassing a much wider scope involving new aircraft and propulsion system configurations.

6.1. BACKGROUND AND MOTIVATION

Currently, technological improvements affecting aero-engine efficiency are mainly targeted to incremental increase of turbomachinery performance, engine turbine inlet temperature (TIT) rise, and larger overall pressure ratio (OPR). Long-range turbofan engines commercially available between year 1990 and 2010 featured a TIT increase from 1600 K to 1800 K, along with an almost doubling of the by-pass ratio (BPR) and an increment of the OPR from 35 to more than 50. These developments led to an overall engine efficiency of up to 37%, with an yearly average increment of approximately 0.5% [2]. However, it is debatable whether the current improvement in TIT (10K/year) can be sustained in the future [3]. Moreover, higher TIT values imply a rise in NO$_x$ emissions. Thus, the aerospace industry is exploring novel propulsion system configurations in order to reduce the environmental footprint of civil aviation.

Heat recovery from engine exhaust is a technical option that may enable significant reduction of specific fuel consumption (SFC) as well as emissions. In a modern aircraft turbofan, wasted thermal power accounts for 50-55% of the fuel energy input. A fraction of this waste energy can be exploited to preheat the combustion air or converted into usable power by means of a prime mover. The first option, the so-called recuperated aero-engine configuration has been investigated since the 1940's. As reported by Mc Donald et al. [4], these research efforts led in the 60's to the realization of the first prototypes for military applications, i.e. the Lycoming T53 turboshaft and the Allison T78 turboprop; the thermal power extracted from exhaust amounted to 820 kW$_{th}$ and 3080 kW$_{th}$, respectively. The research following such early studies focused on the devel-

opment of the intercooled-recuperated engine (IRE) concept. The most recent research results about the IRE show that a SFC reduction of 2% is arguably achievable by redesigning the engine and using compact heat exchangers (HEXs) [5, 6].

Engine waste heat recovery (WHR) has been considered only recently. The study described in Ref. [7] is related to a Combined Cycle Engine (CCE) consisting of a turbofan equipped with a bottoming organic Rankine cycle (ORC) unit supplying additional mechanical power to the high-pressure compressor of the engine and electrical power to the aircraft avionics. The total power output of the WHR system is around 200 kW. The predicted SFC reduction with respect to the SFC of the base case is approximately 2.3%, if pressure drops in the heat exchangers of the ORC unit and the impact of the additional system weight on the required thrust are neglected.

The study documented here examined the viability of a different CCE configuration, whereby the energy content of the gas turbine exhaust is recovered by means of a system based on the supercritical carbon dioxide (scCO$_2$) power cycle concept, see, e.g. [8, 9]. The main advantages of this concept, initially conceived for terrestrial applications, are the very high power density, the thermal stability of the working fluid, and, consequently, the high conversion efficiency that can be achieved.

In order to explore the potential of the proposed solution, first a thermodynamic analysis of the CCE has been performed, and the results compared with a similar analysis carried out on an IRE operating at the same conditions, and for which validated data are available in the literature. Subsequently, the effect of actual equipment on the performance of the engine has been assessed by assuming that the WHR unit is added to a common modern turbofan engine, the GE90-94B. The primary heat exchanger of the scCO$_2$ power system is inserted after the low-pressure turbine, in the core nozzle, while the cooler is placed in the fan duct. Even though such configuration is not representative of the future aircraft for which the CCE is conceived, and related design restrictions heavily penalize the achievable performance, the availability of actual data related to the main engine allowed for a WHR unit preliminary design based on verifiable assumptions. The results of this analysis provide therefore a lower boundary for the achievable performance, and can be used as a starting point for further investigation.

6.1.1. THERMODYNAMIC CYCLE CONFIGURATION AND SIMPLIFIED PERFORMANCE ANALYSIS

In a scCO$_2$ closed Brayton cycle the compression process occurs with the fluid at thermodynamic states close to the vapor-liquid critical point, thus greatly reducing the fraction of turbine work needed to power the compressor, if compared to a conventional gas turbine cycle. Various configurations are currently studied [10] and implemented in the first prototypes and pre-commercial units for terrestrial applications [11].

The simplest regenerated cycle configuration has been selected for this exploratory study, see Figure 6.1. With reference to thermodynamic state points in Figure 6.1a, CO$_2$ is heated by the turbofan exhaust gas from state 2a$_{WHR}$ to state 3$_{WHR}$, and then it expands in the turbine from state 3$_{WHR}$ to 4$_{WHR}$. Subsequently, the working fluid is cooled in the regenerator down to the temperature of state 4a$_{WHR}$ in order to preheat the CO$_2$ from the outlet of the compressor (state 2$_{WHR}$) up to the temperature of state 2a$_{WHR}$. Finally, the working fluid at the cold outlet of the regenerator is further cooled down to the cycle

(a) Simplified process flow diagram

(b) Thermodynamic cycles in the $T - s$ diagram of CO_2.
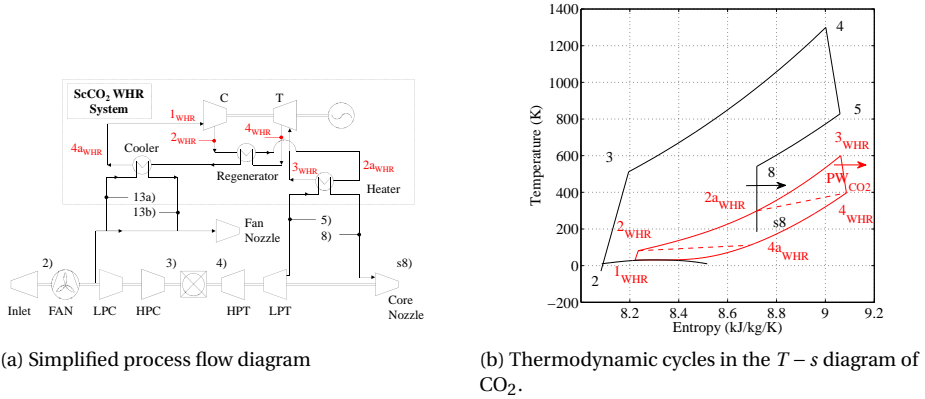
Figure 6.1: Combined-cycle aero engine adopting a $scCO_2$ cycle unit for heat recovery from the gas turbine exhaust. The values of specific entropy of the state points related to the gas turbine engine cycle have been scaled appropriately in order to correctly correspond to the pertinent $scCO_2$ cycle state points, thus neglecting that they refer to different working fluids.

6

minimum temperature (state 1_{WHR}), and compressed from close-to-critical conditions up to the maximum cycle pressure of state 2_{WHR}.

In order to assess the potential of the CCE concept at coarse level, first the thermodynamic performance of a CCE is compared to that of an IRE under the following assumptions:

- the engine operates in stationary cruise conditions (design point), for a given gas turbine engine TIT, BPR, and fan pressure ratio (FPR);

- the effect of weight and size of the equipment on the specific fuel consumption is neglected;

- the performance fo the heat exchangers is determined through the NTU, defined as

$$\text{NTU} = \frac{U_{\text{hex}} A_{\text{hex}}}{C_{\min}},\tag{6.1}$$

where U_{hex} is the global heat transfer coefficient, A_{hex} the heat transfer area, and $C_{\min}$ the value of the minimum heat capacity among those of the two flows;

- pressure losses ΔP are calculated as percentage on the inlet total pressure in the HEX;

- the design parameters of the CCE and IRE engines are those listed in Tables 6.1, 6.2, and 6.3. components efficiencies for the gas turbines are selected so as to be representative of current technology. Performance values related to the $scCO_2$ WHR unit follow the recommendations in Ref. [8];

Air mass flow rate (kg/s)	500
TIT(K)	1,500
BPR (-)	9.0
FPR (-)	1.4
Cruise Altitude (m)	10,000
Cruise Mach number (-)	0.8
Fan efficiency (%)	90
Compressor efficiency (%)	89
Turbine efficiency (%)	91

Table 6.1: Model specifications for the gas turbines

$NTU_{heater/recuperator}$	1 - 4
$NTU_{cooler/intercooler}$	$= NTU_{heater/recuperator}$
$(\Delta P / P_{inlet})_{HEX}$	0 - 0.1
OPR	5 - 115
$\dot{m}_{coolant}$	$= \dot{m}_{air,core}$

Table 6.2: Model specifications for the IRE and the CCE

- - the mechanical power obtained from the $scCO_2$ WHR unit is converted into thrust with an assumed efficiency of 90%;

- - the value of the intercooler pressure for the IRE configuration is taken equal to the square root of the OPR value times the inlet engine pressure, so as to approximate the optimal value.

The steady state modeling of the gas turbines is performed with a well-known object-oriented simulation environment for 0D modeling of gas turbines [12]. On the other hand, the modeling of the $scCO_2$ WHR unit is carried out in a widely adopted technical computing environment [13]. The model of the $scCO_2$ system has been validated by comparison with data reported in Ref. [9] for several $scCO_2$ cycle configurations. In order to evaluate the influence of the heat exchangers performance on the efficiency of the CCE, simulations are carried out by varying i) the NTU value in the range from 2 to 4, and, ii) the pressure losses in the range 0% and 6%. Additionally, the overall pressure ratio of the gas turbine is varied from OPR = 5 to OPR = 115. Such a wide range is adopted because the optimal OPR value is not known a priori, as opposed to the case of the IRE, which has already been investigated extensively in the literature [3, 14]. In order to account for the bleed air required for turbine blade cooling, a correlation calibrated on the data reported in Ref. [15] has been adopted.

Given the specifications listed in Tables 6.1-6.3, the main design variables of the $scCO_2$ WHR system are the minimum and the maximum cycle pressures (P_{min}, P_{max}),

$\Delta T_{\text{pinch,regenerator}}$ (K)	15
$(\Delta P/P_{in})_{\text{regenerator}}$ (%)	2
T_{min} (K)	283
P_{max} (MPa)	10 - 40
P_{min} (MPa)	7.4
Compressor efficiency (%)	85
Turbine efficiency (%)	90
$\eta_{\text{prop,CO}_2}$ (%)	90

Table 6.3: Model specifications for the scCO$_2$ WHR unit
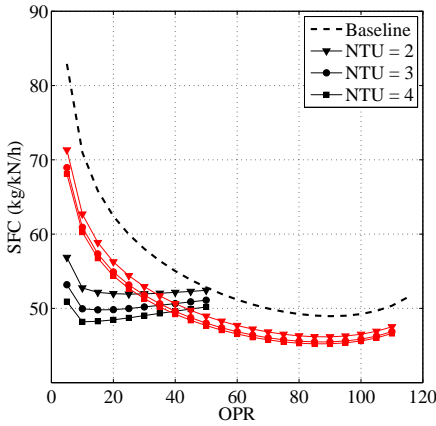
Figure 6.2: Calculated SFC for the IRE (black), the CCE (red) and baseline case (dotted line). $\Delta P = 0$ for the heat exchangers.
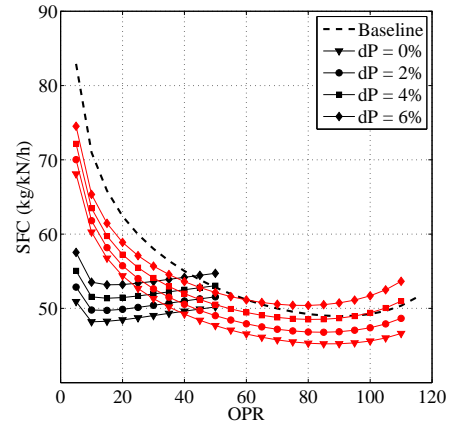
Figure 6.3: Calculated SFC for the IRE (black), the CCE (red) and the baseline case (dotted line). NTU = 4 for the heat exchangers.

and the minimum temperature (T_{min}) reached by the working fluid in the cooler. P_{min} is set to 7.4 MPa, a value just above the critical pressure of CO$_2$, namely 7.36 MPa, while T_{min} is arbitrarily assumed equal to 283 K. An upper limit for the maximum cycle pressure P_{max} of 40MPa is set, in line with the state-of-the-art technology of modern steam power plants. The cooler of the scCO$_2$ unit as well as the intercooler of the IRE use as coolant a portion of the air mass flow rate discharged by the engine fan ($\dot{m}_{\text{coolant}}$). Notably, in this analysis the amount of cooling air is arbitrarily taken equal to the air mass flow rate of the engine core for both the IRE and the CCE configurations.

RESULTS

The optimal scCO$_2$ cycle is that featuring the maximum thermal efficiency, which is achieved for the maximum allowable pressure $P_{\text{max}} = 40$ MPa. Figure 6.2 shows the SFC as a function of the OPR and the NTU for the CCE, the IRE and a simple-cycle engine (indicated as baseline case in the figure). The pressure drop over the heat exchangers is

here neglected. The value of SFC estimated for the CCE is markedly lower that that of the simple-cycle engine over the entire OPR range, and the minimum SFC value is lower than the minimum SFC value calculated for the IRE. The best performance is computed for a pressure ratio of approximately 80 for both the CCE and the baseline case, while in case of the IRE the optimal value is obtained at much lower OPR. The SFC-OPR lines related to the CCE and the baseline case display the same trend, which suggests that the considered engine configuration can be attractive also considering the likely evolution of gas turbine technology.

Figure 6.3 shows the effect of pressure losses on the CCE performance. As expected, the calculated performance of the CCE reduces considerably. Additionally, the estimated SFC becomes larger with increasingly higher pressure drop in the engine core nozzle and in the fan duct. As opposed to the IRE, such trend is more pronounced at high OPR values, shifting the optimum OPR towards lower values. The thermodynamic advantage of recovering thermal energy from the gas turbine vanishes for OPR = 60 and $\Delta P/P_{\text{HEX,inlet}} = 6\%$ (relative heat exchanger pressure drop).

Heat Exchangers. It can be observed that the estimated performance of the CCE is much less sensitive to the NTU value of the heat exchangers than that of the IRE. The SFC of the CCE decreases by a few percentage points for NTU values decreasing from 4 to 2, while the SFC estimated for the IRE rapidly deteriorates for the same variation of the NTU values, especially for low OPR values. Although no general conclusion can be drawn, unless all components are reliably sized, these computations suggest that the CCE arguably requires smaller heat exchangers in comparison to the IRE, allowing for lower pressure drops and weight. The charts of Figure 6.4 and 6.5, reporting the calculated thermal power transferred in the cooler and heater as a function of the OPR for both the CCE and the IRE. Note that the thermal power exchanged by the cooler of the CCE does not vary with the OPR as it is only a function of $\dot{m}_{\text{coolant}}$ and of the assumed NTU value. The thermal duty of the IRE heat exchangers is in general larger that that of the corresponding heat exchangers of the CCE. This is due to the scCO$_2$ cycle internal regeneration, which reduces the thermal load of the cooler and the heater, increasing at the same time the cycle efficiency, see Figure 6.6. Nonetheless, the estimated total thermal duty of the three heat exchangers of the CCE is lower than total thermal duty computed for the heat exchangers of the IRE for any given OPR value.

Cooling air mass flow rate. The mass flow rate of cooling air $\dot{m}_{\text{coolant}}$ strongly influences the performance of the WHR unit as it affects the CO$_2$ mass flow rate, thus, the maximum amount of thermal energy that can be recovered. For instance, Figure 6.7 displays the calculated SFC of the CCE for $\dot{m}_{\text{coolant}} = 2\dot{m}_{\text{core}}$, and no pressure drop in the heat exchangers. It must be remarked that the values in Figure 6.2 are calculated without taking into account the decrease of fan thrust caused by the larger friction losses in the fan duct, which are proportional to the mass flow rate of cooling air diverted to the cooler. However, the increase of $\dot{m}_{\text{coolant}}$ determines a significant improvement in the estimated efficiency of the CCE. For a gas turbine engine with OPR equal to 80, the estimated SFC is almost 7% lower than the minimum SFC value reported in Figure 6.2.
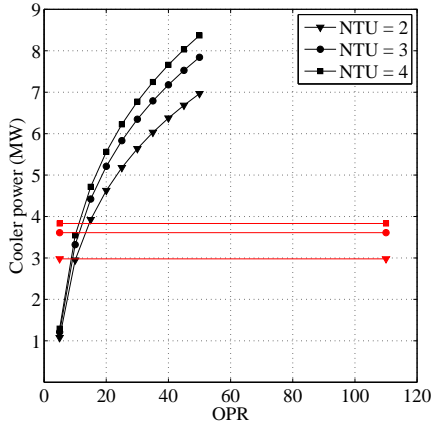
Figure 6.4: Calculated thermal power exchanged in the cooler of the IRE (black) and of the CCE (red). $\Delta P = 0$ over both sides of the heat exchanger.
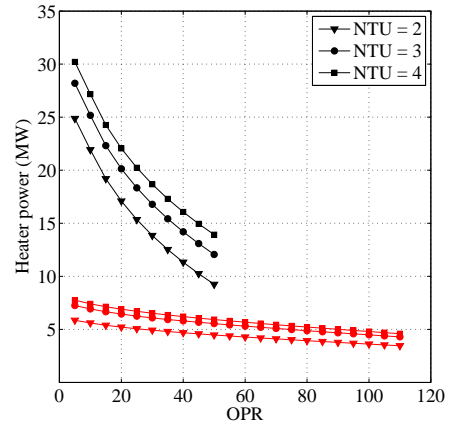
Figure 6.5: Calculated thermal power exchanged in the heater of the IRE (black) and of the CCE (red). $\Delta P = 0$ over both sides of the heat exchanger.
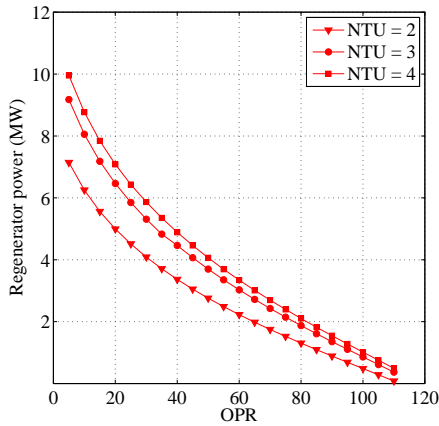
Figure 6.6: Calculated thermal power exchanged in the regenerator of the $scCO_2$ WHR unit. $\Delta P = 0$ over both sides of the heat exchanger.
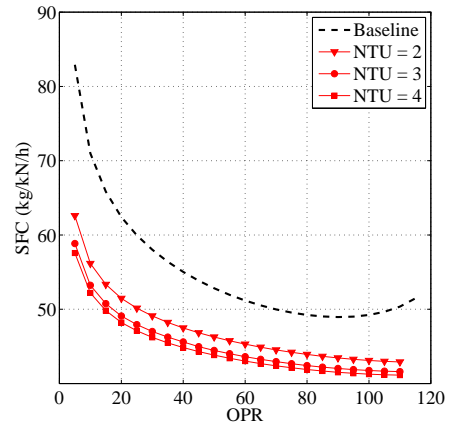
Figure 6.7: Estimated SFC for the CCE (red) and the baseline case (dotted line) assuming $\dot{m}_{coolant} = 2\dot{m}_{core}$. $\Delta P = 0$ over both sides of the heat exchanger.

6.1.2. THE $scCO_2$ POWER SYSTEM AS WASTE HEAT RECOVERY ADD-ON UNIT FOR THE GE90-94B TURBOFAN ENGINE

As a first learning step, the preliminary design of the $scCO_2$ unit is carried out considering such system as simple add-on to an existent turbofan engine, i.e., the GE90-94B engine. The adoption of an existing turbofan configuration allows for the preliminary sizing and design of the heat exchangers based on established data. Note that this infor-

mation is not representative of the level of gas turbine technology suiting this possible development, which targets the mid-term future.

As shown in Figure 6.8, the heater of the scCO$_2$ WHR system is assumed to be located in the engine core nozzle. The cooler is positioned in the fan duct where part of the air flow at the fan outlet is diverted toward it in a separate channel. With reference to Figure 6.9, the cooling air first flows through a diffuser in order to reduce the flow velocity, thus the pressure drops in the cooler. Downstream of the cooler, air is irreversibly mixed with the main air stream from the fan, before being discharged into the atmosphere through the fan nozzle. As far the regenerator of the scCO$_2$ unit is concerned, it is assumed that this component can be located in the aircraft fuselage.

6.1.3. SYSTEM MODELING AND DESIGN

The analysis is carried out at cruise in design conditions. The procedure consists of six main steps:

1. the thermodynamic state points of the turbofan gas turbine cycle are calculated. At this stage, the pressure drop over the fan duct and heat transfer through bounding surfaces are neglected;

2. the specific thermodynamic properties of CO$_2$ at the state points of the cycle are estimated by means of the traditional mass and energy balances;

3. the preliminary design of the cooler is carried out, together with the estimation of the CO$_2$ mass flow rate and the cooling air, by solving a non-linear system of equations;

4. the heater is sized according to a preliminary design procedure similar to that adopted for the cooler;

5. the overall thrust of the CCE is then evaluated, taking into account the reduction in the turbofan thrust due to the cooling of the gas turbine exhaust and the pressure drop in the heat exchangers. A simulation of the turbofan engine is run, this time with values of these penalties as additional inputs. Also in this case, it is assumed that the power output of the scCO$_2$ WHR unit can be converted into thrust with 90 % efficiency;

6. the preliminary design of the regenerator is carried out and the total weight of the scCO$_2$ cycle components is estimated.

In this simplified design method, the impact of the weight of the WHR unit on fuel consumption due to the required additional thrust is neglected. This effect is qualitatively assessed a posteriori, by assuming, to a first approximation, that the percentage increase of SFC is equal to one tenth of that of the engine weight, as suggested in Ref. [16]. Moreover, the procedure does not include the preliminary sizing of the scCO$_2$ turbocompressor since its weight is expected to be a small fraction of the total weight.

The next paragraphs report a brief description of the CCE components, in the order in which the design calculations are performed.
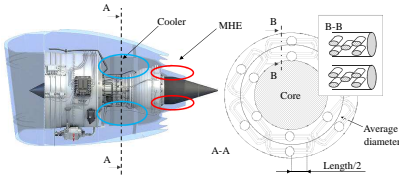
Figure 6.8: Schematic of the modified GE90-94B tur-bofan engine showing the positioning of the cooler and the heater of the scCO$_2$ waste heat recovery unit and a simplified section and detail of the cooler.
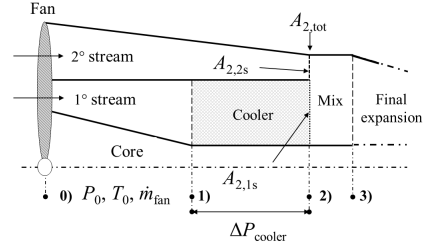
Figure 6.9: Schematic diagram of the layout of the fan duct.

Dry weight (kg)	7,550
Cruise Thrust (kN)	70.6
TIT (K)	1,446
Inlet mass flow rate (kg/s)	532.6
By pass ratio (-)	9.0
OPR (-)	41.7
SFC (kg/kNh)	56.3
Cruise Altitude (m)	10,670
Cruise velocity (m/s)	237.2
Auxiliary power (kW)	300

Table 6.4: Main characteristics and performance of the GE90-94B turbofan at cruise conditions.

Turbofan. The model of the GE90-94B turbofan engine implemented in the in-house gas turbine simulation program has been calibrated by comparison with data available in the open literature for the cruise and take-off operating conditions. The main characteristics of the engine predicted at cruise condition by the model are listed in Table 6.4.

scCO$_2$ unit. The thermodynamic efficiency and the parameters of the scCO$_2$ cycle are estimated by using the in-house code. No cycle parameters optimization is needed, as, according results presented in Sec. 6.1.1, the maximum amount of energy is recovered by the cycle featuring the highest pressure. The design constraints for the scCO$_2$ system components are set as following: i) $\Delta T_{\text{pinch,reg.}} = 15\ ^oC$, ii) $\Delta T_{\text{approach,heater}} = 20\ ^oC$, iii) $P_{\min} = 7.4$MPa, iv) $P_{\max} = 40$MPa, v) $T_{\min} = 283$ K.

Cooler. The geometry chosen for the cooler is similar to the one proposed in Ref. [6]. The HEX consists of six different modules placed in parallel as shown in Figure 6.8. Each module is formed by multiple U-shaped tubes arranged in a staggered configuration and brazed at their ends into two manifolds. In order to minimize the pressure loss on the air side of the heat exchanger, the tubes are assumed to have an elliptical profile, whose

main axis (D_{max}) is aligned with the air flow direction. For the case at hand, D_{max} is equal to 9 mm, while the minor axis of the profile (D_{min}) measures 4.5 mm. The aspect ratio (Ar) of the tube cross-section is thus equal to 2. The adoption of a more flattened shape is not a viable solution for the considered application, although this would allow for a reduction of the pressure drop over the cooling air side. A higher value of Ar would lead to an unrealistically large thickness of the tubes (s_{thick}), due to the relatively high pressure of CO_2 and to the mechanical stress amplification occurring in the two pipe corners, where profile curvature is minimum. Application of the Von Mises criterion at the two ends of the major axis of the ellipse results in a tube thickness that is proportional, to a first approximation, to Ar^2, being

$$s_{thick} = max \left(\frac{P_{CO_2} \cdot D_{max}}{2\sigma_{yield}} \sqrt{3 + Ar^4 - 3Ar^2}, 0.3\text{mm} \right) \quad (6.2)$$

where σ_{yield} is the allowable yield stress of the material. The alloy proposed in Ref. [6], i.e., the Ti-6Al-4V alloy, is taken as reference material for the preliminary sizing of the component.

The design specifications for the heat exchangers are the pressure drop in the cooling air flow ($\Delta P_{air,cooler}$) and the space limitations within the engine nacelle. At this stage of the research, the most suitable design variable is arguably $\Delta P_{air,cooler}$, since a reasonable estimate for its value can be specified, based on the state-of-art design of the intercooler for IRE systems[6]. Accordingly, $\Delta P_{air,cooler}$ has been set to 6% of the total pressure at inlet. The maximum frontal area of the cooler depends, to a first approximation, on the value of $A_{2,tot}$, see Figure 6.9. The unknowns of the preliminary design problem are the mass flow rate of the cooling air $\dot{m}_{coolant}$ and of the working fluid $\dot{m}_{CO_2}$, as well as the cooler heat transfer rate $\dot{Q}_{cooler}$. These values can be determined by solving iteratively a non-linear system of equations, which involves the conservation equations of mass and energy for the fan duct, and simplified relations for the prediction of the thermo-hydraulic characteristics of the heat exchanger. More in detail, the ad-hoc numerical procedure developed to perform the preliminary design of the cooler includes the following main steps:

1. an initial guess for $\dot{m}_{coolant}$ is provided. Since the fan operating conditions are inputs of the problem, this permits to estimate the mass flow rate of the air circulating in the main fan duct $\dot{m}_{duct}$;

2. the thermodynamic properties and velocity of the air stream at station 2,2s in Figure 6.9 are estimated by assuming that the fluid undergoes an isentropic expansion process. The cooler outlet pressure is therefore $P_0 - \Delta P_{air,cooler}$. The area required to accommodate this flow ($A_{2,2s}$) is calculated as $A_{2,2s} = \dot{m}_{duct}/(\bar{\rho}_{2,2s} \cdot v_{2,2s})$;

3. the frontal area of the cooler ($A_{2,1s}$) is evaluated by subtracting $A_{2,2s}$ from the original size of the by-pass duct, i.e., $A_{2,tot}$. Hence, it is possible to determine the number of tubes along the heat exchanger height and their average length, given D_{min} of the adopted elliptical profile and the pitch among the tubes, here assumed equal to 15.4mm, as in [17];

4. The sizing of the cooler is then completed by solving the implicit and non-linear equation system

$$\dot{Q} = F \cdot U \cdot A(N_{\text{tube rows}}) \cdot \Delta T_{lm} \tag{6.3a}$$

$$\dot{Q} = \dot{m}_{\text{coolant}} \cdot \Delta h_{\text{coolant}}(T_{\text{out,coolant}}) \tag{6.3b}$$

$$\dot{Q} = \dot{m}_{CO_2} \cdot \Delta h_{CO_2} \tag{6.3c}$$

$$\Delta P_{\text{air,cooler}} = \frac{1}{2} \cdot f \cdot N_{\text{tube rows}} \cdot \bar{\rho} \cdot \bar{v}^2_{\text{coolant}} \tag{6.3d}$$

for unknowns $\dot{Q}, T_{\text{out,coolant}}, N_{\text{tube rows}}, \dot{m}_{CO_2}$. F is the correction factor of the logarithmic mean temperature difference (ΔT_{lm}) to account for the departure of the actual cooler geometry from that of a counter-current heat exchanger. The value of F is estimated through a numerical correlation calibrated for cross-flow heat exchanger with one fluid unmixed. U and the pressure drops are determined on the basis of the average thermodynamic properties of the streams in the cooler and of empirical relations involving the typical dimensionless groups of heat transfer problems, namely the Reynolds, the Prandtl and the Nusselt number. The correlations reported in Ref. [18] are used to predict the heat transfer coefficient and the friction factor (f) in the CO_2 stream, whereas those documented in Ref. [17] are employed to estimate the same quantities for the cooling air;

5. given the thermodynamic conditions at the cooler outlet and $A_{2,1s}$, a new value of $\dot{m}_{\text{coolant}}$ is computed. If this differs form the previous estimate, the calculations of steps 1-5 are repeated until the average change of $\dot{m}_{\text{coolant}}$ is lower than the specified tolerance.

Heater The heater consists of several heat exchangers modules, similar to those adopted for the cooler. For this component, the main design specification is the heat transfer rate, while the temperature and mass flow rate of the inlet streams are inputs. Thus, the preliminary design problem can be reduced to the non-linear system formed by equation (6.3b)-(6.3d). The pressure loss in the exhausts is subsequently estimated with a relation equivalent to (6.3d). Similarly, the correlations for the prediction of the heat transfer coefficients of the cold and hot stream are the same adopted for the preliminary design of the cooler. Due to the higher operating temperature of the heater with respect to the cooler, a lower value of the material yield stress is assumed. As documented in Ref. [6], σ_{yield} is taken equal to 280 MPa.

Regenerator. The regenerator selected for this application is a printed circuit heat exchanger, because it is extremely compact and capable of sustaining high pressure, and because information about its use in terrestrial applications is available. The main geometrical characteristics of the regenerator are reported in Figure 6.10. The plate length (L) is determined by matching the specified heat transfer duty. The heat transfer coefficient is estimated according to the relations reported in Ref. [19], while the plate thickness is evaluated as

$$s = \max((P_{\max} - P_{\min}) \cdot \frac{D}{\sigma_{\text{yield}}}; 0.5 \text{ mm}), \tag{6.4}$$
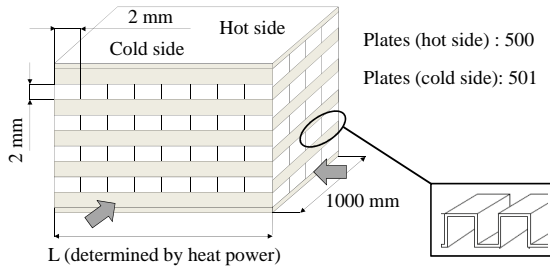
Figure 6.10: Configuration of the printed circuit regenerator of the scCO$_2$ waste heat recovery unit.

The allowable yield stress (σ_{yield}) of the material is taken equal to 300 MPa. No space constraints are considered for the regenerator. It is arbitrarily assumed that it can be properly accommodated in the aircraft fuselage.

RESULTS

The SFC resulting from the simplified simulation of the CCE is 54.7 kg/kN/h, while the total thrust is 72.2 kN, of which 2.8 kN are provided by the WHR unit. The reduction of SFC with respect to the SFC of the GE90-94B is about 2.8%, thus nearly one of order of magnitude lower than the value predicted by the sole thermodynamic cycle analysis. In addition, the model does not take into account the additional fuel consumption due to the weight of scCO$_2$ WHR unit, which is about 3 tons. On the basis of the simplified relation proposed in Ref. [16] the weight of the WHR unit would cause an SFC increase of 4 %, which would disqualify further development of the configuration whereby the WHR unit is an add-on to a conventional turbofan for a conventional aircraft. However, the analysis of the results and of the assumptions provide further insights that suggest further investigation.

According to the simulation results reporter in Table 6.5, the cooler is the most critical component of the system. The relatively low ΔT_{lm} and the poor heat transfer coefficient of the cooling air side determine large values of the required heat transfer surface. Consequently, the tube bundle of each cooler module features a large number of tubes in parallel. This leads to low CO$_2$ velocity inside the tubes, which also negatively affects the global heat transfer coefficient. Despite the large heat transfer area and weight, the thermal duty of the cooler is only 1.6 MW, which poorly compares with the values reported in Figure 6.4. The low duty of the cooler limits the CO$_2$ mass flow rate circulating in the WHR unit, and consequently the thermal power that can be recovered from the gas turbine exhaust.

The calculated duty of the heater is 2.6 MW (see Table 6.5), which is less than half of the value of 7 MW that can be deduced from Figure 6.5. The heat duty of the heater is almost twice the one of the cooler, while its weight is less than half of that of the cooler. The main reason for the better predicted performance of the heater compared to that of the cooler is the higher heat transfer coefficient in both the cold and the hot side. In particular, the heat transfer coefficient of the CO$_2$ side is very high, being more than 2400 W/m^2/K. Additionally, the temperature difference between the hot and cold side of the

heater is much higher compared to that of the cooler. Similar considerations are valid for the regenerator. Its large weight if compared to that of the heater, albeit a 20% lower heat transfer rate, is mainly due to i) the smaller ΔT_{lm}, namely 41 K in lieu of 68 K in the heater, and ii) the lower capability of printed circuit HEXs in handling high pressure if compared to tubular heat exchangers.

	Cooler	Regenerator	Heater
$\dot{m}_{hot}$ (kg/s)	7.0	7.0	54.8
$\dot{m}_{cold}$ (kg/s)	87.1	7.0	7.0
$T_{hot, inlet}$ (K)	324.3	574.0	778.4
$T_{hot, outlet}$ (K)	283.0	324.3	734.9
$T_{cold, inlet}$ (K)	267.4	309.3	481.8
$T_{cold, outlet}$ (K)	284.1	481.8	758.4
h_{hot} (W/m^2/K)	131	677	318
h_{cold} (W/m^2/K)	148	343	2415
ΔP_{hot} (%)	<1	2.2	2.1
ΔP_{cold} (%)	6	< 1	1.4
# of tubes/channels	37,067	29,175 (hot side)	6,506
Thermal duty (kW)	1,598	2,119	2,620
Weight (kg)	1,608	920	692

Table 6.5: Estimated operating conditions and main characteristics of the three heat exchangers of the scCO$_2$ WHR unit for the GE90-94B turbofan.

A more detailed investigation of the cooler configuration, e.g. its positioning on-board of the aircraft, and geometry, e.g. the shape of tube profile or the number of passes of the CO$_2$ stream, is needed to assess the actual potential of the CCE. Furthermore, future analysis must reconsider also the design variables of the scCO$_2$ cycle, here kept as constant as very preliminary estimation. To make an example, the minimum temperature T_{min} has a great impact on the HEX size, and it can be optimized to reduce the required heat transfer surface.

6.1.4. CONCLUSIONS
The results of the investigation reported here suggest the following conclusions:

1. the thermodynamic quality of the combined cycle configuration is higher than that of the intercooled recuperated configuration;

2. the optimal thermodynamic performance of the combined cycle engine is expected to occur at OPR values higher than that of current turbofan engines. This result suggests that heat recovery by means of a scCO$_2$ bottoming unit might be attractive also for next-generation aero gas turbines;

3. simplified calculations aimed at designing a scCO$_2$ waste heat recovery unit as an add-on for GE90-94B turbofan show that the estimated SFC reduction of 2.8% is insufficient, if the additional weight of the unit, about 3 tons per aircraft engine,

is factored in. This is however caused by i) the strong limitations of the add-on configuration due to the limited space available within a conventional nacelle, ii) the adverse effects of locating the cooler in the fan duct and, iii) the lack of proper heat exchanger technology for this highly unconventional application;

4. the cooler is the most critical component of the $scCO_2$ system in terms of volume and weight. As a first attempt, the heat exchanger geometry developed for the intercooler of the intercooled recuperated aero engines has been considered. However, such configuration turns out to be largely sub optimal.

In order to assess the potential of the combined cycle aero engine, future research will investigate with more detailed simulations i) alternative configurations to better exploit the thermal energy at the gas turbine outlet, ii) different configurations of the heat recovery unit and, iii) innovative heat exchangers.

REFERENCES

[1] C. D. Servi, L. Azzini, M. Pini, A. G. Rao, and P. Colonna, *Exploratory assessment of a combined-cycle engine concept for aircraft propulsion*, (2017), global Propulsion and Power Forum, Zurich, Switzerland.

[2] German Aerospace Center, *Analysis of the European Air Transport Market*, Annual Report (European Commission, Bruxelles, 2008).

[3] K. G. Kyprianidis, *Future aero engine designs: an evolving vision*, in *Advances in Gas Turbine Technology*, edited by E. Benini (Intech, 2011) Chap. 1, pp. 1–23.

[4] C. McDonald and C. Rodgers, *Heat exchanged propulsion gas turbines: a candidate for future lower sfc and reduced emission military and civil aeroengines*, in *Proceedings of ASME Turbo Expo*, GT2009-59156 (2009) pp. 33–49.

[5] ARTTIC, with contribution of all partners, *NEWAC - New Aero Engine Core Concepts*, Technical Report NEWAC-ART-DEL-FAR-R1.0 (ARTTIC, 2011) publishable final activity report.

[6] H. Gonser, *Untersuchungen zum Einsatz von Wärmetauschern in zivilen turboflugtriebwerken*, Ph.D. thesis, Institut für Luftfahrtantriebe der universität Stuttgard, Stuttgard (2008).

[7] C. Perullo, D. Mavris, and E. Fonseca, *An integrated assessment of an organic Rankine cycle concept for use in onboard aircraft power generation*, in *Proceedings of ASME Turbo Expo 2013*, Vol. 2, IGTI (ASME, San Antonio, TX, 2013) pp. V002T01A028–8.

[8] G. Angelino, *Carbon dioxide condensation cycles for power production*, J. Eng. Power **90**, 287 (1968).

[9] C. M. Invernizzi, *Closed power cycles. Thermodynamic Fundamentals and Applications*, Lecture Notes in Energy, Vol. 11 (Springer-Verlag London, 2013).

6

[10] V. Dostal, P. Hejzlar, and M. Driscoll, *High-performance supercritical carbon dioxide cycle for next-generation nuclear reactors,* Nucl. Technol. **154**, 265 (2006).

[11] M. Persichilli, T. Held, S. Hostler, E. Zdankiewicz, and D. Klapp, *Transforming waste heat to power through development of a CO_2-based power cycle,* in *Proceedings of Electric Power Expo* (2011) pp. 1–8.

[12] W. P. J. Visser and M. J. Broomhead, *GSP, a generic object-oriented gas turbine simulation environment,* in *Proceedings of ASME Turbo Expo*, Vol. 1, IGTI (ASME, Munich, 2000) pp. V001T01A002–8.

[13] MathWorks, *Matlab, release 2013b,* Software (2013).

[14] M. P. Boyce, *Gas turbine engineering handbook*, 4th ed. (Elsevier, 2012).

[15] J. Kurzke, *Aero-engine design: A state of the art - preliminary design,* in *Von Karman Institute Lecture Series* (Von Karman Institute, 2003).

[16] N. Cumpsty, *Jet propulsion: A simple guide to the aerodynamic and thermodynamic design and performance of jet engines,* (Cambridge University Press, Cambridge, 2015) Chap. 7, p. 94, 3rd ed.

[17] T. A. Ibrahim and A. Gomaa, *Thermal performance criteria of elliptic tube bundle in crossflow,* Int. J. Therm. Sci. **48**, 2148 (2009).

[18] A. Sogni and P. Chiesa, *Calculation code for helically coiled heat recovery boilers,* Energy Procedia **45**, 492 (2014).

[19] L. Pierobon, A. Benato, E. Scolari, F. Haglind, and A. Stoppato, *Waste heat recovery technologies for offshore platforms,* Appl. Energy **136**, 228 (2014).

6

7

CONCLUSIONS AND RECOMMENDATIONS

"Omni fine initium novum"

(trad. "Every new beginning comes from some other beginning's end.")

In this thesis, the metastable condensation of organic fluids in high-speed expansions was investigated, with the aim of developing models specifically conceived for component design and optimization. In particular, three main research questions were formulated in Chapter 1, i.e.,

1. *What are the main parameters that influence the Wilson temperature T_w in high-speed expansions? Is it possible to quantify such dependence?*

2. *Based on scaling analysis, how much does the prediction of the onset of metastable condensation for generic fluids differs with respect ot steam?*

3. *What is the computational cost and memory requirement to perform adjoint-based optimization of devices operating with two-phase condensing flow? What is the performance improvement achievable with this methods?*

In order to summarize the findings of this research, the answers to these questions are here briefly reported.

- *What are the main parameters that influence the Wilson temperature T_w in high-speed expansions? Is it possible to quantify such dependence?*

The dimensionless subcooling Wi can be calculated as a function of i) the activation time t_{act} and ii) the temperature $T_{sat,r}$, through the relation

$$T_w \overset{\text{def}}{=} T_{sat}(s_0) - T_{cr}Wi, \qquad Wi = k_1 \overline{Cr}^{\,k_{cr}}, \qquad k_{cr} = 1 - k_2, \tag{7.1}$$

see Chapter 4. The semi-empirical coefficients k_1, k_2 are introduced to represent the dependence of Wi from i) the molecular mass of the working fluid, ii) the operating conditions, thus, $T_{sat}(s_0)$ and, iii) the cooling rate of the expansion.

- *Based on scaling analysis, how much does the prediction of the onset of metastable condensation for generic fluids differs with respect ot steam?*

The proposed semi-analytical model, or Wi model, can be applied to any compressible fluid, under the following limitations:

1. expansion cooling rate and saturation temperature inside the range of the experimental data analysed (see Chapter 4);

2. non-retrograde fluid, i.e.,

$$\left(\frac{\partial T}{\partial s}\right)_{sat,y=0} < 0; \tag{7.2}$$

3. molecular mass, in the range 18u - 86 g/mol;

4. simple tetrahedral structure with limited number of stable bounding configurations.

The Wilson number Wi appears to be a function of the molecular mass of the fluid, see Figure 4.22. It is arguably possible to derive simplified models for i) the prediction of the Wilson point and ii) the thermodynamic losses associated with condensation along the expansion, providing that sufficient data are available for the determination of k_1, k_2.

- *What is the computational cost and memory requirement to perform adjoint-based optimization of devices operating with two-phase condensing flow? What is the performance improvement achievable with this methods?*

By resorting to the discrete adjoint method, it is possible to perform adjoint-based optimization. The optimization routines applied to RANS, two-phase cases take up to two times the computational time required for single-phase test cases featuring the same total thermodynamic conditions. Additionally, the RAM allocated is around 30% higher.

Considerable reductions of i) liquid fraction in the flow and ii) thermodynamic losses can be achieved, i.e., up to approximately 24% and 44% for the cascades considered.

The following recommendation are drawn for future studies:

1. a systematic analysis, i.e. with tests at same total inlet conditions and different cooling rates, is needed to highlight the single dependencies of T_w from the rate of the expansion and the nozzle geometry. Similarly to what done in Ref.[**?**], in order to observe and quantify the impact of $\overline{Cr}$, $T_{\text{sat}}(s_0)$ on T_w test campaigns on a wide range of total inlet conditions and nozzles are required;

2. the proposed Wi model has been derived for expansions that are supersonic and adiabatic. Additional data on subsonic cases have to be included in the analysis in order to improve the modeling of subsonic expansion processes, as they are more common to turbomachinery applications;

3. the coefficients k_1, k_2 are dependent only on $T_{\text{sat,r}}$. Systematic sets of data, characterized by equal saturation temperature and a wider range of cooling rates, have to be used to include at least $\overline{Cr}$ in this analysis. Additionally, due to the order of magnitude of the activation time, a confidence interval for the coefficients k_1, k_2 has to be calculated;

4. the following models proved to be not suitable in order to attain a higher level of accuracy in the simulation of condensing flows of organic fluids. Additionally, the non-isothermal nucleation rate model has to be replaced. Although no significant issues were encountered in the simulations presented in this thesis, a further analysis revealed that the expression for J has to be modified when the difference in enthalpy between the two phases is not sufficiently high;

5. especially for high-pressure expansions, characterised by a low difference in enthalpy and density between the liquid and the vapor phase, the impact of the assumptions of i) mechanical equilibrium and ii) capillarity on the liquid entropy s_l

has to be assessed, in order to obtain a more accurate estimation of the entropy production due to metastable condensation;

6. a suitable objective function has to be devised for the fluid dynamic optimization of two-phase turbomachinery, to find a trade-off between i) thermodynamic efficiency of the component and ii) maintenance costs due to mechanical damage caused by the impact of droplets on the blades;

7. the code has to be extended for the simulation of entire stages, to allow for the evaluation of the net power output for turbomachinery components.

7

APPENDIX

I promise, this is the last one

APPENDIX A

A.1. MASS SOURCE TERM DERIVATION

It is calculated following the approach proposed in [1]. For the sake of clarity, the next paragraph reports a short derivation for this quantity.

When in presence of condensation, the conservation laws for the vapor phase in (2.1) must consider the mass that is lost during the condensation process, and reaches the liquid state. The quantity S_v is then introduced to represent the mass exchange between phases.

By calling MUV the Mass per Unit of mixture Volume of condensate, the source term can be expressed as

$$S_v = -\frac{\partial (\text{MUV})}{\partial t}. \tag{A.3}$$

At the same time, MUV is given by the total mass of liquid phase per unit of mixture volume inside the flow, or, equivalently,

$$\text{MUV} = \frac{V_l \rho_l}{V_m}, \tag{A.4}$$

where $V_{l,m}$ are the volume of liquid and mixture respectively. Eq. (A.4) can be further developed into

$$\text{MUV} = \frac{4}{3}\pi R^3 N \rho_l \rho_m, \tag{A.5}$$

calling N the number of droplets per unit of mixture mass.

As the equations in system (2.1) and the ones in (2.6) are solved through a decoupled approach, it is assumed that the liquid and the mixture properties are constant for the resolution of system (2.1). Under this assumption, the temporal variation of MUV is governed by the average radius R. Eq.(A.3) then becomes

$$S_v = -\frac{\partial \left(\frac{4}{3}\pi R^3 N \rho_l \rho_m\right)}{\partial t} = -\frac{\partial (\text{MUV})}{\partial t} \approx -4\pi R^2 N \rho_l \rho_m \frac{\partial R}{\partial t}. \tag{A.6}$$

Finally, by replacing the definition of Y and G, i.e., the liquid mass fraction and the growth rate

$$Y = \frac{V_l \rho_l}{V_m \rho_m} = \frac{4}{3}\pi N R^3 \rho_l, \qquad G = \frac{\partial R}{\partial t} \tag{A.7}$$

, it can be obtained

$$S_v = -\rho_m \frac{3Y}{R} G. \tag{A.8}$$

A.2. THERMODYNAMIC PROPERTIES OF THE LIQUID PHASE

The following paragraphs report the thermodynamic models used for the liquid properties. All quantities are expressed in SI.

A.2.1. LIQUID DENSITY

The liquid density at a given temperature T_l is given by the following expression:

A.2.2. LIQUID ENTHALPY

The liquid enthalpy at a given temperature T_l and pressure P_l is calculated though the formula

$$h_l = \tau \Re T_l \sum_{i=0}^{3} 4(b_i n_i 7.1 - \pi_s)^{a_i} (\tau - 1.2221)^{b_i - 1}, \tag{A.9}$$

, where $\Re$ is the gas constant and

$$\pi_s = P_l / 16.53e6, \qquad \tau = 1386 T_l^{-1}. \tag{A.10}$$

For the sake of brevity, the thesis refers to [4] for the coefficients a, b, n.

A.2.3. SATURATION PRESSURE

The saturation pressure at a given temperature T_l is given by

$$\frac{P_{\text{sat}}}{1e6} = \left(\frac{2C}{-B + \sqrt{2B - 4AC}} \right)^4, \tag{A.11}$$

where

$$A = H^2 + z_2 H + z_2, \quad B = z_3 H^2 + z_4 H + z_5, \quad C = z_6 H^2 + z_7 H + z_8, \quad H = \frac{T_l + z_9}{T_l - z_{10}}. \tag{A.12}$$

The coefficients z are

$$
\begin{aligned}
z_1 &= 0.11670521452767e4 & z_6 &= 0.14915108613530e2 \\
z_2 &= \text{-}0.72421316703206e6 & z_7 &= \text{-}0.48232657361591e4 \\
z_3 &= \text{-}0.17073846940092e2 & z_8 &= 0.40511340542057e6 \\
z_4 &= 0.12020824702470e5 & z_9 &= \text{-}0.23855557567849e0 \\
z_5 &= \text{-}0.32325550322333e7 & z_{10} &= 0.65017534844798e3
\end{aligned}
$$

A.2.4. SATURATION TEMPERATURE

The saturation temperature at a given pressure P_v is calculated as

$$T_{sat} = 0.5 \left(D + z_{10} - \sqrt{(z_{10} + D)^2 - 4(z_9 + z_{10}D)} \right),$$ (A.13)

where

$$D = \frac{2G}{-F - \sqrt{(F^2 - 4EG)}}, \quad E = H^2 + z_3 * H + z_6, \quad F = z_1 H^2 + z_4 H + z_7, G = z_2 H^2 + z_5 H + z_8,$$ (A.14)

and

$$H = \left(\frac{P_v}{1e6} \right)^{0.25}.$$ (A.15)

The coefficients z are the same as for the saturation temperature in the previous paragraph.

A.2.5. SURFACE TENSION

The surface tension at given temperature T_v is expressed as

$$\sigma = b_1 \left(b_4 + b_2 \left(\frac{T_v}{T_{cr}} \right) \right) \left(1 - \frac{T_v}{T_{cr}} \right)^{b_3}$$ (A.16)

, where

$$b_1 = 235.8e - 3, \quad b_2 = 0.625, \quad b_3 = 1.256, \quad b_4 = 0.375$$ (A.17)

A.2.6. FREE GIBBS ENERGY VARIATION

The traditional formula employed [1–3] to evaluate the Gibbs free energy variation is

$$\Delta \mathcal{G} = \Delta (\mathcal{G}_v - \mathcal{G}_l) \approx \int_P^{P_{sat}} (v_v - v_l) dp \approx \int_P^{P_{sat}} v_v \, dp \approx \int_P^{P_{sat}} \frac{RT}{P} dp = RT \log \frac{P_{sat}}{P},$$ (A.18)

obtained assuming negligible liquid specific volume and applying the ideal gas model. In this work, $\Delta \mathcal{G}$ is defined as the sum of two contributions

$$\Delta \mathcal{G} = \Delta (\mathcal{G}_v - \mathcal{G}_l) = \Delta \mathcal{G}_v - \Delta \mathcal{G}_l$$ (A.19)

where

$$\Delta \mathcal{G}_v = \mathcal{G}_v(P) - \mathcal{G}_v(P_{sat}), \qquad \Delta \mathcal{G}_l = \mathcal{G}_l(P) - \mathcal{G}_l(P_{sat}).$$ (A.20)

To maintain a fluid-independent approach, $\Delta \mathcal{G}_v$ is evaluated through the same commercial thermodynamic library adopted for the continuum phase, whereas $\Delta \mathcal{G}_l$ is found as in [4].

A.3. THERMODYNAMIC DERIVATIVES FOR A MIXTURE

The speed of sound is defined as

$$c_{\mathrm{m}} = \left(\frac{\partial P}{\partial \rho_{\mathrm{m}}}\right)_{s_{\mathrm{m}}}^{\frac{1}{2}}. \tag{A.21}$$

The introduction of the continuum phase volume title α_{v} and the use of the derivation properties allow to rewrite (A.21) as

$$c_{\mathrm{m}} = \left(\frac{\partial \rho_{\mathrm{m}}}{\partial P}\right)_{s_{\mathrm{m}}}^{-\frac{1}{2}} = \left(\frac{\partial \left(\alpha_{\mathrm{v}}\rho_{\mathrm{v}} + (1 - \alpha_{\mathrm{v}})\rho_{\mathrm{l}}\right)}{\partial P}\right)_{s_{\mathrm{m}}}^{-\frac{1}{2}}, \tag{A.22}$$

thus,

$$c_{\mathrm{m}} = \left[\alpha_{\mathrm{v}}\left(\frac{\partial \rho_{\mathrm{v}}}{\partial P}\right)_{s_{\mathrm{m}}} + (1 - \alpha_{\mathrm{v}})\left(\frac{\partial \rho_{\mathrm{l}}}{\partial P}\right)_{s_{\mathrm{m}}} + (\rho_{\mathrm{v}} - \rho_{\mathrm{l}})\left(\frac{\partial \alpha_{\mathrm{v}}}{\partial P}\right)_{s_{\mathrm{m}}}\right]^{-\frac{1}{2}}, \tag{A.23}$$

Two simplifications are made: i) the derivative of α_{v} is neglected and ii) the two derivatives at s_{m} constant are approximated with the derivative of each phase, at constant s_{v} and s_{l} respectively. Furthermore, the volume title α_{v} is defined as

$$\alpha_{\mathrm{v}} = \frac{V_{\mathrm{v}}}{V_{\mathrm{m}}} = 1 - \frac{V_{\mathrm{l}}}{V_{\mathrm{m}}} = 1 - \frac{\rho_{\mathrm{m}}}{\rho_{\mathrm{l}}}Y. \tag{A.24}$$

Therefore, the final expression for the speed of sound is

$$c_{\mathrm{m}} = \left[\left(1 - \frac{\rho_{\mathrm{m}}}{\rho_{\mathrm{l}}}Y\right)\left(\frac{\partial \rho_{\mathrm{v}}}{\partial P}\right)_{s_{\mathrm{c}}} + \left(\frac{\rho_{\mathrm{m}}}{\rho_{\mathrm{l}}}Y\right)\left(\frac{\partial \rho_{\mathrm{l}}}{\partial P}\right)_{s_{\mathrm{l}}}\right]^{-\frac{1}{2}}, \tag{A.25}$$

thus,

$$c_{\mathrm{m}} = \left[\left(1 - \frac{\rho_{\mathrm{m}}}{\rho_{\mathrm{l}}}Y\right)\frac{1}{c_{\mathrm{v}}^{2}} + \left(\frac{\rho_{\mathrm{m}}}{\rho_{\mathrm{l}}}Y\right)\frac{1}{c_{\mathrm{l}}^{2}}\right]^{-\frac{1}{2}}. \tag{A.26}$$

A.4. NUMERICAL FLUX DERIVATIVES FOR MOMENTS EQUATIONS

A.4.1. SPECTRAL DECOMPOSITION

The flux jacobian A is determined from (2.17) as

$$A = \left(\frac{\partial F}{\partial U}\right) = \begin{bmatrix} a_1 & 0 \\ b_1 & c_1 \end{bmatrix}, \tag{A.27}$$

in which

$$a_1 = \frac{\partial F(1)}{\partial U(1)} = v_{\mathrm{m}}, \tag{A.28}$$

$$b_1 = \frac{\partial F(2)}{\partial U(1)} = -G\frac{x - x_{\mathrm{inlet}}}{x_{\mathrm{outlet}} - x_{\mathrm{inlet}}}\Delta x\left(\rho_{\mathrm{m}}\mu_0\right)^{-\frac{2}{3}}\left(\rho_{\mathrm{m}}\mu_3\right)^{\frac{2}{3}}, \tag{A.29}$$

$$c_1 = \frac{\partial F(2)}{\partial U(2)} = -2G\frac{x - x_{\mathrm{inlet}}}{x_{\mathrm{outlet}} - x_{\mathrm{inlet}}}\Delta x\left(\rho_{\mathrm{m}}\mu_0\right)^{\frac{1}{3}}\left(\rho_{\mathrm{m}}\mu_3\right)^{-\frac{1}{3}} + v_{\mathrm{m}}. \tag{A.30}$$

As A is lower triangular, the eigenvalues matrix Λ is equal to

$$\Lambda = \begin{bmatrix} v_{\mathrm{m}} & 0 \\ 0 & -2G\frac{x - x_{\mathrm{inlet}}}{x_{\mathrm{outlet}} - x_{\mathrm{inlet}}}\Delta x \left(\rho_{\mathrm{m}}\mu_0\right)^{\frac{1}{3}} \left(\rho_{\mathrm{m}}\mu_3\right)^{-\frac{1}{3}} + v_{\mathrm{m}} \end{bmatrix}. \tag{A.31}$$

The right and left eigenvector matrices R_{eig} and L_{eig} are

$$R_{\mathrm{eig}} = \begin{bmatrix} \frac{v_{\mathrm{m}} - c_1}{\sqrt{b_1^2 + (v_{\mathrm{m}} - c_1)^2}} & 0 \\ \frac{b_1}{\sqrt{b_1^2 + (v_{\mathrm{m}} - c_1)^2}} & 1 \end{bmatrix} \tag{A.32}$$

and

$$L_{\mathrm{eig}} = \frac{1}{Det(R_{\mathrm{eig}})} \begin{bmatrix} 1 & 0 \\ -\frac{b_1}{\sqrt{b_1^2 + (v_{\mathrm{m}} - c_1)^2}} & \frac{v_{\mathrm{m}} - c_1}{\sqrt{b_1^2 + (v_{\mathrm{m}} - c_1)^2}} \end{bmatrix}, \tag{A.33}$$

where

$$Det(R_{\mathrm{eig}}) = \left(\frac{v_{\mathrm{m}} - c_1}{\sqrt{b_1^2 + (v_{\mathrm{m}} - c_1)^2}}\right). \tag{A.34}$$

Therefore, $|A|$ is written as

$$|A| = R_{\mathrm{eig}}|\Lambda|L_{\mathrm{eig}} = \begin{bmatrix} a_2 & 0 \\ b_2 & c_2 \end{bmatrix} = \begin{bmatrix} v_{\mathrm{m}} & 0 \\ \frac{b_1(v_{\mathrm{m}} - |c_1|)}{v_{\mathrm{m}} - c_1} & |c_1| \end{bmatrix}, \tag{A.35}$$

A.4.2. BOUNDARY CONDITIONS

The number of boundary conditions that can be imposed is given by the eigenvalue analysis. From (A.31), the first eigenvalue λ_1 is always positive. On the other hand, λ_2 may become negative. In this case, the condition on μ_3 must be imposed at the domain outlet, but no information are known a priori to set this value. It is worth pointing out that the expression for λ_2 in (A.31) contains also an information related to the mesh, i.e. Δx, and not to the thermodynamics itself. Furthermore, from the physics of the problem, it is arguably reasonable to impose the liquid phase fraction at the domain inlet, and to extrapolate at the domain outlet the value coming from inside.

A.5. RESIDUAL JACOBIAN DETERMINATION

Equation (A.35) can be substituted in (2.17) obtaining

$$F_{\frac{i+j}{2}} = \frac{F_i + F_j}{2} - \frac{1}{2}\begin{bmatrix} a_2 \cdot U_j(1) \\ b_2 \cdot U_j(1) + c_2 \cdot U_j(2) \end{bmatrix} + \frac{1}{2}\begin{bmatrix} a_2 \cdot U_i(1) \\ b_2 \cdot U_i(1) + c_2 \cdot U_i(2) \end{bmatrix} =$$

$$\frac{F_i + F_j}{2} - \frac{1}{2}V_j + \frac{1}{2}V_i. \tag{A.36}$$

A

Therefore, the flux derivatives are

$$\frac{\partial F_{\frac{i+j}{2}}}{\partial U_i} = \frac{1}{2}\frac{\partial F_i}{\partial U_i} + \frac{1}{2}\frac{\partial F_j}{\partial U_i} - \frac{1}{2}\frac{\partial V_j}{\partial U_i} + \frac{1}{2}\frac{\partial V_i}{\partial U_i}, \tag{A.37}$$

$$\frac{\partial F_{\frac{i+j}{2}}}{\partial U_j} = \frac{1}{2}\frac{\partial F_i}{\partial U_j} + \frac{1}{2}\frac{\partial F_j}{\partial U_j} - \frac{1}{2}\frac{V_j}{U_j} + \frac{1}{2}\frac{V_i}{U_j}. \tag{A.38}$$

The physical flux derivative has already been shown in (A.27), thus

$$\frac{\partial F_i}{\partial U_i}, \frac{\partial F_j}{\partial U_j} = A_i, A_j. \tag{A.39}$$

Despite of what happens for the conventional single phase, the physical flux F_i depends also on U_j, due to the summatory in (2.17). Therefore

$$\frac{\partial F_i}{\partial U_j}(1, 1:2) = 0, \tag{A.40}$$

$$\frac{\partial F_i}{\partial U_j}(2, 1) = -\frac{x_i - x_{\text{inlet}}}{x_{\text{outlet}} - x_{\text{inlet}}}\left(G\Delta x\left(\rho_m\mu_0\right)^{-\frac{2}{3}}\left(\rho_m\mu_3\right)^{\frac{2}{3}}\right)_j, \tag{A.41}$$

$$\frac{\partial F_i}{\partial U_j}(2, 2) = -2\frac{x_i - x_{\text{inlet}}}{x_{\text{outlet}} - x_{\text{inlet}}}\left(G\Delta x\left(\rho_m\mu_0\right)^{\frac{1}{3}}\left(\rho_m\mu_3\right)^{-\frac{1}{3}}\right)_j. \tag{A.42}$$

The last terms in (A.37) are developed as

$$\frac{\partial V_j}{\partial U_i}(1, 1:2) = 0, \tag{A.43}$$

$$\frac{\partial V_j}{\partial U_i}(2, 1) = U_j(1)\frac{\partial b_2}{\partial U_i(1)} + U_j(2)\frac{\partial c_2}{\partial U_i(1)} \tag{A.44}$$

$$\frac{\partial V_j}{\partial U_i}(2, 2) = U_j(1)\frac{\partial b_2}{\partial U_i(2)} + U_j(2)\frac{\partial c_2}{\partial U_i(2)} \tag{A.45}$$

and

$$\frac{\partial V_i}{\partial U_i}(1, 1) = a_2, \tag{A.46}$$

$$\frac{\partial V_i}{\partial U_i}(1, 2) = 0, \tag{A.47}$$

$$\frac{\partial V_i}{\partial U_i}(2, 1) = U_i(1)\frac{\partial b_2}{\partial U_i(1)} + b_2 + U_i(2)\frac{\partial c_2}{\partial U_i(1)}, \tag{A.48}$$

$$\frac{\partial V_i}{\partial U_i}(2, 2) = U_i(1)\frac{\partial b_2}{\partial U_i(2)} + c_2 + U_i(2)\frac{\partial c_2}{\partial U_i(2)} \tag{A.49}$$

The same procedure for (A.38) leads to

$$\frac{\partial V_i}{\partial U_j}(1, 1) = 0, \tag{A.50}$$

$$\frac{\partial V_i}{\partial U_j}(1,2) = 0, \tag{A.51}$$

$$\frac{\partial V_i}{\partial U_j}(2,1) = U_i(1)\frac{\partial b_2}{\partial U_j(1)} + U_i(2)\frac{\partial c_2}{\partial U_j(1)} \tag{A.52}$$

$$\frac{\partial V_i}{\partial U_j}(2,2) = U_i(1)\frac{\partial b_2}{\partial U_j(2)} + U_i(2)\frac{\partial c_2}{\partial U_j(2)} \tag{A.53}$$

and to

$$\frac{\partial V_j}{\partial U_j}(1,1) = a_2, \tag{A.54}$$

$$\frac{\partial V_j}{\partial U_j}(1,2) = 0, \tag{A.55}$$

$$\frac{\partial V_j}{\partial U_j}(2,1) = U_j(1)\frac{\partial b_2}{\partial U_j(1)} + b_2 + U_j(2)\frac{\partial c_2}{\partial U_j(1)}, \tag{A.56}$$

$$\frac{\partial V_j}{\partial U_j}(2,2) = U_j(1)\frac{\partial b_2}{\partial U_j(2)} + c_2 + U_j(2)\frac{\partial c_2}{\partial U_j(2)} \tag{A.57}$$

Finally, all the quantities a_2, b_2, c_2 are evaluated in

$$U_{\frac{i+j}{2}} = 0.5 \cdot \left(U_i + U_j\right), \tag{A.58}$$

thus, the missing derivatives are

$$\frac{\partial a_2, b_2, c_2}{\partial U_i} = \frac{\partial a_2, b_2, c_2}{\partial U_j} = \frac{\partial a_2, b_2, c_2}{\partial U_{\frac{i+j}{2}}} \cdot \frac{\partial U_{\frac{i+j}{2}}}{\partial U_{i,j}} = \frac{1}{2}\frac{\partial a_2, b_2, c_2}{\partial U_{\frac{i+j}{2}}}, \tag{A.59}$$

$$\frac{\partial a_2}{\partial U_{\frac{i+j}{2}}} = 0 \tag{A.60}$$

$$\frac{\partial b_2}{\partial U_{\frac{i+j}{2}}} = \frac{1}{v_{\mathrm{m}} - c_1}\left((v_{\mathrm{m}} - |c_1|)\frac{\partial b_1}{\partial U_{\frac{i+j}{2}}} - b_1\frac{c_1}{\partial U_{\frac{i+j}{2}}}\frac{|c_1|}{c_1}\right) + \frac{b_1\left(v_{\mathrm{m}} - |c_1|\right)}{(v_{\mathrm{m}} - c_1)^2}\cdot\frac{\partial c_1}{\partial U_{\frac{i+j}{2}}}, \tag{A.61}$$

$$\frac{\partial c_2}{\partial U_{\frac{i+j}{2}}} = \frac{\partial c_1}{\partial U_{\frac{i+j}{2}}}\frac{|c_1|}{c_1}, \tag{A.62}$$

in which

$$\frac{\partial b_1}{\partial U_{\frac{i+j}{2}}(1)} = \frac{2}{3}\left(\frac{x - x_{\mathrm{inlet}}}{x_{\mathrm{outlet}} - x_{\mathrm{inlet}}}G\Delta x\left(\rho_{\mathrm{m}}\mu_0\right)^{-\frac{5}{3}}\left(\rho_{\mathrm{m}}\mu_3\right)^{\frac{2}{3}}\right)_{\frac{i+j}{2}}, \tag{A.63}$$

$$\frac{\partial b_1}{\partial U_{\frac{i+j}{2}}(2)} = -\frac{2}{3}\left(\frac{x - x_{\mathrm{inlet}}}{x_{\mathrm{outlet}} - x_{\mathrm{inlet}}}G\Delta x\left(\rho_{\mathrm{m}}\mu_0\right)^{-\frac{2}{3}}\left(\rho_{\mathrm{m}}\mu_3\right)^{-\frac{1}{3}}\right)_{\frac{i+j}{2}}, \tag{A.64}$$

$$\frac{\partial c_1}{\partial U_{\frac{i+j}{2}}(1)} = -\frac{2}{3}\left(\frac{x - x_{\mathrm{inlet}}}{x_{\mathrm{outlet}} - x_{\mathrm{inlet}}}G\Delta x\left(\rho_{\mathrm{m}}\mu_0\right)^{-\frac{2}{3}}\left(\rho_{\mathrm{m}}\mu_3\right)^{-\frac{1}{3}}\right)_{\frac{i+j}{2}}, \tag{A.65}$$

$$\frac{\partial c_1}{\partial U_{\frac{i+j}{2}}(2)} = -\frac{2}{3}\left(\frac{x - x_{\mathrm{inlet}}}{x_{\mathrm{outlet}} - x_{\mathrm{inlet}}}G\Delta x\left(\rho_{\mathrm{m}}\mu_0\right)^{\frac{1}{3}}\left(\rho_{\mathrm{m}}\mu_3\right)^{-\frac{4}{3}}\right)_{\frac{i+j}{2}}. \tag{A.66}$$

A.6. NOZZLE GEOMETRY

The nozzle area A_c is given by

$$A_c(x) = \begin{cases} a_0 + b_0 x + c_0 x^2 + d_0 x^3 & 0.0 < x < 0.041837 \\ a_1 + b_1 x + c_1 x^2 + d_1 x^3 & 0.041837 < x < 0.10612 \\ a_2 + b_2 x + c_2 x^2 + d_2 x^3 & 0.10612 < x < 0.4 \end{cases} , \qquad (A.67)$$

in which x is expressed in m and A_c in m^2. All the missing coefficient are reported in Table A.1 [2] .

	a	b	c	d
0	$1.52 \cdot 10^{-2}$	$-5.1996 \cdot 10^{-4}$	$6.7416 \cdot 10^{-1}$	-8.7727
1	$1.533 \cdot 10^{-2}$	$8.0338 \cdot 10^{-3}$	$2.6189 \cdot 10^{-2}$	$7.3488 \cdot 10^{-3}$
2	$1.4926 \cdot 10^{-2}$	$1.4733 \cdot 10^{-2}$	$5.4451 \cdot 10^{-5}$	$-2.0589 \cdot 10^{-4}$

Table A.1: Nozzle profile coefficients

APPENDIX B

B.1. DETERMINATION OF r_σ, r_J, r_G

This table reports the steps for the empirical determination of r_σ, r_J, r_G for the test case No. *21As*[*] [5]. To correctly locate the Wilson pressure along the simulation, the minimum and the maximum values for P_w were taken as the limits of the expansion portion with a visible change in the pressure derivative over the nozzle coordinate.

Simulation results								
Corrections			P_w (bar)		$\bar{R}_w$ (m x1e-8)		N_w (1/kg x1e16)	
r_σ	r_J	r_G	from	to	from	to	from	to
1.40	0.29	0.23	54.7	51.4	0.15	0.42	7.35	14.63
1.41	0.29	0.23	54.5	50.9	0.15	0.43	5.51	13.87
1.43	0.29	0.23	53.4	49.0	0.16	0.47	4.91	12.44
1.45	0.29	0.23	52.1	47.8	0.18	0.49	5.61	11.11
1.48	0.29	0.23	50.3	46.5	0.19	0.50	4.82	9.31
1.48	0.26	0.23	50.3	45.8	0.20	0.50	4.70	9.18
1.48	0.26	0.20	49.9	45.3	0.18	0.49	6.23	11.75
1.48	0.23	0.20	49.6	45.8	0.19	0.47	6.97	11.55
1.49	0.23	0.20	49.2	45.0	0.19	0.49	5.89	10.86
1.49	0.23	0.23	50.2	44.4	0.19	0.55	2.80	8.51
1.49	0.26	0.23	49.7	44.8	0.20	0.54	4.20	8.64

Experimental pressure: $P_w = 47.20$ bar
Experimental average radius: $5.86e-8$ m $\leq \bar{R}_w \leq 5.918e-8$ m
Experimental droplet number: $6.15e16$ 1/kg $\leq N_w \leq 6.26e16$ 1/kg

Table B.2: Determination of r_σ, r_J, r_G: example on test case No.*21As*[*] in Ref. [5].

B.2. SIMULATION RESULTS

The following tables report the pressure and temperature P_w, T_w, the average radius $\overline{R}_w$ and the number of drops N_w per unit of total mass in correspondence with the Wilson point obtained from the simulations. The final three columns reports the values of r_σ, r_J, r_G. In particular, r_σ is factor with the main influence on the condensation onset, and visible deviations are present for using a step of ± 0.01. After the surface tension is set, r_J and r_G are changed to match the experimental average radius and number of droplets at the Wilson point. As the effect of these two parameters is not as significant as for r_σ, their value can be determined with a lower accuracy. Due to the uncertainties related to the Wilson point location, for every property the tables report a minimum and a maximum value, as in Ref. [5].

The analysis in the paper considers average pressures and temperatures in such intervals.

Test No.	Nozzle	P_0(bar)	T_0 (K)	P_w (bar)		T_w (K)		$\bar{R}_\mathrm{w}$ (x1e-8 m)		N_w (x1e16 1/kg)		r_σ	r_J	r_G
				from	to	from	to	from	to	from	to			
13B	2B	20.82	574.28	3.97	3.60	383.28	405.60	1.70	6.02	1.01	3.46	1.06	0.89	0.56
13C	2B	20.83	562.45	4.52	4.07	387.06	409.75	1.95	6.84	0.79	2.49	1.09	0.89	0.53
13D	2B	20.82	541.2	6.03	5.57	398.90	419.55	2.49	8.09	0.59	1.36	1.1	0.89	0.56
14B*	2B	61.48	631.63	13.35	11.58	429.35	447.83	2.75	9.26	0.32	1.23	1.24	0.59	0.32
15C	2B	96.78	647.69	28.47	25.34	470.23	485.60	3.35	10.24	0.43	0.99	1.31	0.41	0.29
34A*	2B	50.04	584.26	16.73	14.66	441.51	455.97	2.63	9.36	0.08	1.07	1.26	0.47	0.29
35A	2B	79.46	660.01	15.00	13.34	432.65	451.70	3.18	8.73	0.96	1.46	1.28	0.47	0.26
35B	2B	79.46	634.97	21.79	19.65	454.78	471.00	3.25	9.52	0.56	1.09	1.28	0.47	0.29
36C	2B	106.92	645.71	34.79	31.59	479.19	491.57	3.73	10.68	0.29	0.80	1.4	0.35	0.26
37B	2B	138.30	674.25	43.42	37.81	494.02	506.53	3.01	10.09	0.20	1.28	1.43	0.29	0.2
38B	2B	50.04	619.28	10.25	9.00	416.32	437.05	2.28	7.42	0.79	2.32	1.22	0.5	0.26
38B'	2B	50.04	609.69	11.54	10.34	421.88	442.18	2.57	7.57	1.18	2.09	1.22	0.5	0.26
39D	2B	89.27	619.75	32.91	31.17	476.16	488.25	4.20	9.85	0.56	0.80	1.38	0.35	0.26
40C	2B	108.88	660.44	29.85	27.00	470.03	484.01	3.60	10.18	0.42	0.93	1.37	0.38	0.26
40D	2B	108.88	637.36	40.26	37.75	493.22	503.15	3.89	10.02	0.55	0.93	1.42	0.29	0.23
40E	2B	108.88	619.08	53.06	49.86	508.82	518.82	3.04	9.46	0.30	1.11	1.45	0.26	0.17

* *The comparison with* [5] *is made with a nominal value instead of an uncertainty interval for one of the properties reported*

Table B.3: Properties at Wilson point and corrections adopted for the simulations with nozzle *2B*.

Test No.	Nozzle	P_0(bar)	T_0 (K)	P_w (bar)		T_w (K)		$\bar{R}_\text{w}$ (x1e-8 m)		N_w (x1e16 1/kg)		r_σ	r_J	r_G
				from	to	from	to	from	to	from	to			
18B	*4B*	100.70	638.45	27.71	29.67	463.80	476.80	2.49	4.41	9.90	10.35	1.35	0.35	0.26
18C	*4B*	100.70	615.2	42.48	43.91	493.10	503.20	2.10	4.11	10.52	10.69	1.4	0.29	0.23
19A	*4B*	61.47	610.25	16.23	14.45	435.72	453.42	1.72	4.33	9.93	12.57	1.25	0.41	0.38
19B*	*4B*	61.47	583.4	24.34	22.87	461.47	476.64	2.49	4.85	7.60	7.78	1.26	0.47	0.41
19Cs*	*4B*	61.47	560.55	37.31	34.42	487.12	488.80	1.86	4.10	4.75	3.57	1.26	0.47	0.41
20A	*4B*	40.43	575.18	11.08	10.19	417.01	437.14	1.71	4.05	10.82	12.87	1.22	0.5	0.44
20B	*4B*	40.43	555.72	15.04	14.07	432.35	448.47	1.57	4.15	6.14	10.15	1.23	0.47	0.41
20D	*4B*	40.43	598.1	8.09	7.44	402.28	423.90	1.50	3.64	14.20	17.48	1.2	0.56	0.5
21As*	*4B*	132.10	648.2	50.16	44.39	497.75	510.91	1.86	5.50	2.80	8.51	1.49	0.26	0.23
21Bs*	*4B*	132.10	657	47.79	42.93	499.19	511.93	1.99	5.87	2.48	6.26	1.41	0.29	0.35
21Cs*	*4B*	132.10	671.5	38.04	33.82	481.67	493.28	1.72	5.07	2.23	8.48	1.41	0.35	0.29
23A*	*5B*	100.70	662.6	22.61	19.77	451.12	472.76	1.43	3.85	16.21	22.35	1.3	0.5	0.38
23B	*5B*	100.70	641.74	29.20	26.80	465.36	479.19	2.02	4.27	11.01	13.19	1.35	0.35	0.44
23C	*5B*	100.70	620.55	39.25	36.15	483.26	493.28	2.02	4.44	8.08	10.76	1.4	0.29	0.41
24As*	*5B*	41.00	584	9.96	8.99	411.24	434.45	1.12	3.01	7.73	34.74	1.2	0.71	0.53
25As*	*5B*	148.10	668.6	49.94	43.34	498.68	511.84	1.85	5.07	6.50	12.00	1.45	0.23	0.38
25Bs*	*5B*	148.10	656.7	58.35	52.49	509.82	519.87	2.15	5.36	5.40	9.04	1.49	0.2	0.41
26C	*6B*	61.47	573.93	27.90	25.18	466.68	471.83	1.38	0.34	6.65	15.70	1.26	0.41	0.74
27A	*6B*	100.70	662.93	22.25	19.74	450.83	470.49	1.70	4.11	14.18	17.10	1.29	0.47	0.8
28Ao	*6B*	149.74	642.49	77.52	70.33	535.96	533.67	2.07	4.95	2.17	7.82	1.51	0.26	0.71
29Ao	*6B*	81.09	617.3	26.33	23.08	460.69	475.90	1.32	3.63	12.78	22.97	1.29	0.47	0.71

* *The comparison with* [5] *is made with a nominal value instead of an uncertainty interval for one of the properties reported*

Table B.4: Properties at Wilson point and corrections adopted for the simulations with nozzles *4B, 5B, 6B*.

Test No.	Nozzle	P_0(bar)	T_0 (K)	P_w (bar)		T_w (K)		$\bar{R}_w$ (x1e-8 m)		N_w (x1e16 1/kg)		r_σ	r_J	r_G
				from	to	from	to	from	to	from	to			
A623	*2B*	154.19	623	118.51	113.58	580.81	578.38	4.68	7.32	1.91	2.27	1.55	0.17	0.21
B623	*4B*	154.19	623	115.90	111.83	577.63	575.03	3.19	4.53	6.69	8.21	1.55	0.17	0.25
C623	*5B*	154.19	623	114.59	106.56	576.10	570.85	3.29	5.14	6.86	8.30	1.55	0.17	0.4
D623	*6B*	154.19	623	116.17	107.10	571.06	570.80	3.06	5.35	3.65	6.56	1.55	0.17	0.71

Table B.5: Properties at Wilson point and corrections adopted for the simulations at 623 K.

Test No.	Nozzle	P_0(bar)	T_0 (K)	P_w (bar)		T_w (K)		$\bar{R}_w$ (x1e-8 m)		N_w (x1e16 1/kg)		r_σ	r_J	r_G
				from	to	from	to	from	to	from	to			
A633	*2B*	179.21	633	158.67	149.59	613.44	605.40	2.05	5.56	0.00	4.61	1.57	0.15	0.21
B633	*4B*	179.21	633	5526.23	151.61	611.71	606.94	1.54	3.01	0.57	14.99	1.57	0.15	0.25
C633	*5B*	179.21	633	156.64	146.41	611.52	605.52	1.54	3.92	0.06	13.32	1.57	0.15	0.4
D633	*6B*	179.21	633	157.10	145.55	612.01	605.10	1.63	4.43	0.02	10.48	1.57	0.15	0.7

Table B.6: Properties at Wilson point and corrections adopted for the simulations at 633 K.

Test No.	Nozzle	P_0(bar)	T_0 (K)	P_w (bar)		T_w (K)		$\bar{R}_w$ (x1e-8 m)		N_w (x1e16 1/kg)		r_σ	r_J	r_G
				from	to	from	to	from	to	from	to			
M	1	0.25	358	0.094	0.098	283.54	311.50	1.61	4.52	4.58	5.64	1	1	1
Mx10	10	0.25	358	0.087	0.088	285.51	293.59	7.06	16.97	1.66E-02	2.90E-02	1	1	1
Mx25	25	0.25	358	0.092	0.091	288.33	293.79	12.57	32.99	5.42E-04	2.61E-02	1	1	1
Mx1e5	1e5	0.28	380.20	0.102	0.101	297.88	301.58	3.25e3	6.80e3	2.66e-10	3.10e-10	1	1	1
Mx1e10	1e10	0.28	380.20	0.151	0.146	327.10	329.55	5.62E+05	1.88E+06	4.10E-20	1.39E-17	1	1	1

Table B.7: Properties at Wilson point and corrections adopted for the simulations with the Moore nozzle [6].

B.3. ACTIVATION TIME AND COOLING RATE DATA

The following tables show i) the dimensionless saturation temperature $T_{\text{sat}}(s_0)$ and ii) a second point along the expansion at time $t_{\text{subcooled}} < t_{\text{act}}$ characterized by temperature $T_{\text{subcooled}}$. These informations are used to evaluate the average cooling rate $\overline{Cr}$. The last column reports the activation time t_{act}.

Test No.	$T_{\text{sat}}(s_0)/T_{\text{cr}}$	$t_{\text{subcooled}}$ (s)	$T_{\text{subcooled}}/T_{\text{cr}}$	$\overline{Cr}$ (s^{-1})	t_{act} (s)
13B	0.674	5.01E-05	0.591	1.66E+03	5.07E-05
13C	0.683	5.07E-05	0.598	1.69E+03	5.25E-05
13D	0.700	4.90E-05	0.617	1.70E+03	5.13E-05
14B*	0.759	5.01E-05	0.662	1.94E+03	5.20E-05
15C	0.817	4.31E-05	0.727	2.10E+03	4.53E-05
34A	0.774	5.04E-05	0.678	1.91E+03	5.29E-05
35A*	0.772	5.13E-05	0.669	2.00E+03	5.32E-05
35B	0.797	4.49E-05	0.704	2.06E+03	4.77E-05
36C	0.838	4.54E-05	0.741	2.15E+03	4.82E-05
37B	0.856	4.26E-05	0.761	2.23E+03	4.55E-05
38B	0.741	5.13E-05	0.644	1.89E+03	5.46E-05
38B'	0.750	4.98E-05	0.655	1.91E+03	5.36E-05
39D	0.833	4.44E-05	0.739	2.11E+03	4.83E-05
40C	0.825	4.41E-05	0.730	2.17E+03	4.85E-05
40D	0.851	4.26E-05	0.758	2.18E+03	4.71E-05
40E	0.872	3.78E-05	0.789	2.21E+03	4.27E-05

Table B.8: Cooling rate and activation time for nozzle *2B*.

B.4. TIME-DEPENDENT REPRESENTATION OF THE STATE DIA-GRAMS

As shown in Chapter 3, T_{w} can be expressed as

$$T_{\text{w}} = T_{\text{sat}}(s_0) - T_{\text{cr}} Wi, \qquad Wi = k_1 \left(\frac{k_1}{t_{\text{act}}} \right)^{\left(\frac{1}{k_2} - 1 \right)}, \tag{B.68}$$

highlighting the dependence of Wi from t_{act} (see (3.34)). Therefore, from the mathematical point of view at each value $T_{\text{sat}}(s_0)$ corresponds a set of time-dependent curves $T_{\text{w}}(t)$. Thus, the function $T_{\text{w}}(T_{\text{sat}}(s_0), t)$ can be represented as a 3D-surface in a $T - s - t$ (Temperature - entropy - time) chart. The procedure to plot such condensation surface is the following:

1. a value s_0 is fixed. This identifies a plane Γ parallel to the $T - t$ axis;

2. the temperature $T_{\text{sat}}(s_0)$ is calculated;

3. equation (B.68) allows to draw the curve $T_{\text{w}}(t, s_0)$ in the plane Γ;

Test No.	$T_{\text{sat}}(s_0)/T_{\text{cr}}$	$t_{\text{subcooled}}$ (s)	$T_{\text{subcooled}}/T_{\text{cr}}$	$\overline{Cr}$ (s^{-1})	t_{act} (s)
18B	0.834	9.13E-06	0.735	1.09E+04	1.03E-05
18C	0.862	8.86E-06	0.781	9.09E+03	1.03E-05
19A	0.779	1.03E-05	0.677	9.86E+03	1.14E-05
*19B**	0.808	9.55E-06	0.718	9.40E+03	1.06E-05
*19Cs**	0.835	2.05E-05	0.758	3.76E+03	2.25E-05
20A	0.752	1.13E-05	0.647	9.28E+03	1.21E-05
20B	0.772	1.12E-05	0.673	8.85E+03	1.23E-05
20D	0.731	1.20E-05	0.623	8.99E+03	1.26E-05
*21As**	0.877	1.05E-05	0.766	1.06E+04	1.09E-05
*21Bs**	0.866	8.57E-06	0.771	1.12E+04	9.12E-06
*21Cs**	0.849	9.85E-06	0.742	1.09E+04	1.04E-05

Table B.9: Cooling rate and activation time for nozzle *4B*.

Test No.	$T_{\text{sat}}(s_0)/T_{\text{cr}}$	$t_{\text{subcooled}}$ (s)	$T_{\text{subcooled}}/T_{\text{cr}}$	$\overline{Cr}$ (s^{-1})	t_{act} (s)
*23A**	0.808	5.70E-06	0.697	1.94E+04	5.95E-06
23B	0.829	5.20E-06	0.721	2.09E+04	5.48E-06
23C	0.855	5.66E-06	0.747	1.90E+04	5.99E-06
*24As**	0.744	5.95E-06	0.637	1.79E+04	6.28E-06
*25As**	0.875	4.73E-06	0.770	2.21E+04	5.03E-06
*25Bs**	0.889	4.92E-06	0.787	2.07E+04	5.17E-06

Table B.10: Cooling rate and activation time for nozzle *5B*.

Test No.	$T_{\text{sat}}(s_0)/T_{\text{cr}}$	$t_{\text{subcooled}}$ (s)	$T_{\text{subcooled}}/T_{\text{cr}}$	$\overline{Cr}$ (s^{-1})	t_{act} (s)
26C	0.819	4.13E-06	0.722	2.33E+04	4.36E-06
27A	0.807	2.84E-06	0.698	3.85E+04	3.03E-06
28Ao	0.910	3.72E-06	0.825	2.28E+04	3.96E-06
29Ao	0.818	2.91E-06	0.712	3.66E+04	3.09E-06

Table B.11: Cooling rate and activation time for nozzle *6B*.

Test No.	$T_{\text{sat}}(s_0)/T_{\text{cr}}$	$t_{\text{subcooled}}$ (s)	$T_{\text{subcooled}}/T_{\text{cr}}$	$\overline{Cr}$ (s^{-1})	t_{act} (s)
M	0.506	2.99E-04	0.429	2.55E+02	3.19E-04
Mx10	0.506	2.06E-03	0.443	3.02E+01	2.30E-03
Mx25	0.506	8.53E-03	0.449	6.63E+00	9.42E-03
Mx1e5	0.506	1.19E+01	0.482	2.01E-03	1.29E+01
Mx1e10	0.506	6.06E+05	0.491	2.38E-08	6.90E+05

Table B.12: Cooling rate and activation time, simulations with Moore nozzle.

Test No.	$T_{sat}(s_0)/T_{cr}$	$t_{subcooled}$ (s)	$T_{subcooled}/T_{cr}$	$\overline{Cr}$ (s^{-1})	t_{act} (s)
A623K	0.943	6.05E-05	0.901	6.91E+02	6.99E-05
B623K	0.943	3.04E-05	0.895	1.57E+03	3.04E-05
C623K	0.943	1.73E-05	0.889	3.10E+03	1.73E-05
D623K	0.943	1.16E-05	0.888	4.78E+03	1.16E-05
A633K	0.965	7.49E-05	0.940	3.30E+02	7.49E-05
B633K	0.965	3.46E-05	0.940	7.23E+02	3.46E-05
C633K	0.965	1.84E-05	0.939	1.42E+03	1.84E-05
D633K	0.965	1.27E-05	0.937	2.21E+03	1.27E-05

Table B.13: Cooling rate and activation time, simulations at T_0 equal to 623 K and 633 K.

4. the steps 1-3 are repeated for all the values s_0, defining the envelope of curves $T_w(t, s)$.

Figure B.1 reports the condensation surface obtained. For the sake of clarity, Figure B.1b displays multiple sections on the Γ planes corresponding to $s_0 = -1.616, -1.384, -1, 138$ kJ/kg/K, i.e., $T_{sat}(s_0) = 580, 610, 630$K. Additionally, Figure B.2 reports the projections in the $T - s$ planes for $t = 1e-5, 1e-3, 1e-1, 1e1$s.

(a) 3D representation of the Wilson surface $T_w(t)$ (b) Section of Figure B.1a
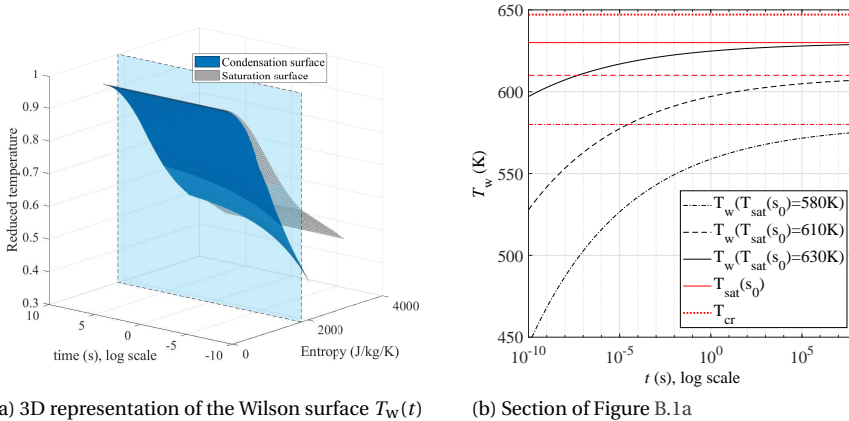
Figure B.1: Metastable T-s-t chart (Temperature-entropy-time) for water, T-t section

$T_w(t, s)$ represents a clear boundary between the vapor and the two-phase region, accounting also for possible metastable states of the vapor phase along the expansion. By definition, nucleation will not occur for all the points in which $T > T_w(t, s)$, thus in the region above the re-defined metastable condensation surface, see Figure 3.21.

Note that the curve $T_w(t, s_0)$ tends asymptotically to $T_{sat}(s_0)$, see Figure B.1b. In other words, the saturation line is the limit of the condensation surface $T_w(t, s)$ for $t \to \infty$, i.e., when the fluid is cooled down in an ideally infinite time, in agreement with the theory
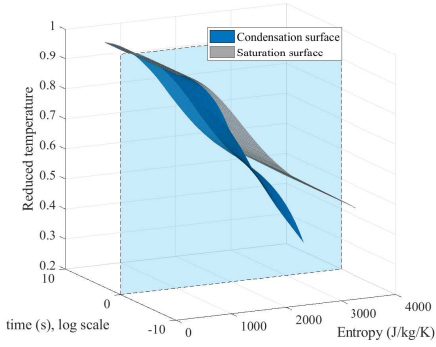
(a) 3D representation of the Wilson surface $T_w(t)$
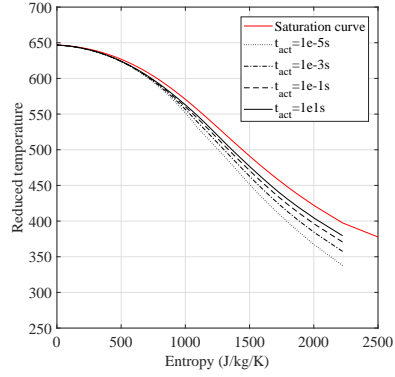
(b) Sections of Figure B.2a parallel to the time axis, $t =$1e-5, 1e-3, 1e-1, 1e1 s

Figure B.2: Metastable *T-s-t* chart for water, *T-s* section

for equilibrium expansions.

APPENDIX C

C.1. LIQUID ENTHALPY

The liquid enthalpy (in SI) is evaluated as the difference between the vapor enthalpy at same temperature and the latent heat, calculated as

$$L = k_1 + k_2 \left(\frac{T_l}{T_{cr}} \right) + k_3 \left(\frac{T_l}{T_{cr}} \right)^2 + k_4 \left(\frac{T_l}{T_{cr}} \right)^3, \tag{C.69}$$

where

$$k_1 = 3.8788e6, \quad , k_2 = -5.9196e6, \quad , k_3 = 8.8253e6, \quad , k_4 = -5.9584e6. \tag{C.70}$$

The last coefficients are derived from a polynomial interpolation of the latent heat calculated through the external thermodynamic library in Ref. [**?**].

C.2. CLOSURE MODELS

The critical radius is evaluated as

$$R_* = \frac{2\sigma}{\rho_l \Delta \mathcal{G}}, \tag{C.71}$$

in which σ is the surface tension, ρ_l the liquid density and $\Delta \mathcal{G}$ is the Gibbs free energy variation of the vapor phase. Despite what reported in Ref. [7], no corrections are applied on σ and R_* to account for the droplet curvature effect. This choice was mainly dictated by the lower numerical stability observed when introducing these factors, as they are dependent on the droplets radius R.

The capillarity model adopted for the liquid phase temperature T_l is [1, 8]

$$T_l = T_{sat}(P) - (T_{sat}(P) - T_v) \frac{R_*}{\overline{R}}. \tag{C.72}$$

where $T_{sat}(P)$ is the saturation temperature at the vapor pressure P and T_v is the vapor temperature.

The nucleation rate J is calculated as [9]

$$J = \frac{1}{1+\theta} \frac{\rho_v}{\rho_l} \sqrt{\frac{2\sigma}{\pi M M^3}} \exp\left(-\frac{4\pi R_*^2 \sigma}{3 k_b T_v}\right), \tag{C.73}$$

in which

$$\theta = 2\frac{\gamma - 1}{\gamma + 1} \frac{h_v - h_l}{\mathcal{R} T_v} \left(\frac{h_v - h_l}{\mathcal{R} T_v} - 0.5 \right), \tag{C.74}$$

MM is the molecular mass, k_b is the Boltzmann constant, $\rho_{v,l}$ and $h_{v,l}$ are the densities and the specific enthalpies of the vapor and the liquid phase, γ is the heat capacity ratio and $\mathfrak{R}$ is the gas constant. The growth rate G for H_2O is in the form [10]

$$G = \frac{\kappa_v \left(T_{\text{sat}}(P_v) - T_v\right)\left(1 - \frac{R_*}{\overline{\overline{R}}}\right)}{\rho_l \left(h_v - h_l\right)\left(1.89 + \overline{R} - 1.89 v \frac{l_v}{Pr}\right)},$$ (C.75)

in which Pr is the Prandtl number, l_v is given by

$$l_v = \frac{1.5\mu_v\sqrt{\mathfrak{R}T_v}}{P_v},$$ (C.76)

κ_v and μ_v are the thermal conductivity and viscosity of the vapor phase and v is defined as

$$v = \frac{\mathfrak{R}T_{\text{sat}}(P_v)}{h_v - h_l}\left[0.5 - \frac{1}{4}\frac{\gamma+1}{\gamma-1}\frac{\mathfrak{R}T_{\text{sat}}(P_v)}{h_v - h_l}\right].$$ (C.77)

On the other hand, the growth rate for CO2 and R22 is equal to [7]

$$G = \alpha\frac{T_l - T_v}{\rho_l\left(h_v - h_l\right)},$$ (C.78)

where

$$\alpha = \frac{k_v}{\overline{R} + \sqrt{2\pi}\frac{k}{C_v + C_p}\delta},$$ (C.79)

C_v, C_p are the heat capacities at constant volume and pressure, and

$$\delta = \frac{64}{15\pi}\frac{1}{\rho_v}\sqrt{\frac{\pi MM}{2k_b T_v}}.$$ (C.80)

C.3. Validation of SU2 with CO_2, R22

This section reports the tests made with CO_2 and R22 to validate the two-phase code. In particular, the tables display i) total inlet conditions, ii) isentropic saturation temperature $T_{\text{sat}}(s_0)$ and, iii) deviation between the Wilson temperature in the simulation and the experiments. Last column of the tables report the relative deviation

$$\Delta T_{\text{err}} = \frac{|T_{\text{w,simulations}} - T_{\text{w,experiments}}|}{T_{\text{cr}}},$$ (C.81)

in which T_{cr} is the critical temperature of the fluid.

To prove that the expansions can be approximated as isentropic, the value T_{sat}, i.e., the non-isoentropic saturation temperature at which the fluid enters in the two-phase region, is also reported.

The Wilson temperature T_w for CO_2 is taken in correspondence with the maximum of the nucleation rate. On the other hand, due to the different shape of J for R22 (see

section 4.2.3), the same criterion s not applicable, and the two-phase code adopted cannot be validated for this fluid. In order to have an estimation of the Wilson point, the temperature T_w is taken as the average temperature of the interval in which the liquid mass fraction y passes from 1e-8 to 1e-6. Both the criteria are deemed by [11] as valid to identify the Wilson point. For the expansions with CO$_2$, the second approach gives a very similar value of T_w, with an uncertainty of less than 1K. however, the value obtained are only used for a qualitative comparison with the experimental data [12], and a more detailed investigation on the nucleation rate J is needed to allow for the correct simulation of R22 with the adopted code.

Note that the deviation $T_w - T_{w,exp}$ for test *N2* in table C.14 and tests *N31, N41* in table C.15, characterized by similar values of $T_{sat}(s_0)$, is of the same order of magnitude. This confirms the repeatability and the coherence of the results obtained through the two-phase code adopted.

Test	P_0(bar)	T_0(K)	$T_{sat}(s_0)$ (K)	$T_{sat,r}(s_0)$	T_{sat}	$T_{sat,r}$	x_w (m)	$x_{w,exp}$ (m)	T_w (K)	$T_{x_{w,exp}}$	$T_w - T_{x_{w,exp}}$ (K)	ΔT_{err}
N2	63.9e5	311.87	282.82	0.93	282.58	0.93	-4.50e-4	2.02e-3	274.15	273.93	0.22	7.2e-4

Note that the simulation temperature calculated at $x_{w,exp}$ is 273.925, in agreement with the experimental data

Table C.14: Validation of the two-phase code with CO_2, test case *N2* from Ref. [13]. The geometry of the nozzle is taken from Ref. [14]. The experimental Wilson point is identified in Ref. [13] by means of the x-coordinate $x_{w,exp}$ along the nozzle.

Test	P_0(bar)	T_0(K)	$T_{sat}(s_0)$ (K)	$T_{sat,r}(s_0)$	T_{sat}	$T_{sat,r}$	T_w (K)	$T_{w,exp}$ (K)	$T_w - T_{w,exp}$ (K)	ΔT_{err}
N16	35	305.76	245.49	0.81	245.35	0.81	200.51	209.94	-9.43	3.1e-2
N19	35	298.42	251.38	0.83	251.21	0.83	211.46	219.49	-8.03	2.6e-2
N5	45	308.24	260.03	0.86	259.97	0.86	228.06	232.35	-4.29	1.4e-2
N9	45	300.12	267.16	0.88	266.97	0.88	246.12	245.49	0.63	2.1e-3
N31	75	327.32	280.84	0.92	280.792	0.92	267.41	267.56	-0.15	4.9e-4
N41	100.1	339.72	290.56	0.95	290.51	0.95	283.91	283.14	0.77	2.5e-3
Range of reliability: $0.86 < T_{sat,r}(s_0) < 0.95$										

Table C.15: Validation of the two-phase code with CO_2, test cases from Ref. [7].

Test	P_0(bar)	T_0(K)	$T_{sat}(s_0)$ (K)	$T_{sat,r}(s_0)$	T_{sat}	$T_{sat,r}$	T_w (K)	$T_{w,exp}$ (K)	$T_w - T_{w,exp}$ (K)	ΔT_{err}
N37	21.31	331.60	315.07	0.85	315.02	0.85	232.42	248.54	4.4e-2	
N46	34.90	361.95	324.99	0.88	324.93	0.88	<Nozzle outlet	260.21		-
N64	24.95	337.55	325.61	0.88	325.59	0.88	274.26	273.13	1.13	3.1e-3
N69	40	364.85	342.41	0.93	342.38	0.93	307.78	302.34	5.44	1.5e-2
N67	40	363.70	344.84	0.94	344.81	0.94	314.44	314.85	-0.41	1.1e-3
Range of reliability: $0.88 < T_{sat,r}(s_0) < 0.94$										

Table C.16: Validation of the two-phase code with R22, test cases from Ref. [7]

Section type	rectangular
Length	0.7 m
Inlet heigh	1.84e-1 m
Throat heigh	0.10 m
Throat radius*	0.50 m
Divergent section angle	2.58°
Outlet high	1.44e-1 m

* Throat radius is not explicitly reported in the original reference [16]

Table C.17: Nozzle *Moore* characterization

Fluid	$T_{\text{sat,r}}(s_0)$	k_1	k_2	Fluid	$T_{\text{sat,r}}(s_0)$	k_1	k_2
H_2O	0.55	4.52E-02	9.04E-01	CO_2	0.86	4.15E-02	9.24E-01
H_2O	0.60	4.50E-02	9.19E-01	CO_2	0.89	3.10E-02	9.14E-01
H_2O	0.65	4.27E-02	9.24E-01	CO_2	0.91	2.38E-02	9.26E-01
H_2O	0.70	3.99E-02	9.30E-01	CO_2	0.94	2.05E-02	9.71E-01
H_2O	0.75	3.48E-02	9.31E-01	R22	0.89	1.35E-01	9.03E-01
H_2O	0.80	2.94E-02	9.36E-01	R22	0.91	8.52E-02	9.17E-01
H_2O	0.86	2.14E-02	9.27E-01	R22	0.94	4.16E-02	9.58E-01

Table C.18: Coefficients k_1, k_2 for the fitting functions in the form of (4.7)

C.4. NOZZLE PROFILE: *Moore, Moorex25*

Table C.17 reports the main parameters for the profile of nozzle *Moore*. Nozzle *Moorex25* is obtained simply stretching *Moore* by a factor x25, as in Ref. [15]. This nozzle was added to have an expansion with a very low cooling rate.

C.5. FITTING COEFFICIENTS FOR THE ACTIVATION TIME

Table C.18 reports the fitting coefficients k_1, k_2 in 4.7 for all the simulation sets carried out.

C.6. MOLECULAR PROPERTIES OF THE FLUID UNDER SCRUTINY

Table C.19 reports i) the molar mass, ii) the critical point and iii) the molecular dipole moment for the fluids considered in this work.

Fluid	M	T_{cr} (K)	P_{cr} (bar)	Dipole (D)
H_2O	18.02	647.29	220.90	1.85
CO_2	44.01	304.21	73.82	non-polar
R22	86.48	369.20	49.80	1.46
R12	120.91	385.00	40.70	0.51

Table C.19: Main physical and molecular properties of the fluid under scrutiny

C.7. SIMULATION SETS FOR H_2O, CO_2, R22

This section reports all the simulation sets that were carried out with H_2O, CO_2, R22. The complete list of the tests is the following:

- H_2O: seven simulation sets at $T_{sat,r}(s_0) =$ 0.55, 0.60, 0.65, 0.70, 0.75, 0.80, 0.86;

- CO_2: four simulation sets at $T_{sat,r}(s_0) =$ 0.86, 0.89, 0.91, 0.94;

- R22: three simulation sets at $T_{sat,r}(s_0) =$ 0.89, 0.91, 0.94.

For each of the simulation sets, six tests were carried out adopting nozzles with different cooling rates, i.e. *2B, 4B, 5B, 6B, Moore, Moorex25*.

The tables report i) the Wilson point, ii) the activation time, iii) the cooling rate, iv) velocity and Mach number in correspondence with T_w and the degree of subcooling.

The last three columns of the tables report the outlet temperature, outlet velocity and the loss coefficient in correspondence with a static pressure of $0.25P_0$. Note that the analysis in 4.4.1 does not include R22 as the results cannot be validated, see 4.2.3. However, the values are reported for the sake of completeness.

Finally, table C.34 shows the single phase simulations carried out with R12. The values t_{act}, $\overline{Cr}$, Wi, ΔT_{sub} are calculated using the experimental Wilson temperature T_w.

	Condensation onset location								Outlet static pressure $P = 0.25P_0$			
Nozzle	P_w (bar)	T_w (bar)	t_{act} (s)	$\overline{Cr}$ (s^{-1})	v_w (m/s)	M_w (-)	Wi (-)	ΔT_{sub} (K)	ζ (%)	T_{out} (K)	v_{out} (m/s)	Notes
2B	0.26	300.59	7.65E-05	1.10E+03	5.91E+02	1.38	8.43E-02	54.59	2.05	327.46	653.78	
4B	0.22	289.62	2.00E-05	5.11E+03	6.25E+02	1.49	1.02E-01	66.02	2.36	310.88	648.84	
5B	0.20	284.20	1.11E-05	9.92E+03	6.41E+02	1.54	1.10E-01	71.11	0.24	283.83	646.37	*
6B	0.18	276.07	7.19E-06	1.71E+04	6.60E+02	1.61	1.23E-01	79.44	0.03	281.20	642.75	*
Moore	0.30	308.83	2.89E-04	2.52E+02	5.63E+02	1.30	7.28E-02	47.11	1.29	331.15	662.87	
Moorex25	0.33	317.16	5.51E-03	1.09E+01	5.33E+02	1.21	6.00E-02	38.81	0.74	332.32	664.22	

* Condensation occurs at a pressure equal to $0.25P_0$ or lower

Table C.20: Simulation with $T_{sat,r}(s_0)=0.55$ for H_2O, total conditions $P_0 = 0.796$ bar, $T_0 = 392.70$ K

	Condensation onset location								Outlet static pressure $P = 0.25P_0$			
Nozzle	P_w (bar)	T_w (bar)	t_{act} (s)	$\overline{Cr}$ (s^{-1})	v_w (m/s)	M_w (-)	Wi (-)	ΔT_{sub} (K)	ζ (%)	T_{out} (K)	v_{out} (m/s)	
2B	0.94	337.78	5.98E-05	1.28E+03	5.83E+02	1.29	7.69E-02	49.76	1.36	356.26	683.55	
4B	0.85	329.29	1.52E-05	5.94E+03	6.10E+02	1.37	9.06E-02	58.64	1.89	354.71	680.55	
5B	0.79	325.02	8.29E-06	1.16E+04	6.24E+02	1.41	9.64E-02	62.42	2.13	349.14	676.17	
6B	0.74	319.33	5.51E-06	1.92E+04	6.38E+02	1.45	1.06E-01	68.33	2.06	336.94	669.60	
Moore	1.02	342.84	2.14E-04	3.28E+02	5.65E+02	1.24	7.02E-02	45.46	0.86	359.49	691.51	
Moorex25	1.13	351.18	4.46E-03	1.28E+01	5.37E+02	1.17	5.73E-02	37.09	0.51	359.93	693.46	

Table C.21: Simulation with $T_{sat,r}(s_0)=0.60$ for H_2O, total conditions $P_0 = 2.55$ bar, $T_0 = 428.2$ K

	Condensation onset location								Outlet static pressure $P = 0.25P_0$			
Nozzle	P_w (bar)	T_w (bar)	t_{act} (s)	$\overline{Cr}$ (s^{-1})	v_w (m/s)	M_w (-)	Wi (-)	ΔT_{sub} (K)	ζ (%)	T_{out} (K)	v_{out} (m/s)	
2B	2.71	374.13	4.79E-05	1.47E+03	5.75E+02	1.22	7.02E-02	45.47	0.96	383.93	708.26	
4B	2.52	367.16	1.23E-05	6.65E+03	5.98E+02	1.28	8.18E-02	52.97	1.26	383.33	706.94	
5B	2.09	358.55	6.54E-06	1.39E+04	6.50E+02	1.41	9.08E-02	58.80	1.46	379.33	704.83	
6B	2.25	358.94	4.55E-06	2.07E+04	6.25E+02	1.35	9.40E-02	60.85	1.80	378.89	695.29	
Moore	2.87	377.71	1.82E-04	3.64E+02	5.62E+02	1.19	6.64E-02	42.97	0.56	386.95	715.85	
Moorex25	3.13	385.62	3.72E-03	1.44E+01	5.35E+02	1.12	5.37E-02	34.79	0.35	387.16	717.49	

Table C.22: Simulation with $T_{sat,r}(s_0)=0.65$ for H_2O, total conditions $P_0 = 6.67$ bar, $T_0 = 463.91$ K

	Condensation onset location								Outlet static pressure $P = 0.25 P_0$		
Nozzle	P_w (bar)	T_w (bar)	t_{act} (s)	$\overline{Cr}$ (s^{-1})	v_w (m/s)	M_w (-)	Wi (-)	ΔT_{sub} (K)	ζ (%)	T_{out} (K)	v_{out} (m/s)
2B	6.69	411.01	3.85E-05	1.65E+03	5.61E+02	1.15	6.35E-02	41.11	0.72	410.93	728.28
4B	6.32	405.19	1.01E-05	7.24E+03	5.81E+02	1.20	7.31E-02	47.30	0.89	410.64	727.72
5B	5.86	399.49	5.72E-06	1.41E+04	6.00E+02	1.25	8.06E-02	52.18	1.26	407.23	722.34
6B	5.96	399.91	3.74E-06	2.16E+04	5.97E+02	1.24	8.09E-02	52.37	1.33	407.75	714.84
Moore	7.00	414.14	1.57E-04	3.82E+02	5.51E+02	1.13	6.01E-02	38.93	0.37	413.73	735.62
Moorex25	7.50	421.17	3.26E-03	1.51E+01	5.27E+02	1.07	4.92E-02	31.87	0.27	413.85	736.37

Table C.23: Simulation with $T_{sat,r}(s_0)$=0.70 for H_2O, total conditions P_0 = 15.00 bar, T_0 = 499.95 K

	Condensation onset location								Outlet static pressure $P = 0.25 P_0$		
Nozzle	P_w (bar)	T_w (bar)	t_{act} (s)	$\overline{Cr}$ (s^{-1})	v_w (m/s)	M_w (-)	Wi (-)	ΔT_{sub} (K)	ζ (%)	T_{out} (K)	v_{out} (m/s)
2B	14.46	448.23	3.22E-05	1.74E+03	5.43E+02	1.09	5.61E-02	36.33	0.55	437.77	742.07
4B	14.01	443.90	8.27E-06	7.65E+03	5.57E+02	1.13	6.33E-02	40.96	0.67	437.42	742.08
5B	13.19	438.21	4.69E-06	1.51E+04	5.73E+02	1.17	7.08E-02	45.82	0.97	435.76	736.74
6B	13.42	439.64	3.11E-06	2.22E+04	5.70E+02	1.16	6.91E-02	44.73	1.02	435.19	729.77
Moore	15.20	451.92	1.32E-04	3.93E+02	5.30E+02	1.06	5.17E-02	33.48	0.30	440.02	749.12
Moorex25	15.98	457.61	2.83E-03	1.51E+01	5.11E+02	1.02	4.29E-02	27.74	0.28	440.09	749.44

Table C.24: Simulation with $T_{sat,r}(s_0)$=0.75 for H_2O, total conditions P_0 = 29.97 bar, T_0 = 536.50 K

	Condensation onset location								Outlet static pressure $P = 0.25 P_0$		
Nozzle	P_w (bar)	T_w (bar)	t_{act} (s)	$\overline{Cr}$ (s^{-1})	v_w (m/s)	M_w (-)	Wi (-)	ΔT_{sub} (K)	ζ (%)	T_{out} (K)	v_{out} (m/s)
2B	28.65	486.81	2.59E-05	1.79E+03	5.15E+02	1.03	4.62E-02	29.92	0.49	463.92	749.35
4B	27.97	483.34	7.06E-06	7.39E+03	5.27E+02	1.05	5.22E-02	33.78	0.57	463.70	749.10
5B	27.23	481.05	3.71E-06	1.47E+04	5.34E+02	1.07	5.45E-02	35.31	0.70	462.98	745.17
6B	27.05	479.69	2.71E-06	2.13E+04	5.38E+02	1.08	5.77E-02	37.34	0.83	462.12	737.48
Moore	29.95	490.76	1.16E-04	3.58E+02	5.02E+02	1.00	4.17E-02	26.99	0.42	465.69	754.89
Moorex25	30.84	494.57	2.61E-03	1.37E+01	4.90E+02	0.97	3.57E-02	23.12	0.26	466.04	755.75

Table C.25: Simulation with $T_{sat,r}(s_0)$=0.80 for H_2O, total conditions P_0 = 54.57 bar, T_0 = 573.75 K

| Nozzle | Condensation onset location | | | | | | | | Outlet static pressure $P = 0.25P_0$ | | |
	P_w (bar)	T_w (bar)	t_{act} (s)	$\overline{Cr}$ (s^{-1})	v_w (m/s)	M_w (-)	Wi (-)	ΔT_{sub} (K)	ζ (%)	T_{out} (K)	v_{out} (m/s)
2B	56.46	529.15	2.31E-05	1.76E+03	4.88E+02	0.98	4.06E-02	26.28	0.49	495.98	746.31
4B	57.87	532.14	5.74E-06	6.47E+03	4.81E+02	0.97	3.71E-02	24.02	0.46	495.53	746.63
5B	55.58	527.51	3.22E-06	1.36E+04	4.94E+02	0.99	4.37E-02	28.27	0.67	494.49	742.70
6B	55.65	526.98	2.21E-06	2.00E+04	4.96E+02	1.00	4.43E-02	28.70	0.78	493.92	735.41
Moore	60.16	537.08	1.14E-04	2.65E+02	4.67E+02	0.93	3.02E-02	19.52	0.31	497.03	752.38
Moorex25	61.32	539.86	2.33E-03	1.11E+01	4.58E+02	0.91	2.59E-02	16.74	0.20	497.20	753.05

Table C.26: Simulation with $T_{sat,r}(s_0)$=0.86 for H_2O, total conditions $P_0 = 102.07$ bar, $T_0 = 619.50$ K

| Nozzle | Condensation onset location | | | | | | | | Outlet static pressure $P = 0.25P_0$ | | | Notes |
	P_w (bar)	T_w (bar)	t_{act} (s)	$\overline{Cr}$ (s^{-1})	v_w (m/s)	M_w (-)	Wi (-)	ΔT_{sub} (K)	ζ (%)	T_{out} (K)	v_{out} (m/s)	
2B	18.38	240.28	7.32E-05	9.40E+02	229.51	1.08	6.88E-02	20.93	0.85	229.12	321.83	
4B	17.56	237.04	1.97E-05	4.07E+03	237.36	1.12	7.99E-02	24.32	1.05	228.85	321.30	
5B	13.41	220.16	1.56E-05	8.57E+03	271.24	1.32	1.34E-01	40.74	2.44	227.99	314.67	
6B	6.86	180.82	1.83E-05	1.44E+04	333.98	1.74	2.64E-01	80.37	0.00	197.95	307.86	*
Moore	19.28	242.84	3.00E-04	2.06E+02	224.03	1.05	6.17E-02	18.76	0.46	230.85	325.64	
Moorex25	20.33	246.49	6.40E-03	7.66E+00	215.27	1.01	4.90E-02	14.91	0.42	230.90	325.79	

* Condensation occurs at a pressure lower than $0.25P_0$

Table C.27: Simulation with $T_{sat,r}(s_0)$=0.86 for CO_2, total conditions $P_0 = 37.30$ bar, $T_0 = 291.38$ K

| Nozzle | Condensation onset location | | | | | | | | Outlet static pressure $P = 0.25P_0$ | | |
	P_w (bar)	T_w (bar)	t_{act} (s)	$\overline{Cr}$ (s^{-1})	v_w (m/s)	M_w (-)	Wi (-)	ΔT_{sub} (K)	ζ (%)	T_{out} (K)	v_{out} (m/s)
2B	25.5632	253.39	6.25E-05	8.85E+02	2.15E+02	1.02	5.53E-02	16.82	0.80	237.00	318.88
4B	25.734	253.73	1.61E-05	3.41E+03	2.15E+02	1.02	5.49E-02	16.70	0.95	236.03	318.54
5B	21.7836	242.45	1.13E-05	8.00E+03	2.38E+02	1.15	9.06E-02	27.56	1.42	236.88	315.50
6B	21.2162	240.23	7.94E-06	1.25E+04	2.42E+02	1.18	9.92E-02	30.17	1.92	236.21	310.62
Moore	27.3835	257.85	2.77E-04	1.53E+02	2.05E+02	0.97	4.24E-02	12.88	0.64	237.80	321.99
Moorex25	28.1167	259.81	5.98E-03	6.00E+00	2.01E+02	0.95	3.59E-02	10.91	0.39	238.11	322.72

Table C.28: Simulation with $T_{sat,r}(s_0)$=0.89 for CO_2, total conditions $P_0 = 48.37$ bar, $T_0 = 302.01$ K

		Condensation onset location							Outlet static pressure $P = 0.25 P_0$		
Nozzle	P_w (bar)	T_w (bar)	t_{act} (s)	$\overline{Cr}$ (s^{-1})	v_w (m/s)	M_w (-)	Wi (-)	ΔT_{sub} (K)	ζ (%)	T_{out} (K)	v_{out} (m/s)
2B	30.6435	260.25	6.04E-05	8.81E+02	2.09E+02	0.96	5.32E-02	16.19	0.84	249.95	284.69
4B	32.2126	263.94	1.45E-05	2.88E+03	2.02E+02	0.97	4.18E-02	12.71	0.85	249.01	285.11
5B	28.7904	255.85	9.25E-06	7.25E+03	2.18E+02	1.06	6.70E-02	20.38	1.29	249.14	282.16
6B	27.904	253.50	6.92E-06	1.09E+04	2.24E+02	1.09	7.52E-02	22.88	1.69	248.19	278.26
Moore	33.6334	266.89	2.73E-04	1.20E+02	1.96E+02	0.93	3.26E-02	9.92	0.60	250.45	287.73
Moorex25	34.3058	268.39	5.51E-03	5.02E+00	1.92E+02	0.91	2.77E-02	8.42	0.38	250.69	288.35

Table C.29: Simulation with $T_{sat,r}(s_0)$=0.91 for CO_2, total conditions $P_0 = 57.18$ bar, $T_0 = 309.13$ K

		Condensation onset location							Outlet static pressure $P = 0.25 P_0$		
Nozzle	P_w (bar)	T_w (bar)	t_{act} (s)	$\overline{Cr}$ (s^{-1})	v_w (m/s)	M_w (-)	Wi (-)	ΔT_{sub} (K)	ζ (%)	T_{out} (K)	v_{out} (m/s)
2B	43.5337	278.17	4.38E-05	5.65E+02	1.86E+02	0.90	2.48E-02	7.53	0.61	249.75	309.72
4B	43.7572	278.46	1.03E-05	2.33E+03	1.86E+02	0.90	2.39E-02	7.27	0.63	249.54	309.63
5B	40.8814	273.50	7.42E-06	5.36E+03	1.96E+02	0.96	3.98E-02	12.11	0.82	250.40	307.54
6B	40.9602	273.44	5.06E-06	7.93E+03	1.97E+02	0.96	4.02E-02	12.22	0.94	250.28	304.75
Moore	43.4557	277.84	2.58E-04	1.03E+02	1.91E+02	0.92	2.66E-02	8.08	0.43	251.00	329.88
Moorex25	44.6449	279.85	4.85E-03	4.13E+00	1.83E+02	0.88	2.00E-02	6.09	0.24	250.97	313.26

Table C.30: Simulation with $T_{sat,r}(s_0)$=0.94 for CO_2, total conditions $P_0 = 73.30$ bar, $T_0 = 319.78$ K

		Condensation onset location							Outlet static pressure $P = 0.25 P_0$		
Nozzle	P_w (bar)	T_w (bar)	t_{act} (s)	$\overline{Cr}$ (s^{-1})	v_w (m/s)	M_w (-)	Wi (-)	ΔT_{sub} (K)	ζ (%)	T_{out} (K)	v_{out} (m/s)
2B	4.53	241.36	5.68E-04	4.13E+02	286.13	1.89	2.35E-01	86.59	4.43E-07	266.95	245.37
4B	T_w < nozzle outlet temperature										
5B	2.70	218.90	1.05E-04	2.80E+03	319.00	2.15	2.95E-01	109.05	4.36E-08	267.06	244.77
6B	2.42	214.21	6.88E-05	4.48E+03	324.64	2.20	3.08E-01	113.79	2.68E-08	266.94	242.73
Moore	T_w < nozzle outlet temperature										
Moorex25	8.85	273.88	6.33E-02	2.34E+00	232.26	1.53	1.48E-01	54.66	6.58E-05	272.21	234.37

Table C.31: Simulation with $T_{sat,r}(s_0)$=0.89 for R22, total conditions $P_0 = 30.72$ bar, $T_0 = 351.00$ K

			Condensation onset location						Outlet static pressure $P = 0.25 P_0$		
Nozzle	P_w (bar)	T_w (bar)	t_{act} (s)	$\overline{Cr}$ (s^{-1})	v_w (m/s)	M_w (-)	Wi (-)	ΔT_{sub} (K)	ζ (%)	T_{out} (K)	v_{out} (m/s)
2B	11.45	284.04	3.18E-04	4.39E+02	219.42	1.47	1.39E-01	51.48	4.19E-04	270.80	241.80
4B	10.24	277.75	7.71E-05	2.04E+03	229.92	1.54	1.57E-01	57.92	1.05E-04	270.66	241.64
5B	9.16	271.94	4.38E-05	3.92E+03	239.21	1.60	1.72E-01	63.33	4.37E-05	270.91	241.41
6B	8.50	267.98	2.68E-05	6.81E+03	243.48	1.63	1.83E-01	67.51	2.52E-05	270.82	239.36
Moore	13.48	293.09	1.35E-03	8.59E+01	204.29	1.38	1.16E-01	42.87	7.47E-03	270.35	242.89
Moorex25	15.02	299.54	2.76E-02	3.57E+00	192.56	1.31	9.85E-02	36.37	7.18E-02	278.80	225.92

Table C.32: Simulation with $T_{sat,r}(s_0)$=0.91 for R22, total conditions $P_0 = 35.85$ bar, $T_0 = 359.29$ K

			Condensation onset location						Outlet static pressure $P = 0.25 P_0$		
Nozzle	P_w (bar)	T_w (bar)	t_{act} (s)	$\overline{Cr}$ (s^{-1})	v_w (m/s)	M_w (-)	Wi (-)	ΔT_{sub} (K)	ζ (%)	T_{out} (K)	v_{out} (m/s)
2B	25.07	327.04	1.16E-04	4.59E+02	150.19	1.08	5.32E-02	19.64	3.07	275.60	234.01
4B	24.64	325.70	3.00E-05	1.92E+03	153.17	1.10	5.74E-02	21.18	0.76	275.43	233.81
5B	24.37	325.02	1.61E-05	3.63E+03	153.79	1.11	5.87E-02	21.66	0.36	275.62	233.54
6B	24.21	324.50	1.08E-05	5.54E+03	155.10	1.12	6.01E-02	22.17	0.19	275.64	231.43
Moore	25.69	328.63	5.07E-04	9.83E+01	148.18	1.07	4.98E-02	18.40	16.98	277.48	231.41
Moorex25	26.40	330.63	1.11E-02	4.00E+00	144.32	1.04	4.44E-02	16.40	20.82	277.57	231.44

Table C.33: Simulation with $T_{sat,r}(s_0)$=0.94 for R22, total conditions $P_0 = 44.80$ bar, $T_0 = 371.66$ K

Test	P_0 (bar)	T_0 (K)	$T_{sat}(s_0)$	$T_{sat,r}(s_0)$	$T_{w,exp}$ (K)	$P_{w,exp}$ (bar)	t_{act} (s)	$\overline{Cr}$ (s^{-1})	Wi	ΔT_{sub} (K)
N44	46.04	397.01	377.15	0.979	340.89	21.92	5.78E-05	1630.89	9.42E-02	36.26
N29	47.88	399.39	378.40	0.982	350.37	25.35	4.52E-05	1613.71	7.29E-02	28.03
N41	49.97	401.91	379.64	0.986	360.32	29.17	3.28E-05	1529.56	5.02E-02	19.32
N52	52.00	403.60	381.94	0.992	371.50	33.96	2.05E-05	1324.99	2.72E-02	10.44
N58	55.98	406.59	384.93	0.999	378.78	37.60	1.30E-05	1234.83	1.60E-02	6.15

Table C.34: Single-phase simulations for R12. Activation time and cooling rate are calculated using the experimental Wilson temperature reported in Ref. [7]
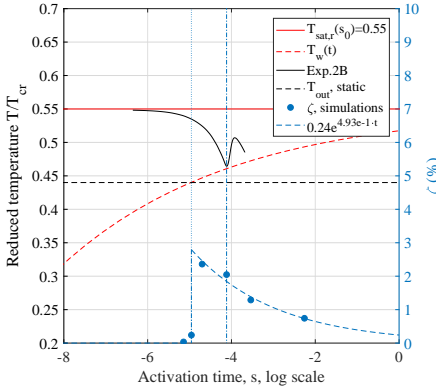
Figure C.3: *T-t* chart reporting i) T_w as in (4.8), ii) ζ for H_2O and, iii) expansion *2B* in table C.20 at $T_{sat,r}(s_0)=0.55$.
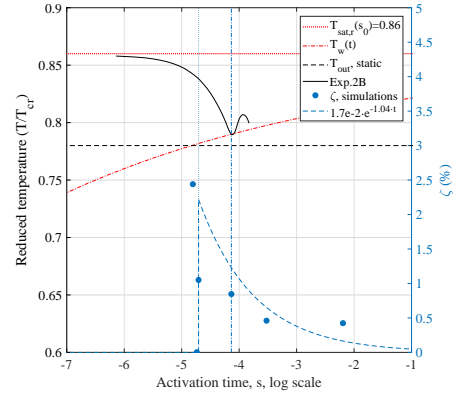
Figure C.4: *T-t* chart reporting i) T_w as in (4.8), ii) ζ for CO_2 and, iii) expansion *2B* in table C.27 at $T_{sat,r}(s_0)=0.86$.

C.8. TIME-DEPENDENT REPRESENTATION OF THE ENTROPY LOSSES

In analogy with B.4, the loss coefficient ζ can be also plotted as a function of the activation time t_{act}. Figures C.3, C.4 show the Wilson curve as in Ref. [15] and the loss coefficient as a function of t_{act} for H_2O at $T_{sat,r}(s_0) = 0.55$ and CO_2 at $T_{sat,r}(s_0) = 0.86$. Additionally, the expansions made with nozzle *2B* from C.23 and C.27 are plotted.

The representation of Wi and ζ as function of t_{act} can be exploited for optimal nozzle design at reduced computational cost, as shown in 4.

APPENDIX D

D.1. BLADE PROFILES

Tables D.35, D.36, D.37, D.38, D.39 report, respectively,

1. the blade profile for the cascade in [17];

2. the optimized profile for minimum volume liquid fraction for the cascade [18];

3. the optimized profile for minimum losses for the cascade [18];

4. the optimized profile for minimum volume liquid fraction for the cascade [17];

5. the optimized profile for minimum losses for the cascade [17].

All coordinates are in m.

D

Pressure side		Suction side	
x	y	x	y
0.00000	0.00000	0.09741	-0.09000
0.00022	-0.00057	0.09505	-0.08400
0.00262	-0.00378	0.08889	-0.06340
0.00733	-0.00654	0.08348	-0.04735
0.01632	-0.00997	0.07751	-0.03222
0.02564	-0.01318	0.07196	-0.02075
0.03463	-0.01731	0.06324	-0.00780
0.04296	-0.02201	0.05395	0.00069
0.05128	-0.02729	0.04343	0.00619
0.05970	-0.03382	0.03201	0.00860
0.06681	-0.04070	0.02213	0.00848
0.07337	-0.04815	0.01190	0.00688
0.07893	-0.05572	0.00486	0.00482
0.08460	-0.06478	0.00255	0.00378
0.08884	-0.07372	0.00034	0.00183
0.09285	-0.08335	0.00000	0.00000
0.09410	-0.08713		
0.09618	-0.09250		
0.09741	-0.09401		
0.09785	-0.09400		

Table D.35: Tapping points from Ref. [17]

Point #	x	y	Point #	x	y	Point #	x	y
1	2.267E-03	2.959E-03	37	1.476E-01	-6.947E-02	73	4.373E-03	-1.629E-02
2	6.199E-03	8.055E-03	38	1.499E-01	-7.443E-02	74	1.124E-03	-1.244E-02
3	1.092E-02	1.145E-02	39	1.521E-01	-7.940E-02	75	1.000E-07	-6.199E-03
4	1.570E-02	1.439E-02	40	1.543E-01	-8.439E-02	76	1.328E-03	8.031E-04
5	2.054E-02	1.692E-02	41	1.564E-01	-8.936E-02	77	1.729E-01	-1.429E-01
6	2.544E-02	1.905E-02	42	1.416E-01	-8.474E-02	78	1.722E-01	-1.409E-01
7	3.039E-02	2.082E-02	43	1.383E-01	-8.041E-02	79	1.714E-01	-1.389E-01
8	3.539E-02	2.223E-02	44	1.349E-01	-7.611E-02	80	1.707E-01	-1.370E-01
9	4.043E-02	2.333E-02	45	1.315E-01	-7.189E-02	81	1.699E-01	-1.350E-01
10	4.552E-02	2.406E-02	46	1.279E-01	-6.774E-02	82	1.691E-01	-1.330E-01
11	5.066E-02	2.430E-02	47	1.243E-01	-6.366E-02	83	1.672E-01	-1.286E-01
12	5.583E-02	2.409E-02	48	1.206E-01	-5.965E-02	84	1.650E-01	-1.238E-01
13	6.101E-02	2.343E-02	49	1.168E-01	-5.573E-02	85	1.627E-01	-1.191E-01
14	6.617E-02	2.235E-02	50	1.129E-01	-5.190E-02	86	1.603E-01	-1.144E-01
15	7.128E-02	2.088E-02	51	1.089E-01	-4.817E-02	87	1.577E-01	-1.098E-01
16	7.631E-02	1.901E-02	52	1.048E-01	-4.448E-02	88	1.551E-01	-1.052E-01
17	8.125E-02	1.679E-02	53	1.007E-01	-4.094E-02	89	1.523E-01	-1.006E-01
18	8.606E-02	1.422E-02	54	9.646E-02	-3.757E-02	90	1.494E-01	-9.610E-02
19	9.074E-02	1.135E-02	55	9.211E-02	-3.437E-02	91	1.464E-01	-9.161E-02
20	9.529E-02	8.205E-03	56	8.767E-02	-3.135E-02	92	1.433E-01	-8.717E-02
21	9.969E-02	4.802E-03	57	8.315E-02	-2.852E-02	93	1.594E-01	-9.646E-02
22	1.039E-01	1.139E-03	58	7.855E-02	-2.589E-02	94	1.613E-01	-1.013E-01
23	1.080E-01	-2.770E-03	59	7.387E-02	-2.346E-02	95	1.632E-01	-1.061E-01
24	1.118E-01	-6.910E-03	60	6.912E-02	-2.125E-02	96	1.650E-01	-1.109E-01
25	1.155E-01	-1.125E-02	61	6.430E-02	-1.925E-02	97	1.667E-01	-1.156E-01
26	1.188E-01	-1.577E-02	62	5.943E-02	-1.750E-02	98	1.683E-01	-1.203E-01
27	1.219E-01	-2.045E-02	63	5.451E-02	-1.599E-02	99	1.699E-01	-1.250E-01
28	1.248E-01	-2.524E-02	64	4.954E-02	-1.476E-02	100	1.714E-01	-1.297E-01
29	1.276E-01	-3.012E-02	65	4.453E-02	-1.382E-02	101	1.726E-01	-1.336E-01
30	1.302E-01	-3.501E-02	66	3.950E-02	-1.319E-02	102	1.731E-01	-1.355E-01
31	1.329E-01	-3.990E-02	67	3.444E-02	-1.289E-02	103	1.737E-01	-1.373E-01
32	1.355E-01	-4.480E-02	68	2.936E-02	-1.295E-02	104	1.742E-01	-1.391E-01
33	1.380E-01	-4.971E-02	69	2.428E-02	-1.339E-02	105	1.747E-01	-1.410E-01
34	1.405E-01	-5.464E-02	70	1.918E-02	-1.425E-02	106	1.751E-01	-1.428E-01
35	1.429E-01	-5.958E-02	71	1.409E-02	-1.555E-02			
36	1.453E-01	-6.452E-02	72	9.020E-03	-1.703E-02			

Table D.36: Optimized profile for test case in Dykas [18], minimum liquid volume fraction

Point #	x	y	Point #	x	y	Point #	x	y
1	8.610E-05	6.141E-04	37	6.160E-02	-1.893E-02	73	1.471E-01	-6.853E-02
2	1.931E-03	5.614E-03	38	1.084E-01	-8.007E-03	74	1.479E-01	-7.029E-02
3	1.041E-04	-2.373E-03	39	6.591E-02	-2.070E-02	75	1.507E-01	-1.039E-01
4	8.811E-03	1.053E-02	40	7.124E-02	-2.315E-02	76	1.523E-01	-1.064E-01
5	1.463E-02	1.278E-02	41	1.106E-01	-1.004E-02	77	1.514E-01	-7.869E-02
6	5.211E-03	8.827E-03	42	7.751E-02	-2.645E-02	78	1.551E-01	-1.110E-01
7	1.839E-02	1.405E-02	43	8.112E-02	-2.855E-02	79	1.566E-01	-1.136E-01
8	2.271E-02	1.534E-02	44	1.151E-01	-1.466E-02	80	1.543E-01	-8.613E-02
9	2.764E-02	1.659E-02	45	8.817E-02	-3.312E-02	81	1.548E-01	-8.739E-02
10	2.984E-02	1.708E-02	46	9.114E-02	-3.524E-02	82	1.606E-01	-1.204E-01
11	3.987E-02	1.872E-02	47	9.357E-02	-3.707E-02	83	1.627E-01	-1.242E-01
12	3.539E-02	1.810E-02	48	9.550E-02	-3.858E-02	84	1.640E-01	-1.264E-01
13	4.382E-02	1.910E-02	49	1.195E-01	-1.988E-02	85	1.589E-01	-9.870E-02
14	4.834E-03	-9.860E-03	50	1.016E-01	-4.375E-02	86	1.660E-01	-1.300E-01
15	5.066E-02	1.919E-02	51	1.039E-01	-4.583E-02	87	1.605E-01	-1.030E-01
16	5.526E-02	1.885E-02	52	1.066E-01	-4.843E-02	88	1.615E-01	-1.061E-01
17	5.698E-02	1.864E-02	53	1.232E-01	-2.491E-02	89	1.690E-01	-1.353E-01
18	6.388E-02	1.737E-02	54	1.129E-01	-5.463E-02	90	1.692E-01	-1.358E-01
19	6.788E-02	1.631E-02	55	1.150E-01	-5.690E-02	91	1.695E-01	-1.364E-01
20	7.296E-02	1.461E-02	56	1.193E-01	-6.153E-02	92	1.708E-01	-1.390E-01
21	7.520E-02	1.374E-02	57	1.273E-01	-3.109E-02	93	1.709E-01	-1.391E-01
22	7.797E-02	1.256E-02	58	1.206E-01	-6.296E-02	94	1.713E-01	-1.398E-01
23	8.179E-02	1.074E-02	59	1.299E-01	-3.548E-02	95	1.722E-01	-1.417E-01
24	1.692E-02	-1.102E-02	60	1.259E-01	-6.922E-02	96	1.727E-01	-1.430E-01
25	1.975E-02	-1.099E-02	61	1.326E-01	-3.995E-02	97	1.672E-01	-1.224E-01
26	9.074E-02	5.602E-03	62	1.335E-01	-4.145E-02	98	1.737E-01	-1.441E-01
27	2.428E-02	-1.109E-02	63	1.311E-01	-7.562E-02	99	1.742E-01	-1.441E-01
28	2.710E-02	-1.125E-02	64	1.363E-01	-4.656E-02	100	1.709E-01	-1.321E-01
29	3.162E-02	-1.164E-02	65	1.334E-01	-7.864E-02	101	1.750E-01	-1.436E-01
30	3.500E-02	-1.205E-02	66	1.391E-01	-5.181E-02	102	1.751E-01	-1.431E-01
31	1.016E-01	-2.156E-03	67	1.383E-01	-8.525E-02	103	1.729E-01	-1.374E-01
32	1.011E-01	-1.780E-03	68	1.397E-01	-8.730E-02	104	1.734E-01	-1.386E-01
33	4.565E-02	-1.401E-02	69	1.416E-01	-8.987E-02	105	1.740E-01	-1.400E-01
34	1.025E-01	-2.911E-03	70	1.440E-01	-9.349E-02	106	1.741E-01	-1.404E-01
35	1.044E-01	-4.448E-03	71	1.443E-01	-6.223E-02			
36	5.560E-02	-1.679E-02	72	1.461E-01	-9.660E-02			

Table D.37: Optimized profile for test case in Dykas [18], minimum thermodynamic losses

Point #	x	y	Point #	x	y	Point #	x	y
1	2,80E-05	-6,09E-04	38	8,37E-02	-7,06E-02	75	7,94E-02	-4,53E-02
2	1,04E-03	-3,03E-03	39	8,51E-02	-7,34E-02	76	7,83E-02	-4,22E-02
3	3,22E-03	-4,89E-03	40	8,63E-02	-7,62E-02	77	7,72E-02	-3,91E-02
4	5,96E-03	-5,93E-03	41	8,76E-02	-7,90E-02	78	7,61E-02	-3,58E-02
5	8,73E-03	-6,93E-03	42	8,88E-02	-8,19E-02	79	7,49E-02	-3,25E-02
6	1,15E-02	-7,89E-03	43	8,99E-02	-8,49E-02	80	7,37E-02	-2,91E-02
7	1,43E-02	-8,88E-03	44	9,10E-02	-8,79E-02	81	7,24E-02	-2,56E-02
8	1,71E-02	-9,90E-03	45	9,21E-02	-9,10E-02	82	7,11E-02	-2,22E-02
9	1,98E-02	-1,10E-02	46	9,31E-02	-9,41E-02	83	6,96E-02	-1,87E-02
10	2,26E-02	-1,21E-02	47	9,36E-02	-9,54E-02	84	6,81E-02	-1,53E-02
11	2,53E-02	-1,33E-02	48	9,38E-02	-9,61E-02	85	6,65E-02	-1,19E-02
12	2,80E-02	-1,45E-02	49	9,41E-02	-9,67E-02	86	6,47E-02	-8,69E-03
13	3,07E-02	-1,59E-02	50	9,48E-02	-9,68E-02	87	6,28E-02	-5,64E-03
14	3,33E-02	-1,72E-02	51	9,53E-02	-9,64E-02	88	6,08E-02	-2,79E-03
15	3,60E-02	-1,87E-02	52	9,54E-02	-9,58E-02	89	5,87E-02	-1,68E-04
16	3,86E-02	-2,02E-02	53	9,52E-02	-9,52E-02	90	5,64E-02	2,24E-03
17	4,11E-02	-2,18E-02	54	9,51E-02	-9,46E-02	91	5,41E-02	4,40E-03
18	4,37E-02	-2,35E-02	55	9,49E-02	-9,40E-02	92	5,16E-02	6,30E-03
19	4,62E-02	-2,52E-02	56	9,47E-02	-9,33E-02	93	4,91E-02	7,92E-03
20	4,87E-02	-2,70E-02	57	9,46E-02	-9,27E-02	94	4,65E-02	9,27E-03
21	5,12E-02	-2,88E-02	58	9,43E-02	-9,18E-02	95	4,37E-02	1,03E-02
22	5,36E-02	-3,08E-02	59	9,36E-02	-8,91E-02	96	4,09E-02	1,11E-02
23	5,59E-02	-3,28E-02	60	9,28E-02	-8,64E-02	97	3,81E-02	1,16E-02
24	5,83E-02	-3,49E-02	61	9,21E-02	-8,37E-02	98	3,52E-02	1,19E-02
25	6,05E-02	-3,71E-02	62	9,13E-02	-8,12E-02	99	3,22E-02	1,20E-02
26	6,27E-02	-3,94E-02	63	9,06E-02	-7,87E-02	100	2,93E-02	1,18E-02
27	6,49E-02	-4,17E-02	64	8,99E-02	-7,63E-02	101	2,63E-02	1,14E-02
28	6,70E-02	-4,42E-02	65	8,91E-02	-7,39E-02	102	2,34E-02	1,10E-02
29	6,89E-02	-4,66E-02	66	8,83E-02	-7,15E-02	103	2,05E-02	1,05E-02
30	7,09E-02	-4,92E-02	67	8,76E-02	-6,91E-02	104	1,76E-02	9,93E-03
31	7,27E-02	-5,18E-02	68	8,68E-02	-6,68E-02	105	1,47E-02	9,28E-03
32	7,45E-02	-5,44E-02	69	8,59E-02	-6,44E-02	106	1,18E-02	8,57E-03
33	7,62E-02	-5,71E-02	70	8,51E-02	-6,19E-02	107	9,00E-03	7,82E-03
34	7,78E-02	-5,97E-02	71	8,42E-02	-5,93E-02	108	6,23E-03	6,84E-03
35	7,94E-02	-6,24E-02	72	8,33E-02	-5,67E-02	109	3,53E-03	5,75E-03
36	8,09E-02	-6,51E-02	73	8,23E-02	-5,40E-02	110	1,33E-03	3,88E-03
37	8,24E-02	-6,79E-02	74	8,14E-02	-5,12E-02	111	1,78E-04	1,25E-03

Table D.38: Optimized profile for test case in White [17], minimum liquid volume fraction

D

Point #	x	y	Point #	x	y	Point #	x	y
1	3,51E-03	-4,78E-03	38	7,47E-02	-3,18E-02	75	8,66E-02	-7,71E-02
2	1,23E-03	-3,03E-03	39	7,59E-02	-3,52E-02	76	8,54E-02	-7,44E-02
3	2,80E-05	-3,42E-04	40	7,71E-02	-3,85E-02	77	8,41E-02	-7,18E-02
4	5,61E-04	2,75E-03	41	7,82E-02	-4,18E-02	78	8,27E-02	-6,91E-02
5	2,18E-03	5,12E-03	42	7,93E-02	-4,50E-02	79	8,13E-02	-6,64E-02
6	4,69E-03	6,53E-03	43	8,03E-02	-4,82E-02	80	7,98E-02	-6,37E-02
7	7,44E-03	7,51E-03	44	8,13E-02	-5,13E-02	81	7,82E-02	-6,11E-02
8	1,02E-02	8,31E-03	45	8,23E-02	-5,43E-02	82	7,66E-02	-5,84E-02
9	1,31E-02	8,93E-03	46	8,32E-02	-5,72E-02	83	7,49E-02	-5,57E-02
10	1,60E-02	9,49E-03	47	8,42E-02	-6,01E-02	84	7,31E-02	-5,31E-02
11	1,88E-02	9,97E-03	48	8,51E-02	-6,28E-02	85	7,13E-02	-5,04E-02
12	2,18E-02	1,03E-02	49	8,59E-02	-6,55E-02	86	6,94E-02	-4,79E-02
13	2,47E-02	1,06E-02	50	8,68E-02	-6,81E-02	87	6,74E-02	-4,54E-02
14	2,76E-02	1,08E-02	51	8,76E-02	-7,06E-02	88	6,54E-02	-4,29E-02
15	3,05E-02	1,09E-02	52	8,85E-02	-7,30E-02	89	6,32E-02	-4,05E-02
16	3,35E-02	1,08E-02	53	8,92E-02	-7,54E-02	90	6,10E-02	-3,82E-02
17	3,64E-02	1,04E-02	54	9,00E-02	-7,77E-02	91	5,88E-02	-3,60E-02
18	3,93E-02	9,88E-03	55	9,08E-02	-8,00E-02	92	5,65E-02	-3,38E-02
19	4,21E-02	9,11E-03	56	9,15E-02	-8,23E-02	93	5,41E-02	-3,17E-02
20	4,49E-02	8,12E-03	57	9,23E-02	-8,47E-02	94	5,17E-02	-2,98E-02
21	4,76E-02	6,89E-03	58	9,30E-02	-8,71E-02	95	4,93E-02	-2,78E-02
22	5,02E-02	5,42E-03	59	9,38E-02	-8,96E-02	96	4,68E-02	-2,60E-02
23	5,27E-02	3,73E-03	60	9,45E-02	-9,22E-02	97	4,43E-02	-2,42E-02
24	5,51E-02	1,81E-03	61	9,52E-02	-9,49E-02	98	4,17E-02	-2,25E-02
25	5,74E-02	-3,06E-04	62	9,54E-02	-9,55E-02	99	3,92E-02	-2,08E-02
26	5,96E-02	-2,63E-03	63	9,54E-02	-9,58E-02	100	3,66E-02	-1,92E-02
27	6,17E-02	-5,14E-03	64	9,53E-02	-9,62E-02	101	3,39E-02	-1,77E-02
28	6,36E-02	-7,84E-03	65	9,51E-02	-9,64E-02	102	3,13E-02	-1,63E-02
29	6,55E-02	-1,07E-02	66	9,48E-02	-9,66E-02	103	2,86E-02	-1,49E-02
30	6,72E-02	-1,38E-02	67	9,45E-02	-9,66E-02	104	2,59E-02	-1,36E-02
31	6,87E-02	-1,70E-02	68	9,42E-02	-9,65E-02	105	2,32E-02	-1,23E-02
32	7,02E-02	-2,02E-02	69	9,39E-02	-9,62E-02	106	2,05E-02	-1,11E-02
33	7,16E-02	-2,36E-02	70	9,38E-02	-9,58E-02	107	1,77E-02	-1,00E-02
34	7,29E-02	-2,69E-02	71	9,12E-02	-8,82E-02	108	1,49E-02	-8,94E-03
35	9,38E-02	-9,58E-02	72	9,02E-02	-8,53E-02	109	1,21E-02	-7,92E-03
36	9,28E-02	-9,26E-02	73	8,90E-02	-8,25E-02	110	9,35E-03	-6,92E-03
37	7,35E-02	-2,84E-02	74	8,78E-02	-7,98E-02	111	6,57E-03	-5,92E-03

Table D.39: Optimized profile for test case in White [17], minimum thermodynamic losses

APPENDIX E

E.1. TWO-PHASE MODEL FOR 3D SIMULATIONS

The two phase model was tested on a complex 3D blade. The blade profiles are reported in Table E.42. The rotation angle (around the x-axis) is 9°. Figure E.5 shows the blade geometry. The total inlet conditions and the static outlet pressure of the test from [19] in Chapter 5 are used. Note that the purpose of this 3D test is to verify the presence of possible anomalies in the solver for multi-D domains. Additionally, this simulation can provide an estimation for the computational resources required to run 3D domains. Figures E.6, E.7 report the pressure and the conservative variable μ_3, proportional to the liquid volume fraction, in the domain. Hub and shroud sections are displayed. Additionally, Figure E.8 shows the liquid volume fraction on a section parallel to the Y-Z plane. No significant issues are encountered for the convergence of the simulations, and a CFL of 50 can be adopted throughout all the iterations.
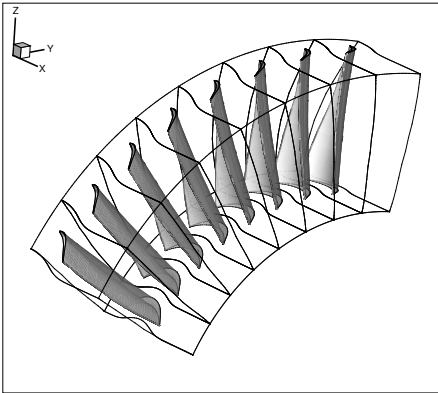
Figure E.5: Simulation domain. The profile sections of the blades are reported in section E.42.
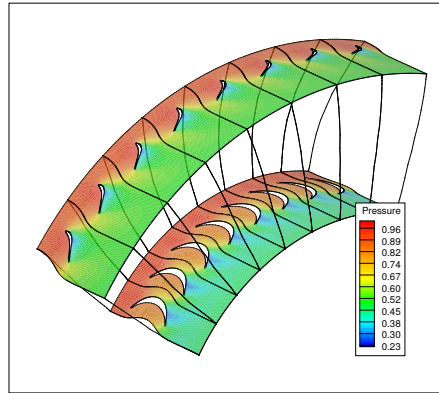
Figure E.6: Static pressure P/P_0 in the domain, hub and shroud.

A comparison is carried out between the single- and the two-phase solver in terms of time and memory requirements. Two simulations are run for 200 iterations, starting from a constant motion field. CFL is kept constant and equal to 50. A first order accuracy scheme is used. Simulations are carried out with 3 Intel(R) Core(TM) i7-7500CPU
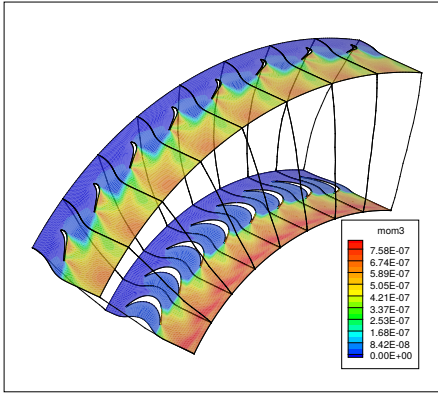
Figure E.7: Moment μ_3, proportional to the liquid volume fraction, in the domain, hub and shroud.
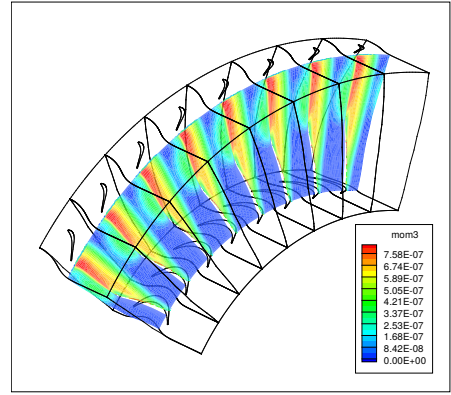
Figure E.8: Moment μ_3, proportional to the liquid volume fraction, section parallel to the x-axis.

2.7GHz 2.90GHz cores on a 233K elements mesh. Table E.40 shows the results. The performance of the two-phase solver is around 20% longer than the one of the single phase solver, and requires 30% more memory allocated.

	Single-phase	Two-phase	Ratio
Physical time	34m, 33.85s	44m, 25.25s	1.28
Max memory allocated	2671776 kB	3201408 kB	1.2

Table E.40: Comparison in terms of time and memory requirements for the single- and two-phase solver

A second comparison is carried out on the adjoint solver for the single- and the two-phase case. Due to the high memory required, a coarse mesh with 74k elements has to be adopted. Table E.41 shows the result. In agreement with Chapter 5, the two-phase adjoint is from 1.3 to 1.6 times more demanding than the single-phase one.

	Adjoint single-phase	Adjoint two-phase	Ratio
Physical time	41m, 51.24s	68m, 34.31s	1.64
Max memory allocated	8962496 kB	11972832 kB	1.34

Table E.41: Comparison in terms of time and memory requirements for the single- and two-phase discrete adjoint solver

Table E.42: Profile sections along the blade height for the 3D testcase. The table reports i) the profile number # and ii) the coordinates of the points (cartesian).

#	x(m)	y(m)	z(m)	#	x(m)	y(m)	z(m)	#	x(m)	y(m)	z(m)
1	0.1034	-0.0407	0.8382	2	0.0994	-0.0486	0.9065	3	0.0979	-0.0514	0.9292
1	0.1014	-0.0374	0.8384	2	0.0975	-0.0455	0.9066	3	0.0959	-0.0484	0.9294
1	0.0989	-0.0336	0.8385	2	0.0952	-0.0419	0.9068	3	0.0937	-0.0448	0.9296
1	0.0960	-0.0293	0.8387	2	0.0925	-0.0377	0.9070	3	0.0911	-0.0407	0.9298
1	0.0927	-0.0243	0.8388	2	0.0894	-0.0329	0.9072	3	0.0880	-0.0359	0.9299
1	0.0888	-0.0186	0.8390	2	0.0858	-0.0274	0.9074	3	0.0845	-0.0305	0.9301
1	0.0842	-0.0123	0.8391	2	0.0816	-0.0213	0.9075	3	0.0805	-0.0245	0.9303
1	0.0786	-0.0055	0.8392	2	0.0766	-0.0147	0.9077	3	0.0756	-0.0179	0.9305
1	0.0716	0.0014	0.8392	2	0.0705	-0.0077	0.9077	3	0.0698	-0.0109	0.9306
1	0.0631	0.0082	0.8392	2	0.0631	-0.0004	0.9078	3	0.0628	-0.0035	0.9306
1	0.0530	0.0148	0.8391	2	0.0543	0.0070	0.9078	3	0.0545	0.0040	0.9306
1	0.0410	0.0205	0.8389	2	0.0438	0.0139	0.9077	3	0.0446	0.0114	0.9306
1	0.0271	0.0250	0.8388	2	0.0314	0.0200	0.9076	3	0.0328	0.0181	0.9305
1	0.0113	0.0276	0.8387	2	0.0170	0.0246	0.9074	3	0.0190	0.0235	0.9303
1	-0.0061	0.0277	0.8387	2	0.0007	0.0270	0.9074	3	0.0031	0.0266	0.9303
1	-0.0219	0.0252	0.8388	2	-0.0144	0.0266	0.9074	3	-0.0117	0.0269	0.9303
1	-0.0359	0.0208	0.8389	2	-0.0281	0.0241	0.9075	3	-0.0252	0.0250	0.9303
1	-0.0480	0.0150	0.8391	2	-0.0401	0.0200	0.9076	3	-0.0372	0.0214	0.9304
1	-0.0584	0.0085	0.8392	2	-0.0505	0.0147	0.9077	3	-0.0476	0.0167	0.9305
1	-0.0670	0.0016	0.8392	2	-0.0591	0.0088	0.9077	3	-0.0563	0.0113	0.9306
1	-0.0742	-0.0054	0.8392	2	-0.0664	0.0028	0.9078	3	-0.0636	0.0056	0.9306
1	-0.0802	-0.0118	0.8391	2	-0.0725	-0.0030	0.9078	3	-0.0698	0.0001	0.9306
1	-0.0854	-0.0179	0.8390	2	-0.0777	-0.0084	0.9077	3	-0.0751	-0.0052	0.9306
1	-0.0897	-0.0233	0.8389	2	-0.0821	-0.0134	0.9077	3	-0.0794	-0.0100	0.9306
1	-0.0932	-0.0282	0.8387	2	-0.0857	-0.0179	0.9076	3	-0.0831	-0.0144	0.9305
1	-0.0962	-0.0326	0.8386	2	-0.0886	-0.0219	0.9075	3	-0.0860	-0.0183	0.9305
1	-0.0986	-0.0363	0.8384	2	-0.0910	-0.0255	0.9074	3	-0.0884	-0.0218	0.9304
1	-0.1006	-0.0395	0.8383	2	-0.0930	-0.0285	0.9073	3	-0.0904	-0.0247	0.9303
1	-0.1021	-0.0422	0.8381	2	-0.0945	-0.0310	0.9073	3	-0.0921	-0.0272	0.9302
1	-0.1034	-0.0443	0.8380	2	-0.0957	-0.0331	0.9072	3	-0.0934	-0.0292	0.9302
1	-0.1043	-0.0461	0.8379	2	-0.0966	-0.0348	0.9071	3	-0.0945	-0.0308	0.9301
1	-0.1049	-0.0475	0.8379	2	-0.0973	-0.0361	0.9071	3	-0.0952	-0.0321	0.9301
1	-0.1051	-0.0486	0.8378	2	-0.0977	-0.0371	0.9070	3	-0.0957	-0.0331	0.9300
1	-0.1052	-0.0494	0.8377	2	-0.0980	-0.0379	0.9070	3	-0.0959	-0.0340	0.9300
1	-0.1050	-0.0499	0.8377	2	-0.0979	-0.0385	0.9070	3	-0.0958	-0.0346	0.9300
1	-0.1048	-0.0503	0.8377	2	-0.0977	-0.0389	0.9069	3	-0.0956	-0.0350	0.9300
1	-0.1045	-0.0505	0.8377	2	-0.0974	-0.0391	0.9069	3	-0.0953	-0.0353	0.9300
1	-0.1042	-0.0506	0.8377	2	-0.0971	-0.0393	0.9069	3	-0.0950	-0.0355	0.9300
1	-0.1039	-0.0507	0.8377	2	-0.0967	-0.0394	0.9069	3	-0.0945	-0.0357	0.9300
1	-0.1033	-0.0506	0.8377	2	-0.0961	-0.0394	0.9069	3	-0.0939	-0.0357	0.9300
1	-0.1027	-0.0503	0.8377	2	-0.0955	-0.0390	0.9069	3	-0.0932	-0.0354	0.9300
1	-0.1018	-0.0497	0.8377	2	-0.0947	-0.0384	0.9070	3	-0.0923	-0.0349	0.9300
1	-0.1009	-0.0487	0.8378	2	-0.0936	-0.0376	0.9070	3	-0.0912	-0.0341	0.9300
1	-0.0997	-0.0474	0.8379	2	-0.0923	-0.0365	0.9070	3	-0.0899	-0.0330	0.9301
1	-0.0983	-0.0457	0.8380	2	-0.0906	-0.0351	0.9071	3	-0.0882	-0.0316	0.9301
1	-0.0965	-0.0436	0.8381	2	-0.0886	-0.0334	0.9072	3	-0.0861	-0.0299	0.9302
1	-0.0942	-0.0412	0.8382	2	-0.0862	-0.0314	0.9072	3	-0.0836	-0.0280	0.9302
1	-0.0914	-0.0384	0.8383	2	-0.0833	-0.0290	0.9073	3	-0.0807	-0.0258	0.9303
1	-0.0881	-0.0352	0.8385	2	-0.0798	-0.0263	0.9074	3	-0.0771	-0.0232	0.9304

F

#	x(m)	y(m)	z(m)	#	x(m)	y(m)	z(m)	#	x(m)	y(m)	z(m)
1	-0.0841	-0.0317	0.8386	2	-0.0757	-0.0233	0.9075	3	-0.0730	-0.0204	0.9304
1	-0.0794	-0.0279	0.8387	2	-0.0709	-0.0200	0.9076	3	-0.0681	-0.0173	0.9305
1	-0.0738	-0.0238	0.8389	2	-0.0653	-0.0166	0.9076	3	-0.0625	-0.0140	0.9305
1	-0.0673	-0.0195	0.8390	2	-0.0588	-0.0131	0.9077	3	-0.0560	-0.0107	0.9306
1	-0.0597	-0.0152	0.8391	2	-0.0512	-0.0097	0.9077	3	-0.0485	-0.0075	0.9306
1	-0.0509	-0.0111	0.8391	2	-0.0426	-0.0065	0.9078	3	-0.0400	-0.0046	0.9306
1	-0.0410	-0.0072	0.8392	2	-0.0329	-0.0037	0.9078	3	-0.0303	-0.0022	0.9306
1	-0.0297	-0.0039	0.8392	2	-0.0219	-0.0016	0.9078	3	-0.0195	-0.0004	0.9306
1	-0.0171	-0.0015	0.8392	2	-0.0098	-0.0002	0.9078	3	-0.0076	0.0004	0.9306
1	-0.0031	-0.0003	0.8392	2	0.0035	-0.0001	0.9078	3	0.0054	0.0001	0.9306
1	0.0121	-0.0006	0.8392	2	0.0178	-0.0016	0.9078	3	0.0194	-0.0020	0.9306
1	0.0259	-0.0024	0.8392	2	0.0306	-0.0045	0.9078	3	0.0318	-0.0055	0.9306
1	0.0382	-0.0053	0.8392	2	0.0420	-0.0085	0.9077	3	0.0428	-0.0100	0.9306
1	0.0491	-0.0089	0.8392	2	0.0519	-0.0131	0.9077	3	0.0522	-0.0150	0.9305
1	0.0587	-0.0130	0.8391	2	0.0604	-0.0182	0.9076	3	0.0603	-0.0203	0.9304
1	0.0670	-0.0174	0.8390	2	0.0677	-0.0232	0.9075	3	0.0673	-0.0256	0.9303
1	0.0742	-0.0217	0.8389	2	0.0739	-0.0281	0.9073	3	0.0733	-0.0306	0.9301
1	0.0803	-0.0260	0.8388	2	0.0793	-0.0328	0.9072	3	0.0784	-0.0354	0.9300
1	0.0855	-0.0300	0.8387	2	0.0838	-0.0371	0.9070	3	0.0827	-0.0397	0.9298
1	0.0899	-0.0337	0.8385	2	0.0876	-0.0410	0.9069	3	0.0864	-0.0437	0.9296
1	0.0936	-0.0371	0.8384	2	0.0909	-0.0445	0.9067	3	0.0895	-0.0472	0.9294
1	0.0967	-0.0402	0.8382	2	0.0936	-0.0477	0.9065	3	0.0922	-0.0503	0.9293
1	0.0992	-0.0429	0.8381	2	0.0959	-0.0504	0.9064	3	0.0944	-0.0530	0.9291
1	0.1013	-0.0452	0.8380	2	0.0978	-0.0527	0.9062	3	0.0962	-0.0553	0.9290
1	0.1031	-0.0472	0.8379	2	0.0993	-0.0547	0.9061	3	0.0977	-0.0573	0.9289
1	0.1044	-0.0489	0.8378	2	0.1006	-0.0564	0.9060	3	0.0990	-0.0590	0.9288
1	0.1056	-0.0503	0.8377	2	0.1016	-0.0578	0.9059	3	0.1000	-0.0604	0.9287
1	0.1065	-0.0514	0.8376	2	0.1025	-0.0589	0.9059	3	0.1008	-0.0615	0.9286
1	0.1072	-0.0524	0.8376	2	0.1032	-0.0599	0.9058	3	0.1015	-0.0625	0.9285
1	0.1078	-0.0532	0.8375	2	0.1037	-0.0607	0.9058	3	0.1020	-0.0633	0.9285
1	0.1083	-0.0539	0.8375	2	0.1042	-0.0613	0.9057	3	0.1025	-0.0640	0.9284
1	0.1088	-0.0545	0.8374	2	0.1046	-0.0620	0.9057	3	0.1029	-0.0646	0.9284
1	0.1092	-0.0550	0.8374	2	0.1050	-0.0625	0.9056	3	0.1034	-0.0652	0.9284
1	0.1096	-0.0556	0.8374	2	0.1054	-0.0631	0.9056	3	0.1037	-0.0658	0.9283
1	0.1101	-0.0560	0.8373	2	0.1059	-0.0636	0.9056	3	0.1043	-0.0662	0.9283
1	0.1108	-0.0562	0.8373	2	0.1066	-0.0637	0.9055	3	0.1049	-0.0664	0.9283
1	0.1114	-0.0559	0.8373	2	0.1073	-0.0635	0.9056	3	0.1056	-0.0661	0.9283
1	0.1119	-0.0554	0.8374	2	0.1077	-0.0630	0.9056	3	0.1060	-0.0656	0.9283
1	0.1120	-0.0548	0.8374	2	0.1079	-0.0623	0.9056	3	0.1062	-0.0650	0.9284
1	0.1118	-0.0541	0.8375	2	0.1077	-0.0617	0.9057	3	0.1060	-0.0643	0.9284
1	0.1115	-0.0535	0.8375	2	0.1073	-0.0611	0.9057	3	0.1056	-0.0637	0.9285
1	0.1111	-0.0529	0.8375	2	0.1069	-0.0605	0.9058	3	0.1052	-0.0631	0.9285
1	0.1107	-0.0522	0.8376	2	0.1065	-0.0598	0.9058	3	0.1048	-0.0624	0.9285
1	0.1102	-0.0514	0.8376	2	0.1060	-0.0590	0.9059	3	0.1043	-0.0616	0.9286
1	0.1095	-0.0504	0.8377	2	0.1053	-0.0580	0.9059	3	0.1037	-0.0606	0.9287
1	0.1088	-0.0491	0.8378	2	0.1046	-0.0568	0.9060	3	0.1029	-0.0594	0.9287
1	0.1078	-0.0476	0.8378	2	0.1036	-0.0553	0.9061	3	0.1020	-0.0580	0.9288
1	0.1066	-0.0457	0.8380	2	0.1025	-0.0535	0.9062	3	0.1009	-0.0562	0.9289
1	0.1052	-0.0434	0.8381	2	0.1011	-0.0513	0.9063	3	0.0995	-0.0540	0.9291

F

#	x(m)	y(m)	z(m)	#	x(m)	y(m)	z(m)	#	x(m)	y(m)	z(m)
4	0.0942	-0.0563	0.9747	5	0.0890	-0.0611	1.0203	6	0.0842	-0.0628	1.0507
4	0.0923	-0.0533	0.9749	5	0.0872	-0.0582	1.0204	6	0.0824	-0.0601	1.0508
4	0.0900	-0.0499	0.9751	5	0.0851	-0.0549	1.0206	6	0.0804	-0.0569	1.0510
4	0.0874	-0.0460	0.9753	5	0.0827	-0.0511	1.0208	6	0.0781	-0.0532	1.0512
4	0.0844	-0.0414	0.9755	5	0.0799	-0.0467	1.0210	6	0.0755	-0.0490	1.0514
4	0.0809	-0.0363	0.9757	5	0.0768	-0.0417	1.0212	6	0.0725	-0.0442	1.0516
4	0.0769	-0.0305	0.9759	5	0.0732	-0.0360	1.0214	6	0.0691	-0.0388	1.0518
4	0.0724	-0.0240	0.9761	5	0.0691	-0.0297	1.0216	6	0.0652	-0.0328	1.0520
4	0.0672	-0.0169	0.9762	5	0.0643	-0.0228	1.0218	6	0.0608	-0.0261	1.0522
4	0.0609	-0.0093	0.9763	5	0.0588	-0.0153	1.0220	6	0.0556	-0.0188	1.0524
4	0.0534	-0.0015	0.9764	5	0.0523	-0.0073	1.0221	6	0.0496	-0.0110	1.0525
4	0.0444	0.0064	0.9763	5	0.0445	0.0009	1.0221	6	0.0426	-0.0028	1.0526
4	0.0338	0.0141	0.9763	5	0.0352	0.0092	1.0220	6	0.0344	0.0058	1.0525
4	0.0211	0.0207	0.9761	5	0.0240	0.0169	1.0219	6	0.0243	0.0140	1.0525
4	0.0062	0.0253	0.9760	5	0.0107	0.0232	1.0218	6	0.0121	0.0210	1.0524
4	-0.0080	0.0268	0.9760	5	-0.0026	0.0262	1.0217	6	-0.0003	0.0250	1.0523
4	-0.0212	0.0258	0.9760	5	-0.0151	0.0266	1.0217	6	-0.0121	0.0265	1.0522
4	-0.0329	0.0231	0.9761	5	-0.0265	0.0253	1.0218	6	-0.0231	0.0260	1.0522
4	-0.0431	0.0193	0.9762	5	-0.0366	0.0227	1.0218	6	-0.0328	0.0241	1.0523
4	-0.0519	0.0147	0.9762	5	-0.0454	0.0191	1.0219	6	-0.0414	0.0212	1.0523
4	-0.0593	0.0097	0.9763	5	-0.0529	0.0150	1.0220	6	-0.0488	0.0178	1.0524
4	-0.0656	0.0048	0.9763	5	-0.0592	0.0107	1.0220	6	-0.0551	0.0142	1.0525
4	-0.0709	0.0001	0.9764	5	-0.0646	0.0065	1.0221	6	-0.0605	0.0105	1.0525
4	-0.0754	-0.0043	0.9764	5	-0.0691	0.0026	1.0221	6	-0.0650	0.0069	1.0525
4	-0.0791	-0.0082	0.9763	5	-0.0728	-0.0012	1.0221	6	-0.0688	0.0035	1.0526
4	-0.0822	-0.0118	0.9763	5	-0.0759	-0.0046	1.0221	6	-0.0720	0.0005	1.0526
4	-0.0847	-0.0149	0.9762	5	-0.0786	-0.0075	1.0221	6	-0.0747	-0.0021	1.0526
4	-0.0868	-0.0175	0.9762	5	-0.0808	-0.0100	1.0220	6	-0.0770	-0.0043	1.0526
4	-0.0884	-0.0198	0.9762	5	-0.0827	-0.0120	1.0220	6	-0.0788	-0.0062	1.0525
4	-0.0897	-0.0216	0.9761	5	-0.0842	-0.0137	1.0220	6	-0.0803	-0.0078	1.0525
4	-0.0906	-0.0231	0.9761	5	-0.0855	-0.0151	1.0220	6	-0.0815	-0.0092	1.0525
4	-0.0911	-0.0244	0.9761	5	-0.0864	-0.0163	1.0220	6	-0.0824	-0.0103	1.0525
4	-0.0914	-0.0254	0.9760	5	-0.0869	-0.0172	1.0219	6	-0.0831	-0.0111	1.0525
4	-0.0915	-0.0261	0.9760	5	-0.0873	-0.0181	1.0219	6	-0.0834	-0.0119	1.0525
4	-0.0914	-0.0266	0.9760	5	-0.0873	-0.0187	1.0219	6	-0.0835	-0.0125	1.0525
4	-0.0913	-0.0269	0.9760	5	-0.0871	-0.0192	1.0219	6	-0.0833	-0.0130	1.0525
4	-0.0911	-0.0272	0.9760	5	-0.0869	-0.0196	1.0219	6	-0.0831	-0.0134	1.0525
4	-0.0908	-0.0274	0.9760	5	-0.0865	-0.0199	1.0219	6	-0.0828	-0.0138	1.0525
4	-0.0905	-0.0275	0.9760	5	-0.0861	-0.0202	1.0219	6	-0.0823	-0.0140	1.0525
4	-0.0900	-0.0275	0.9760	5	-0.0854	-0.0203	1.0219	6	-0.0817	-0.0142	1.0525
4	-0.0893	-0.0273	0.9760	5	-0.0846	-0.0202	1.0219	6	-0.0810	-0.0140	1.0525
4	-0.0885	-0.0270	0.9760	5	-0.0836	-0.0198	1.0219	6	-0.0800	-0.0137	1.0525
4	-0.0873	-0.0265	0.9760	5	-0.0824	-0.0193	1.0219	6	-0.0788	-0.0131	1.0525
4	-0.0860	-0.0257	0.9760	5	-0.0810	-0.0184	1.0219	6	-0.0773	-0.0125	1.0525
4	-0.0844	-0.0245	0.9761	5	-0.0792	-0.0174	1.0219	6	-0.0755	-0.0117	1.0525
4	-0.0823	-0.0231	0.9761	5	-0.0770	-0.0162	1.0220	6	-0.0734	-0.0106	1.0525
4	-0.0798	-0.0215	0.9761	5	-0.0743	-0.0148	1.0220	6	-0.0708	-0.0094	1.0525
4	-0.0768	-0.0196	0.9762	5	-0.0712	-0.0131	1.0220	6	-0.0677	-0.0080	1.0525
4	-0.0732	-0.0174	0.9762	5	-0.0676	-0.0113	1.0220	6	-0.0641	-0.0064	1.0525
4	-0.0691	-0.0151	0.9762	5	-0.0633	-0.0092	1.0220	6	-0.0600	-0.0047	1.0525

F

#	x(m)	y(m)	z(m)	#	x(m)	y(m)	z(m)	#	x(m)	y(m)	z(m)
4	-0.0642	-0.0125	0.9763	5	-0.0585	-0.0070	1.0221	6	-0.0552	-0.0029	1.0526
4	-0.0586	-0.0097	0.9763	5	-0.0529	-0.0046	1.0221	6	-0.0497	-0.0010	1.0526
4	-0.0522	-0.0068	0.9763	5	-0.0466	-0.0022	1.0221	6	-0.0435	0.0008	1.0526
4	-0.0448	-0.0040	0.9764	5	-0.0394	0.0001	1.0221	6	-0.0364	0.0024	1.0526
4	-0.0365	-0.0015	0.9764	5	-0.0312	0.0020	1.0221	6	-0.0285	0.0036	1.0526
4	-0.0270	0.0004	0.9764	5	-0.0221	0.0032	1.0221	6	-0.0197	0.0041	1.0526
4	-0.0165	0.0016	0.9764	5	-0.0119	0.0034	1.0221	6	-0.0100	0.0035	1.0526
4	-0.0049	0.0017	0.9764	5	-0.0009	0.0023	1.0221	6	0.0004	0.0016	1.0526
4	0.0076	0.0002	0.9764	5	0.0107	-0.0006	1.0221	6	0.0113	-0.0020	1.0526
4	0.0209	-0.0033	0.9764	5	0.0229	-0.0053	1.0221	6	0.0225	-0.0074	1.0525
4	0.0325	-0.0080	0.9763	5	0.0334	-0.0111	1.0220	6	0.0322	-0.0135	1.0525
4	0.0426	-0.0136	0.9763	5	0.0424	-0.0172	1.0219	6	0.0405	-0.0198	1.0524
4	0.0513	-0.0193	0.9762	5	0.0502	-0.0234	1.0218	6	0.0478	-0.0259	1.0522
4	0.0588	-0.0249	0.9760	5	0.0569	-0.0293	1.0217	6	0.0540	-0.0318	1.0521
4	0.0652	-0.0305	0.9759	5	0.0627	-0.0349	1.0215	6	0.0594	-0.0374	1.0519
4	0.0707	-0.0357	0.9757	5	0.0677	-0.0402	1.0213	6	0.0640	-0.0426	1.0517
4	0.0755	-0.0405	0.9755	5	0.0719	-0.0450	1.0211	6	0.0680	-0.0473	1.0515
4	0.0796	-0.0448	0.9753	5	0.0756	-0.0494	1.0209	6	0.0715	-0.0515	1.0513
4	0.0831	-0.0487	0.9751	5	0.0788	-0.0533	1.0207	6	0.0745	-0.0553	1.0511
4	0.0861	-0.0522	0.9750	5	0.0815	-0.0567	1.0205	6	0.0770	-0.0586	1.0509
4	0.0886	-0.0552	0.9748	5	0.0839	-0.0598	1.0203	6	0.0792	-0.0615	1.0508
4	0.0908	-0.0579	0.9746	5	0.0858	-0.0624	1.0202	6	0.0811	-0.0641	1.0506
4	0.0925	-0.0602	0.9745	5	0.0874	-0.0646	1.0200	6	0.0826	-0.0663	1.0505
4	0.0940	-0.0621	0.9744	5	0.0888	-0.0665	1.0199	6	0.0839	-0.0681	1.0504
4	0.0953	-0.0637	0.9743	5	0.0899	-0.0681	1.0198	6	0.0850	-0.0697	1.0503
4	0.0963	-0.0651	0.9742	5	0.0909	-0.0695	1.0197	6	0.0859	-0.0710	1.0502
4	0.0971	-0.0662	0.9741	5	0.0916	-0.0706	1.0196	6	0.0867	-0.0721	1.0501
4	0.0977	-0.0671	0.9741	5	0.0923	-0.0716	1.0196	6	0.0873	-0.0730	1.0500
4	0.0983	-0.0679	0.9740	5	0.0928	-0.0723	1.0195	6	0.0878	-0.0738	1.0500
4	0.0988	-0.0685	0.9740	5	0.0933	-0.0730	1.0195	6	0.0882	-0.0745	1.0499
4	0.0992	-0.0691	0.9739	5	0.0937	-0.0737	1.0194	6	0.0886	-0.0751	1.0499
4	0.0996	-0.0697	0.9739	5	0.0941	-0.0743	1.0194	6	0.0890	-0.0757	1.0498
4	0.1000	-0.0703	0.9738	5	0.0945	-0.0748	1.0193	6	0.0894	-0.0763	1.0498
4	0.1005	-0.0707	0.9738	5	0.0950	-0.0753	1.0193	6	0.0899	-0.0767	1.0498
4	0.1012	-0.0709	0.9738	5	0.0956	-0.0754	1.0193	6	0.0906	-0.0769	1.0497
4	0.1019	-0.0706	0.9738	5	0.0963	-0.0752	1.0193	6	0.0913	-0.0767	1.0498
4	0.1023	-0.0701	0.9738	5	0.0968	-0.0747	1.0193	6	0.0917	-0.0762	1.0498
4	0.1025	-0.0695	0.9739	5	0.0969	-0.0741	1.0194	6	0.0919	-0.0755	1.0498
4	0.1023	-0.0688	0.9739	5	0.0967	-0.0734	1.0194	6	0.0917	-0.0748	1.0499
4	0.1019	-0.0682	0.9740	5	0.0963	-0.0728	1.0195	6	0.0913	-0.0743	1.0499
4	0.1015	-0.0676	0.9740	5	0.0960	-0.0722	1.0195	6	0.0909	-0.0736	1.0500
4	0.1011	-0.0670	0.9741	5	0.0955	-0.0715	1.0196	6	0.0905	-0.0730	1.0500
4	0.1006	-0.0662	0.9741	5	0.0950	-0.0707	1.0196	6	0.0900	-0.0722	1.0501
4	0.1000	-0.0652	0.9742	5	0.0944	-0.0698	1.0197	6	0.0894	-0.0713	1.0501
4	0.0992	-0.0640	0.9743	5	0.0937	-0.0686	1.0198	6	0.0887	-0.0701	1.0502
4	0.0983	-0.0626	0.9744	5	0.0928	-0.0672	1.0199	6	0.0879	-0.0688	1.0503
4	0.0972	-0.0608	0.9745	5	0.0918	-0.0655	1.0200	6	0.0868	-0.0671	1.0504
4	0.0958	-0.0588	0.9746	5	0.0905	-0.0635	1.0201	6	0.0856	-0.0652	1.0505

F

#	x(m)	y(m)	z(m)	#	x(m)	y(m)	z(m)	#	x(m)	y(m)	z(m)
7	0.0790	-0.0639	1.0812	8	0.0740	-0.0645	1.1117	9	0.0702	-0.0645	1.1422
7	0.0774	-0.0613	1.0813	8	0.0725	-0.0620	1.1118	9	0.0687	-0.0621	1.1423
7	0.0755	-0.0582	1.0815	8	0.0707	-0.0591	1.1120	9	0.0670	-0.0593	1.1425
7	0.0733	-0.0547	1.0817	8	0.0686	-0.0557	1.1121	9	0.0650	-0.0561	1.1426
7	0.0708	-0.0507	1.0819	8	0.0662	-0.0519	1.1123	9	0.0627	-0.0524	1.1428
7	0.0679	-0.0461	1.0821	8	0.0635	-0.0475	1.1125	9	0.0601	-0.0482	1.1430
7	0.0647	-0.0409	1.0823	8	0.0604	-0.0426	1.1127	9	0.0572	-0.0435	1.1432
7	0.0610	-0.0351	1.0825	8	0.0570	-0.0371	1.1129	9	0.0539	-0.0382	1.1434
7	0.0569	-0.0287	1.0827	8	0.0531	-0.0310	1.1131	9	0.0502	-0.0324	1.1435
7	0.0521	-0.0217	1.0828	8	0.0487	-0.0242	1.1133	9	0.0460	-0.0260	1.1437
7	0.0466	-0.0142	1.0829	8	0.0437	-0.0169	1.1134	9	0.0414	-0.0189	1.1438
7	0.0403	-0.0061	1.0830	8	0.0379	-0.0091	1.1135	9	0.0361	-0.0113	1.1439
7	0.0329	0.0025	1.0830	8	0.0312	-0.0007	1.1135	9	0.0299	-0.0031	1.1440
7	0.0240	0.0109	1.0830	8	0.0234	0.0079	1.1135	9	0.0227	0.0053	1.1440
7	0.0130	0.0186	1.0829	8	0.0137	0.0160	1.1134	9	0.0139	0.0135	1.1439
7	0.0018	0.0235	1.0828	8	0.0035	0.0218	1.1133	9	0.0047	0.0199	1.1438
7	-0.0093	0.0260	1.0827	8	-0.0066	0.0253	1.1132	9	-0.0045	0.0243	1.1437
7	-0.0196	0.0266	1.0827	8	-0.0164	0.0268	1.1132	9	-0.0136	0.0266	1.1437
7	-0.0291	0.0255	1.0827	8	-0.0253	0.0266	1.1132	9	-0.0221	0.0272	1.1437
7	-0.0374	0.0234	1.0828	8	-0.0334	0.0252	1.1132	9	-0.0299	0.0266	1.1437
7	-0.0446	0.0205	1.0828	8	-0.0405	0.0232	1.1133	9	-0.0368	0.0252	1.1437
7	-0.0508	0.0175	1.0829	8	-0.0466	0.0207	1.1133	9	-0.0428	0.0233	1.1438
7	-0.0562	0.0144	1.0829	8	-0.0518	0.0180	1.1134	9	-0.0480	0.0211	1.1438
7	-0.0607	0.0113	1.0830	8	-0.0564	0.0154	1.1134	9	-0.0525	0.0189	1.1438
7	-0.0646	0.0084	1.0830	8	-0.0603	0.0130	1.1134	9	-0.0563	0.0168	1.1439
7	-0.0679	0.0058	1.0830	8	-0.0636	0.0107	1.1135	9	-0.0596	0.0148	1.1439
7	-0.0706	0.0035	1.0830	8	-0.0663	0.0087	1.1135	9	-0.0624	0.0130	1.1439
7	-0.0729	0.0015	1.0830	8	-0.0687	0.0069	1.1135	9	-0.0647	0.0114	1.1439
7	-0.0748	-0.0003	1.0830	8	-0.0706	0.0053	1.1135	9	-0.0666	0.0100	1.1440
7	-0.0763	-0.0018	1.0830	8	-0.0721	0.0040	1.1135	9	-0.0680	0.0087	1.1440
7	-0.0774	-0.0031	1.0830	8	-0.0734	0.0029	1.1135	9	-0.0692	0.0075	1.1440
7	-0.0783	-0.0041	1.0830	8	-0.0743	0.0018	1.1135	9	-0.0701	0.0065	1.1440
7	-0.0790	-0.0050	1.0830	8	-0.0749	0.0010	1.1135	9	-0.0707	0.0058	1.1440
7	-0.0794	-0.0057	1.0830	8	-0.0752	0.0002	1.1135	9	-0.0711	0.0050	1.1440
7	-0.0794	-0.0064	1.0830	8	-0.0753	-0.0005	1.1135	9	-0.0712	0.0044	1.1440
7	-0.0793	-0.0069	1.0830	8	-0.0752	-0.0010	1.1135	9	-0.0711	0.0038	1.1440
7	-0.0791	-0.0073	1.0830	8	-0.0749	-0.0015	1.1135	9	-0.0709	0.0034	1.1440
7	-0.0787	-0.0076	1.0830	8	-0.0746	-0.0018	1.1135	9	-0.0705	0.0030	1.1440
7	-0.0783	-0.0079	1.0830	8	-0.0742	-0.0021	1.1135	9	-0.0701	0.0027	1.1440
7	-0.0777	-0.0081	1.0830	8	-0.0735	-0.0023	1.1135	9	-0.0695	0.0025	1.1440
7	-0.0769	-0.0080	1.0830	8	-0.0727	-0.0023	1.1135	9	-0.0687	0.0025	1.1440
7	-0.0760	-0.0076	1.0830	8	-0.0718	-0.0021	1.1135	9	-0.0677	0.0028	1.1440
7	-0.0748	-0.0072	1.0830	8	-0.0706	-0.0017	1.1135	9	-0.0666	0.0031	1.1440
7	-0.0733	-0.0066	1.0830	8	-0.0692	-0.0011	1.1135	9	-0.0651	0.0035	1.1440
7	-0.0715	-0.0059	1.0830	8	-0.0674	-0.0004	1.1135	9	-0.0634	0.0039	1.1440
7	-0.0694	-0.0050	1.0830	8	-0.0653	0.0004	1.1135	9	-0.0613	0.0045	1.1440
7	-0.0669	-0.0039	1.0830	8	-0.0629	0.0013	1.1135	9	-0.0589	0.0052	1.1440
7	-0.0639	-0.0027	1.0830	8	-0.0599	0.0022	1.1135	9	-0.0560	0.0059	1.1440
7	-0.0604	-0.0014	1.0830	8	-0.0565	0.0032	1.1135	9	-0.0526	0.0066	1.1440

F

#	x(m)	y(m)	z(m)	#	x(m)	y(m)	z(m)	#	x(m)	y(m)	z(m)
7	-0.0563	-0.0001	1.0830	8	-0.0525	0.0042	1.1135	9	-0.0488	0.0072	1.1440
7	-0.0516	0.0013	1.0830	8	-0.0479	0.0051	1.1135	9	-0.0443	0.0077	1.1440
7	-0.0463	0.0026	1.0830	8	-0.0427	0.0059	1.1135	9	-0.0393	0.0080	1.1440
7	-0.0402	0.0037	1.0830	8	-0.0369	0.0064	1.1135	9	-0.0337	0.0080	1.1440
7	-0.0334	0.0046	1.0830	8	-0.0303	0.0065	1.1135	9	-0.0275	0.0076	1.1440
7	-0.0258	0.0049	1.0830	8	-0.0231	0.0061	1.1135	9	-0.0207	0.0066	1.1440
7	-0.0174	0.0046	1.0830	8	-0.0152	0.0049	1.1135	9	-0.0133	0.0048	1.1440
7	-0.0083	0.0033	1.0830	8	-0.0068	0.0028	1.1135	9	-0.0054	0.0021	1.1440
7	0.0014	0.0006	1.0830	8	0.0022	-0.0005	1.1135	9	0.0029	-0.0016	1.1440
7	0.0114	-0.0036	1.0830	8	0.0114	-0.0052	1.1135	9	0.0114	-0.0066	1.1440
7	0.0217	-0.0095	1.0830	8	0.0207	-0.0115	1.1135	9	0.0200	-0.0130	1.1439
7	0.0305	-0.0158	1.0829	8	0.0287	-0.0179	1.1134	9	0.0274	-0.0193	1.1438
7	0.0382	-0.0220	1.0828	8	0.0357	-0.0241	1.1133	9	0.0339	-0.0255	1.1437
7	0.0448	-0.0281	1.0827	8	0.0418	-0.0301	1.1131	9	0.0396	-0.0313	1.1436
7	0.0506	-0.0339	1.0825	8	0.0471	-0.0358	1.1129	9	0.0445	-0.0368	1.1434
7	0.0556	-0.0393	1.0823	8	0.0518	-0.0410	1.1128	9	0.0488	-0.0419	1.1432
7	0.0599	-0.0443	1.0821	8	0.0558	-0.0458	1.1126	9	0.0526	-0.0466	1.1431
7	0.0636	-0.0488	1.0819	8	0.0594	-0.0501	1.1124	9	0.0559	-0.0507	1.1429
7	0.0669	-0.0529	1.0817	8	0.0624	-0.0540	1.1122	9	0.0589	-0.0545	1.1427
7	0.0697	-0.0565	1.0816	8	0.0651	-0.0575	1.1120	9	0.0614	-0.0579	1.1425
7	0.0721	-0.0597	1.0814	8	0.0674	-0.0606	1.1119	9	0.0636	-0.0608	1.1424
7	0.0742	-0.0626	1.0812	8	0.0694	-0.0633	1.1117	9	0.0655	-0.0634	1.1422
7	0.0760	-0.0650	1.0811	8	0.0710	-0.0656	1.1116	9	0.0671	-0.0657	1.1421
7	0.0775	-0.0671	1.0810	8	0.0725	-0.0677	1.1115	9	0.0685	-0.0676	1.1420
7	0.0787	-0.0689	1.0808	8	0.0737	-0.0694	1.1114	9	0.0696	-0.0693	1.1419
7	0.0798	-0.0705	1.0807	8	0.0747	-0.0709	1.1113	9	0.0706	-0.0708	1.1418
7	0.0806	-0.0718	1.0807	8	0.0755	-0.0721	1.1112	9	0.0714	-0.0720	1.1417
7	0.0813	-0.0728	1.0806	8	0.0762	-0.0732	1.1111	9	0.0721	-0.0730	1.1417
7	0.0820	-0.0738	1.0805	8	0.0768	-0.0741	1.1111	9	0.0727	-0.0739	1.1416
7	0.0825	-0.0745	1.0805	8	0.0773	-0.0748	1.1110	9	0.0732	-0.0746	1.1416
7	0.0829	-0.0752	1.0804	8	0.0777	-0.0755	1.1110	9	0.0737	-0.0753	1.1415
7	0.0833	-0.0759	1.0804	8	0.0781	-0.0761	1.1109	9	0.0741	-0.0759	1.1415
7	0.0837	-0.0765	1.0803	8	0.0785	-0.0767	1.1109	9	0.0745	-0.0765	1.1414
7	0.0841	-0.0771	1.0803	8	0.0789	-0.0773	1.1108	9	0.0749	-0.0771	1.1414
7	0.0846	-0.0775	1.0803	8	0.0794	-0.0778	1.1108	9	0.0754	-0.0776	1.1414
7	0.0853	-0.0777	1.0803	8	0.0801	-0.0779	1.1108	9	0.0760	-0.0777	1.1414
7	0.0859	-0.0775	1.0803	8	0.0807	-0.0777	1.1108	9	0.0767	-0.0775	1.1414
7	0.0864	-0.0770	1.0803	8	0.0812	-0.0772	1.1108	9	0.0772	-0.0770	1.1414
7	0.0866	-0.0763	1.0803	8	0.0814	-0.0766	1.1109	9	0.0773	-0.0763	1.1415
7	0.0864	-0.0756	1.0804	8	0.0812	-0.0759	1.1109	9	0.0771	-0.0757	1.1415
7	0.0860	-0.0750	1.0804	8	0.0808	-0.0753	1.1110	9	0.0768	-0.0751	1.1415
7	0.0856	-0.0744	1.0805	8	0.0804	-0.0747	1.1110	9	0.0764	-0.0745	1.1416
7	0.0852	-0.0737	1.0805	8	0.0800	-0.0740	1.1111	9	0.0760	-0.0738	1.1416
7	0.0847	-0.0730	1.0806	8	0.0795	-0.0733	1.1111	9	0.0755	-0.0730	1.1417
7	0.0841	-0.0720	1.0806	8	0.0790	-0.0723	1.1112	9	0.0749	-0.0722	1.1417
7	0.0834	-0.0709	1.0807	8	0.0783	-0.0713	1.1112	9	0.0743	-0.0711	1.1418
7	0.0826	-0.0696	1.0808	8	0.0775	-0.0700	1.1113	9	0.0735	-0.0698	1.1419
7	0.0816	-0.0680	1.0809	8	0.0765	-0.0685	1.1114	9	0.0726	-0.0684	1.1420
7	0.0804	-0.0661	1.0810	8	0.0754	-0.0666	1.1115	9	0.0715	-0.0666	1.1421

F

#	x(m)	y(m)	z(m)	#	x(m)	y(m)	z(m)	#	x(m)	y(m)	z(m)
10	0.0634	-0.0636	1.2033	11	0.0543	-0.0610	1.2950	12	0.0499	-0.0589	1.3408
10	0.0621	-0.0613	1.2034	11	0.0530	-0.0590	1.2951	12	0.0488	-0.0569	1.3409
10	0.0605	-0.0587	1.2035	11	0.0516	-0.0566	1.2952	12	0.0475	-0.0546	1.3410
10	0.0586	-0.0557	1.2037	11	0.0501	-0.0538	1.2953	12	0.0460	-0.0520	1.3411
10	0.0566	-0.0523	1.2038	11	0.0482	-0.0508	1.2954	12	0.0443	-0.0490	1.3412
10	0.0542	-0.0485	1.2040	11	0.0462	-0.0473	1.2955	12	0.0424	-0.0457	1.3413
10	0.0516	-0.0442	1.2042	11	0.0439	-0.0434	1.2957	12	0.0402	-0.0420	1.3415
10	0.0486	-0.0393	1.2043	11	0.0414	-0.0390	1.2958	12	0.0378	-0.0378	1.3416
10	0.0453	-0.0340	1.2045	11	0.0385	-0.0342	1.2960	12	0.0352	-0.0332	1.3417
10	0.0416	-0.0280	1.2046	11	0.0354	-0.0288	1.2961	12	0.0322	-0.0281	1.3418
10	0.0375	-0.0216	1.2048	11	0.0319	-0.0229	1.2962	12	0.0289	-0.0225	1.3419
10	0.0328	-0.0145	1.2049	11	0.0279	-0.0165	1.2963	12	0.0252	-0.0164	1.3420
10	0.0275	-0.0069	1.2049	11	0.0233	-0.0097	1.2964	12	0.0211	-0.0098	1.3421
10	0.0213	0.0010	1.2050	11	0.0182	-0.0024	1.2964	12	0.0166	-0.0026	1.3421
10	0.0138	0.0090	1.2049	11	0.0123	0.0053	1.2964	12	0.0114	0.0050	1.3421
10	0.0063	0.0158	1.2049	11	0.0063	0.0119	1.2963	12	0.0060	0.0115	1.3421
10	-0.0011	0.0214	1.2048	11	0.0003	0.0176	1.2963	12	0.0005	0.0170	1.3420
10	-0.0087	0.0253	1.2047	11	-0.0058	0.0221	1.2962	12	-0.0050	0.0216	1.3419
10	-0.0161	0.0277	1.2046	11	-0.0118	0.0255	1.2961	12	-0.0105	0.0252	1.3419
10	-0.0231	0.0288	1.2046	11	-0.0175	0.0280	1.2961	12	-0.0157	0.0280	1.3418
10	-0.0296	0.0287	1.2046	11	-0.0230	0.0295	1.2961	12	-0.0207	0.0300	1.3418
10	-0.0353	0.0277	1.2046	11	-0.0281	0.0302	1.2960	12	-0.0253	0.0312	1.3418
10	-0.0402	0.0264	1.2047	11	-0.0326	0.0302	1.2960	12	-0.0296	0.0318	1.3417
10	-0.0446	0.0249	1.2047	11	-0.0367	0.0298	1.2961	12	-0.0334	0.0319	1.3417
10	-0.0483	0.0233	1.2047	11	-0.0401	0.0291	1.2961	12	-0.0368	0.0317	1.3417
10	-0.0515	0.0218	1.2048	11	-0.0431	0.0282	1.2961	12	-0.0397	0.0313	1.3418
10	-0.0542	0.0203	1.2048	11	-0.0457	0.0273	1.2961	12	-0.0421	0.0307	1.3418
10	-0.0565	0.0190	1.2048	11	-0.0479	0.0265	1.2961	12	-0.0442	0.0302	1.3418
10	-0.0584	0.0178	1.2048	11	-0.0497	0.0257	1.2961	12	-0.0460	0.0297	1.3418
10	-0.0600	0.0168	1.2048	11	-0.0512	0.0251	1.2962	12	-0.0474	0.0291	1.3418
10	-0.0612	0.0159	1.2049	11	-0.0525	0.0245	1.2962	12	-0.0486	0.0287	1.3418
10	-0.0622	0.0151	1.2049	11	-0.0535	0.0240	1.2962	12	-0.0495	0.0283	1.3418
10	-0.0629	0.0143	1.2049	11	-0.0542	0.0235	1.2962	12	-0.0502	0.0279	1.3418
10	-0.0634	0.0136	1.2049	11	-0.0548	0.0230	1.2962	12	-0.0508	0.0276	1.3418
10	-0.0635	0.0129	1.2049	11	-0.0551	0.0225	1.2962	12	-0.0511	0.0272	1.3418
10	-0.0635	0.0123	1.2049	11	-0.0552	0.0220	1.2962	12	-0.0512	0.0268	1.3419
10	-0.0634	0.0118	1.2049	11	-0.0551	0.0215	1.2962	12	-0.0513	0.0264	1.3419
10	-0.0631	0.0113	1.2049	11	-0.0550	0.0211	1.2962	12	-0.0512	0.0260	1.3419
10	-0.0626	0.0109	1.2049	11	-0.0547	0.0206	1.2962	12	-0.0510	0.0256	1.3419
10	-0.0621	0.0106	1.2049	11	-0.0543	0.0202	1.2962	12	-0.0507	0.0252	1.3419
10	-0.0613	0.0105	1.2049	11	-0.0537	0.0200	1.2962	12	-0.0501	0.0249	1.3419
10	-0.0603	0.0105	1.2049	11	-0.0528	0.0198	1.2962	12	-0.0494	0.0246	1.3419
10	-0.0591	0.0107	1.2049	11	-0.0518	0.0197	1.2963	12	-0.0485	0.0243	1.3419
10	-0.0577	0.0109	1.2049	11	-0.0505	0.0195	1.2963	12	-0.0474	0.0239	1.3419
10	-0.0560	0.0111	1.2049	11	-0.0490	0.0193	1.2963	12	-0.0460	0.0235	1.3419
10	-0.0539	0.0114	1.2049	11	-0.0472	0.0190	1.2963	12	-0.0444	0.0230	1.3419
10	-0.0516	0.0116	1.2049	11	-0.0450	0.0187	1.2963	12	-0.0424	0.0225	1.3419
10	-0.0488	0.0118	1.2049	11	-0.0426	0.0182	1.2963	12	-0.0402	0.0218	1.3419
10	-0.0456	0.0119	1.2049	11	-0.0398	0.0176	1.2963	12	-0.0375	0.0210	1.3420

F

#	x(m)	y(m)	z(m)	#	x(m)	y(m)	z(m)	#	x(m)	y(m)	z(m)
10	-0.0420	0.0118	1.2049	11	-0.0366	0.0168	1.2963	12	-0.0346	0.0200	1.3420
10	-0.0378	0.0116	1.2049	11	-0.0330	0.0157	1.2963	12	-0.0313	0.0187	1.3420
10	-0.0332	0.0111	1.2049	11	-0.0291	0.0144	1.2963	12	-0.0276	0.0172	1.3420
10	-0.0281	0.0102	1.2049	11	-0.0247	0.0127	1.2963	12	-0.0235	0.0153	1.3420
10	-0.0226	0.0089	1.2049	11	-0.0200	0.0106	1.2964	12	-0.0191	0.0130	1.3421
10	-0.0165	0.0070	1.2049	11	-0.0149	0.0079	1.2964	12	-0.0144	0.0101	1.3421
10	-0.0100	0.0044	1.2050	11	-0.0096	0.0046	1.2964	12	-0.0094	0.0067	1.3421
10	-0.0032	0.0010	1.2050	11	-0.0039	0.0007	1.2964	12	-0.0042	0.0026	1.3421
10	0.0038	-0.0034	1.2050	11	0.0020	-0.0040	1.2964	12	0.0012	-0.0022	1.3421
10	0.0110	-0.0088	1.2049	11	0.0081	-0.0094	1.2964	12	0.0068	-0.0077	1.3421
10	0.0184	-0.0152	1.2049	11	0.0144	-0.0156	1.2963	12	0.0126	-0.0139	1.3420
10	0.0249	-0.0213	1.2048	11	0.0200	-0.0215	1.2962	12	0.0177	-0.0198	1.3420
10	0.0306	-0.0272	1.2047	11	0.0249	-0.0270	1.2961	12	0.0221	-0.0255	1.3419
10	0.0356	-0.0327	1.2045	11	0.0293	-0.0322	1.2960	12	0.0260	-0.0307	1.3418
10	0.0400	-0.0379	1.2044	11	0.0331	-0.0370	1.2959	12	0.0296	-0.0355	1.3417
10	0.0437	-0.0427	1.2042	11	0.0365	-0.0414	1.2957	12	0.0327	-0.0398	1.3415
10	0.0471	-0.0470	1.2040	11	0.0395	-0.0454	1.2956	12	0.0355	-0.0438	1.3414
10	0.0500	-0.0510	1.2039	11	0.0421	-0.0491	1.2955	12	0.0380	-0.0473	1.3413
10	0.0526	-0.0545	1.2037	11	0.0444	-0.0523	1.2953	12	0.0402	-0.0505	1.3412
10	0.0549	-0.0576	1.2036	11	0.0464	-0.0553	1.2952	12	0.0421	-0.0533	1.3411
10	0.0569	-0.0604	1.2034	11	0.0482	-0.0578	1.2951	12	0.0438	-0.0558	1.3410
10	0.0587	-0.0628	1.2033	11	0.0497	-0.0601	1.2950	12	0.0453	-0.0580	1.3409
10	0.0602	-0.0649	1.2032	11	0.0511	-0.0621	1.2949	12	0.0466	-0.0599	1.3408
10	0.0614	-0.0667	1.2031	11	0.0522	-0.0638	1.2948	12	0.0477	-0.0616	1.3407
10	0.0625	-0.0683	1.2030	11	0.0532	-0.0653	1.2948	12	0.0487	-0.0631	1.3406
10	0.0635	-0.0696	1.2029	11	0.0541	-0.0666	1.2947	12	0.0495	-0.0643	1.3406
10	0.0643	-0.0708	1.2029	11	0.0548	-0.0677	1.2946	12	0.0502	-0.0654	1.3405
10	0.0649	-0.0718	1.2028	11	0.0554	-0.0687	1.2946	12	0.0508	-0.0663	1.3405
10	0.0655	-0.0726	1.2028	11	0.0559	-0.0695	1.2945	12	0.0513	-0.0671	1.3404
10	0.0660	-0.0733	1.2027	11	0.0564	-0.0702	1.2945	12	0.0518	-0.0678	1.3404
10	0.0665	-0.0740	1.2027	11	0.0568	-0.0709	1.2945	12	0.0522	-0.0685	1.3404
10	0.0669	-0.0746	1.2026	11	0.0572	-0.0715	1.2944	12	0.0526	-0.0691	1.3403
10	0.0673	-0.0752	1.2026	11	0.0576	-0.0721	1.2944	12	0.0530	-0.0697	1.3403
10	0.0677	-0.0758	1.2026	11	0.0579	-0.0727	1.2944	12	0.0534	-0.0702	1.3403
10	0.0682	-0.0763	1.2025	11	0.0585	-0.0732	1.2943	12	0.0539	-0.0707	1.3403
10	0.0689	-0.0764	1.2025	11	0.0591	-0.0734	1.2943	12	0.0545	-0.0709	1.3402
10	0.0696	-0.0762	1.2025	11	0.0598	-0.0732	1.2943	12	0.0552	-0.0707	1.3403
10	0.0700	-0.0757	1.2026	11	0.0603	-0.0727	1.2944	12	0.0557	-0.0702	1.3403
10	0.0702	-0.0750	1.2026	11	0.0605	-0.0720	1.2944	12	0.0558	-0.0695	1.3403
10	0.0700	-0.0743	1.2027	11	0.0603	-0.0713	1.2944	12	0.0557	-0.0688	1.3404
10	0.0696	-0.0737	1.2027	11	0.0599	-0.0707	1.2945	12	0.0553	-0.0683	1.3404
10	0.0693	-0.0731	1.2027	11	0.0596	-0.0701	1.2945	12	0.0550	-0.0676	1.3404
10	0.0688	-0.0724	1.2028	11	0.0592	-0.0694	1.2945	12	0.0546	-0.0670	1.3404
10	0.0684	-0.0717	1.2028	11	0.0587	-0.0687	1.2946	12	0.0542	-0.0663	1.3405
10	0.0679	-0.0708	1.2029	11	0.0582	-0.0678	1.2946	12	0.0537	-0.0654	1.3405
10	0.0672	-0.0698	1.2029	11	0.0577	-0.0668	1.2947	12	0.0532	-0.0645	1.3406
10	0.0665	-0.0686	1.2030	11	0.0570	-0.0657	1.2947	12	0.0525	-0.0634	1.3406
10	0.0656	-0.0672	1.2031	11	0.0562	-0.0644	1.2948	12	0.0518	-0.0621	1.3407
10	0.0646	-0.0655	1.2032	11	0.0553	-0.0628	1.2949	12	0.0509	-0.0606	1.3408

F

#	x(m)	y(m)	z(m)	#	x(m)	y(m)	z(m)
13	0.0458	-0.0569	1.3867	13	-0.0327	0.0235	1.3876
13	0.0447	-0.0550	1.3868	13	-0.0296	0.0219	1.3877
13	0.0435	-0.0528	1.3868	13	-0.0262	0.0202	1.3877
13	0.0421	-0.0503	1.3869	13	-0.0224	0.0181	1.3877
13	0.0405	-0.0475	1.3870	13	-0.0183	0.0156	1.3878
13	0.0387	-0.0443	1.3871	13	-0.0140	0.0125	1.3878
13	0.0366	-0.0408	1.3872	13	-0.0094	0.0089	1.3878
13	0.0344	-0.0368	1.3874	13	-0.0046	0.0046	1.3878
13	0.0319	-0.0324	1.3875	13	0.0004	-0.0003	1.3878
13	0.0291	-0.0275	1.3876	13	0.0056	-0.0058	1.3878
13	0.0260	-0.0221	1.3877	13	0.0109	-0.0122	1.3878
13	0.0227	-0.0163	1.3877	13	0.0155	-0.0182	1.3877
13	0.0190	-0.0098	1.3878	13	0.0194	-0.0239	1.3876
13	0.0150	-0.0028	1.3878	13	0.0230	-0.0292	1.3875
13	0.0104	0.0045	1.3878	13	0.0262	-0.0340	1.3874
13	0.0056	0.0110	1.3878	13	0.0291	-0.0383	1.3873
13	0.0007	0.0166	1.3877	13	0.0317	-0.0422	1.3872
13	-0.0043	0.0212	1.3877	13	0.0341	-0.0456	1.3871
13	-0.0092	0.0249	1.3876	13	0.0362	-0.0488	1.3870
13	-0.0140	0.0279	1.3876	13	0.0380	-0.0515	1.3869
13	-0.0185	0.0303	1.3875	13	0.0397	-0.0539	1.3868
13	-0.0227	0.0321	1.3875	13	0.0411	-0.0561	1.3867
13	-0.0265	0.0333	1.3874	13	0.0424	-0.0579	1.3866
13	-0.0301	0.0340	1.3874	13	0.0434	-0.0596	1.3866
13	-0.0332	0.0344	1.3874	13	0.0444	-0.0610	1.3865
13	-0.0360	0.0345	1.3874	13	0.0452	-0.0622	1.3864
13	-0.0383	0.0344	1.3874	13	0.0459	-0.0632	1.3864
13	-0.0404	0.0342	1.3874	13	0.0465	-0.0641	1.3864
13	-0.0421	0.0340	1.3874	13	0.0470	-0.0649	1.3863
13	-0.0435	0.0338	1.3874	13	0.0475	-0.0655	1.3863
13	-0.0446	0.0336	1.3874	13	0.0479	-0.0662	1.3863
13	-0.0455	0.0334	1.3874	13	0.0483	-0.0667	1.3862
13	-0.0462	0.0332	1.3874	13	0.0487	-0.0673	1.3862
13	-0.0468	0.0329	1.3874	13	0.0491	-0.0679	1.3862
13	-0.0471	0.0326	1.3875	13	0.0496	-0.0683	1.3862
13	-0.0473	0.0323	1.3875	13	0.0502	-0.0685	1.3862
13	-0.0473	0.0319	1.3875	13	0.0508	-0.0683	1.3862
13	-0.0473	0.0316	1.3875	13	0.0513	-0.0678	1.3862
13	-0.0472	0.0312	1.3875	13	0.0515	-0.0671	1.3862
13	-0.0470	0.0309	1.3875	13	0.0513	-0.0665	1.3862
13	-0.0465	0.0305	1.3875	13	0.0510	-0.0659	1.3863
13	-0.0459	0.0302	1.3875	13	0.0506	-0.0653	1.3863
13	-0.0451	0.0298	1.3875	13	0.0502	-0.0647	1.3863
13	-0.0441	0.0293	1.3875	13	0.0498	-0.0640	1.3864
13	-0.0429	0.0287	1.3875	13	0.0494	-0.0632	1.3864
13	-0.0414	0.0279	1.3876	13	0.0489	-0.0623	1.3864
13	-0.0397	0.0271	1.3876	13	0.0483	-0.0612	1.3865
13	-0.0377	0.0260	1.3876	13	0.0476	-0.0600	1.3865
13	-0.0354	0.0248	1.3876	13	0.0468	-0.0586	1.3866

F

APPENDIX F

F.1. SOURCE CODE: FEATURES AND DOWNLOAD

The code used for the simulation of multi-dimensional, metastable condensing flows can be found on the SU2 portal, at the link https://github.com/su2code/SU2, in two branches, *feature_2phase* and *feature_turbo2phase*. In particular, the branch *feature_2phase* features:

1. High-order resolution schemes for the two-phase solver

2. RANS equations (SA, SST models)

3. Classical nucleation theory, models for J and G as in Appendix C.2

4. PRSV (Peng-Robinson, SV modification) equation of state

5. Coupling with an external thermodynamic library [20] for the simulation of generic fluids

In order to execute the code in this branch, it is required to install the thermodynamic library used, see http://www.asimptote.nl/software/fluidprop. Note that discrete adjoint optimization cannot be carried out in this branch, as the library variables are not updated for automatic differentiation.

The branch *feature_turbo2phase* features:

1. High-order resolution schemes for the two-phase solver

2. RANS equations (SA, SST models)

3. Classical nucleation theory, models for J and G as in Appendix C.2

4. PRSV (Peng-Robinson, SV modification) equation of state

5. Liquid thermodynamic models hard-coded for the fluids H_2O, CO_2, according to references [4, 7]

6. Routines for the evaluation of turbomachinery performance (single cascade)

7. Coupling with the discrete adjoint for design optimization (single cascade)

No additional libraries are required to work with this branch. For fluids other than H_2O and CO_2, liquid properties has to be implemented manually.

REFERENCES

[1] A. Gerber and M. Kermani, *A pressure based eulerian–eulerian multi-phase model for non-equilibrium condensation in transonic steam flow,* International Journal of Heat and Mass Transfer **47**, 2217 (2004), elsevier BV.

[2] M. Giordano, S. Hercus, and P. Cinnella, *Effects of modelling uncertainties in condensing wet-steam flows through supersonic nozzles,* V European Conference on Computational Fluid Dynamics ECCOMAS, Lisbon, Portugal (2010).

[3] S. Dykas and W. Wróblewski, *Numerical modelling of steam condensing flow in low and high-pressure nozzles,* International Journal of Heat and Mass Transfer **55**, 6191 (2012), elsevier BV.

[4] W. Wagner *et al.*, *IAPWS industrial formulation 1997 for the thermodynamic properties of water and steam,* (2008) pp. 7–150, springer Science + Business Media.

[5] G. Gyarmathy, *Nucleation of steam in high-pressure nozzle experiments,* Proceedings of the Institution of Mechanical Engineers, Part A: Journal of Power and Energy **219**, 511 (2005).

[6] L. Azzini, T. P. Van Der Stelt, and M. Pini, *Numerical investigation of metastable condensing flows with an implicit upwind method,* in *ECCOMAS Congress - Proceedings of the 7th European Congress on Computational Methods in Applied Sciences and Engineering*, Vol. 4 (2016) pp. 7165–7181.

[7] G. Theis, *Spontankondensation in übersättigten Dampfströmungen von Kohlendioxid und von Difluordichlormethan*, Ph.D. thesis, Uni Karlsruhe (1985).

[8] G. Gyarmathy, *Grundlagen einer Theorie der Naßdampfturbine*, Phd thesis, Eidgenössischen technischen hochschuole, Zurich (1962).

[9] F. Bakhtar, J. B. Young, A. J. White, and D. A. Simpson, *Classical nucleation theory and its application to condensing steam flow calculations,* Proceedings of the Institution of Mechanical Engineers, Part C: Journal of Mechanical Engineering Science **219**, 1315 (2005).

[10] J. Young, *Spontaneous condensationof steam in supersonic nozzles,* PCH. Physicochemical hydrodynamics **3**, 57 (1982).

[11] Y. A. Ryzhov, U. G. Pirumov, and V. N. Gorbunov, *Nonequilibrium Condensation in High-Speed Gas Flows* (New York : Gordon and Breach Science Publishers, 1989).

[12] K. Bier, F. Ehrler, G. Kissau, V. Lippig, and R. Schorsch, *Homogene spontankondensation in expandierenden dampfstrahlen des kältemittels r 22 bei hohen normierten drücken,* Forschung im Ingenieurwesen **43**, 165 (1977).

[13] C. Lettieri, D. Paxson, Z. Spakovszky, and P. Bryanston-Cross, *Characterization of non-equilibrium condensation of supercritical carbon dioxide in a de laval nozzle,* in *Oil and Gas Applications; Supercritical CO2 Power Cycles; Wind Energy*, Vol. 9 (ASME, 2017).

F

[14] D. E. Paxson, *Experimental characterization of condensation behavior for metastable carbon dioxide*, S.m., Massachusetts Institute of Technology, Department of Aeronautics and Astronautics (2016).

[15] L. Azzini, M. Pini, and P. Colonna, *Semi-analytical model for the prediction of the wilson point for homogeneously condensing steam flow,* Internation Journal of Heat and Fluid Flows **70**, 1 (2018).

[16] M. Moore, P. Walters, R. Crane, and B. Davidson, *Predicting the fog-drop size in wet-steam turbines,* in *Proceedings of the IMechE Conference on Heat and Fluid Flow in Steam and Gas Turbine Plant*, paper C37/73 (1973) pp. 101–109.

[17] A. J. White, J. B. Young, and P. T. Walters, *Experimental validation of condensing flow theory for a stationary cascade of steam turbine blades,* Philosophical Transactions of the Royal Society A: Mathematical, Physical and Engineering Sciences **354**, 59 (1996).

[18] S. Dykas, M. Majkut, M. Strozik, and K. Smołka, *Experimental study of condensing steam flow in nozzles and linear blade cascade,* International Journal of Heat and Mass Transfer **80**, 50 (2015).

[19] A. J. White, *A comparison of modelling methods for polydispersed wet-steam flow,* International Journal for Numerical Methods in Engineering **57**, 819 (2003), wiley-Blackwell.

[20] P. Colonna, T. V. der Stelt, and A. Guardone, *Fluidprop (version 3.0.6): A program for the estimation of thermo physical properties of fluids. a computer program since 2004,* (2018).

F

ACKNOWLEDGEMENTS

At first, if I can present a thesis today is thanks to my supervisor and my promotor, that helped me writing every word of it. Thanks for all the time and help you gave me through all these years.

That said, I want to add a few things.

I would like to thank Matteo, Carlo, Mauro and Antonio, for the support and all the advices they gave me. They are extraordinary people, and it was an honour to work with them during these years.

Of course I have to thank all the PhDs I met here at TUDelft, without them I am not sure I would have resisted for so long in here. We had a wonderful time, and I guess we killed quite some bottles at De Atmosfeer. I hope we will have a great time also outside TU, as doctors, eheh (keep in mind while I am writing these lines I am still not sure I will become one...). I will miss you all, and of course, I must organize a nice trip to Turin soon. And for my closest office- and drinking- mates, Stella, Juan, you were just the best. I did not choose you as paranimphs so that you did not have to wear another penguin suite in your life, consider it as a personal favour ;) .

To all the amazing people I had the pleasure to live with in Smitsteeg, Kloksteeg, Rotterdamseweg, Harmenkokslaan, Noordeinde, Van der Kamlaan (I know, I changed quite some houses..) and, last but not least, Bizetstraat 55 and Mahlerstraat 26, my two homes. Such a pity we are all leaving, but I will always remember living there with you. To write these two sentences costed me liters and liters of tears, you know me guys, so don't complain if they are short. Specially you, David, you know I am crying, you little Dickens.

To my family, always very supportive in every moment of my PhD. Devo ammettere che vi ho dato delle notizie abbastanza scioccanti, ma le avete prese sorprendentemente bene. Grazie per il vostro aiuto e supporto in tutti questi anni. Cercherò di chiamare piu spesso...

Last, but not least, I would like to thank my husband. Yes, in these four years I also got married. After I met him I started travelling so much, visiting new places, and I hope we will do it for many years from now. He must have had a lot of patience to deal with me for all this time, but he was always there, and he still is. These are the best years of my life, thank you for making them so special.

CURRICULUM VITÆ

Lucia AZZINI

02/10/1990	Born in Asola, Italy.

WORKING EXPERIENCE

08/2010–09/2010	Intern at Storti s.p.a, Motta Baluffi (Cr), Italy Mechanical design for manufacturing and wooden machinery
12/2018–present	Lube system engineer, GE Avio Aero, Rivalta di Torino, Italy

EDUCATION

2009–2012	Bachelor degree cum laude in Mechanical Engineering Universita degli studi di Brescia, Italy GPA: 3.95/4, N. exams *cum laude*: 8/21
2012–2014	Master degree cum laude in Mechanical Engineering - specialization in Energy Universita degli studi di Brescia, Italy GPA: 3.99/4, N. exams *cum laude*: 8/11
2014-2018	PhD. Aerospace Engineering Delft University of Technology

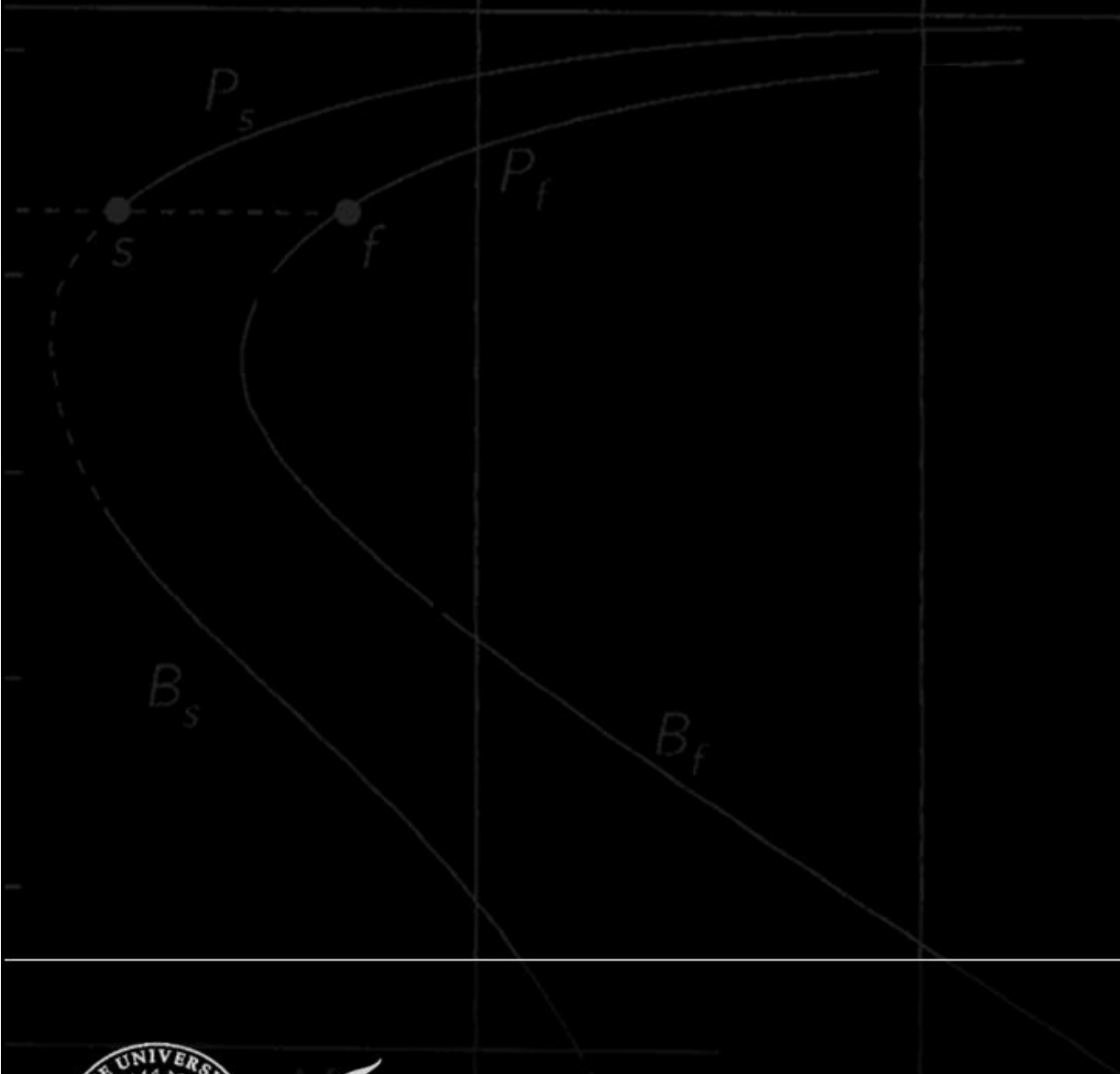|	
Thesis:	Numerical investigation of dense condensing flows for next-generation power units
Promotor:	Prof. dr. P. Colonna
Co-promotor:	Dr. M. Pini

AWARDS

2013	Prize from Rotary Club Brescia Franciacorta Oglio

PUBLICATIONS

5. **M. Pini, L. Azzini, S. Vitale, P. Colonna**, *A two-phase discrete adjoint method applied to the shape optimization of steam turbine cascades*, submitted to the Journal of Turbomachinery.

4. **L. Azzini, M. Pini, P. Colonna** (2018), *Semi-analytical model for the prediction of the Wilson point for homogeneously condensing steam flows*, International Journal of Heat and Fluid Flow, vol 70, pages 1–14.

3. **L. Azzini, M. Pini** (2017), *Numerical investigation of high pressure condensing flows in supersonic nozzles*, Journal of Physics: Conference Series, vol 821, pag. 012008

2. **L. Azzini, M. Pini, T. van der Stelt** (2016), *Numerical investigation of metastable condensing flows with an implicit upwind method*, Proceedings of the VII European Congress on Computational Methods in Applied Sciences and Engineering, vol 4, pag.7165-7181, June 5 - 10, Crete, Greece.

1. **C. De Servi, L. Azzini, M. Pini, A. Gangoli Rao, P. Colonna** (2017), *Exploratory assessment of a Combined-Cycle engine for future passenger aircraft*, Proceedings of the 1st Global Power and Propulsion Forum, Zurich, Switzerland, pag. 16–18